Acta Pharmacologica Sinica (2011) 32: 1085–1086
 1671-4083/11 $32.00
www.nature.com/aps

Research Highlight

Castration reverses immunosenescence in aged mice

Shang-xue YAN, Wei WEI*

Acta Pharmacologica Sinica (2011) 32: 1085–1086; doi: 10.1038/aps.2011.110; published online 1 Aug 2011

The increasing aged population poses new challenges to healthcare systems. The elderly frequently suffers from severe infections and end-stage organ disease, which are associated with an age-dependent decline in immune reactivity[1, 2]. Immunosenescence, defined as the changes in the immune system associated with age, is gathering interest in the scientific and healthcare communities alike.

Immunosenescence is generally related with weaker immune responses, which produce a progressive deterioration in the ability to respond to new stimulants. One might expect the elderly to be less reactive against transplanted organs than younger patients, thus to show better transplant outcomes. It is reasonable to assume that older individuals would be more easily rendered tolerant of transplanted organs[3]. Paradoxically, experimental studies and clinical data of organ transplantation have shown that the graft is more rapidly rejected in the elderly than in the younger. Thus, the age-related muting of the immune responses does not improve tolerance induction and reduce rejection after cell or organ transplantation. The effects of aging on acute and chronic allograft rejection have been extensively studied[4]. Many researches showed that the effects of immunosenescence on the induction of tolerance is one of the major factors[5].

How does immunosenescence affect the transplantation tolerance? Experimental and clinical studies have shown that reversion or blockade of age-related atrophy of the thymus might be one of the promising therapeutic measures to reconstitute immune functions in the elderly. In mice, transplantation of aged thymuses into juvenile recipients led to reconstruction of the structure and function of the thymus[6]. Recently, Zhao and colleagues[7] showed that surgical and chemical castration could restore the induction of transplant tolerance in aged mice. The authors found that old mice (age of 12 months) exhibited resistance to tolerance induction for cardiac transplants even after the anti-CD45RB monoclonal antibody therapy, in contrast to the robust tolerance induced in young mice (2 months). Surgical castration could lead to long-term graft acceptance and restoration of thymic cellularity. Furthermore, they found similar results from prostate cancer patients who received Lupron Depot injections, which could temporarily disrupt gonadal function. Both surgical and chemical castration could restore thymic architecture, increase thymic weight and numbers of developing regulating T cells (Treg) in aged mice (Figure 1). The tolerance-restorative effects of gonadectomy and hormonal suppression (with antiCD25 treatment) would not happen in aged mice with thymectomy or Treg depletion. These results indicated that surgical castration or Lupron Depot injections could restore the thymic function and promote transplant tolerance-induction, reverse the inhibition of transplantation tolerance by immunosenescence in aged mice.

In the aged, the thymus undergoes progressive involution, and the output of new cells significantly falls, which results in decreased thymic output of naïve T cells and decreased concentration of these cells in peripheral blood and lymph nodes[8]. Naïve T cells from aged mice exhibit reduced activation, differentiation and cytokine production following antigen presentation[9]. These age-associated changes in cell-mediated immunity strongly depend on thymic functions. Transplanting cultured thymic fragments to patients with DiGeorge syndrome who lack a functional thymus has been proved successful[6] and may be an approach to restore naïve T lymphocyte numbers in the elderly. Zhao' study showed that surgical and chemical castration could promote the restoration of thymic architecture, increase the thymus weight and the absolute numbers of Treg (CD4+Foxp3+) thymocytes, and reduced the graft rejection. Their results suggest that endocrine modulation could represent a potential therapy to modify age-induced thymic involution.

Sex steroids may have a direct effect on immune function in the periphery by augmenting Treg and other peripheral T cell functions. However, increased levels of sex hormones may cause thymus involution[10]. Luteinizing hormone-releasing hormone (LHRH) synthesized in the hypothalamus is transported to

Institute of Clinical Pharmacology, Anhui Medical University, Key Laboratory of Anti-inflammatory and Immunopharmacology of Education Ministry of China, Hefei, 230032, China
Correspondence: Prof Wei WEI
(wwei@ahmu.edu.cn)

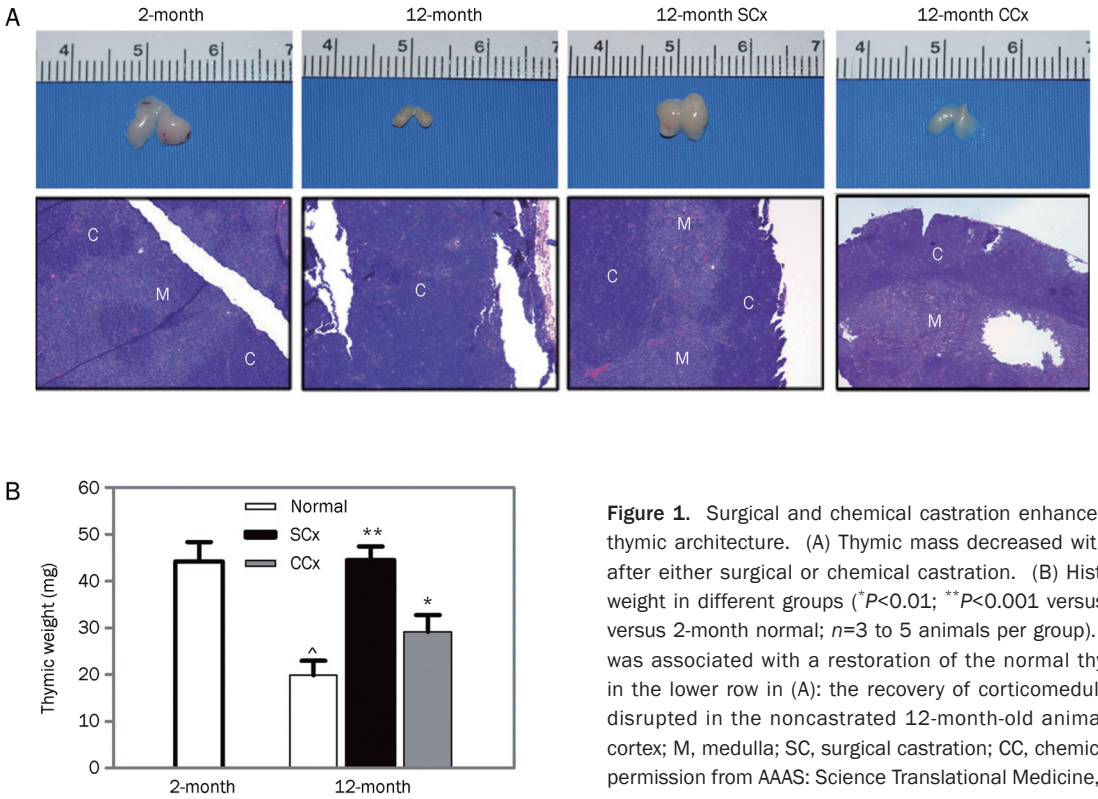

Figure 1. Surgical and chemical castration enhanced thymic mass and restored thymic architecture. (A) Thymic mass decreased with age. The mass increased after either surgical or chemical castration. (B) Histograms showing the thymic weight in different groups ($^{*}P<0.01$; $^{**}P<0.001$ versus 12-month normal; $^{\wedge}P<0.01$ versus 2-month normal; n=3 to 5 animals per group). The increased thymic mass was associated with a restoration of the normal thymic architecture as shown in the lower row in (A): the recovery of corticomedullary differentiation that was disrupted in the noncastrated 12-month-old animal (H&E staining, ×100). C, cortex; M, medulla; SC, surgical castration; CC, chemical castration. Reprinted with permission from AAAS: Science Translational Medicine, copyright 2011.

the anterior pituitary, where it controls the synthesis and release of luteinizing hormone (LH) and follicle-stimulating hormone (FSH), which govern the synthesis of gonadal steroids. Gonadal steroids have negative effects on the thymus and bone marrow, while LHRH itself is a positive immunomodulator. Using LHRH analogues or gonadectomy could reverse age-related thymic atrophy[11]. In Zhao's study, the results verified that Lupron-mediated gonadal suppression could restore the transplantation tolerance induction.

The mechanisms underlying immunosenescence is complex and not completely understood. Multiple factors, such as oxidative stress, gender differences, innate immunity, humoral and cellular immunity, thymus atrophy and persistent microbial infections, may contribute to immunosenescence[5]. Zhao' study has made an important progress in the treatment of immunosenescence, and established an effective therapeutic protocol for restoration of transplantation tolerance in aged mice, and afforded a potential approach to organs transplantation of the elders. Although it's hard to extrapolate a mouse's age to a human's, their results suggest that hormone modification may improve transplant acceptance in older patients by restoring exuberance in the immune system.

1 Agarwal S, Busse PJ. Innate and adaptive immunosenescence. Ann Allergy Asthma Immunol 2010; 104: 183–90.
2 Burns EA, Leventhal EA. Aging, immunity, and cancer. Cancer Control 2000; 7: 513–22.
3 Salama AD, Remuzzi G, Harmon WE, Sayegh MH. Challenges to achieving clinical transplantation tolerance. J Clin Invest 2001; 108: 943-8.
4 Martins PN, Pratschke J, Pascher A, Fritsche L, Frei U, Neuhaus P, *et al*. Age and immune response in organ transplantation. Transplantation 2005; 79: 127–32.
5 Ongrádi J, Kövesdi V. Factors that may impact on immunosenescence: an appraisal. Immun Ageing 2010; 7: 7.
6 Markert ML, Boeck A, Hale LP, Kloster AL, McLaughlin TM, Batchvarova MN, *et al*. Transplantation of thymus tissue in complete DiGeorge syndrome. N Engl J Med 1999; 341: 1180–9.
7 Zhao G, Moore DJ, Kim JI, Lee KM, O'Connor MR, Duff PE, *et al*. Inhibition of transplantation tolerance by immune senescence is reversed by endocrine modulation. Sci Transl Med 2011; 3: 87ra52.
8 Gruver AL, Hudson LL, Sempowski GD. Immunosenescence of ageing. J Pathol 2007; 211: 144–56.
9 Haynes L, Eaton SM, Burns EM, Randall TD, Swain SL. Newly generated CD4 T cells in aged animals do not exhibit age-related defects in response to antigen. J Exp Med 2005; 201: 845–51.
10 Hince M, Sakkal S, Vlahos K, Dudakov J, Boyd R, Chidgey A. The role of sex steroids and gonadectomy in the control of thymic involution. Cell Immunol 2008; 252: 122–38.
11 Sutherland JS, Goldberg GL, Hammett MV, Uldrich AP, Berzins SP, Heng TS, *et al*. Activation of thymic regeneration in mice and humans following androgen blockade. J Immunol 2005; 175: 2741–53.

Acta Pharmacologica Sinica (2011) 32: 1087–1088
 1671-4083/11 $32.00
www.nature.com/aps

Research Highlight

Blocking NMDA receptor at rest: a possible alleviation of depression

Wei LU

Acta Pharmacologica Sinica (2011) 32: 1087–1088; doi: 10.1038/aps.2011.113; published online 1 Aug 2011

Depression is a common but serious illness, which is described as a state of low mood or mood disorder that involves feelings of sadness lasting for two weeks or longer[1]. Depressed people may suffer from a spectrum of syndromes, including change of sleep habitation or pattern, dramatic weight loss, cognitive impairments or even suicide. One conventional antidepressant medication is selective serotonin re-uptake inhibitor[2, 3]. However, the weeks delay of its efficacy constitutes the major drawback of this treatment[3]. Therefore, fast-acting antidepressants are urgently needed for clinical treatment of depression. Autry *et al* reported in a recent issue of *Nature* that *N*-methyl-*D*-aspartate receptor (NMDAR) antagonists could be such candidates by triggering rapid behavioural antidepressant responses[4].

It was previously observed that patients with major depressive disorder symptoms could be relieved shortly after a single low-dose intravenous infusion of ketamine, a non-competitive NMDAR antagonist, with the effects lasting up to two weeks[5, 6]. This exciting observation inspires the authors to investigate the underlying cellular mechanisms. The authors first found that non-competitive NMDAR antagonists ketamine, CPP and MK-801 reduced immobility of wiled-type C57BL/6 mice in notable behavioural responses, such as the forced swim test (FST) and novelty-suppressed feeding (NSF), and the antidepressant-like behavioural effects of ketamine and CPP emerged as early as 30 min after the administration and persisted for at least 24 h. Because NMDAR antagonists applied acutely *in vivo* are eliminated within hours, it is more likely that the long-lasting antidepressant effects come from synaptic plasticity caused by the acute blockade of NMDAR. Brain-derived neurotrophic factor (BDNF) has been proved to be involved in both synaptic plasticity and antidepressant action[7, 8]. This study further demonstrated that fast-acting antidepressant responses required rapid increase in the translation of BDNF protein and TrkB activation, which might in turn initiated synaptic plasticity. Many forms of activity-dependent plasticity require NMDAR activation[9]. Thus, blockade of NMDAR does not seem to be in favor of triggering plasticity that might underlie the fast-acting antidepressant responses.

It has been found that the spontaneous and evoked forms of glutamatergic activity may utilize distinct signaling pathway[10, 11]. It is possible that NMDAR blockade would initiate a different signaling pathway that depends on spontaneous activity. Eukaryotic elongation factor 2 (eEF2) is a critical catalytic factor for ribosomal translation during protein synthesis. It has been proposed that NMDAR activity at rest would affect eEF2 phosphorylation and subsequent translation of target transcripts[12]. The authors demonstrated that ketamine at rest inhibited spontaneous mEPSCs and dose-dependently de-phosphorylated eEF2, allowing translation of target proteins. These results demonstrated that ketamine's rapid antidepressant effect results from inhibition of NMDAR-mediated spontaneous synaptic responses, leading to decreased eEF2K activity and subsequent attenuated eEF2 phosphorylation, which in turn rapidly increases BDNF translation.

The authors elegantly elucidate the cellular mechanisms underlying fast-antidepressant responses of a single, low-dose intravenous infusion of ketamine under clinical treatment and provides the first evidence that tonic resting glutamatergic neurotransmission is involved in behavior. Moreover, this study shed new light on the potential of therapeutic approaches on translational machinery. eEF2 is proposed to be the key molecule involved in synaptic BDNF translation that act downstream of NMDAR blockade and could be novel therapeutic targets for the development of faster-acting antidepressants.

Future challenge will be to examine the possible involvement of extrasynaptic NMDAR blockade in the fast-acting antidepressant responses. Ambient

Department of Neurobiology, Nanjing Medical University, Nanjing, 210029, China
Correspondence: Prof Wei LU
(luweishmu2@yahoo.com.cn)

tonic NMDAR activation by extracellular glutamate has been detected under basal condition[13]. Ketamine can abolish both spontaneous synaptic and extrasynaptic NMDAR responses. Recent evidence suggests that activation of extrasynaptic NMDAR induces neuronal death in pathological conditions, whereas synaptic NMDAR promotes neuronal survival in physiological conditions[14, 15]. Blockade of spontaneous activity of the extrasynaptic NMDARs might be able to trigger a distinct signaling pathway involving eEF2. In addition, previous studies support the involvement of cortical mTOR signaling in ketamine-mediated antidepressant responses and the blockade of the responses by rapamycin[16]. These findings are obviously inconsistent with the results of this study. More works are needed to resolve the discrepancies. Moreover, considering the fundamental roles of NMDAR in neuronal functions, possible side effects should be also mindful if the period of clinical ketamine treatment needs to be prolonged.

1 Frances A. Diagnostic and Statistical Manual of Mental Disorders. 4th ed. Washington, DC: American psychiatric press 2000, p 354–6.
2 Neumeister A, Nugent AC, Waldeck T, Geraci M, Schwarz M, Bonne O, *et al*. Neural and behavioral responses to tryptophan depletion in unmedicated patients with remitted major depressive disorder and controls. Arch Gen Psychiat 2004; 61: 765–73.
3 Berton O, Nestler EJ. New approaches to antidepressant drug discovery: beyond monoamines. Nat Rev Neurosci 2006; 7: 137–51.
4 Autry AE, Adachi M, Nosyreva E, Na ES, Los MF, Cheng P, *et al*. NMDA recepor blockade at rest triggers rapid behavioural antidepressant responses. Nature 2011; 475: 91–5.
5 Berman RM, Cappiello A, Anand A, Oren DA, Heninger GR, Charney DS, *et al*. Antidepressant effects of ketamine in depressed patients. Biol Psychiatry 2000; 47: 351–4.
6 Price RB, Nock MK, Charney DS, Mathew SJ. Effects of intravenous ketamine on explicit and implicit measures of suicidality in treatment-resistant depression. Biol Psychiatry 2009; 66: 522–6.
7 Kovalchuk Y, Hanse E, Kafitz KW, Konnerth A. Postsynaptic induction of BDNF-mediated long-term potentiation. Science 2001; 295: 1729–34.
8 Shirayama Y, Chen AC, Nakagawa S, Russell DS, Duman RS. Brain-derived neurotrophic factor produces antidepressant effects in behavioral models of depression. J Neurosci 2002; 22: 3251–61.
9 Bear MF, Malenka RC. Synaptic plasticity: LTP and LTD. Curr Opin Neurobiol 1994; 4: 389–99.
10 Sutton MA, Schuman EM. Partitioning the synaptic landscape: distinct microdomains for spontaneous and spike-triggered neurotransmission. Sci Signal 2009; 2: pe19.
11 Atasoy D, Ertunc M, Moulder KL, Blackwell J, Chung C, Su J, *et al*. Spontaneous and evoked glutamate release activates two populations of NMDA receptors with limited overlap. J Neurosci 2008; 28: 10151–66.
12 Sutton MA, Taylor AM, Ito HT, Pham A, Schuman EM. Postsynaptic decoding of neural activity: eEF2 as a biochemical sensor coupling miniature synaptic transmission to local protein synthesis. Neuron 2007; 55: 648–61.
13 Sah P, Hestrin S, Nicoll RA. Tonic activation of NMDA receptors by ambient glutamate enhances excitability of neurons. Science 1989; 246: 815–8.
14 Hardingham GE, Fukunaga Y, Bading H. Extrasynaptic NMDARs oppose synaptic NMDARs by triggering CREB shut-off and cell death pathways. Nat Neurosci 2002; 5: 405–14.
15 Hardingham GE, Bading H. The yin and yang of NMDA receptor signalling. Trends Neurosci 2003; 26: 81–9.
16 Li N, Lee B, Liu RJ, Banasr M, Dwyer JM, Iwata M, Li XY, Aghajanian G, Duman RS. mTOR-dependent synapse formation underliers the rapid antidepressant effects of NMDA antagonists. Science 2010; 329: 959–64.

Acta Pharmacologica Sinica (2011) 32: 1089–1099
 1671-4083/11 $32.00
www.nature.com/aps

Review

Death and survival of neuronal and astrocytic cells in ischemic brain injury: a role of autophagy

Min XU[1, 2], Hui-ling ZHANG[1, 2, *]

[1]*Department of Pharmacology and Laboratory of Cerebrovascular Pharmacology, College of Pharmaceutical Science, Soochow University, Suzhou 215123, China;* [2]*Suzhou Institute of Chinese Materia Medica, Suzhou 215007, China*

Autophagy is a highly regulated cellular mechanism that leads to degradation of long-lived proteins and dysfunctional organelles. The process has been implicated in a variety of physiological and pathological conditions relevant to neurological diseases. Recent studies show the existence of autophagy in cerebral ischemia, but no consensus has yet been reached regarding the functions of autophagy in this condition. This article highlights the activation of autophagy during cerebral ischemia and/or reperfusion, especially in neurons and astrocytes, as well as the role of autophagy in neuronal or astrocytic cell death and survival. We propose that physiological levels of autophagy, presumably caused by mild to modest hypoxia or ischemia, appear to be protective. However, high levels of autophagy caused by severe hypoxia or ischemia and/or reperfusion may cause self-digestion and eventual neuronal and astrocytic cell death. We also discuss that oxidative and endoplasmic reticulum (ER) stresses in cerebral hypoxia or ischemia and/or reperfusion are potent stimuli of autophagy in neurons and astrocytes. In addition, we review the evidence suggesting a considerable overlap between autophagy on one hand, and apoptosis, necrosis and necroptosis on the other hand, in determining the outcomes and final morphology of damaged neurons and astrocytes.

Keywords: autophagy; brain ischemia; hypoxia; neuron; astrocyte; apoptosis; necrosis

Acta Pharmacologica Sinica (2011) 32: 1089–1099; doi: 10.1038/aps.2011.50; published online 1 Aug 2011

Introduction

Autophagy is a highly regulated process involving the bulk degradation of cytoplasmic macromolecules and organelles in mammalian cells via the lysosomal system. In addition, autophagy is induced under starvation, differentiation, and normal growth control to maintain homeostasis and survival[1–3]; however, it is also involved in neurodegenerative disorders and can trigger a form of programmed cell death (Type II death) distinct from apoptosis in neurons[4–7]. Accumulating evidence indicates that autophagy is activated and may be involved in the regulation of neuronal death in different animal models of ischemic brain injury, including hypoxia-ischemia (HI) and global and focal ischemia[7–17]. Recently, using a permanent focal cerebral ischemia model of stroke and an oxygen and glucose deprivation (OGD) model in primary cultured astrocytes, the authors show that autophagy is activated in ischemic astrocytes and contributes to astrocytic cell death[18]. Therefore, in this review, we systematically discuss the activation of autophagy during cerebral ischemia and/or reperfusion not only in neurons but also in astrocytes, the role of autophagy in neuronal and astrocytic cell death and survival, and the mechanisms of autophagy activation and its regulation. In addition, we review what is known about the crosstalk between autophagy and apoptosis, between autophagy and necrosis, and between autophagy and necroptosis in determining the outcomes and final morphology of damaged neurons and astrocytes.

* To whom correspondence should be addressed.
E-mail huilingzhang07@hotmail.com
Received 2010-11-22 Accepted 2011-04-08

Different types of neural cell death in the ischemic region

There are three types of neural programmed cell death (PCD) induced by cerebral ischemic and/or hypoxic injury: (1) necrosis, (2) apoptosis, and (3) autophagy.

Neuronal cell death following cerebral ischemia has traditionally been termed necrosis. Necrosis is the end result of a bioenergetic catastrophe that results from ATP depletion to a level incompatible with cell survival and is thought to be initiated mainly by cellular "accidents," such as toxic insults or physical damage (Figure 1E). In contrast to apoptosis, necrosis has traditionally been thought to be a passive form of cell death with more similarities to a train wreck than a suicide. However, recent research has found that necrosis

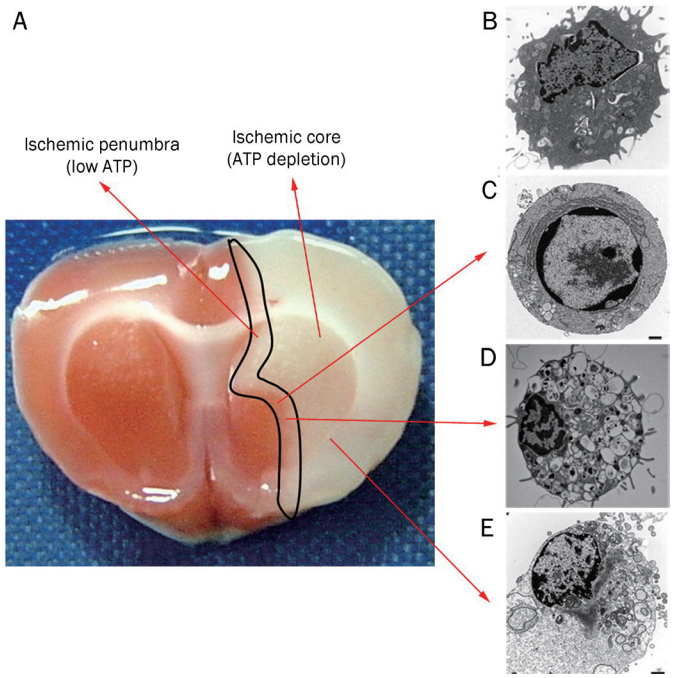

Figure 1. Necrosis, apoptosis and autophagy in focal cerebral ischemia. A: TTC staining showing the ischemic core region (white color) and the ischemic penumbra (periinfarct, A). B, C, D, and E: Electron micrographs[82]. Necrosis is predominant in the ischemic core, whereas apoptosis and autophagy are often observed in the penumbra after focal cerebral ischemia. The main morphological characteristics of necrosis are the vacuolation of the cytoplasm and the breakdown of the plasma membrane (E). Morphologically, apoptosis is characterized by nuclear and cytoplasmic condensation and cellular fragmentation into apoptotic bodies (C). Morphological characteristics of autophagy include vacuolization, degradation of cytoplasmic contents, and slight chromatin condensation (D). B: Normal cell.

is not merely an accident. When caspases were originally identified as the mediators of apoptosis, it was hypothesized that many of their substrates were essential proteins whose destruction ensured the inevitability of cell death. However, caspase-independent cell death is observed in many systems where cells still die even if the executioner is absent. Following an apoptotic stimulus, such as the expression of Bax or treatment with tumor necrosis factor (TNF) or Fas ligand (FasL), the cells will die even in the presence of non-specific caspase inhibitors, such as zVAD-fmk (benzyloxycarbonyl-Val-Ala-Asp(OMe)-fluoromethylketone), or antiapoptotic molecules, such as Bcl-xL, that prevent caspase activation[19, 20]. Under these conditions, the cells that would normally die by apoptosis exhibit all the hallmarks of necrosis. In some cases, caspase-independent necrotic cell death can be forestalled by treatment with antioxidants or by eliminating the activity of the protein kinase receptor-interacting protein (RIP). These results lead to the idea that necrosis could be "programmed" cellular signaling events that initiate necrotic destruction and could be blocked by inhibiting discrete cellular processes. In 2005, Yuan *et al* at Harvard University termed "programmed necrosis" as necroptosis.

Apoptosis is a process of cell suicide regulated by different cell signaling pathways, which consists of a series of biochemical events including cell shrinkage, chromatin condensation, and formation of cytoplasmic blebs and fragmentation of nuclear DNA into membrane-bound structure, called "apoptotic bodies", that contain the contents of the cell (Figure 1C). At the biochemical level, apoptosis of mammalian cells is characterized by phosphatidylserine exposure and effector caspase activation, the main executors of apoptotic cell death. Studies have proven that delayed cell death induced by cerebral ischemia is apoptotic.

Autophagy is a dynamic and carefully regulated process for the intracellular maintenance of proteins, lipids, and aging organelles[21–23]. It is characterized by the formation of autophagic vesicles in the cytoplasm, which contain a great deal of cellular components (macromolecules and organelles, Figure 1D). The degradation of the Golgi apparatus, polyribosomes and endoplasmic reticulum (ER) occurs earlier than nuclear disintegration. During this process, intact mitochondria provide autophagy with the required energy. Research shows that a well-preserved cytoskeleton structure is necessary for autophagic degradation. It has become increasing clear that necrosis predominates in the ischemic core (Figure 1A), whereas apoptosis and autophagy are often observed in the penumbra (Figure 1A) after cerebral ischemia.

Although the roles of apoptosis and necrosis in ischemic and/or hypoxic brain injury have been studied intensively, the implication of autophagic cell death has only recently been considered.

Autophagy is activated in ischemic and/or hypoxic damaged brain tissue

In recent years, through the use of electron microscopy, immunohistochemistry and Western blots, scholars have confirmed from morphological and biochemical evidence that autophagy is activated in the damaged brain tissue in animal models of ischemic and/or hypoxic cerebral injury, including the transient global cerebral ischemia model, hypoxia-ischemia (HI) model and focal cerebral ischemia model (Table 1). The first hint of autophagy activation dates back to 1995, when using electron microscopic analysis in a transient global cerebral ischemia model in gerbils, researchers found that the volume density of cathepsin B-positive lysosomes markedly increased 3 d after the ischemic insult, while that of autophagic vacuole-like structures also increased at this stage, suggesting that the cathepsin B-immunopositive lysosomes that increase in the neurons after ischemic insult are mostly autolysosomes. Further studies have demonstrated that the delayed death of the CA1 pyramidal neurons after brief ischemia is not necrotic but apoptotic[8]. However, before 2005, there are relatively few examples of neuronal death that meet the necessary morphological criteria of autophagy. One possible reason is that, until recently, sensitive markers for autophagy, similar to those existing for apoptosis, have not been available. Currently, there is increasing interest in whether autophagic cell death

Table 1. Autophagy is activated after ischemic (hypoxic) brain injury.

Model	Sites	Autophagy activation marker	Lysosome activation marker	Reference
Transient global cerebral ischemia in gerbils	Damaged hippocampus	Electron microscopy: autophagic vesicle-like structure in the cytoplasm↑	Electron microscopy: the volume density of cathepsin B-positive lysosomes↑	[8]
Ischemia-hypoxia in mice	Damaged brain tissue	Western blot: LC3-II↑		[9] [10]
Ischemia-hypoxia in mice	Damaged brain tissue	Electron miroscopy: autophagic vesicle↑ Immunofluorescence: punctate GFP-LC3 Western blot: LC3-I↓		[11] [12]
Ischemia-hypoxia in neonatal rats	Damaged cortex and hippocampus	Immunohistochemistry and Western blot: beclin1 in the neurons↑		
Ischemia-hypoxia in neonatal rats	Damaged brain tissue	Electron microscopy: autophagic vesicle↑ Immunohistochemistry and Western blot: LC3-II↑; or punctate GFP-LC3	Immunohistochemistry and Western blot: LAMP1↑; cathepsin D↑; activity of acid phosphatase (AP) and β-*N*-acetylhexosaminidase (AcHex)↑ Double-label immunofluorescence: punctate LC3 and LAMP1 or cathepsin D co-expression	[13]
Ischemia-hypoxia in neonatal mice (Atg7 deficit)	Damaged brain tissue	Electron microscopy: autophagic vesicle↑ Immunohistochemistry and Western blot: LC3-II↑; or punctate GFP-LC3		[7]
Permanent middle cerebral artery occlusion in rats	Damaged brain tissue	Electron microscopy: autophagic vesicle↑; autolysosome↑ Western blot: LC3-II↑	Electron microscopy: darkened lysosomes Western blot: cathepsin B↑	[17]
Transient middle cerebral artery occlusion in mice	Damaged brain tissue	Western blot: LC3-II↑		[14]
Transient middle cerebral artery occlusion in rats (ischemia/reperfusion)	Neurons in damaged brain tissue and periinfarct	Western blot: Beclin1↑ Double-lable immunofluorescence: Beclin1↑; punctate LC3↑; Beclin1 and caspase 3 co-expression		[15]
Transient middle cerebral artery occlusion in neonatal mice (ischemia/reperfusion)	Damaged brain tissue and periinfarct	Electron microscopy: autophagic vesicle↑ Immunohistochemistry: punctate LC3↑	Immunohistochemistry: LAMP1↑; cathepsin D↑	[16]
Permanent middle cerebral artery occlusion in rats	Astrocytes in damaged brain tissue	Electron microscopy: autophagic vesicle↑; autolysosome↑; lysosome↑		[18]
Oxygen-glucose deprivation in primary cultured astrocytes	Primary cultured brain cortex astrocytes	Electron microscopy: autophagic vesicle↑; autolysosome↑; lysosome↑ Western blot: LC3-II↑; Beclin1↑ Immunohistochemistry: punctate LC3↑ MDC-labeled fluorescent vacuoles↑	Western blot: cathepsin B↑, LAMP2↑	[18]

might be involved in the regulation of neuronal or astrocytic cell death after ischemia, especially after ischemic-hypoxic and focal cerebral ischemic injury.

The activation of autophagy induced by HI has been intensively investigated. The extent of ischemic-hypoxic injury depends on the degree of maturation of the brain as well as

on the severity and duration of the insult[24–30]. Neurons in the immature brain can tolerate a longer period of oxygen deprivation and/or ischemia than the neurons in the adult brain[25, 27]. However, there are conflicting reports that show that the immature brain is less resistant to ischemic-hypoxic brain damage than its adult counterpart[28]. Furthermore, clinical data suggest that outcome and mortality after acute cerebral injury are age-dependent, with more severe injuries in infants than in adults[31, 32]. In 2005, Zhu *et al* have found that after unilateral HI, the autophagosome-related marker microtubule-associated protein 1 light chain 3-II (LC3-II) is three times more pronounced in adult brains, compared with immature brains, indicating for the first time that autophagy is involved in delayed cell death after cerebral ischemia[9]. Sex-related differences in cerebral injury and outcome following cerebral stroke or trauma have been considered attributable to the differences in brain structure and function induced by estrogen[33]. In 2006, another report from Zhu *et al* showed that there are no sex differences in cerebral injury and LC3-II increases after a severe ischemic-hypoxic insult in neonatal mice, suggesting that there is no sex dependence in the induction of autophagy after neonatal HI[10]. Additionally, in 2006, using a modified Levine/Vannucci procedure in adult mice that consists of unilateral common carotid artery occlusion and hypoxia, Adhami *et al* demonstrated that at the tissue level, HI causes persistent cerebral perfusion deficits even after release of the carotid artery occlusion, which is associated with both platelet deposition and fibrin accumulation within the cerebral circulation[11]. At the cellular level, caspase-3 is not activated, and very few cells completed the apoptotic process. Instead, many damaged neurons show features of autophagic/lysosomal cell death. Together, these results suggest that HI is a powerful stimulus for spontaneous coagulation leading to reperfusion deficits and autophagic/lysosomal cell death in the brain. In 2008, Carloni *et al* showed that the autophagy marker, Beclin1, is significantly increased a short time after HI, both in the hippocampus and in the cerebral cortex in the neonatal cerebral HI model[12]. More recently, Ginet *et al* provide strong evidence that severe HI increases not only autophagosomal abundance (increase in LC3-II) but also lysosomal activities (cathepsin D, acid phosphatase, and β-*N*-acetylhexosaminidase) in the cortex and hippocampus, demonstrating an increase in autophagic flux[13].

Increasing evidence demonstrates that autophagy is also activated in damaged brain tissue after focal cerebral ischemia (Table 1). The evidence comes from a 2005 study showing that the expression of autophagy marker LC3-II is increased in damaged brain tissue after transient middle cerebral artery occlusion (tMCAO) in mice[14]. In 2008, by morphological and biochemical analysis, we have confirmed that focal cerebral ischemia activates the autophagosome/lysosome pathway using a rat model of permanent middle cerebral artery occlusion (pMCAO). Electron microscopic analysis has revealed that autophagosomes and autolysosomes are significantly increased in neuronal cytoplasm in the ischemic cortex after pMCAO in rats. Western blot analysis also has shown that the expression of LC3-II and cathepsin B (a main lysosomal protease of the brain parenchyma) are increased in the ischemic cortex[17]. These observations are also supported by Rami *et al*, who showed that a dramatic elevation in Beclin1 and LC3 levels in the penumbra of rats challenged by tMCAO[15], and by Puyal *et al*, who indicated that lysosomal and autophagic activities are increased in the ischemic neurons after transient focal cerebral ischemia[16].

In which cells is autophagy activated in the ischemic region?

Autophagy is activated in neurons in the ischemic region

Accumulating evidence detected by electron microscopic and immunohistochemical analysis shows that autophagy is activated in neurons in the ischemic cerebral tissue in different animal models of ischemic and/or hypoxic cerebral injury, including the transient global cerebral ischemia model, HI and the focal cerebral ischemia model (Table 1).

Evidence from electron microscopy is as follows:

With electron microscopy, the intense vacuolization and numerous autophagosomes are observed in neurons in the ischemic region[8, 11, 13, 17]. More importantly, in an adult mouse HI model, the activation of autophagy in different degrees of neuronal injury has been examined in detail. Cortical neurons on the challenged side show vacuole-associated damage ranging from cells harboring multiple cytoplasmic vacuoles (Figure 2C) to cells completely lacking cytoplasmic contents (Figure 2F). There is also diffuse myelin degeneration and loss of synapses (Figure 2, compare B with G). In less damaged neurons, judging from the morphology of healthy mitochondria, there are many vacuole-related structures containing electron-dense material (Figure 2D, avd) or whorls of membranous material (Figure 2D and 2E; avm). More severely damaged neurons show condensed chromatin in the nucleus, cup-shaped endoplasmic reticulum fragments, swollen mitochondria, and vacuoles that contain little material (Figure 2G, asterisk) in the cytoplasm. Moreover, many severely damaged neurons exhibit a shrunken nucleus with condensed chromatin surrounded by an extensively lysed cytoplasm but retain an intact plasma membrane (Figure 2F). These morphological features are not typical of apoptosis or necrosis. Instead, they suggest an induction of the autophagosomal-lysosomal compartment of programmed cell death[11]. Furthermore, the time point changes of the activation of autophagy/lysosome in neurons after ischemia has been revealed by electron microscopy by finding autophagosomes and autolysosomes that appear in neurons as early as 1 h after pMCAO and continue to increase from 3 to 12 h. Sometimes, autophagosomes with engulfed organelles are found. At 6 h after ischemia, damaged neurons display fragmented ER membranes and condensed chromatin. At 24 h after ischemia, cell shrinkage, large chromatin clumps, nuclear condensation/fragmentation, swollen cytoplasm, damaged organelles and deteriorated membranes co-exist in the same neuron[17]. In addition, intense vacuolization and numerous autophagosomes appear at 6 h post-HI and are

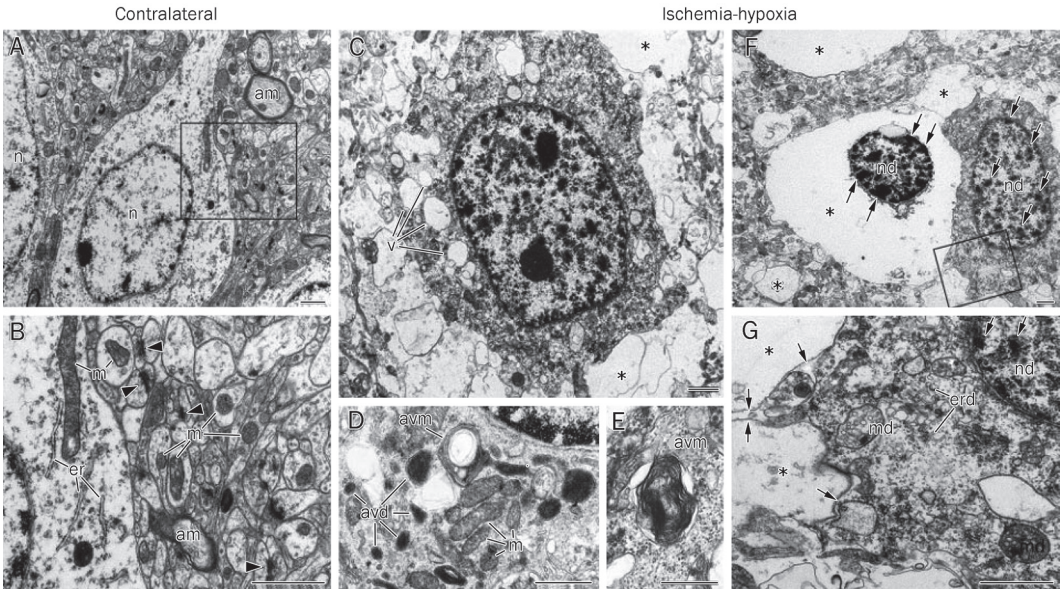

Figure 2. Ischemia-hypoxia induces vacuolization and lysis of cellular organelles. A and B: Contralateral hemisphere illustrates normal structures of neuronal cell bodies and the neuropil. Notice homogenous nuclear chromatin (n), myelinated axons (am), intact mitochondria (m), cisterns of endoplasmic reticulum (er), and numerous synapses (arrowheads). C–G: Damaged neurons in the cerebral cortex at 6 h after ischemia-hypoxia show multiple vacuoles (v in C) in the cytoplasm and different degrees of cell destruction. Electron micrographs of the cytoplasm in less damaged neurons (D and E; notice intact mitochondria, m) exhibit autophagy-like vacuoles containing electron-dense material (avd) and whorls of membranous material (avm). In more advanced cell destruction, many cells demonstrate the near-complete lysis of organelles (asterisks in C, F, and G), but the plasma membrane of such cells is preserved (arrows in G). Moderately damaged cells (G) display fragmented endoplasmic reticulum membranes (erd), condensed chromatin (double arrows) in damaged nuclei (nd), and swollen mitochondria (md) containing an electron transparent matrix. Condensation of chromatin (double arrows in F and G) in damaged nuclei might be the result of a proapoptotic reaction or represent aborted apoptosis. B and G represent the enlarged framed areas in A and F, respectively. Scale bars: 1 μm (A–C, F, G); 0.5 μm (D, E). Used with permission from Adhami *et al* whose original article was published in the American Journal of Pathology, Volume 169, Issue 2, August 2006, Pages 566–583 (Copyright © 2006 American Society for Investigative Pathology Published by Elsevier Inc)[11].

more abundant at 24 h in the dying neurons[13].

Evidence from double immunolabeling was observed as follows: An increase in punctate LC3 or Beclin1 is observable in the ischemic neurons by double immunolabeling[12, 13]. This increase in the expression of autophagy markers mainly occurs in the border of the lesion but also in some neurons inside of the lesion[13].

Autophagy is activated in astrocytes in the ischemic region

Whether autophagy is activated in astrocytes in ischemic brain injury and contributes to astrocytic cell death is largely unknown. More recently, using a rat model of pMCAO *in vivo* and OGD in primary cultured astrocytes *in vitro*, the authors have dynamically observed that autophagosomes appear in the cytoplasm of astrocytes in both the ischemic cortex 1 h after pMCAO and the primary astrocytes 1 h after OGD. The most abundant autophagosomes are observed 3 h after pMCAO and OGD. The number of lysosomes is significantly increased 6 h after pMCAO and OGD. Both apoptotic and necrotic morphological features are seen in the same astrocytes 12–24 h after pMCAO and OGD. Autophagic vacuole analysis with MDC (monodansylcadaverine) staining shows that a large number of fluorescent particles appears in the astrocytes 0.5 h after OGD[18] and reaches a peak at 3 h (Figure 3). Western blot analysis in primary cultured astrocytes after OGD

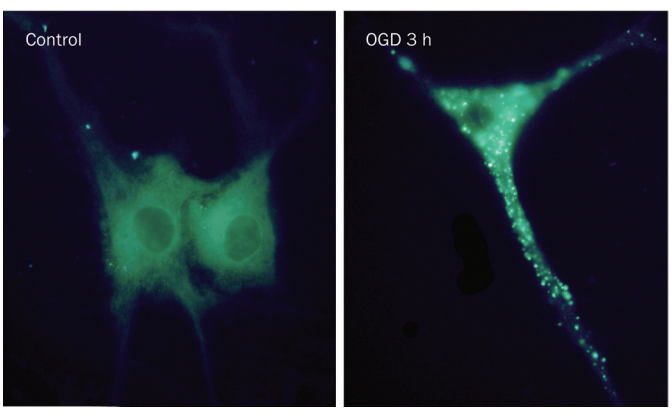

Figure 3. Increased autophagic vacuoles in primary astrocytes after OGD injury. Astrocytes were cultured and labeled with MDC. Representative MDC staining shows MDC-labeled vesicles in the cytoplasm, perinuclear regions and neurites 3 h after OGD, indicating the increased formation of autophagic vacuoles in astrocytes.

demonstrates that autophagy-related proteins LC3 and Beclin1 as well as the lysosomal-related protein cathepsin B and the lysosome associated membrane protein 2 (LAMP2) increase in the injured astrocytes. Taken together, the autophagy/lysosome pathway (ALP) is activated in the ischemic astrocytes in both *in vivo* and *in vitro* ischemic or hypoxic models[18].

Autophagy is activated in endothelial cells in the ischemic region

Autophagy activation has recently been implicated in endothelial cells in the ischemic region. Many blood vessels in the peri-infarct region show a higher level of GFP (green fluorescent protein)-LC3 expression and punctate GFP-LC3 dots in the endothelial cells at 18 h in the HI-induced GFP-LC3 transgenic mice[11].

Mechanisms of autophagy activation in ischemic and/or hypoxic brain injury

Ischemic brain injury causes death in both neurons and astrocytes[34]. Calcium-overload, excitotoxicity, ER stress and oxidative injury, and caspase-mediated apoptosis have been implicated as major injury mechanisms[35, 36].

ER stress and oxidative stress

Previous reports have demonstrated that the ER is involved in ischemic neuronal cell death, protein synthesis inhibition[37, 38], phosphorylation of phospho-extracellular signal-regulated kinase (PERK)[39] and eukaryotic initiation factor 2 alpha (eIF2α)[40], depletion of the ER calcium pool[41], accumulation of unfolded proteins in the ER[42], and induction of the ER molecular chaperone[43]. An increasing number of studies indicates that autophagy is induced by ER stress in organisms from yeast to mammals[44, 45]. Hypoxia activates the ER-resident translation initiation factor eIF2α and PERK, and eIF2α kinase regulates starvation- and virus-induced autophagy.

Another common intracellular stress that effectively leads to the induction of autophagy is oxidative stress. More recently, it has been demonstrated that oxidative stress activates autophagy in dopaminergic neuronal cell lines and cultured primary astrocytes[46–48]. Together, ER stress and oxidative stress may be important mechanisms of autophagy activation in ischemic brain injury. However, there is still a lack of direct evidence.

Excitotoxicity

Glutamate excitotoxicity mediated by *N*-methyl-*D*-aspartic acid (NMDA) receptor activation plays a key role in many aspects of cerebral ischemic injury. Excitotoxicity is the basis for necrotic cell death in the ischemic core and the initiator of programmed cell death in the ischemic penumbra. NMDA agonists induce the activation of autophagy in damaged neurons in the striatum[49]. Excitotoxicity-mediated activation of autophagy may be associated with the activation of the c-Jun N-terminal kinase (JNK) signaling pathway, which is one of the most important NMDA receptor-mediated signal pathways. JNK are mitogen-activated protein kinases encoded by three genes: *Jnk1*, *Jnk2*, and *Jnk3*[50]. Each gene is alternatively spliced to produce one or two variants of 46 and 54 kDa, which generates a total of at least 10 JNK isoforms with potentially different pro-survival and pro-death roles[51]. Among its pro-death roles, JNK has been shown to be important for neuronal death after excitotoxic stress because of its involvement in necrosis and apoptosis[52–54]. In cerebral ischemia, JNK has become an accepted target for neuroprotection because small-molecule inhibitors[55] or cell-penetrating peptides[56, 57] such as D-JNKI1 (d-c-Jun N-terminal kinase 1 inhibitor), a cell-permeable peptide inhibitor of the JNK pathway, have been shown to be a powerful neuroprotective agent after focal cerebral ischemia in adult mice and young rats. D-JNKI1 has also been found to have a potential neuroprotective effect in a clinically relevant model of neonatal cerebral HI and to reduce autophagosome formation in the thalamus, suggesting that the JNK signaling pathway involves HI-induced autophagic cell death[58].

Contributions of autophagy activation to neural cell survival and death in ischemic and/or hypoxic cerebral injury

Mild or moderate activation of autophagy promotes neural cell survival

Autophagy plays a key role in neuronal survival. Knockout mouse studies targeting Atg5 or Atg7 elegantly demonstrate that neurons require at least basal levels of autophagy for the maintenance of health and function *in vivo*[59, 60]. 3-methyladenine (3-MA) and wortmannin, two inhibitors of autophagy, dramatically reduce Beclin1 expression and switch the mechanism of cell death modes from apoptosis to necrosis. Conversely, rapamycin, an inducer of autophagy, augments Beclin1 expression, diminishes necrotic cell death, and decreases brain injury after neonatal HI. A prophylactic treatment with simvastatin or hypoxic preconditioning also up-regulates Beclin1 expression. Taken together, these data indicate that autophagy is increased in neuronal cells after neonatal HI and suggest that the activation of autophagic pathways represents a potential protective mechanism in the early stages of brain injury[12]. Elevated amounts of caspase-3-positive- and Beclin1-positive cells have been found in the penumbra of rats challenged by cerebral ischemia at 6–24 h. However, not all caspase-3-positive cells are also Beclin1-positive and not all Beclin1-expressing cells are caspase-3-positive. Semi-quantitative assessment shows that approximately 30% of cells in the penumbra present both the activation of caspase-3 and the up-regulation of Beclin1, indicating that Beclin1 may possess a repair function via autophagy[15].

Overactivation of autophagy promotes neural cell death

Theoretically, autophagic cell death is caused by lysosomal enzymes; thus, we and other scholars hypothesize that persistent or severe cerebral ischemia overactivates autophagy, which causes cell self-digestion and induces neural cell death. Emerging evidence indicates that ALP activation induced by focal cerebral ischemia contributes to neuronal cell death. Cerebral ventricular microinjection of 3-MA, bafilomycin

A1 [Baf, a specific inhibitor of vacuolar-type H(+)-ATPases], which inhibits fusion between autophagosomes and lysosomes, or Z-FA-fmk (benzyloxycarbonyl-phenyl-alanyl-fluoromethylketone, a cathepsin B and L inhibitor) reduces cerebral infarct volume, decreases brain edema and improves neurological deficits. In addition, 3-MA can largely reduce infarct volume even administered 4 h after ischemia, indicating 3-MA has a wide therapeutic window. Furthermore, 3-MA and Baf significantly reduce the death of astrocytes and play a protective role in astrocytic injury induced by cerebral ischemia in a rat model of pMCAO *in vivo* and in OGD-induced primary cultured astrocytes *in vitro*[18]. These neuroprotective effects are associated with the inhibition of the up-regulation of LC3-II and cathepsin B in the rat brain or primary cultured astrocytes challenged by cerebral ischemia or OGD. These studies strongly suggest that ALP is activated not only in ischemic neurons, but also in ischemic astrocytes and participates in the demise of neurons and astrocytes. Notably, 3-MA and Baf may have diverse effects on neural cells that extend beyond autophagy regulation to include the modulation of survival/death kinases by 3-MA. Thus, the issue of whether autophagy observed in dying neural cells reflects a death mechanism, failed adaptation, or epiphenomenon requires additional approaches to establish causality. The identification of autophagy (*Atg*) genes involved in specific ubiquitin-like conjugation reactions that are essential for the extension of autophagic membranes has revolutionized the field, allowing for the development of specific markers for autophagic vacuole formation and maturation and providing molecular genetic tools for knocking out or knocking down essential *Atg* gene products. Recently, evidence on the genetic level showing that ribonucleic acid interference (RNAi)-mediated down-regulation of Beclin1 decreases infarct volume and inhibits histological injury and neurological deficits induced by focal cerebral ischemia[61] supports the present conclusion.

In addition, ALP activation induced by severe HI also contributes to neuronal cell death. The direct evidence comes from neuron Atg7-deficient neonatal mice showing strong neuroprotection 7 d after HI injury [62].

The next issue we need to resolve is which modes of neural cell death ALP activation is involved in.

ALP activation is involved in cerebral ischemia-induced pure autophagic programmed cell death

The morphological characteristics of autophagic programmed cell death can be observed by electron microscopy in the adult mouse HI model by Adhami *et al*[11] and in a rat model of pMCAO by Qin *et al*[18], suggesting that cerebral ischemia and/or hypoxia may induce pure autophagic programmed cell death (See Figure 2 for more details).

ALP activation participates in cerebral ischemia-induced apoptosis

A defining biochemical feature of apoptosis is the requirement for caspases acting through one of two general pathways. An intrinsic pathway, commonly used by neurons, relies on mitochondria for the release of apoptotic factors (cytochrome *c* and Smac/Diablo) that activate the initiator caspase-9 and downstream effector caspases. An extrinsic pathway, initiated by extracellular death ligands (*eg*, tumor necrosis factor and Fas), activates effector caspases via the initiator caspase-8 and caspase-10 and additionally via crosstalk with the mitochondrial pathway[63]. It has been demonstrated that the activation of downstream caspase-3 is a crucial event in neuronal death following global and focal ischemia and HI in the brain. The number of caspase-3-positive and Beclin1-positive cells in the penumbra of rats challenged by focal cerebral ischemia is elevated at 6–24 h by immunohistochemical double staining. Semi-quantitative assessment shows that approximately 30% of cells in the penumbra present both the activation of caspase-3 and the up-regulation of Beclin1, indicating that autophagy and apoptosis interact with each other in the penumbra following focal cerebral ischemia[15]. An increase in Beclin1 expression colocalized with the activation of caspase-3 in neurons has also been found in neonatal cerebral HI[12]. In addition, there are dying neurons with numerous autophagosomes in their cytosol beginning 6 h after HI. However, these neurons never exhibit the morphology of pure autophagic cell death but show features of apoptosis, and cortical neurons with strong lysosomal expression (LAMP1 labeling) also express cleaved caspase-3[13]. Furthermore, Atg7 deficiency largely prevents caspase-dependent death of pyramidal neurons in the neonatal hippocampus after severe hypoxic-ischemic injury[62]. These results indicate that the simultaneous activation of autophagic and apoptotic mechanisms can occur in the same dying neuron. Therefore, a new term of cell death "Apophagy" from apoptosis and autophagy, a kind of apoptotic cell death with a concomitant up-regulation of Beclin1 and activation of caspase-3, has been introduced[63]. Moreover, neurons presenting strong autophagic features in the border of the lesion 24 h after HI are TdT-mediated dUTP-biotin nick end labeling (TUNEL)-negative and display moderate chromatin condensation without being pyknotic, which suggests that autophagy precedes apoptosis and might even initiate apoptosis.

Ischemia-induced APL activation may cause neuronal and astrocytic apoptotic cell death through the cathepsin-caspase signaling pathway. Cathepsins are acidic endopeptidases, which belong to the papain superfamily of proteases[64]. Under physiologic conditions, their activity is restricted to the lysosomal compartment, where they participate in protein turnover by degrading unneeded proteins into amino acids[65]. It has been demonstrated that cerebral ischemia induces the release of cathepsins into the cytoplasm, where they extensively perform their proteolytic function and can promote ischemia-induced apoptosis through alterations of mitochondrial homeostasis and the activation of proapoptotic members of the Bcl-2 family[7, 8, 66, 67]. Cathepsin B possesses a caspase-processing activity, which mainly appears on caspase-11 and caspase-1. Caspase-1 and caspase-11 play important roles in brain ischemia by promoting both apoptotic and inflammatory processes. In addition, cathepsin B proteolytic effects

also include the activation of Bax and Bak, two proapoptotic members of the Bcl-2 family, and the subsequent release of cytochrome *c* through permeabilization of the mitochondrial membrane. Cytochrome *c* is a key activator of the apoptosome, which regulates the mitochondrial caspase activation pathway mediated by caspase-9[66]. Cathepsin L can activate caspase-3, and cathepsin D can activate caspase-8. The inhibition of cathepsins leads to significant neuroprotection in a cathepsin-caspase dependent manner in the experimental model of stroke[66, 68–71]. Therefore, ischemia-induced ALP activation may be involved in neuronal and astrocytic apoptotic cell death via a cathepsin-caspase dependent manner in ischemic brain injury.

On the other hand, there is a crosstalk between autophagy and apoptosis in Bcl-2 levels after cerebral ischemia. The Bcl-2 protein family was initially characterized as apoptotic cell death regulators, but it has recently become clear that they also control autophagy because they can inhibit Beclin1-dependent autophagy[72–74]. The anti-apoptotic proteins of the Bcl-2 family constitutively interact with Beclin1, which serve as inhibitors of autophagy. Bcl-2 can block caspase-independent cell death and mitochondrial degradation and the two processes involved in autophagy. In growth factor-deprived neural progenitor cells and serum and potassium-deprived cerebellar granule cells, overexpression of Bcl-2 inhibits autophagy. Our findings show that the cerebral ventricular microinjection of autophagy inhibitor 3-MA, Baf, or Z-FA-fmk, can block ischemia-induced Bcl-2 degradation in a rat model of pMCAO and suppress OGD-induced Bcl-2 degradation in primary cultured astrocytes. Taken together, ischemia-induced APL activation may cause neuronal and astrocytic apoptotic cell death via regulating Bcl-2.

Autophagy activation participates in cerebral ischemia-induced necrosis

Some suggest that autophagy blockage may interrupt the activation of the apoptotic process and switch the mechanism of cell death from apoptosis to necrosis. As mentioned above, 3-MA and wortmannin, which inhibit autophagy, significantly reduce the expression of Beclin1 and augment the number of necrotic cells in the rat model of neonatal cerebral HI, indicating that when autophagy is blocked, neurons rapidly progress toward necrosis[75]. However, a growing body of evidence reveals that autophagy is required for necrotic cell death. Recently, Samara *et al* have reported overlap between autophagic and necrotic cell death. Utilizing an exceptionally well-characterized and genetically tractable model of necrotic neuronal cell death in *C elegans*, they found that excessive autophagosome formation is induced early during necrotic cell death in *C elegans* neurons and that autophagy is required for neuronal necrotic cell death. Impairment of autophagy by genetic inactivation of autophagy genes or by pharmacological treatment suppresses necrosis. Autophagy synergizes with lysosomal catabolic mechanisms to further facilitate neuronal necrotic cell death. Further studies reveal that calpain protease activity is also required for necrosis in *C elegans* neurons and induces autophagy in neuronal necrotic cell death[76]. Taken together, activation of autophagy may be associated with neuronal or astrocytic necrotic death following cerebral ischemia. However, this still needs to be further confirmed in the many animal models of cerebral ischemia.

Autophagy is a response to necroptotic cell death

Experiments using a specific necroptotic inhibitor, necrostatin-1 (Nec-1), and one of its derivatives, 7-chloroindole-necrostatin-1 (7-Cl-Nec-1), have confirmed that necroptosis is involved in the ischemic brain injury induced by focal cerebral ischemia and neonatal HI[14, 77]. The protection effect of 7-Cl-Nec-1 is readily detectable, even when the compound is administered 6 h after the onset of cerebral ischemic injury[14], at which point the administration of zVAD-fmk no longer decreases infarct volume[78], indicating that necroptosis may participate in ischemia-induced delayed cell death. LC3-II is clearly induced after ischemic cerebral injury, but it does not reach its maximal level until 8 h post-MCAO, and delayed injection of 7-Cl-Nec-1 at 4 h and 6 h postocclusion still efficiently blocks the increase of LC3-II at the 8 h time point, confirming that the late induction of LC3-II *in vivo* indeed reflects the delayed activation of necroptosis.

In *in vitro* experiments, autophagy vesicles are commonly observed in necroptotic cells, leading some to propose that autophagy is an execution mechanism for necroptosis. In L929 cells, treatment with autophagy inhibitors 3-MA and wortmanin is able to partially inhibit zVAD-induced cell death. Knockdown of autophagy-related genes, such as *Beclin1* and *Atg7*, is shown to be able to inhibit necroptosis in L929 cells[79]. However, in other cell types, this finding has not been supported. Jurkat cells, BALB/c mouse embryonic fibroblast cells (Balb c/3T3 cells), and mouse embryonic fibroblast cells (MEFs) have been extensively tested for the effect of autophagic inhibitors or the knockdown of *Beclin1* and *Atg5*. None of these inhibitors of autophagy is able to reduce cell death[14].

Therefore, it remains to be determined if autophagy is actually a response to necroptotic cell death.

It is possible that autophagy plays dual roles in determining cell fate, depending on specific cell types and stimuli. It seems that physiological levels of autophagy caused by mild or moderate cerebral ischemia and/or hypoxia appear to be protective via the production of energy to prevent cell necrosis by catabolism and inhibit cell apoptosis by removing damaged mitochondria. However, high levels of autophagy caused by severe cerebral ischemia and/or hypoxia (focal cerebral ischemia or severe HI) may lead to self-digestion and eventual cell death (Figure 4).

Outlook

Initial neuroprotective clinical stroke trials primarily used antiexcitotoxic drugs to limit acute calcium-mediated injury attributable to cerebral ischemia. However, the excitotoxic phase mediated by the release of excitatory acids into the brain peaks within 1 to 2 h after ischemia, and treatments with anti-

excitotoxic drugs are only effective when given within 1 to 2 h after focal ischemia in animal models[80]. Considering that the median hospital arrival time for stroke patients is 3 to 6 h[81] and all of the trials of antiexcitotoxic drugs have been used to treat patients up to at least 6 h after the onset of symptoms, the negative outcomes of the 35 completed trials of antiexcitotoxic agents are not surprising. In the development of new therapies, focus must be placed on targets producing long-lasting protection and efficacy even when treatments are given during or at the 4 to 6 h after symptom onset, which is when patients generally arrive at the hospital. Therefore, a promising strategy for the development of such therapeutics is to inhibit the mechanisms that destabilize mitochondria via targeting pro-death signaling upstream of mitochondrial damage. APL activation regulates neural cell death mainly through cathepsin-mediated mitochondrial damage. One of the mechanisms of the regulation of neural cell death by APL activation is the activation of the cathepsin-mediated mitochondrial apoptotic pathway, and 3-MA can reduce infarct volume even when administered 4 h after ischemia onset, indicating that 3-MA may have a wide therapeutic window. Therefore, 3-MA might have the potential to exhibit long-lasting protection in the clinic, targeting APL to develop stroke therapeutics. However, more work is required to determine the requirements under which the activation of autophagy reflects a protective or harmful response in cerebral ischemia. A profound understanding of the biological effects and the mechanisms underlying ischemia-induced autophagy in neurons and astrocytes might be helpful in seeking effective new treatment for ischemic brain injury.

Acknowledgements

This work is supported by grants from the National Natural Science Foundation of China (No 30973510) and the Scientific Research Foundation for the Returned Overseas Chinese Scholars, State Education Ministry.

References

1 Komatsu M, Waguri S, Ueno T, Iwata J, Murata S, Tanida I, *et al*. Impairment of starvation-induced and constitutive autophagy in Atg7-deficient mice. J Cell Biol 2005; 169: 425–34.
2 Kuma A, Hatano M, Matsui M, Yamamoto A, Nakaya H, Yoshimori T, *et al*. The role of autophagy during the early neonatal starvation period. Nature 2004; 432: 1032–6.
3 Shintani T, Klionsky DJ. Autophagy in health and disease: a double-edged sword. Science 2004; 306: 990–5.
4 Canu N, Tufi R, Serafino AL, Amadoro G, Ciotti MT, Calissano P. Role of the autophagic-lysosomal system on low potassium-induced apoptosis in cultured cerebellar granule cells. J Neurochem 2005; 92: 1228–42.
5 Clarke PG. Developmental cell death: morphological diversity and multiple mechanisms. Anat Embryol (Berl) 1990; 181: 195–213.
6 Ohsawa Y, Isahara K, Kanamori S, Shibata M, Kametaka S, Gotow T, *et al*. An ultrastructural and immunohistochemical study of PC12 cells during apoptosis induced by serum deprivation with special reference to autophagy and lysosomal cathepsins. Arch Histol Cytol 1998; 61: 395–403.
7 Uchiyama Y. Autophagic cell death and its execution by lysosomal cathepsins. Arch Histol Cytol 2001; 64: 233–46.
8 Nitatori T, Sato N, Waguri S, Karasawa Y, Araki H, Shibanai K, *et al*. Delayed neuronal death in the CA1 pyramidal cell layer of the gerbil hippocampus following transient ischemia is apoptosis. J Neurosci 1995; 15: 1001–11.
9 Zhu C, Wang X, Xu F, Bahr BA, Shibata M, Uchiyama Y, *et al*. The influence of age on apoptotic and other mechanisms of cell death after cerebral hypoxia-ischemia. Cell Death Differ 2005; 12: 162–76.
10 Zhu C, Xu F, Wang X, Shibata M, Uchiyama Y, Blomgren K, *et al*. Different apoptotic mechanisms are activated in male and female brains after neonatal hypoxia-ischaemia. J Neurochem 2006; 96: 1016–27.

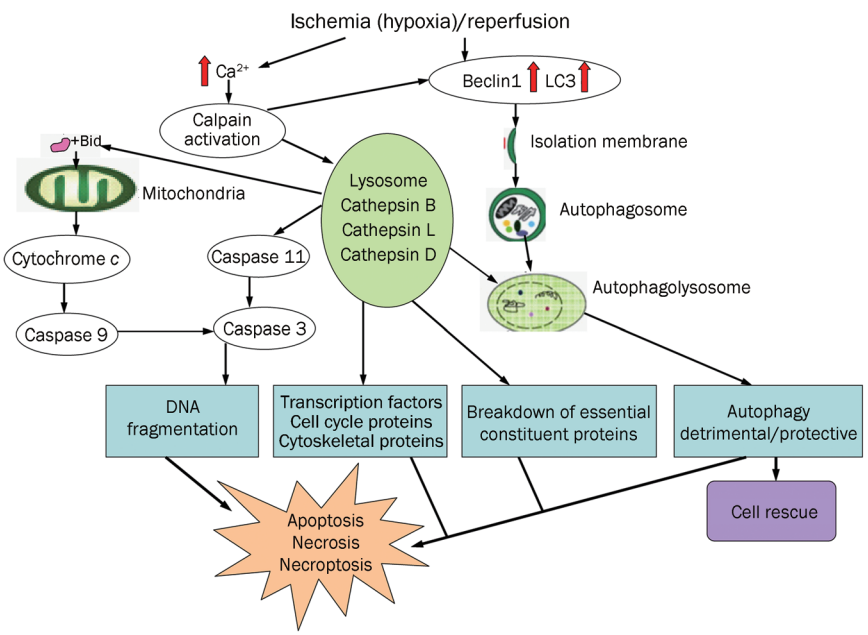

Figure 4. Roles of autophagy activation in neural cell survival and death in ischemic cerebral injury[63]. Cerebral ischemia (or hypoxia) and/or reperfusion induces the up-regulation of Beclin1 and LC3 and activates APL. APL activation either rescues the injured neural cells or induces cell death by necrosis, necroptosis, or apoptosis.

11 Adhami F, Liao G, Morozov YM, Schloemer A, Schmithorst VJ, Lorenz JN, *et al*. Cerebral ischemia-hypoxia induces intravascular coagulation and autophagy. Am J Pathol 2006; 169: 566–83.
12 Carloni S, Buonocore G, Balduini W. Protective role of autophagy in neonatal hypoxia-ischemia induced brain injury. Neurobiol Dis 2008; 32: 329–39.
13 Ginet V, Puyal J, Clarke PG, Truttmann AC. Enhancement of autophagic flux after neonatal cerebral hypoxia-ischemia and its region-specific relationship to apoptotic mechanisms. Am J Pathol 2009; 175: 1962–74.
14 Degterev A, Huang Z, Boyce M, Li Y, Jagtap P, Mizushima N, *et al*. Chemical inhibitor of nonapoptotic cell death with therapeutic potential for ischemic brain injury. Nat Chem Biol 2005; 1: 112–9.
15 Rami A, Langhagen A, Steiger S. Focal cerebral ischemia induces upregulation of Beclin1 and autophagy-like cell death. Neurobiol Dis 2008; 29: 132–41.
16 Puyal J, Vaslin A, Mottier V, Clarke PG. Postischemic treatment of neonatal cerebral ischemia should target autophagy. Ann Neurol 2009; 66: 378–89.
17 Wen YD, Sheng R, Zhang LS, Han R, Zhang X, Zhang XD, *et al*. Neuronal injury in rat model of permanent focal cerebral ischemia is associated with activation of autophagic and lysosomal pathways. Autophagy 2008; 4: 762–9.
18 Qin AP, Liu CF, Qin YY, Hong LZ, Xu M, Yang L, *et al*. Autophagy was activated in injured astrocytes and mildly decreased cell survival following glucose and oxygen deprivation and focal cerebral ischemia. Autophagy 2010; 6: 738–53.
19 Lockshin RA, Zakeri Z. Caspase-independent cell death? Oncogene 2004; 23: 2766–73.
20 Jaattela M, Tschopp J. Caspase-independent cell death in T lymphocytes. Nat Immunol 2003; 4: 416–23.
21 Klionsky DJ, Abeliovich H, Agostinis P, Agrawal DK, Aliev G, Askew DS, *et al*. Guidelines for the use and interpretation of assays for monitoring autophagy in higher eukaryotes. Autophagy 2008; 4: 151–75.
22 Singh R, Kaushik S, Wang Y, Xiang Y, Novak I, Komatsu M, *et al*. Autophagy regulates lipid metabolism. Nature 2009; 458: 1131–5.
23 Todde V, Veenhuis M, van der Klei IJ. Autophagy: principles and significance in health and disease. Biochim Biophys Acta 2009; 1792: 3–13.
24 Rice JE 3rd, Vannucci RC, Brierley JB. The influence of immaturity on hypoxic-ischemic brain damage in the rat. Ann Neurol 1981; 9: 131–41.
25 Hu BR, Liu CL, Ou-yang Y, Blomgren K, Siesjo BK. Involvement of caspase 3 in cell death after hypoxia-ischemia declines during brain maturation. J Cereb Blood Flow Metab 2000; 20: 1294–300.
26 Romero AA, Gross SR, Cheng KY, Goldsmith NK, Geller HM. An age-related increase in resistance to DNA damage-induced apoptotic cell death is associated with development of DNA repair mechanisms. J Neurochem 2003; 84: 1275–87.
27 Towfighi J, Mauger D, Vannucci RC, Vannucci SJ. Influence of age on the cerebral lesions in an immature rat model of cerebral hypoxia-ischemia: a light microscopic study. Brain Res Dev Brain Res 1997; 100: 149–60.
28 Yager JY, Shuaib A, Thornhill J. The effect of age on susceptibility to brain damage in a model of global hemispheric hypoxia-ischemia. Brain Res Dev Brain Res 1996; 93: 143–54.
29 Sutherland GR, Dix GA, Auer RN. Effect of age in rodent models of focal and forebrain ischemia. Stroke 1996; 27: 1663–7; discussion 1668.
30 Papadopoulos MC, Koumenis IL, Yuan TY, Giffard RG. Increasing vulnerability of astrocytes to oxidative injury with age despite constant antioxidant defenses. Neuroscience 1998; 82: 915–25.
31 McDonald JW, Silverstein FS, Johnston MV. Neurotoxicity of *N*-methyl-*D*-aspartate is markedly enhanced in developing rat central nervous system. Brain Res 1988; 459: 200–3.
32 Adelson PD, Kochanek PM. Head injury in children. J Child Neurol 1998; 13: 2–15.
33 MacLusky NJ, Naftolin F. Sexual differentiation of the central nervous system. Science 1981; 211: 1294–302.
34 Rossi DJ, Brady JD, Mohr C. Astrocyte metabolism and signaling during brain ischemia. Nat Neurosci 2007; 10: 1377–86.
35 Hansson MJ, Mansson R, Morota S, Uchino H, Kallur T, Sumi T, *et al*. Calcium-induced generation of reactive oxygen species in brain mitochondria is mediated by permeability transition. Free Radic Biol Med 2008; 45: 284–94.
36 Yu JH, Kim KH, Kim H. Role of NADPH oxidase and calcium in cerulein-induced apoptosis: involvement of apoptosis–inducing factor. Ann N Y Acad Sci 2006; 1090: 292–7.
37 Kato H, Kogure K, Nakata N, Araki T, Itoyama Y. Facilitated recovery from postischemic suppression of protein synthesis in the gerbil brain with ischemic tolerance. Brain Res Bull 1995; 36: 205–8.
38 Nowak TS, Fried RL, Lust WD, Passonneau JV. Changes in brain energy metabolism and protein synthesis following transient bi-lateral ischemia in the gerbil. J Neurochem 1985; 44: 487–94.
39 Kumar R, Azam S, Sullivan JM, Owen C, Cavener DR, Zhang P, *et al.* Brain ischemia and reperfusion activates the eukaryotic initiation factor 2a kinase, PERK. J Neurochem 2001; 77: 1418–21.
40 Althausen S, Mengesdorf T, Mies G, Olah L, Nairn AC, Proud CG, *et al*. Changes in the phosphorylation of initiation factor eIF-2alpha, elongation factor eEF-2 and p70 S6 kinase after transient focal cerebral ischaemia in mice. J Neurochem 2001; 78: 779–87.
41 Parsons JT, Churn SB, DeLorenzo RJ. Ischemia-induced inibition of calcium uptake into rat brain microsomes mediated by Mg^{2+}/Ca^{2+} ATPase. J Neurochem 1997; 68: 1124–34.
42 Hu BR, Martone ME, Jones YZ, Liu CL. Protein aggregation after transient cerebral ischemia. J Neurosci 2000; 20: 3191–9.
43 Kitao Y, Ozawa K, Miyazaki M, Tamatani M, Kobayashi T, Yanagi H, *et al*. Expression of the endoplasmic reticulum molecular chaperone (ORP150) rescues hippocampal neurons from glutamate toxicity. J Clin Invest 2001; 108: 1439–50.
44 Yorimitsu T, Nair U, Yang Z, Klionsky DJ. Endoplasmic reticulum stress triggers autophagy. J Biol Chem 2006; 281: 30299–304.
45 Li J, Ni M, Lee B, Barron E, Hinton DR, Lee AS. The unfolded protein response regulator GRP78/BiP is required for endoplasmic reticulum integrity and stress-induced autophagy in mammalian cells. Cell Death Differ 2008; 15: 1460–71.
46 Choi KC, Kim SH, Ha JY, Kim ST, Son JH. A novel mTOR activating protein protects dopamine neurons against oxidative stress by repressing autophagy related cell death. J Neurochem 2010; 112: 366–76.
47 Zukor H, Song W, Liberman A, Mui J, Vali H, Fillebeen C, *et al*. HO-1-mediated macroautophagy: a mechanism for unregulated iron deposition in aging and degenerating neural tissues. J Neurochem 2009; 109: 776–91.
48 Lee SJ, Cho KS, Koh JY. Oxidative injury triggers autophagy in astrocytes: the role of endogenous zinc. Glia 2009; 57: 1351–61.
49 Wang Y, Dong XX, Cao Y, Liang ZQ, Han R, Qin ZH, *et al*. p53 induction contributes to excitotoxic neuronal death in rat striatum through apoptotic and autophagic mechanisms. Eur J Neurosci 2009; 30: 2258–70.
50 Gupta S, Barrett T, Whitmarsh AJ, Cavanagh J, Sluss HK, Derijard B, *et al*. Selective interaction of JNK protein kinase isoforms with

transcription factors. EMBO J 1996; 15: 2760–70.
51 Waetzig V, Herdegen T. Context-specific inhibition of JNKs: overcoming the dilemma of protection and damage. Trends Pharmacol Sci 2005; 26: 455–61.
52 Yang DD, Kuan CY, Whitmarsh AJ, Rincon M, Zheng TS, Davis RJ, *et al*. Absence of excitotoxicity induced apoptosis in the hippocampus of mice lacking the Jnk3 gene. Nature 1997; 389: 865–70.
53 Centeno C, Repici M, Chatton JY, Riederer BM, Bonny C, Nicod P, *et al*. Role of the JNK pathway in NMDA-mediated excitotoxicity of cortical neurons. Cell Death Differ 2006; 14: 240–53.
54 Arthur PG, Matich GP, Pang WW, Yu DY, Bogoyevitch MA. Necrotic death of neurons following an excitotoxic insult is prevented by a peptide inhibitor of c-jun N-terminal kinase. J Neurochem 2007; 102: 65–76.
55 Guan QH, Pei DS, Liu XM, Wang XT, Xu TL, Zhang GY. Neuroprotection against ischemic brain injury by SP600125 via suppressing the extrinsic and intrinsic pathways of apoptosis. Brain Res 2006; 1092: 36–46.
56 Hirt L, Badaut J, Thevenet J, Granziera C, Regli L, Maurer F, *et al*. D-JNKI1, a cell-penetrating c-Jun-N-terminal kinase inhibitor, protects against cell death in severe cerebral ischemia. Stroke 2004; 35: 1738–43.
57 Guan QH, Pei DS, Zong YY, Xu TL, Zhang GY. Neuroprotection against ischemic brain injury by a small peptide inhibitor of c-Jun N-terminal kinase (JNK) via nuclear and non-nuclear pathways. Neuroscience 2006b; 139: 609–27.
58 Ginet V, Puyal J, Magnin G, Clarke PGH, Truttmann AC. Limited role of the c-Jun N-terminal kinase pathway in a neonatal rat model of cerebral hypoxia-ischemia. J Neurochem 2009; 108: 552–62.
59 Hara T, Nakamura K, Matsui M, Yamamoto A, Nakahara Y, Suzuki-Migishima R, *et al*. Suppression of basal autophagy in neural cells causes neurodegenerative disease in mice. Nature 2006; 441: 885–9.
60 Komatsu M, Waguri S, Chiba T, Murata S, Iwata J, Tanida I, *et al*. Loss of autophagy in the central nervous system causes neurodegeneration in mice. Nature 2006; 441: 880–4.
61 Zheng YQ, Liu JX, Li XZ, Xu L, Xu YG. RNA interference-mediated downregulation of Beclin1 attenuates cerebral ischemic injury in rats. Acta Pharmacol Sin 2009; 30: 919–27.
62 Uchiyama Y, Koike M, Shibata M. Autophagic neuron death in neonatal brain ischemia/hypoxia. Autophagy 2008; 4: 404–8.
63 Rami A, Kögel D. Apoptosis meets autophagy-like cell death in the ischemic penumbra: two sides of the same coin? Autophagy 2008; 4: 422–6.
64 Turk B, Turk V, Turk D. Structural and functional aspects of papain–like cysteine proteinases and their protein inhibitors. Biol Chem 1997; 378: 141–50.
65 Kirschke H, Langner J, Reimann S, Weideranders B, Ansorge S, Bohley P. Lysosomal cystein propteinases. In: protein degradation in health and disease, Ciba Foundation Symposium (Evered D, Whelan J, eds). Amsterdam: Excerpta Medica 1980; pp5–35.
66 Benchoua A, Braudeau J, Reis A, Couriaud C, Onténiente B. Activation of proinflammatory caspases by cathepsin B in focal cerebral ischemia. J Cereb Blood Flow Metab 2004; 24: 1272–9.
67 Unal-Cevik I, Kilinç M, Can A, Gürsoy-Ozdemir Y, Dalkara T. Apoptotic and necrotic death mechanisms are concomitantly activated in the same cell after cerebral ischemia. Stroke 2004; 35: 2189–94.
68 Seyfried DM, Veyna R, Han Y, Li K, Tang N, Betts RL, *et al*. A selective cysteine protease inhibitor is non-toxic and cerebroprotective in rats undergoing transient middle cerebral artery ischemia. Brain Res 2001; 901: 94–101.
69 Hou Q, Ling L, Wang F, Xing S, Pei Z, Zeng J. Endostatin expression in neurons during the early stage of cerebral ischemia is associated with neuronal apoptotic cell death in adult hypertensive rat model of stroke. Brain Res 2010; 1311: 182–8.
70 Yoshida M, Yamashima T, Zhao L, Tsuchiya K, Kohda Y, Tonchev AB, *et al*. Primate neurons show different vulnerability to transient ischemia and response to cathepsin inhibition. Acta Neuropathol 2002; 104: 267–72.
71 Yamashima T, Kohda Y, Tsuchiya K, Ueno T, Yamashita J, Yoshioka T, *et al*. Inhibition of ischaemic hippocampal neuronal death in primates with cathepsin B inhibitor CA-074: a novel strategy for neuroprotection based on 'calpain-cathepsin hypothesis'. Eur J Neurosci 1998; 10: 1723–33.
72 Levine B, Yuan J. Autophagy in cell death: an innocent convict? J Clin Invest 2005; 115: 2679–88.
73 Levine B, Sinha S, Kroemer G. Bcl2 family members: dual regulators of apoptosis and autophagy. Autophagy 2008; 4: 600–6.
74 Pattingre S, Tassa A, Qu X, Garuti R, Liang XH, Mizushima N, *et al*. Bcl2 antiapoptotic proteins inhibit Beclin1-dependent autophagy. Cell 2005; 122: 927–39.
75 Balduini W, Carloni S, Buonocore G. Autophagy in hypoxia-ischemia induced brain injury: evidence and speculations. Autophagy 2009; 5: 221–3.
76 Samara C, Syntichaki P, Tavernarakis N. Autophagy is required for necrotic cell death in *Caenorhabditis elegans*. Cell Death Differ 2008; 15: 105–12.
77 Northington FJ, Chavez-Valdez R, Graham EM, Razdan S, Gauda EB, Martin LJ. Necrostatin decreases oxidative damage, inflammation, and injury after neonatal HI. J Cereb Blood Flow Metab 2011; 31: 178–89.
78 Endres M, Namura S, Shimizu-Sasamata M, Waeber C, Zhang L, Gómez-Isla T, *et al*. Attenuation of delayed neuronal death mild focal ischemia in mice by inhibition of the caspase family. J Cereb Blood Flow Metab 1998; 18: 238–47.
79 Yu L, Alva A, Su H, Dutt P, Freundt E, Welsh S, *et al*. Regulation of an ATG7-becline1 program of autophagic cell death by caspase-8. Science 2004; 304: 1500–2.
80 Dirnagl U, Iadecola C, Moskowitz MA. Pathobiology of ischaemic stroke: an integrated view. Trends Neurosci 1999; 22: 391–7.
81 Evenson KR, Rosamond WD, Morris DL. Prehospital and in–hospital delays in acute stroke care. Neuroepidemiology 2001; 20: 65–76.
82 Edinger AL, Thompson CB. Death by design: apoptosis, necrosis and autophagy. Curr Opin Cell Biol 2004; 16: 663–9.

Acta Pharmacologica Sinica (2011) 32: 1100–1108
 1671-4083/11 $32.00
www.nature.com/aps

Original Article

T33, a novel peroxisome proliferator-activated receptor γ/α agonist, exerts neuroprotective action via its anti-inflammatory activities

Ying WANG, Yu-she YANG, Xi-can TANG, Hai-yan ZHANG*

State Key Laboratory of Drug Research, Shanghai Institute of Materia Medica, Chinese Academy of Sciences, Shanghai 201203, China

Aim: To examine the neuroprotective effects of T33, a peroxisome proliferator-activated receptor gamma/alpha (PPARγ/α) agonist, in acute ischemic models *in vitro* and *in vivo.*
Methods: Primary astrocytes subjected to oxygen-glucose deprivation/reperfusion (O/R) and BV-2 cells subjected to hypoxia were used as a model simulating the ischemic core and penumbra, respectively. The mRNA levels of tumor necrosis factor-α (TNF-α) and interleukin-1β (IL-1β) were measured using qPCR. The levels of TNF-α secreted by BV-2 cells were measured using ELISA. Protein levels of cyclooxygenase-2 (COX-2), p65, phosphorylated I-κBα/I-κBα, phosphorylated I-κB kinase (pIKK), phosphorylated eukaryote initiation factor 2α (p-eIF-2α)/eIF-2α and p-p38/p38 were detected using Western blot. PPARγ activity was measured using EMSA. The neuroprotection *in vivo* was examined in rat middle cerebral artery occlusion (MCAO) model with neurological scoring and TTC staining.
Results: Addition of T33 (0.5 μmol/L) increased the level of I-κBα protein in primary astrocytes subjected to O/R, which was due to promoting protein synthesis without affecting degradation. In primary astrocytes subjected to O/R, addition of T33 amplified I-κBα gene transcription and mRNA translation, thus suppressing the nuclear factor-kappa B (NF-κB) pathway and reducing inflammatory mediators (TNF-α, IL-1β, and COX-2). In BV-2 cells subjected to hypoxia, T33 (0.5 μmol/L) reduced TNF-α, COX-2, and p-P38 production, which was antagonized by pre-administration of the specific PPARγ antagonist GW9662 (30 μmol/L). T33 (2 mg/kg, ip) attenuated MCAO-induced inflammatory responses and brain infarction, which was antagonized by pre-administered GW9662 (4 mg/kg, ip).
Conclusion: T33 exerted anti-inflammatory effects in the ischemic core and penumbra via PPARγ activation, which contributed to its neuroprotective action.

Keywords: stroke; middle cerebral artery occlusion; oxygen-glucose deprivation; astrocytes; BV-2 cells; inflammation; nuclear factor-kappa B; T33; peroxisome proliferator-activated receptor γ

Acta Pharmacologica Sinica (2011) 32: 1100–1108; doi: 10.1038/aps.2011.69; published online 1 Aug 2011

Introduction

Acute brain ischemia leads to a damaged ischemic core and salvageable surrounding tissue (penumbra). In addition to treatments targeting the ischemic core, interventions preventing the progression of the penumbra to infarction help to reduce the final infarct area[1, 2]. Although different mechanisms are involved in the pathogenesis of strokes, appreciable evidence supports the fact that massive inflammation accounts for the progression of strokes, at least in the acute phase[3, 4]. Obstruction of blood flow to the brain elicits the activation of glial cells and infiltration of peripheral leukocytes facilitated by pro-inflammatory factors. Reperfusion leads to the over-production of reactive oxygen species, further stimulating ischemic glial cells to secrete inflammatory mediators, resulting in subsequent brain infarction. Recent research found compounds able to curtail neuroinflammation were effective in alleviating stroke-induced brain injury[5, 6]. Therefore, simultaneously interfering with the inflammatory responses in both the ischemic core and the penumbra has become an important area of research in the treatment of ischemic stroke, whose therapeutic management is limited to thrombolysis[7, 8].

Peroxisome proliferator-activated receptors (PPARs) are ligand-activated nuclear transcription factors regulating cell proliferation, differentiation, insulin sensitivity and inflammatory responses[9]. To date, three PPAR isoforms, designated α, β, and γ, have been identified. The PPARγ isoform is involved in controlling immune reactions and reduces

* To whom correspondence should be addressed.
E-mail hzhang@mail.shcnc.ac.cn
Received 2011-02-14 Accepted 2011-04-22

inflammatory mediators upon activation[10, 11]. Most of the anti-inflammatory activities of PPARγ have been suggested to arise through the inhibition of NF-κB, a transcription factor controlling the expression of multiple inflammatory genes during ischemia[10]. Moreover, emerging evidence implies that PPARγ activation is protective against brain damage after stroke, and PPARγ deficiency promotes brain damage after stroke[12–14]. Synthesized PPARγ agonists, including the well-known thiazolidinediones (TZDs), exhibit potent neuroprotective effects in stroke models mainly by blocking the production of inflammatory mediators[15, 16]. PPARγ/α dual agonists, expected to prevent weight gain and exert cardioprotective effects due to PPARα activation, are currently being developed[17, 18]. Whereas some PPARγ/α agonists such as aleglitazar have entered clinical trials for the treatment of diabetes, little research concerning the potency of dual agonists toward brain ischemia-induced inflammation has been reported.

T33, a benzopyran derivative, is a novel dual PPARγ/α agonist that has been demonstrated to alleviate diabetic injuries[19, 20]. The present study is the first to investigate the effects of T33 on inflammation and brain injury in the CNS, as well as the underlying mechanisms, by employing both *in vitro* and *in vivo* ischemic models.

Materials and methods

T33 preparation

T33 was provided by Prof Yu-she YANG of the Shanghai Institute of Materia Medica, Chinese Academy of Sciences. For *in vitro* experiments, T33 was dissolved in DMSO and diluted with culture medium before it was added to cell cultures. For *in vivo* administration, T33 was dissolved in DMSO and Cremaphor (Sigma-Aldrich) and diluted with saline.

Primary astrocytes

Primary astrocyte cultures were prepared from cerebral hemispheres of neonatal Sprague-Dawley (SD) pups (12–24 h old) according to published procedures with minor modifications[21]. Briefly, brain cortices were digested in 0.25% trypsin before they were dissociated into single cell suspensions in culture medium (DMEM/F12 containing 10% FBS). Cell suspensions were centrifuged at 1000 revolutions per minute for 10 min and pellets were re-suspended in culture medium. Cells were then placed into culture flasks coated with poly-*L*-lysine. Cultures were incubated at 37 °C in a 5% CO_2 incubator. The medium was changed the following day and then twice a week until the cells reached confluence.

Ischemic surgery and drug administration

All surgical procedures used in this study followed the National Institutes of Health Guide for the Care and Use of Laboratory Animals (NIH Publications No 8023, revised 1978), as well as the guidelines of the Animal Care and Use Committee of Shanghai Institute of Materia Medica. SD rats were randomly divided into four groups: sham-operated, middle cerebral artery occlusion (MCAO), T33-treated MCAO and T33+GW9662-treated MCAO (GW9662 is a PPARγ antagonist).

Rats (male, 200–250 g) were anesthetized with chloral hydrate (400 mg/kg, ip). Focal cerebral ischemia was produced by MCAO as previously described[22]. Briefly, the right external carotid artery (ECA) and internal carotid artery (ICA) were dissected from the surrounding connective tissue through a midline neck incision. A 4–0 monofilament nylon suture with a flame-rounded leading end was advanced from the common carotid artery (CCA) to the ICA until resistance was felt and a slight curving of the advancing suture was observed. MCAO caused a sustained decrease in rat cerebral blood flow (rCBF) levels, which remained stable at approximately 20% of baseline, indicating that the filament was positioned properly to occlude blood flow to the middle cerebral artery (MCA). After 1 h of occlusion, the suture was withdrawn to allow for cerebral reperfusion. Core body temperature was maintained at 37.0±0.5 °C with a heating carpet. T33 (2 mg/kg) was administered intraperitoneally once the filament reached the MCA. GW9662 (4 mg/kg) was injected 30 min before T33 administration. The sham-operated and MCAO groups were administered solvent alone.

Evaluation of neurological deficits

One day after MCAO, neurological deficits were evaluated before euthanization according to a previous report[23]. Four consecutive individual tests were carried out: (a) spontaneous activity (moving and exploring=0, moving without exploring=1, staying still or moving only when pulled by the tail=2); (b) left drifting during displacement (none=0, drifting only when pushed or pulled by the tail=1, spontaneous drifting=2, circling without displacement or spinning=3); (c) parachute reflex (symmetrical=0, asymmetrical=1, contralateral forelimb retracted=2); (d) resistance to left forepaw stretching (resistant to stretching=0, reduced resistance=1, no resistance=2). Neurological scores ranging from 0–9 were calculated as the sum of the scores from the four individual tests described above. Higher scores indicated worse neurological performance.

Cerebral infarction measurement

After 24 h of reperfusion, rats were sacrificed. Brains were sectioned into six 2-mm coronal planes and stained with 2% 2, 3, 5-triphenyl tetrazolium chloride (TTC, Sinopharm Chemical Reagent Co Ltd) at 37 °C for 15 min before they were fixed in 10% formalin overnight. Images of the slices were digitalized, and infarct areas outlined in white were measured using Image-Pro Plus software. Infarct volumes were determined by multiplying the average slice thickness (2 mm) by the sum of the infarct areas in all six brain slices. The percentage of the total infarct area was also calculated for each of the six brain slices.

Oxygen-glucose deprivation (OGD)

For OGD insult, the original medium was removed and primary astrocytes were washed with EBSS. The cultures were then placed in glucose-free DMEM and kept in an incubator containing 95% (*v/v*) N_2 and 5% (*v/v*) CO_2 at 37 °C for 4 h.

T33 was added to the cultures at the beginning of OGD at a final concentration of 0.5 μmol/L. At the end of the exposure period, cells were either collected immediately to be used in experiments (OGD), or glucose was added and the cells were returned to normal conditions for another 24 h before collection (OGD and reperfusion, O/R).

Hypoxia

To simulate hypoxia in the penumbra area, BV-2 cells were transferred to an incubator containing 2.5% O_2 and 5% CO_2, balanced in N_2 at 37 °C. Cells were kept in hypoxic conditions for 10 h before collection. T33 and GW9662 were added to the cell cultures 1 h prior to hypoxia at a final concentration of 0.5 μmol/L and 30 μmol/L, respectively.

TNF-α level analysis

TNF-α secreted in the BV-2 culture medium was measured using a specific enzyme-linked immunosorbent assay (ELISA) kit (Biosource, Camarillo) according to the manufacturer's protocol. Briefly, samples were incubated with biotinylated anti-TNF-α antibody in microtiter wells for 90 min and subsequently with streptavidin-HRP working solution for 30 min. Stabilized chromogen was then added to each well and maintained in the dark for 15 min before termination. Each plate was then read at 450 nm.

RNA extraction and real-time PCR analysis

Total RNA was extracted with TRIzol (Invitrogen) following the manufacturer's protocol and then reverse transcribed into cDNA using the PrimeScript™ RT reagent kit (Takara Biotechnology). Real-time PCR was performed using the SYBR Premix Real-time PCR kit (Takara Biotechnology) according to the manufacturer's instructions. mRNA levels were normalized against β-actin and presented as $2^{-\Delta\Delta CT}$. The primer sequences are listed in Table 1.

Protein extraction and Western blot analysis

For whole cell/tissue protein extraction, samples were lysed in RIPA buffer (50 mmol/L Tris-HCl, pH 7.5, 150 mmol/L NaCl, 0.5% DOC, 1% NP40, 0.1% SDS, 1 mmol/L NaF, 1 mmol/L Na_3VO_4) before they were centrifuged at 10000×*g* for 10 min at 4 °C (an additional sonication step before centrifugation was necessary for rat brain tissue). The supernatants were collected to determine protein concentrations. Nuclear protein extraction was carried out using a kit produced by Beyotimes (China) with minor modifications. Briefly, cells were vortexed vigorously in cytoplasmic protein extraction reagent A for 5 s and left on ice for 10–15 min. Reagent B was then added and the cells were vortexed vigorously for 5 s before being placed in an ice bath for 1 min. The samples were subsequently vortexed for 5 s and centrifuged at 12000–16000×*g* for 5 min at 4 °C. The supernatants containing the cytoplasmic protein were carefully removed. The pellets containing the nuclear protein were resuspended with nuclear protein extraction reagent and sonicated at 25% amplitude (AML). The lysates containing the nuclear protein were placed on ice for 1–2 min before being vortexed for 30 s. After 30 min, the lysates were centrifuged at 12000–16000×*g* for 10 min at 4 °C. Supernatants were collected in pre-chilled tubes for nuclear protein concentration determination. Protein concentrations were determined using a BCA assay kit (Pierce) with bovine serum albumin as the standard. Proteins were separated by 10% sodium dodecyl sulfate-polyacrylamide gel electrophoresis (SDS-PAGE) and transferred to a nitrocellulose membrane. Blots were blocked in skim milk before being incubated overnight with one of the following primary antibodies: goat anti-COX-2, mouse anti-α-tubulin (Santa Cruz), rabbit anti-IκB, rabbit anti-phospho-IKKβ, rabbit anti-eIF-2α, rabbit anti-phospho-eIF-2α, rabbit anti-p38, rabbit anti-phospho-p38 (Cell signaling), rabbit anti-p65 (Millipore), or mouse anti-TBP (Abcam). Blots were then incubated with secondary antibody (Kangcheng, China) conjugated with horseradish peroxidase for 1 h at room temperature and then developed using the ECL plus (Amersham GE Healthcare) detection system. Immunoreactive bands were visualized by autoradiography and the intensity of each band was quantified with Image J software.

Electrophoretic mobility shift assay (EMSA)

EMSA was carried out using the "Gel Shift" kit closely following the manual (Panomics).

Statistical analysis

Data were expressed as mean±SEM. Neurological deficits were analyzed by the non-parametric Mann-Whitney *U* test. Multiple comparisons were analyzed by one way ANOVA followed by the LSD test unless otherwise specified. At least three independent experiments were carried out. $P<0.05$ was considered to be statistically significant.

Results

T33 alleviates O/R-induced inflammatory responses in astrocytes

Astrocyte activation constitutes one of the major events occur-

Table 1. Primer sequences for real-time PCR analysis.

Gene	Primer sequence	
	Upstream	Downstream
β-actin	5′-GAAGATCAAGATCATTGCTCC-3′	5′-GACTCATCGTACTCCTGCTTG-3′
TNF-α	5′-GACCCTCACACTCAGATCATC-3′	5′-GAACCTGGGAGTAGATAAGG-3′
IL-1β	5′-CAGAAGAATCTAGTTGTCCGTG-3′	5′-CATCAATGAAAGAACTCAGTGC-3′
I-κBα	5′-GGAAGTGATTGGTCAGGTGAAG-3′	5′-GAGTCAAGACTGCTACACTG-3′

ring after focal cerebral ischemia, initiating inflammatory reactions by over-expressing pro-inflammatory factors, thus contributing largely to post-ischemic brain infarction[24–26]. Astrocytes subjected to O/R, a model simulating inflammatory responses in the ischemic core, showed a prominent increase in the mRNA levels of TNF-α and IL-1β and the protein levels of COX-2, which were attenuated by the addition of 0.5 μmol/L T33 (Figure 1, $P<0.05$).

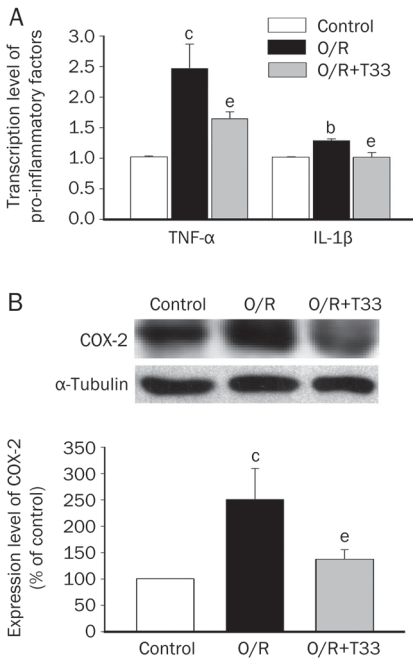

Figure 1. Anti-inflammatory effects of T33 (0.5 μmol/L) on primary astrocytes subjected to O/R. (A) T33 reduced the mRNA levels of TNF-α and IL-1β. $n=4$. (B) T33 reduced the protein level of COX-2 in astrocytes subjected to O/R. $n=6$. $^{b}P<0.05$, $^{c}P<0.01$ *vs* control group; $^{e}P<0.05$ *vs* O/R group.

Since the expression of inflammatory mediators is regulated by NF-κB in the nucleus[27], the effect of T33 on the levels of nuclear p65, a subunit of NF-κB, was subsequently analyzed. Compared to the vehicle-treated group, the nuclear protein levels of p65 were reduced in T33-treated astrocytes subjected to O/R or OGD (Figure 2A and 2B, $P<0.05$). Since the nuclear protein levels of p65 are modulated by the inhibitory protein I-κBα, further research was conducted on I-κBα in astrocytes subjected to O/R or OGD. The protein levels of I-κBα declined in astrocytes subjected to O/R or OGD ($P<0.01$) and were recovered by treatment with T33 (Figure 2C and 2D, $P<0.05$).

I-κBα, like other proteins, is regulated at multiple levels, including transcription, translation and degradation. The mRNA levels of I-κBα dramatically declined after 4 h of OGD (Figure 3A, $P<0.05$) and self-restored after 24 h of reperfusion to a level higher than that in control astrocytes (Figure 3A, $P<0.05$). T33 rescued I-κBα mRNA levels in astrocytes subjected to 4 h of OGD (Figure 3A, $P<0.01$), but there was no

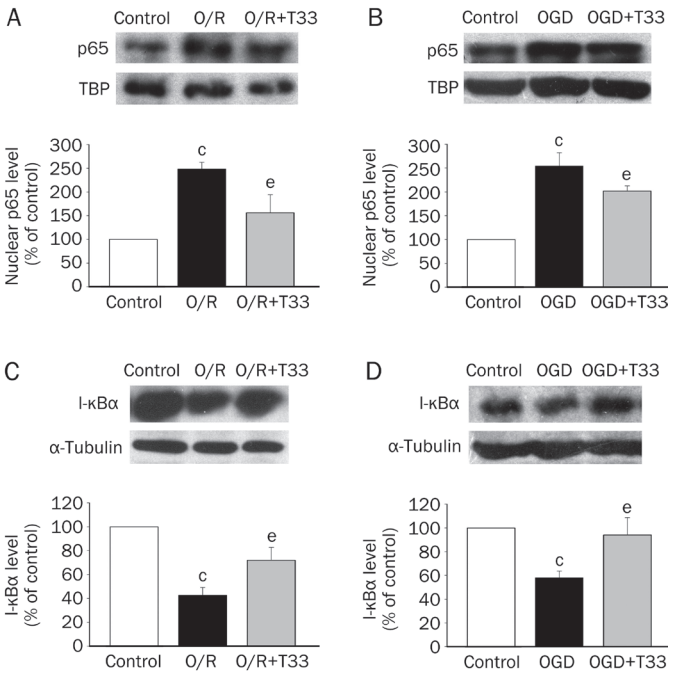

Figure 2. Modulation of the I-κBα/NF-κB pathway by T33 (0.5 μmol/L) in astrocytes subjected to O/R (A, C) ($n=5$) or OGD alone (B, D) ($n=4$). $^{c}P<0.01$ *vs* control group; $^{e}P<0.05$ *vs* correspondent OGD or O/R group.

change after reperfusion.

Phospho-IKKβ catalyzes the dual phosphorylation of I-κBα on serines 32 and 36, leading to the degradation of I-κBα. A distinct elevation of phospho-IKKβ levels was observed in astrocytes subjected to 4 h of OGD (Figure 3B, $P<0.05$), but there were no dramatic changes after 24 h of reperfusion (Figure 3B, $P>0.05$). T33 did not influence the phosphorylation of IKKβ in astrocytes subjected to OGD or O/R.

These results suggest that a severe transcriptional deficiency and accelerated degradation account for the reduced I-κBα protein levels in astrocytes subjected to OGD, but neither transcription nor degradation contributes to the drop in I-κBα protein levels in astrocytes subjected to O/R. eIF-2α, a factor controlling mRNA translation in eukaryotes, was found to be over-phosphorylated in astrocytes subjected to O/R (Figure 3C, $P<0.01$), indicating that mRNA translation was disrupted during reperfusion. T33 alleviated phosphorylated eIF-2α levels, restoring mRNA translation during reperfusion (Figure 3C, $P<0.05$).

Given the role of PPARγ in regulating inflammatory reactions, further detection of PPARγ activity was carried out. As indicated by EMSA analysis, PPARγ activity was dramatically impaired after 4 h of OGD in astrocytes (Figure 3D, lane 4; Figure 3E, $P<0.01$), and T33 restored the majority of the activity (Figure 3D, lane 3; Figure 3E, $P<0.01$). There were little changes in PPARγ activity in astrocytes subjected to O/R compared to astrocytes cultured under normal conditions (Figure 3D, lane 5–9).

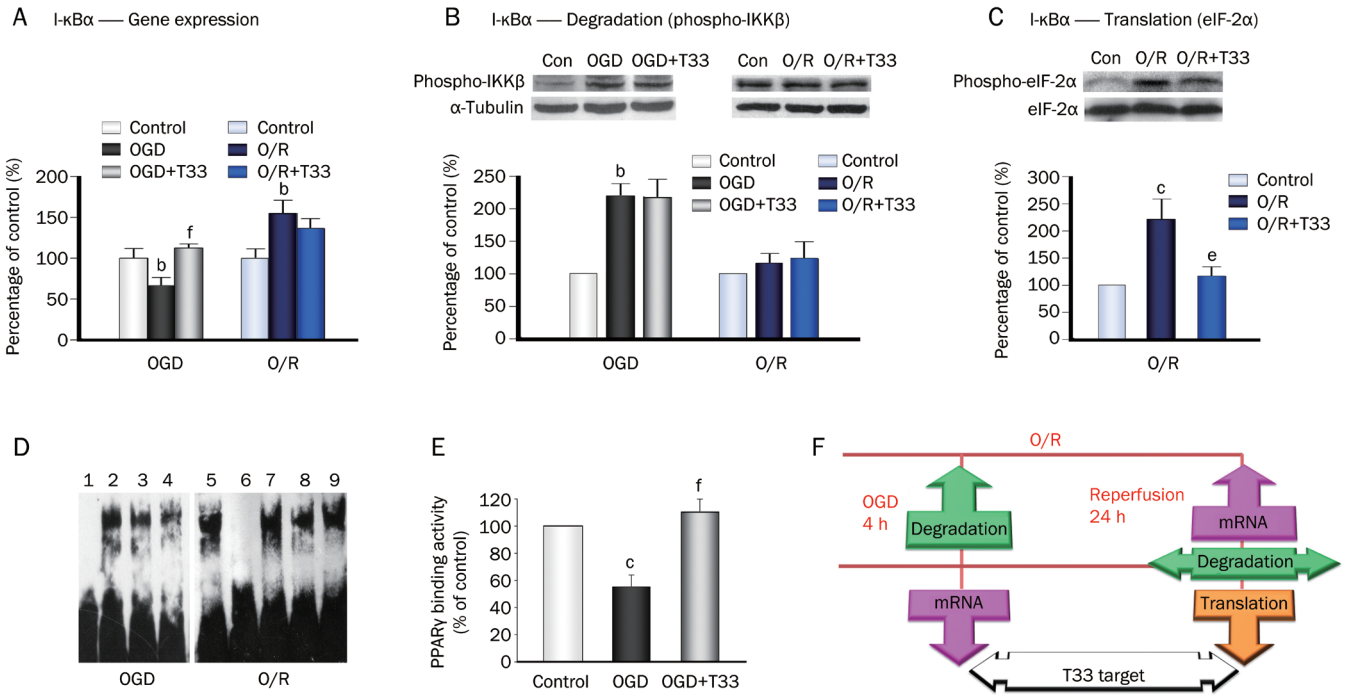

Figure 3. Effects of T33 (0.5 μmol/L) on the gene transcription (A), degradation (B), and translation (C) of I-κBα in primary atrocytes subjected to OGD or O/R (n=4). (D) A representative picture shows the effect of T33 (0.5 μmol/L) on PPARγ binding activity in primary atrocytes subjected to OGD or O/R. [Lane 1) positive control+200-fold cold probe; 2) control sample; 3) OGD+T33 sample; 4) OGD sample; 5) positive control; 6) positive control+200-fold cold probe; 7) control sample; 8) O/R sample; 9) O/R+T33 sample]. (E) Statistical analysis of PPARγ binding activity is shown (n=3). (F) A generalization of the multi-level regulation of I-κBα in ischemic core models and the T33 target is shown. ^{b}P<0.05, ^{c}P<0.01 *vs* control group; ^{e}P<0.05, ^{f}P<0.01 *vs* correspondent OGD or O/R group.

T33 alleviates hypoxia-induced inflammatory responses in BV-2 cells subjected to hypoxia

Since inflammation cascades in the penumbra facilitate its progression into infarction, the anti-inflammatory effects of T33 in models simulating the inflammatory responses in the penumbra were evaluated. We detected a marked increase in TNF-α levels (73.86 pg/mL) in the culture medium from BV-2 cells subjected to hypoxia compared to normoxia treated cells (6.87 pg/mL). Pre-treatment with T33 reduced the level of TNF-α to 25 pg/mL (Figure 4A, P<0.05), and GW9662 restored the content to 85.86 pg/mL (Figure 4A, P<0.05). Similar results were observed for the protein levels of COX-2, which were elevated in hypoxia-treated BV-2 cells compared to the normoxia treated group (Figure 4B and 4C, P<0.05) and were alleviated by treatment with T33 (Figure 4B and 4C, P<0.05). P38 phosphorylation, which mediates inflammatory responses in BV-2 cells subjected to hypoxia, was reduced by T33 pre-treatment (Figure 4B and 4D, P<0.01). The ameliorating effects of T33 on COX-2 and p-p38 levels were antagonized by pre-administration with GW9662 (COX-2: Figure 4C, P<0.05; p-p38: Figure 4D, P<0.01).

Anti-inflammatory and neuroprotective effects of T33 in rats subjected to MCAO

Given the strong anti-inflammatory activities of T33 in *in vitro* models, further *in vivo* evaluation of the compound in the MCAO model was necessary. The infarct area in all six consecutive coronal sections was reduced by the administration of T33 (Figure 5A, 5C, and 5D, P<0.05). Correspondingly, the neurological score was improved by T33 treatment (Figure 5B, P<0.01). In addition, inflammatory responses were investigated in ipsilateral (ischemic)/contralateral striatum and cortex. The transcriptional levels of TNF-α and IL-1β and the protein level of COX-2 were reduced in the ischemic cortex and striatum of rats treated with T33 (P<0.05, P<0.01), whereas the expression of these inflammatory mediators remained the same in the contralateral side (Figure 6). These neuroprotective and anti-inflammatory effects of T33 were reversed by pre-administration with GW9662 (P<0.05, P<0.01).

Discussion

Inflammatory mediators synthesized in astrocytes contribute largely to inflammatory reactions in the ischemic core. Consistent with previous findings[5, 28], we found that O/R induced an overexpression of TNF-α, IL-1β, and COX-2 in primary astrocytes. The ability of T33 to alleviate the increased expression of these inflammatory mediators could be ascribed at least in part to a reduction in the activation of NF-κB, a principal mediator of post-ischemic inflammatory responses[27, 29]. Inhibiting NF-κB activation by T33 was achieved by restoring the protein levels of I-κBα, which binds to NF-κB in the cytosol and masks the nuclear localization signal within the p65 sub-

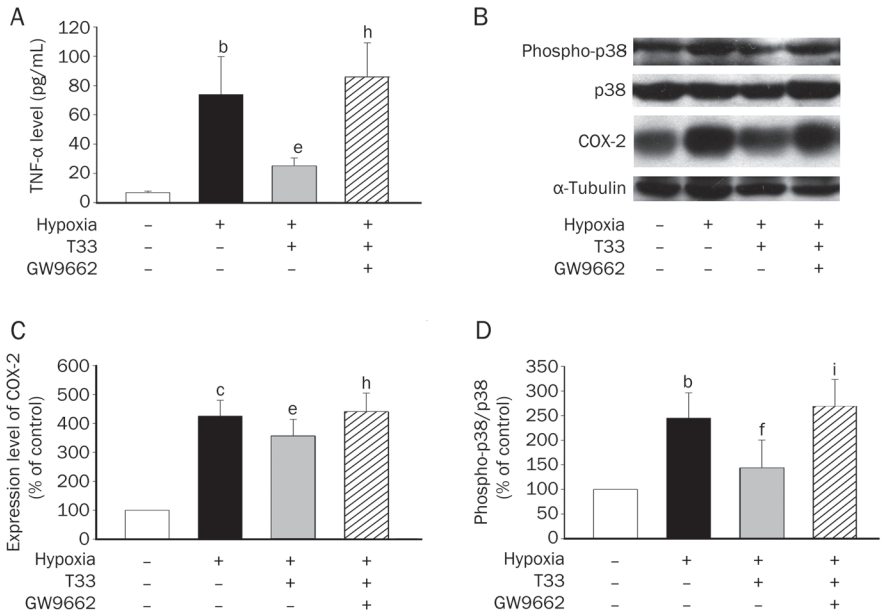

Figure 4. Anti-inflammatory effects of T33 (0.5 μmol/L) in BV-2 cells subjected to hypoxia. (A) The effects of T33 on TNF-α levels in culture medium are shown. (B, C, D) The effects of T33 on the protein levels of COX-2 and p38 phosphorylation are shown (B: representative Western blots; C, D: statistical results). n=4. Comparisons were made using a paired sample t-test. $^{b}P<0.05$, $^{c}P<0.01$ *vs* control group; $^{e}P<0.05$, $^{f}P<0.01$ *vs* hypoxia group; $^{h}P<0.05$, $^{i}P<0.01$ *vs* hypoxia+T33 group.

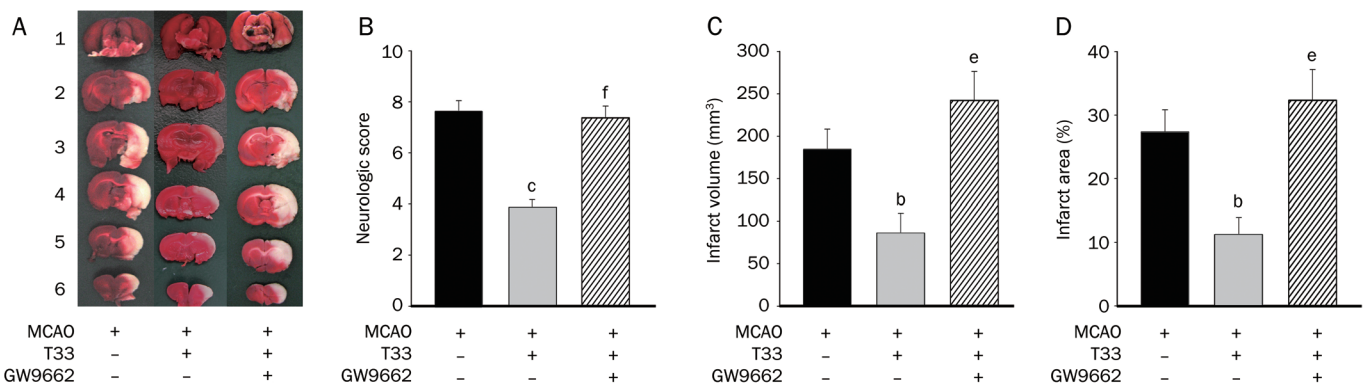

Figure 5. Neuroprotective effects of T33 (2 mg/kg) in rats subjected to MCAO. (A) T33 reduces cerebral infarct size. Six consecutive TTC-stained coronal brain slices are arranged in cranial to caudal order. (B) T33 alleviates the neurological deficits of rats subjected to MCAO. (C) T33 reduces total infarct volume (statistical results). (D) Infarct percentages are shown. n=8. $^{b}P<0.05$, $^{c}P<0.01$ *vs* MCAO group; $^{e}P<0.05$, $^{f}P<0.01$ *vs* MCAO+T33 group.

unit[30–32]. Both a transcriptional deficiency and an accelerated degradation contributed to the I-κBα protein content decline in astrocytes subjected to OGD, whereas after reperfusion, a decrease in mRNA translation resulted in a sharp reduction in I-κBα protein content. In contrast to other compounds that block I-κBα degradation[33], T33 suppressed the I-κBα/NF-κB pathway by restoring I-κBα synthesis. mRNA translation, found to be severely impaired in ischemic areas, was shown to be related to eIF-2α over-phosphorylation, which blocks the initiation of protein translation and leads to a depression of protein synthesis[34]. In areas vulnerable to ischemia, mRNA translation is persistently inhibited, even after reperfusion, which facilitates excessive toxic reactions and abrogates survival cascades, leading to the formation of the ischemic core[34]. Inhibiting eIF-2α over-phosphorylation restored I-κBα translation after incubation with T33[35]. In addition to ameliorating inflammatory responses, promoting mRNA translation might also rescue pathways that help cells survive and function normally, such as by restoring the expression of growth factors and down-stream molecules. These actions help to reduce the area of ischemic core. Therefore, by rescuing protein translation in the ischemic core model, T33 is potent in protecting areas vulnerable to ischemic injuries.

I-κBα mRNA levels were dramatically reduced in astrocytes subjected to OGD and were restored after reperfusion. Rescuing I-κBα gene transcription enabled T33 to restore I-κBα protein synthesis in astrocytes subjected to OGD and alleviate the activation of the I-κBα/NF-κB pathway. These results suggest that T33 regulates I-κBα protein levels via pleiotropic mechanisms, which involve both the genomic restoration of I-κBα transcription and the non-genomic restoration of I-κBα mRNA translation (Figure 3F).

Although an induction of PPARγ expression has been reported in transient cerebral ischemic models[36], the activ-

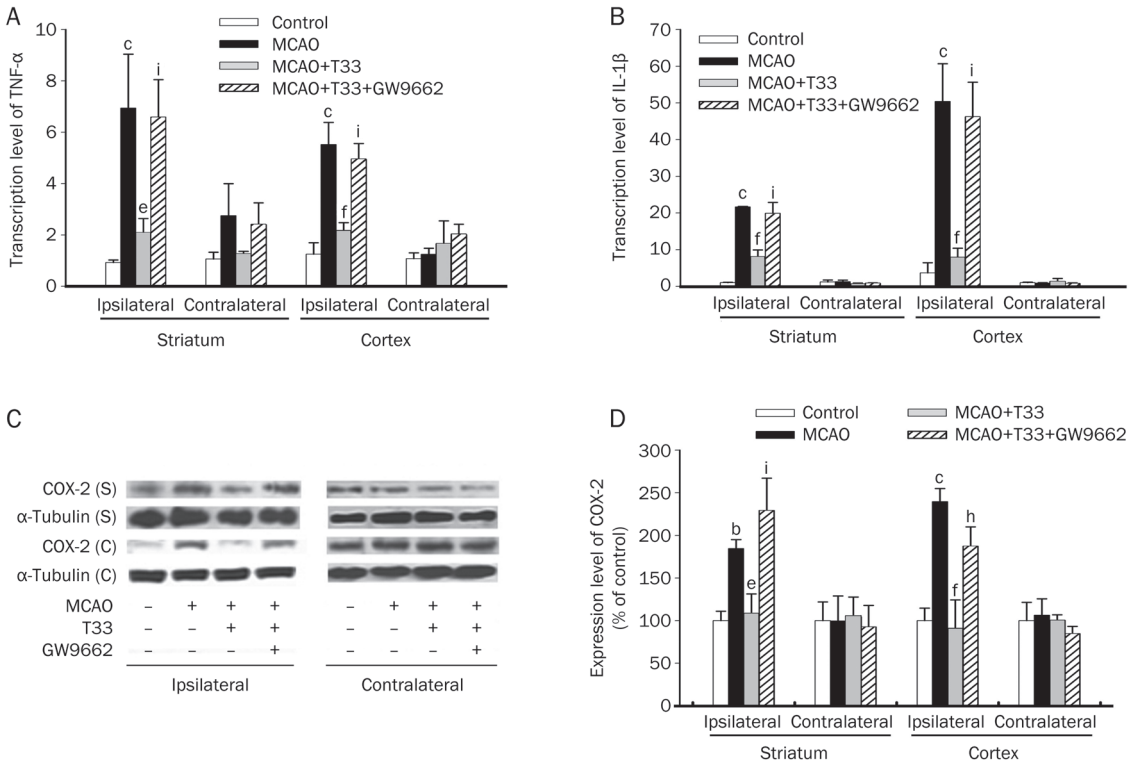

Figure 6. Anti-inflammatory effects of T33 (2 mg/kg) in rats subjected to MCAO. (A) T33 alleviates the mRNA levels of TNF-α in ischemic striatum and cortex, but not in contralateral striatum or cortex. (B) T33 alleviates the mRNA levels of IL-1β in ischemic striatum and cortex, but not in contralateral striatum or cortex. (C, D) T33 reduces the protein levels of COX-2 in ischemic striatum and cortex. n=4. ^{b}P<0.05, ^{c}P<0.01 *vs* control group; ^{e}P<0.05, ^{f}P<0.01 *vs* MCAO group; ^{h}P<0.05, ^{i}P<0.01 *vs* MCAO+T33 group.

ity of PPARγ was found to be severely defective upon ischemia[37]. The phenomenon that the severely depressed PPARγ activity levels in astrocytes subjected to OGD is restored to nearly normal levels after reperfusion might result from stress-induced self-protection. The activation of PPARγ by T33 at the beginning of OGD did not lead to a higher level of activity of PPARγ after reperfusion, which could be attributed to mitigated stress by the treatment of T33. Moreover, previous studies have suggested that the activation of PPARγ promotes the repression of the exaggerated expression of inflammatory mediators that occurs in response to transient cerebral ischemia[12, 38]. These actions of PPARγ could be mediated, at least in part, by inhibiting the I-κBα/NF-κB pathway, since I-κBα is a PPARγ target gene[39]. PPARγ activation has been shown to amplify I-κBα expression, negatively interfering with the NF-κB signaling cascade[40]. This notion was further confirmed by the present research, as the alterations in PPARγ activity during OGD and reperfusion paralleled in the changes in the mRNA levels of I-κBα. However, an elevation of gene transcription failed to rescue the protein levels of I-κBα after reperfusion. This phenomenon could be explained by the blunted I-κBα translation function mentioned previously and suggests that the self-recovery of PPARγ activity during reperfusion might be too late to exert further anti-inflammatory effects. Therefore, preserving PPARγ activity by T33 treatment from the start of OGD is crucial in reducing inflammatory responses during ischemia and could also contribute to the late curtailed inflammatory cascades during reperfusion in the current ischemic core model. This result coincides with a recent *in vivo* study demonstrating that the administration of TZDs after reperfusion does not exert a neuroprotective effect toward ischemia[41]. However, we cannot rule out that non-PPARγ dependent pathways may be involved in reserving I-κBα protein levels by T33, because it still remains unknown how PPARγ activation influences eIF-2α phosphorylation. Further studies are needed to clarify the precise mechanisms.

According to existing studies, inflammatory mediators synthesized in microglia upon activation contribute largely to ischemic brain injury, promoting neuronal death in the penumbra and the progression of penumbra into ischemic infarction[42, 43]. The phosphorylation and activation of p38 is of particular importance in regulating the production of inflammatory mediators induced by hypoxia[44, 45]. Treatment with specific inhibitors of p38 could blunt the inflammatory responses[46] and reduce brain injury induced by cerebral focal ischemia[47]. The potency of T33 in suppressing p38-mediated inflammatory reactions dependent on PPARγ provided additional evidence concerning the beneficial effects of this compound in treating hypoxic-ischemic brain injury. Although we focused on the activated inflammatory cascades, it is important to note that p38 over-phosphorylation is involved in other abnormal responses under pathological circumstances

like ischemia. Reactive oxygen species-induced injuries[48] and Aβ-induced neurotoxicity, for example, are also mediated by p38 over-phosphorylation. Since oxidative reactions stimulated soon after ischemia are toxic to neuronal cells, inhibiting p38 phosphorylation might alleviate brain injury by blocking oxidative reactions. Given that post-stroke dementia is associated with the generation of Aβ[49], we predict that the administration of T33 would not only alleviate acute ischemia-induced brain injury but also might reduce post-stroke dementia through the dual reduction of ischemia-induced inflammation and Aβ-induced neurotoxicity.

The above *in vitro* findings provide novel insight into the anti-inflammatory effects and mechanisms of T33 in ischemic core and penumbra models. Because PPARγ agonists are capable of modulating inflammatory responses by reducing the activation of p38 and NF-κB in activated glial cells[50], we hypothesized that PPARγ agonizing might contribute to the anti-inflammatory activity of T33 in an *in vivo* MCAO ischemic model. Since post-ischemic brain inflammation contributes largely to the formation of brain infarction, the neuroprotective effect of T33 was further evaluated. A vigorous neuroprotective effect was observed without affecting the CBF (data not shown). The neuroprotective effect of T33 was shown to be dependent on PPARγ activation and was comparable to the effects of other PPARγ agonists in ischemia-induced brain injuries[51, 52]. In addition, the dose of 2 mg/kg was comparable to that of TZDs in rat ischemic models, indicating that T33 could be neuroprotective at a clinically relevant dosage. The reason that a PPARα antagonist was not used in the present study was that the effects of T33 were completely blocked by a PPARγ antagonist. It seems that the current dosage might not be sufficient for PPARα to exert anti-inflammatory actions in the MCAO model, especially if T33 is administered systemically. These results suggest that T33 could be of therapeutic value for ischemic stroke.

Our study demonstrated for the first time that T33, a novel PPARγ/α agonist with potent neuroprotective activity in a rat transient ischemic model, exerts strong anti-inflammatory effects in ischemic core and penumbra models. These effects occurred via genomic and non-genomic regulation of I-κBα expression and p38 activation. The activation of PPARγ was required for most of the actions of T33, although it is possible that a non-PPARγ pathway might be partially involved. The present study provides a good example of the beneficial effects of T33 and encourages further development of PPARγ/α agonists for the treatment of ischemic stroke.

Acknowledgements

The authors are grateful to Prof Shu-min DUAN for providing the BV-2 cell line.

This research was funded by the National Natural Science Foundation of China (No 30801402), the Scientific Research Foundation for the Returned Overseas Chinese Scholars, State Education Ministry, the National Science & Technology Major Project "Key New Drug Creation and Manufacturing Program" of China (No 2009ZX09301-001; 2009ZX09301-063) and the Shanghai Science and Technology Development Fund (No 10QA1408100).

Author contribution

Hai-yan ZHANG and Ying WANG designed the research; Ying WANG performed the research; Yu-she YANG provided T33; Ying WANG, Xi-can TANG, and Hai-yan ZHANG analyzed the results and wrote the paper.

References

1 Kaufmann AM, Firlik AD, Fukui MB, Wechsler LR, Jungries CA, Yonas H. Ischemic core and penumbra in human stroke. Stroke 1999; 30: 93–9.
2 Hughes JL, Beech JS, Jones PS, Wang D, Menon DK, Baron JC. Mapping selective neuronal loss and microglial activation in the salvaged neocortical penumbra in the rat. Neuroimage 2010; 49: 19–31.
3 Barone FC, Feuerstein GZ. Inflammatory mediators and stroke: new opportunities for novel therapeutics. J Cereb Blood Flow Metab 1999; 19: 819–34.
4 Chamorro A, Hallenbeck J. The harms and benefits of inflammatory and immune responses in vascular disease. Stroke 2006; 37: 291–3.
5 Wang ZF, Wang J, Zhang HY, Tang XC. Huperzine A exhibits anti-inflammatory and neuroprotective effects in a rat model of transient focal cerebral ischemia. J Neurochem 2008; 106: 1594–603.
6 Kim HJ, Rowe M, Ren M, Hong JS, Chen PS, Chuang DM. Histone deacetylase inhibitors exhibit anti-inflammatory and neuroprotective effects in a rat permanent ischemic model of stroke: multiple mechanisms of action. J Pharmacol Exp Ther 2007; 321: 892–901.
7 Barone FC, Parsons AA. Therapeutic potential of anti-inflammatory drugs in focal stroke. Expert Opin Investig Drugs 2000; 9: 2281–306.
8 Lakhan SE, Kirchgessner A, Hofer M. Inflammatory mechanisms in ischemic stroke: therapeutic approaches. J Transl Med 2009; 7: 97.
9 Vamecq J, Latruffe N. Medical significance of peroxisome proliferator-activated receptors. Lancet 1999; 354: 141–8.
10 Petrova TV, Akama KT, Van Eldik LJ. Cyclopentenone prostaglandins suppress activation of microglia: down-regulation of inducible nitric-oxide synthase by 15-deoxy-Delta12,14-prostaglandin J2. Proc Natl Acad Sci U S A 1999; 96: 4668–73.
11 Ricote M, Li AC, Willson TM, Kelly CJ, Glass CK. The peroxisome proliferator-activated receptor-gamma is a negative regulator of macrophage activation. Nature 1998; 391: 79–82.
12 Culman J, Zhao Y, Gohlke P, Herdegen T. PPAR-gamma: therapeutic target for ischemic stroke. Trends Pharmacol Sci 2007; 28: 244–9.
13 Fong WH, Tsai HD, Chen YC, Wu JS, Lin TN. Anti-apoptotic actions of PPAR-gamma against ischemic stroke. Mol Neurobiol 2010; 41: 180–6.
14 Zhao X, Strong R, Zhang J, Sun G, Tsien JZ, Cui Z, *et al*. Neuronal PPARgamma deficiency increases susceptibility to brain damage after cerebral ischemia. J Neurosci 2009; 29: 6186–95.
15 Wu JS, Cheung WM, Tsai YS, Chen YT, Fong WH, Tsai HD, *et al*. Ligand-activated peroxisome proliferator-activated receptor-gamma protects against ischemic cerebral infarction and neuronal apoptosis by 14-3-3 epsilon upregulation. Circulation 2009; 119: 1124–34.
16 Glatz T, Stock I, Nguyen-Ngoc M, Gohlke P, Herdegen T, Culman J, *et al*. Peroxisome-proliferator-activated receptors gamma and peroxisome-proliferator-activated receptors beta/delta and the regulation of interleukin 1 receptor antagonist expression by pioglitazone in ischaemic brain. J Hypertens 2010; 28: 1488–97.
17 Das SK, Chakrabarti R. Role of PPAR in cardiovascular diseases.

Recent Pat Cardiovasc Drug Discov 2006; 1: 193–209.
18 Rizos E, Mikhailidis DP. Are high density lipoprotein (HDL) and triglyceride levels relevant in stroke prevention? Cardiovasc Res 2001; 52: 199–207.
19 Hu X, Feng Y, Liu X, Zhao XF, Yu JH, Yang YS, *et al*. Effect of a novel non-thiazolidinedione peroxisome proliferator-activated receptor alpha/gamma agonist on glucose uptake. Diabetologia 2007; 50: 1048–57.
20 Hu X, Feng Y, Shen Y, Zhao XF, Yu JH, Yang YS, *et al*. Antidiabetic effect of a novel non-thiazolidinedione PPAR gamma/alpha agonist on *ob/ob* mice. Acta Pharmacol Sin 2006; 27: 1346–52.
21 Wu DC, Xiao XQ, Ng AK, Chen PM, Chung W, Lee NT, *et al*. Protection against ischemic injury in primary cultured mouse astrocytes by *bis*(7)-tacrine, a novel acetylcholinesterase inhibitor [corrected]. Neurosci Lett 2000; 288: 95–8.
22 Nagasawa H, Kogure K. Correlation between cerebral blood flow and histologic changes in a new rat model of middle cerebral artery occlusion. Stroke 1989; 20: 1037–43.
23 Bederson JB, Pitts LH, Tsuji M, Nishimura MC, Davis RL, Bartkowski H. Rat middle cerebral artery occlusion: evaluation of the model and development of a neurologic examination. Stroke 1986; 17: 472–6.
24 Nilupul Perera M, Ma HK, Arakawa S, Howells DW, Markus R, Rowe CC, *et al*. Inflammation following stroke. J Clin Neurosci 2006; 13: 1–8.
25 Swanson RA, Ying W, Kauppinen TM. Astrocyte influences on ischemic neuronal death. Curr Mol Med 2004; 4: 193–205.
26 Wang Q, Tang XN, Yenari MA. The inflammatory response in stroke. J Neuroimmunol 2007; 184: 53–68.
27 Nurmi A, Lindsberg PJ, Koistinaho M, Zhang W, Juettler E, Karjalainen-Lindsberg ML, *et al*. Nuclear factor-kappaB contributes to infarction after permanent focal ischemia. Stroke 2004; 35: 987–91.
28 Niu F, Zhang X, Chang L, Wu J, Yu Y, Chen J, *et al*. Trichostatin A enhances OGD-astrocyte viability by inhibiting inflammatory reaction mediated by NF-kappaB. Brain Res Bull 2009; 78: 342–6.
29 Schneider A, Martin-Villalba A, Weih F, Vogel J, Wirth T, Schwaninger M. NF-kappaB is activated and promotes cell death in focal cerebral ischemia. Nat Med 1999; 5: 554–9.
30 Baeuerle PA, Baltimore D. I kappa B: a specific inhibitor of the NF-kappa B transcription factor. Science 1988; 242: 540–6.
31 Baeuerle PA, Baltimore D. A 65-kappaD subunit of active NF-kappaB is required for inhibition of NF-kappaB by I kappaB. Genes Dev 1989; 3: 1689–98.
32 Beg AA, Ruben SM, Scheinman RI, Haskill S, Rosen CA, Baldwin AS Jr. I kappa B interacts with the nuclear localization sequences of the subunits of NF-kappa B: a mechanism for cytoplasmic retention. Genes Dev 1992; 6: 1899–913.
33 Wang ZF, Tang XC. Huperzine A protects C6 rat glioma cells against oxygen-glucose deprivation-induced injury. FEBS Lett 2007; 581: 596–602.
34 Hu BR, Wieloch T. Stress-induced inhibition of protein synthesis initiation: modulation of initiation factor 2 and guanine nucleotide exchange factor activities following transient cerebral ischemia in the rat. J Neurosci 1993; 13: 1830–8.
35 Deng J, Lu PD, Zhang Y, Scheuner D, Kaufman RJ, Sonenberg N, *et al*. Translational repression mediates activation of nuclear factor kappa B by phosphorylated translation initiation factor 2. Mol Cell Biol 2004; 24: 10161–8.
36 Patzer A, Zhao Y, Stock I, Gohlke P, Herdegen T, Culman J. Peroxisome proliferator-activated receptors gamma (PPARgamma) differently modulate the interleukin-6 expression in the peri-infarct cortical tissue in the acute and delayed phases of cerebral ischaemia. Eur J Neurosci 2008; 28: 1786–94.
37 Victor NA, Wanderi EW, Gamboa J, Zhao X, Aronowski J, Deininger K, *et al*. Altered PPARgamma expression and activation after transient focal ischemia in rats. Eur J Neurosci 2006; 24: 1653–63.
38 Bordet R, Ouk T, Petrault O, Gele P, Gautier S, Laprais M, *et al*. PPAR: a new pharmacological target for neuroprotection in stroke and neurodegenerative diseases. Biochem Soc Trans 2006; 34: 1341–6.
39 Buroker NE, Barboza J, Huang JY. The *IκBα* gene is a peroxisome proliferator-activated receptor cardiac target gene. FEBS J 2009; 276: 3247–55.
40 Dehmer T, Heneka MT, Sastre M, Dichgans J, Schulz JB. Protection by pioglitazone in the MPTP model of Parkinson's disease correlates with I kappa B alpha induction and block of NF kappa B and iNOS activation. J Neurochem 2004; 88: 494–501.
41 Gamboa J, Blankenship DA, Niemi JP, Landreth GE, Karl M, Hilow E, *et al*. Extension of the neuroprotective time window for thiazolidinediones in ischemic stroke is dependent on time of reperfusion. Neuroscience 2010; 170: 846–57.
42 Kaushal V, Schlichter LC. Mechanisms of microglia-mediated neurotoxicity in a new model of the stroke penumbra. J Neurosci 2008; 28: 2221–30.
43 Zhang Q, Chen C, Lu J, Xie M, Pan D, Luo X, *et al*. Cell cycle inhibition attenuates microglial proliferation and production of IL-1beta, MIP-1alpha, and NO after focal cerebral ischemia in the rat. Glia 2009; 57: 908–20.
44 Wang J, Zhang HY, Tang XC. Huperzine a improves chronic inflammation and cognitive decline in rats with cerebral hypoperfusion. J Neurosci Res 2010; 88: 807–15.
45 Irving EA, Bamford M. Role of mitogen- and stress-activated kinases in ischemic injury. J Cereb Blood Flow Metab 2002; 22: 631–47.
46 Park SY, Lee H, Hur J, Kim SY, Kim H, Park JH, *et al*. Hypoxia induces nitric oxide production in mouse microglia via p38 mitogen-activated protein kinase pathway. Brain Res Mol Brain Res 2002; 107: 9–16.
47 Barone FC, Irving EA, Ray AM, Lee JC, Kassis S, Kumar S, *et al*. SB 239063, a second-generation p38 mitogen-activated protein kinase inhibitor, reduces brain injury and neurological deficits in cerebral focal ischemia. J Pharmacol Exp Ther 2001; 296: 312–21.
48 McCubrey JA, Lahair MM, Franklin RA. Reactive oxygen species-induced activation of the MAP kinase signaling pathways. Antioxid Redox Signal 2006; 8: 1775–89.
49 Zhang T, Pan BS, Zhao B, Zhang LM, Huang YL, Sun FY. Exacerbation of poststroke dementia by type 2 diabetes is associated with synergistic increases of beta-secretase activation and beta-amyloid generation in rat brains. Neuroscience 2009; 161: 1045–56.
50 Collino M, Aragno M, Mastrocola R, Gallicchio M, Rosa AC, Dianzani C, *et al*. Modulation of the oxidative stress and inflammatory response by PPAR-gamma agonists in the hippocampus of rats exposed to cerebral ischemia/reperfusion. Eur J Pharmacol 2006; 530: 70–80.
51 Chen SD, Wu HY, Yang DI, Lee SY, Shaw FZ, Lin TK, *et al*. Effects of rosiglitazone on global ischemia-induced hippocampal injury and expression of mitochondrial uncoupling protein 2. Biochem Biophys Res Commun 2006; 351: 198–203.
52 Schmerbach K, Schefe JH, Krikov M, Muller S, Villringer A, Kintscher U, *et al*. Comparison between single and combined treatment with candesartan and pioglitazone following transient focal ischemia in rat brain. Brain Res 2008; 1208: 225–33.

Acta Pharmacologica Sinica (2011) 32: 1109–1115
 1671-4083/11 $32.00
www.nature.com/aps

Original Article

Synergism of irbesartan and amlodipine on hemodynamic amelioration and organ protection in spontaneously hypertensive rats

Wen SHANG[1, #], Ping HAN[1, #, §], Cheng-bing YANG[1, 2, #], Xiao-wen GU[1], Wei ZHANG[1], Li-ping XU[1], Shou-ting FU[1, 2], Ding-feng SU[1], He-hui XIE[1, *]

[1]*Department of Pharmacology, Second Military Medical University, Shanghai 200433, China;* [2]*School of the Life Science and Biopharmaceutics, Shenyang Pharmaceutical University, Shenyang 110016, China*

Aim: To investigate the synergism of low-doses of amlodipine and irbesartan on reduction of blood pressure variability (BPV), amelioration of baroreflex sensitivity (BRS) and organ protection in spontaneously hypertensive rats (SHR).
Methods: The rats were administered amlodipine (1 mg·kg^{-1}·d^{-1}) alone, irbesartan (10 mg·kg^{-1}·d^{-1}) alone, or the combination of the two drugs for 4 months. The drugs were mixed into the rat chow. Blood pressure (BP) was continuously monitored in conscious animals. After the determination of BRS, the rats were killed for morphological evaluation of organ damages.
Results: The combination of low-dose irbesartan and amlodipine had statistically significant synergism on reduction of BP and BPV, amelioration of BRS and organ protection in SHR. Multiple regression analysis showed that the decrease in left ventricular hypertrophy was associated with the decrease in systolic BPV (r=0.665, P<0.01); the decrease in aortic hypertrophy was associated with the increase in BRS (r=0.656, P<0.01); and the amelioration in renal lesion was associated with the increase in BRS (r=0.763, P<0.01) and the decrease in systolic BPV (r=0.706, P<0.01).
Conclusion: Long-term treatment with a combination of low-doses of amlodipine and irbesartan showed significant synergism on reduction of BP and BPV, restoration of BRS and organ protection in SHR. Besides BP reduction, the enhancement of BRS and reduction of BPV might contribute to the organ protection.

Keywords: hypertension; spontaneously hypertensive rats (SHR); amlodipine; irbesartan; hypertension; end organ damage; blood pressure variability; baroreflex sensitivity

Acta Pharmacologica Sinica (2011) 32: 1109–1115; doi: 10.1038/aps.2011.88; published online 1 Aug 2011

Introduction

It is well known that blood pressure (BP) level is an important determinant for the end-organ damage in hypertensive patients or hypertensive animals. However, BP level is certainly not the unique determinant for end-organ damage. Recently, it has been proposed that blood pressure variability (BPV) and baroreflex sensitivity (BRS) may be two important factors determining organ damage in hypertension[1–6]. This implies that antihypertensive treatment should aim at not only reducing BP values but also reducing BPV and enhancing BRS.

The importance of a combination therapy has been well recognized in the treatment of hypertension[7, 8]. To better control BP is the main objective of the combination therapy. Generally speaking, a combination of two drugs belonging to different classes may possess a synergism on BP reduction. However, limited imformation is available about whether such a combination possesses a synergism on BPV reduction, BRS restoration and organ protection. Irbesartan, an angiotensin II receptor blocker, and amlodipine, a dihydropyridine calcium antagonist, are two widely used drugs in the treatment of hypertension. They belong to two different classes of antihypertensives and the mechanisms of action are quite different for these two drugs. Therefore, the present work was designed to investigate the possible synergism of irbesartan and amlodipine on BP and BPV reduction, BRS restoration and organ protection in spontaneously hypertensive rats (SHR).

# The first three authors contributed equally to this work.
§ Now in *Center for Disease Control and Prevention, Ji-nan Military Region, PLA, Ji-nan 250012, China.*
* To whom correspondence should be addressed.
E-mail xhhtom@263.net
Received 2010-06-29 Accepted 2011-05-04

Materials and methods

Animals and chemicals

Male SHRs with an age of 18 weeks were provided by the animal center of Second Military Medical University. The rats were housed with controlled temperature (22–24 °C) and lighting (8:00–20:00 light, 20:00–8:00 dark) and with free access to food and tap water. All the animals used in this work received humane care in compliance with institutional animal care guidelines. Antihypertensive drugs used in this study are as follows: amlodipine (Nanjing Pharmaceutical Co Ltd, Nanjing, China) and irbesartan (Jiangsu Hengrui Pharmaceutical Co Ltd, Lianyungang, China).

Drug administration

Studies were performed in four groups of SHR. Irbesartan, amlodipine or combination of these two drugs were mixed in the rat chow. The consumption of rat chow containing drugs was determined previously. The content of drugs in the rat chow was calculated according to the chow consumption, and the ingested doses of drugs were approximately 10 $mg \cdot kg^{-1} \cdot d^{-1}$ for irbesartan, 1 $mg \cdot kg^{-1} \cdot d^{-1}$ for amlodipine and 1+10 $mg \cdot kg^{-1} \cdot d^{-1}$ for the combination of these two drugs. The control SHR group received the same diet without the drugs. We used relatively low doses of drugs to avoid a very remarkable normalization of BP in the treatment, which would make it much difficult to distinguish the contribution of blood pressure variability and baroreflex sensitivity to organ protection from that of blood pressure. After 4 months of drug administration, BP was recorded during 24 h, and then BPV was calculated and BRS was determined in conscious freely moving rats. Histopathological examinations were performed after BP recording and BRS studies.

BP measurement

Systolic BP (SBP), diastolic BP (DBP) and heart period (HP) of rats were continuously recorded using a previously described technique[9, 10]. Briefly, rats were anesthetized with a combination of ketamine (40 mg/kg) and diazepam (6 mg/kg). A floating polyethylene catheter was inserted into the lower abdominal aorta via the left femoral artery for BP measurement, and another catheter was placed into the left femoral vein for intravenous injection. The catheters were exteriorized through the interscapular skin. After a 3-d recovery period, the animals were placed for BP recording in individual cylindrical cages containing food and water. The aortic catheter was connected to a BP transducer via a rotating swivel that allowed the animals to move freely in the cage. The hemodynamic recording system used in the present work is MPA-HBBS blood pressure and heart rate analysis system (Model: MPA-HBBS. Shanghai Alcott Biotech Co, LTD, Shanghai, China). The transducer is ALC-AP12 blood pressure sensor (Model: ALC-AP12. Shanghai Alcott Biotech Co, Ltd, Shanghai, China). After about 14-h habituation, the BP signal was digitized by a microcomputer. SBP, DBP and HP values from every heartbeat were determined on line. The mean values and standard deviation of these parameters (including all beats) during a period of 24 h were calculated. The standard deviation was defined as the quantitative parameter of BPV, ie systolic BPV (SBPV), diastolic BPV (DBPV), and HP variability (HPV).

BRS measurement

To determine the function of arterial baroreflex in conscious rats, the methods widely used are derived from that of Smyth firstly applied for humans[11]. The principle of this method is to measure the prolongation of HP in response to an elevation of BP. With some modifications, this method was used in conscious rats[12, 13]. A bolus injection of phenylephrine was used to induce an elevation of BP. The dose of phenylephrine was adjusted to raise SBP between 20 and 40 mmHg. HP was plotted against SBP for linear regression analysis and the slope of SBP-HP was expressed as BRS (ms/mmHg).

Morphological examination

The animal was weighed and killed by decapitation. The thoracic and peritoneal cavities were immediately opened. The right kidney, aorta and heart were excised and rinsed in cold physiological saline. The right kidney was blotted, and weighed. The left ventricle was isolated, blotted, and weighed. At the same time, the aorta was cleaned of adhering fat and connective tissue. Just below the branch of the left subclavicular artery, a 30-mm-long segment of thoracic aorta was harvested, blotted, and weighed. Ratios of left ventricular weight to body weight (LVW/BW), and aortic weight to the length of aorta (AW/length) were calculated[14]. Histopathological observation was also carried out with our conventional method[15]. Briefly, immediately after gross detection, all samples of left ventricles in 2- to 3-mm-thick slices, aortae and kidney were immersed in formalin solution for more than 1 week, dehydrated in ethanol, cleared in dimethylbenzene and embedded in paraffin. Then 5-μm-thick sections were prepared and stained with hematoxylin and eosin for light microscopic evaluation.

Glomerulosclerosis score

For the semiquantitative evaluation of glomerular damage, the glomerulosclerosis score (GSS) was defined as previously described[16]. On the light microscopic specimens, approximately 50 glomeruli from the outer cortex and the same number of glomeruli from the inner cortex for each kidney were graded according to the degree of sclerosis: 0, if no mesangial expansion; 1, if mild mesangial expansion (less than 30% of a glomerular area); 2, if moderate mesangial expansion (30%–60% of a glomerular area); 3, if marked mesangial expansion (more than 60% of a glomerular area); and 4, if the sclerosis was global. This was performed by one observer in a blind fashion using coded slides. A weighted composite sclerosis score was then calculated for each kidney according to the following formula: glomerulosclerosis score=[1×(number of grade 1 glomeruli)+2×(number of grade 2 glomeruli) +3×(number of grade 3 glomeruli)+4×(number of grade 4 glomeruli)]×100/(number of glomeruli observed).

Probability sum test

To determine whether the combination was synergistic, we tried to use the probability sum test. This came from classic probability analysis and it was proposed for evaluating the synergism of the combination of 2 drugs (q test)[13, 17, 18]. In the present work, we used the following criteria. Compared with the mean values of control rats, treated rats with a decrease in BP (SBP or DBP) ≥20 mmHg were defined as responders according to clinical experiences. For other parameters, treated rats with a decrease or increase ≥20% of the mean values of the control group were defined as responders. The formula is as follows: $q=P_{A+B}/(P_A+P_B-P_A\times P_B)$. Here, A and B indicate drug A and drug B; P (probability) is the percentage of responders in each group. P_{A+B} is real percentage of responder and $(P_A+P_B-P_A\times P_B)$ is expected response rate. (P_A+P_B) indicates the sum of the probabilities when drug A and drug B were used alone. $(P_A\times P_B)$ is the probability of rats responding to both drugs when they were used alone, *ie*, assuming the two drugs act independently. When $q<0.85$, the combination is antagonistic; when $q>1.15$, it is synergistic; and when q between 0.85 and 1.15, it is additive.

Statistical analysis

Data are expressed as mean±SEM. Comparisons among groups were made by ANOVA followed by Duncan test. The relationships between hemodynamic parameters and organ damage parameters were analyzed by classic univariate correlation analysis. Stepwise multiple-regression analysis was performed to study the independent effect of hemodynamic parameters on organ damage. F to enter and F to remove were set to $P<0.05$ and $P>0.10$, respectively. $P<0.05$ was considered statistically significant. Statistical analysis was performed by using software SPSS 11.0.0.

Results

Effects on BP, BPV, and BRS in SHR

Both long-term amlodipine (1 mg·kg^{-1}·d^{-1}) and irbesartan (10 mg·kg^{-1}·d^{-1}) had no obvious effect on BP level, whereas combination of these two drugs significantly decreased SBP and DBP values in SHR. Amlodipine did not significantly affect the BPV and BRS values, but both irbesartan and the combination marketly decreased SBPV (-21%, $P<0.01$; -34%, $P<0.01$, respectively), DBPV (-24%, $P<0.05$; and -36%, $P<0.01$, respectively) and obviously enhanced BRS (+77%, $P<0.05$; and +155%, $P<0.05$, respectively) in SHR. The extents of BPV reduction and BRS amelioration in combination-treated rats were significantly greater than those in irbesartan-treated rats. No obvious change was found in HP and HPV in any treatment group (Table 1, Figure 1).

Table 1. Effects of long-term treatment with irbesartan, amlodipine alone and in combination on hemodynamics in spontaneously hypertensive rats. Values are mean±SEM. $^bP<0.05$, $^cP<0.01$ *vs* SHR.

	SHR (n=11)	Irb (n=8)	Aml (n=9)	Irb+Aml (n=9)
SBP (mmHg)	188±2.9	185±1.2	182±4.3	175±3.6^c
DBP (mmHg)	126±4.2	123±1.6	117±4.2	112±4.0^b
HP (ms)	159±4.0	158±5.4	158±4.2	164±2.9
SBPV (mmHg)	15.9±0.7	12.5±0.2^c	13.9±0.8	10.5±0.3^c
DBPV (mmHg)	12.6±0.9	9.6±0.2^b	11.4±0.8	8.1±0.1^c
HPV (ms)	29.0±2.0	24.4±2.3	32.1±2.2	26.5±1.4
BRS (ms/mmHg)	0.28±0.05	0.48±0.05^b	0.39±0.09	0.71±0.04^c

SHR, spontaneously hypertensive rats; Irb, irbesartan-treated rats; Aml, amlodipine-treated rats; Irb+Aml, combination-treated rats; SBP, systolic blood pressure; DBP, diastolic blood pressure; HP, heart period; SBPV, systolic blood pressure variability; DBPV, diastolic blood pressure variability; HPV, heart period variability; BRS, baroreflex sensitivity.

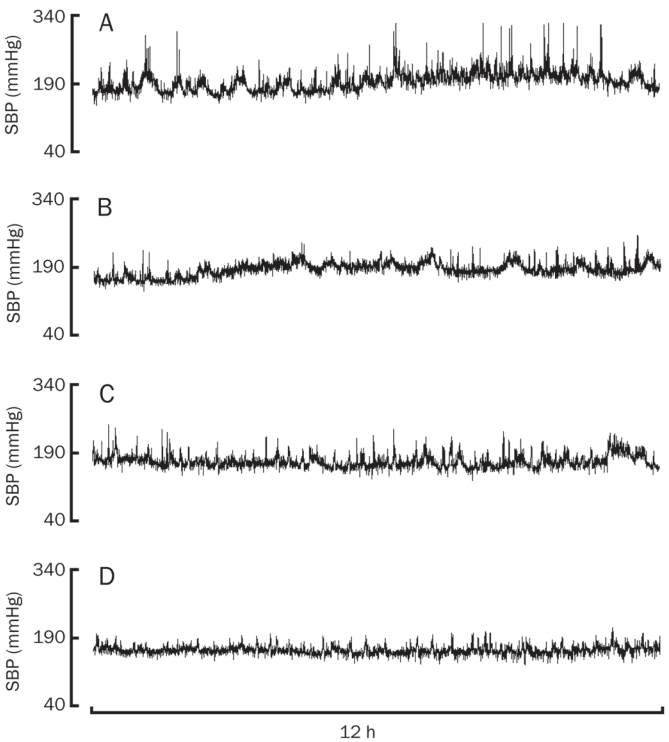

Figure 1. Representative tracings of systolic blood pressure in conscious spontaneously hypertensive rats. SBP, systolic blood pressure; A, spontaneously hypertensive rats; B, irbesartan-treated rats; C, amlodipine-treated rats; D, combination-treated rats.

Effects on organ damages in SHR

Among organ damage parameters studied, some representative parameters are shown in Figure 2. They are LVW/BW (reflecting left ventricular hypertrophy), AW/length (reflecting aortic hypertrophy) and GSS (reflecting renal damage). It was found that long-term treatment with irbesartan, which had no effect on SBP and DBP levels, significantly decreased LVW/BW (-9.8%, $P<0.05$), AW/length (-13%, $P<0.01$) and GSS (-17%, $P<0.01$) in SHR. No significant decrease in all the three organ damage parameters was found in amlodipine-treated

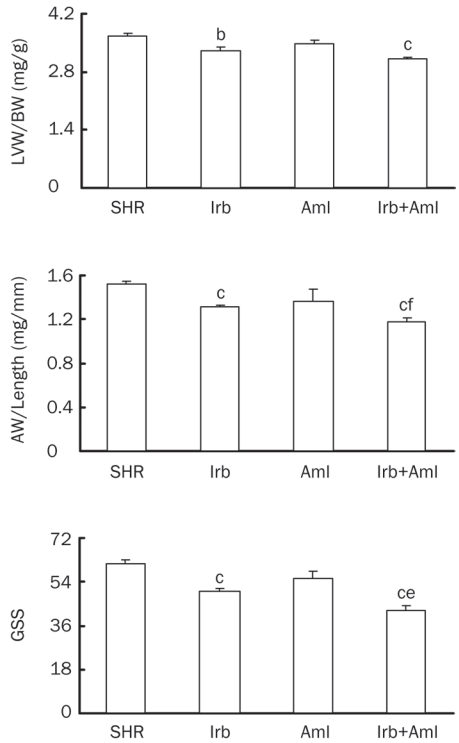

Figure 2. Effects of long-term treatment with irbesartan, amlodipine alone and in combination on pathological changes in ventricles, aortae, and kidneys in spontaneously hypertensive rats. SHR, spontaneously hypertensive rats (n=11); Irb, irbesartan-treated rats (n=8); Aml, amlodipine-treated rats (n=9); Irb+Aml, combination-treated rats (n=9); LVW, left ventricular weight; BW, body weight; AW, aortic weight; GSS, glomerulosclerosis score. ^{b}P<0.05, ^{c}P<0.01 *vs* SHR; ^{e}P<0.05, ^{f}P<0.01 *vs* Irb.

rats. Treatment with the combination significantly decreased all the three organ damage parameters, and the extents of decrease in AW/length (-24%, P<0.01) and GSS (-30%, P<0.01) were greater than those in irbesartan-treated rats.

Synergism of irbesartan and amlodipine in SHR

Table 2 showed the result of the probability sum test in data from SHR treated with irbesartan, amlodipine and the combination. All q values were larger than 1.15. It was found that the combination of irbesartan and amlodipine possesses a significant synergism on BP and BPV reduction, BRS amelioration and organ protection in SHR.

Relationships between BP, BPV, BRS, and organ damages in SHR

When all the SHRs employed in the present study were pooled as a whole (n=37) for linear regression analysis, relationships between BP, BPV, BRS and organ damages are shown in Table 3. It was found that LVW/BW, AW/length and GSS were all negatively related to BRS and positively related to SBP, SBPV and DBPV, but not to DBP. Both HP and HPV were not correlated with all the three organ damage parameters (data not shown). Some examples for important correlations are shown in Figure 3.

Table 2. The result of probability sum test in spontaneously hypertensive rats treated with long-term irbesartan and amlodipine.

SBP	Irb	P_{Irb}=0%	
	Aml	P_{Aml}=22%	q=1.50
	Irb+Aml	$P_{Irb+Aml}$=33%	
SBPV	Irb	P_{Irb}=50%	
	Aml	P_{Aml}=33%	q=1.50
	Irb+Aml	$P_{Irb+Aml}$=100%	
DBP	Irb	P_{Irb}=0%	
	Aml	P_{Aml}=22%	q=1.50
	Irb+Aml	$P_{Irb+Aml}$=33%	
DBPV	Irb	P_{Irb}=63%	
	Aml	P_{Aml}=33%	q=1.33
	Irb+Aml	$P_{Irb+Aml}$=100%	
BRS	Irb	P_{Irb}=63%	
	Aml	P_{Aml}=44%	q=1.26
	Irb+Aml	$P_{Irb+Aml}$=100%	
LVW/BW	Irb	P_{Irb}=13%	
	Aml	P_{Aml}=0%	q=1.78
	Irb+Aml	$P_{Irb+Aml}$=22%	
AW/Length	Irb	P_{Irb}=13%	
	Aml	P_{Aml}=33%	q=1.87
	Irb+Aml	$P_{Irb+Aml}$=78%	
GSS	Irb	P_{Irb}=13%	
	Aml	P_{Aml}=22%	q=2.43
	Irb+Aml	$P_{Irb+Aml}$=8%	

See Table 1 and Figure 2 for abbreviations. q>=1.15 means synergism.

Table 3. Linear regression coefficient (r) between BP, BPV, BRS values, and organ damages in treated and untreated spontaneously hypertensive rats (n=37). ^{b}P<0.05, ^{c}P<0.01. See Table 1 and Figure 2 for abbreviations.

	LVW/BW	AW/length	GSS
SBP	0.475^{c}	0.520^{c}	0.534^{c}
DBP	0.126	0.275	0.318
SBPV	0.665^{c}	0.674^{c}	0.706^{c}
DBPV	0.476^{c}	0.490^{c}	0.621^{c}
BRS	-0.457^{c}	-0.656^{c}	-0.763^{c}

As aforementioned, irbesartan produced organ protective action independent of its BP-lowering effect. To elucidate the role of BPV and BRS in the protection, the relationships between BP, BPV, BRS and organ damages were also analyzed in irbesartan-treated and untreated rats (Table 4). Considering the limited number (n=8) of irbesartan-treated rats would reduced the validity of linear regression analysis, irbesartan-

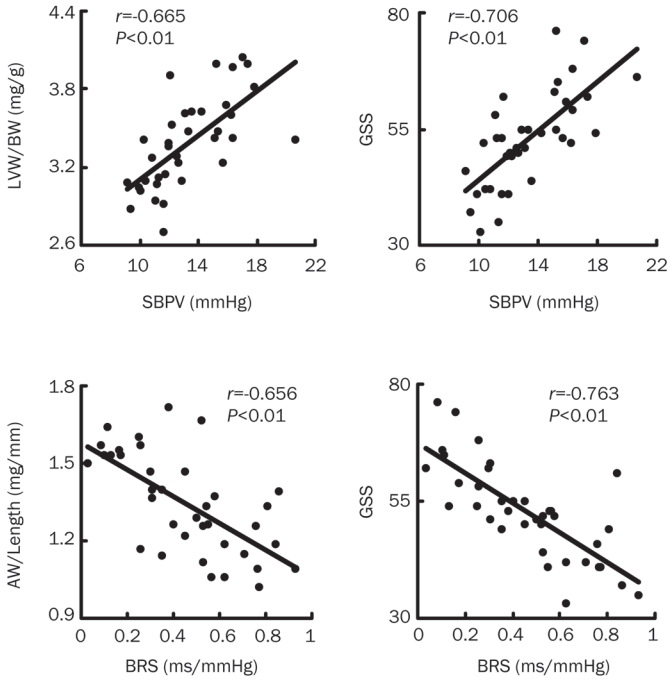

Figure 3. Examples of correlation between hemodynamic parameters and organ-damage parameters in treated and untreated spontaneously hypertensive rats. n=37. See Table 1 and Figure 2 for abbreviations.

Table 4. Linear regression coefficient (r) between BP, BPV, BRS values, and organ damages in irbesartan-treated and untreated spontaneously hypertensive rats (n=19). $^bP<0.05$, $^cP<0.01$. See Table 1 and Figure 2 for abbreviations.

	LVW/BW	AW/length	GSS
SBP	0.178	0.118	0.307
DBP	-0.032	0.153	0.134
SBPV	0.459[b]	0.527[b]	0.541[b]
DBPV	0.225	0.422	0.455
BRS	-0.227	-0.543[b]	-0.755[c]

treated rats and control SHRs were pooled as a whole. It was found that both AW/length and GSS were markedly correlated with BRS, and all the three pathological parameters were significantly related to SBPV, but not to SBP or DBP level.

Furthermore, when all the SHRs employed in the present study were pooled as a whole, the relative dependencies of organ damage on hemodynamic parameters were assessed by stepwise multiple-regression analysis. LVW/BW was independently associated with higher SBPV (β=0.657, P<0.01; where β is the standardized partial regressive coefficient). AW/length was independently associated with higher SBPV (β=0.422, P<0.05) and lower BRS (β=-0.371, P<0.05). Glomerulosclerosis score was independently associated with lower BRS (β=-0.525, P<0.01) and higher SBPV (β=0.354, P<0.05).

Discussion

The present work clearly demonstrated the synergism of low-dose irbesartan and amlodipine in reducing BP and BPV, restoring BRS and protecting end organs in SHRs.

It was found that both amlodipine (1 $mg \cdot kg^{-1} \cdot d^{-1}$) and irbesartan (10 $mg \cdot kg^{-1} \cdot d^{-1}$) had no obvious effect on BP level, whereas combination of these two drugs significantly decreased SBP and DBP values in SHR. A synergistic effect on SBP and DBP reduction was found in combination therapy (q=1.5 for both SBP and DBP). This synergistic effect would reduce the dose of each drug required in the treatment of hypertension and then could minimize the clinical and metabolic side effects of each individual component in larger dosage when used alone. It has been proposed that dihydropyridines have a natriuretic effect, which is expected to render blood pressure maintenance more angiotensin II-dependent[19, 20]. This may account for the synergistic effect of amlodipine and irbesartan on BP reduction. In addition, the response of the sympathetic nervous system to the vasodilation induced by dihydropyridines is buffered by concomitant blockade of the renin-angiotensin system, which may contribute to enhancement of the BP reduction as well as to prevention of the reflex increase in heart rate and the palpitations possibly occurring during calcium channel blockade [19, 21].

Clinical observations suggested that BPV was related to organ damages in hypertensive patients [1, 22–24]. In animal studies, it has been reported that the organ damages induced by sinoaortic denervation were related to the high BPV but not to BP level[25, 26]. Accordingly, it seems very important to emphasize the role of BPV in antihypertensive therapy[6]. However, little information is available about how to better control BPV in the treatment of hypertension. In the present work, chronic treatment with combination of low-dose irbesartan and amlodipine markedly decreased BPV in SHR and an obvious synergism on BPV reduction was found in combination therapy. These results suggested that combination therapy might be more effective in control of BPV than monotherapy.

Arterial baroreflex dysfunction is another feature of hypertension. It has been well recognized that BRS is impaired in hypertensive humans and animals[4, 5, 27]. It should be noted that baroreflex sensitivity as measured in the present work provides rather limited insight into baroreflex vascular regulation. However, baroreflex sensitivity measured with this technique may mainly reflect the vagal component of baroreflex and is important in the pathology of cardiovascular diseases[28–30]. Our previous study proposed that BRS was one of the independent variables related to end-organ damage score in hypertension[31]. In the present work, long-term treatment with combination of low-dose irbesartan and amlodipine markedly enhanced BRS in SHR, and an obvious synergism on BRS restoration was found in combination therapy. In hypertension, the impairment of baroreflex is mainly the result of elevated BP level[32–34]. Therefore, BRS will be enhanced when BP level is lowered by an antihypertensive drug. However, the present work showed that the enhancement of BRS was

not attributable to the normalization of BP level in irbesartan-treated rats. It has been reported that endogenous angiotensin II acted at AT_1 receptors in the nucleus of the solitary tract (NTS) to attenuate the arterial baroreflex (ABR) function in SHRs and WKY rats, and that microinjection of CV-11974 (AT_1 receptors antagonist) in the NTS enhanced the ABR function in SHRs and WKY rats without altering the prevailing level of blood pressure at the same time[32]. Accordingly, irbesartan, an AT_1 receptor antagonist, may act at AT_1 receptors in the NTS level to enhance the ABR function in SHRs.

The present work demonstrated that long-term treatment with the combination of irbesartan and amlodipine possessed the obvious effects on organ protection in SHR, and an obvious synergism on organ protection was found in combination therapy. It was found that LVW/BW, AW/length, and GSS were all positively related to SBP, SBPV, and DBPV, and negatively related to BRS in treated and untreated SHRs. In multiple-regression analysis, decrease in left ventricular hypertrophy was most closely associated with the decrease in SBPV, the decrease in aortic hypertrophy was most closely associated with the increase in BRS and the decrease in SBPV, and amelioration in renal lesion was most closely associated with the increase in BRS and the decrease in SBPV. These results suggest that the decrease in BP and BPV and the enhancement of baroreflex function may co-contribute to the organ protective action of drugs in SHR. But, it should be noted that, from a statistical point of view, the aforementioned results of multiple-regression analysis did not necessarily prove that reducing BPV and improving BRS may lead to a higher organ protection.

In addition, the present work showed that irbesartan produced organ protective action independent of its BP-lowering effect. It has been reported that candesartan (an AT_1 bloker) was effective in protection against hypertensive organ damage even at dose having no effect on BP, and the blockade of rennin-angiotensin system (RAS) was one of the major mechanisms[35–37]. The present work showed that both AW/length and GSS were markedly correlated with BRS, and all the three pathological parameters were significantly related to SBPV, but not to SBP or DBP level in the irbesartan-treated and untreated rats. Therefore, in addition to known mechanisms for RAS antagonists, the present work might show another two possible mechanisms for this BP-independent organ protection of irbesartan: reduction of BPV and enhancement of BRS.

In conclusion, long-term treatment with a combination of amlodipine and irbesartan possessed an obvious synergism in BP and BPV reduction, BRS restoration and organ protection in SHR. Besides BP reduction, the enhancement of BRS and reduction of BPV might importantly contribute to this organ protection.

Acknowledgements

This work was supported by the National Science and Technology Major Project (2009ZX09303-002) and the National Natural Science Foundation of China (No 30971158).

Author contribution

Wen SHANG, Ping HAN, Cheng-bing YANG, Xiao-wen GU, Wei ZHANG, Li-ping XU, and Shou-ting FU performed research and analyzed data; Ding-feng SU designed research; He-hui XIE designed research, analyzed data, and wrote the paper.

References

1 Kikuya M, Hozawa A, Ohokubo T, Tsuji I, Michimata M, Matsubara M, *et al*. Prognostic significance of blood pressure and heart rate variabilities: the Ohasama study. Hypertension 2000; 36: 901–6.
2 Parati G, Mancia G. Blood pressure variability as a risk factor. Blood Press Monit 2001; 6: 341–7.
3 Su DF, Miao CY. Reduction of blood pressure variability: a new strategy for the treatment of hypertension. Trends Pharmacol Sci 2005; 26: 388–90.
4 Su DF, Miao CY. Functional studies of arterial baroreflex function in conscious rats. Acta Pharmacol Sin 2002; 23: 673–9.
5 Sleight P. The importance of autonomic nervous system in health and disease. Aust N Z J Med 1997; 27: 467–73.
6 Liu JG, Xu LP, Chu ZX, Miao CY, Su DF. Contribution of blood pressure variability to the effect of nitrendipine on end-organ damage in spontaneously hypertensive rats. J Hypertens 2003; 21: 1961–7.
7 Gupta AK, Arshad S, Poulter NR. Compliance, safety, and effectiveness of fixed-dose combinations of antihypertensive agents: a meta-analysis. Hypertension 2010; 55: 399–407.
8 Chobanian AV, Bakris GL, Black HR, Cushman WC, Green LA, Izzo JL Jr, *et al*. Seventh report of the Joint National Committee on Prevention, Detection, Evaluation, and Treatment of High Blood Pressure. Hypertension 2003; 42: 1206–52.
9 Xie HH, Miao CY, Liu JG, Su DF. Effects of long-term treatment with candesartan on organ damages in sinoaortic denervated rats. J Cardiovasc Pharmacol 2003; 41: 325–31.
10 Norman RA Jr, Coleman TG, Dent AC. Continuous monitoring of arterial pressure indicates sinoaortic denervated rats are not hypertensive. Hypertension 1981; 3: 119–25.
11 Smyth HS, Sleight P, Pickering GW. Reflex regulation of arterial pressure during sleep in man: a quantitative method of assessing baroreflex sensitivity. Circ Res 1969; 24: 109–21.
12 Su DF, Chen L, Kong XB, Cheng Y. Determination of arterial baroreflex-blood pressure control in conscious rats. Acta Pharmacol Sin 2002; 23: 103–9.
13 Xie HH, Miao CY, Jiang YY, Su DF. Synergism of atenolol and nitrendipine on hemodynamic amelioration and organ protection in hypertensive rats. J Hypertens 2005; 23: 193–201.
14 Hayakawa H, Raij L. The link among nitric oxide synthase activity, endothelial function, and aortic and ventricular hypertrophy in hypertension. Hypertension 1997; 29: 235–41.
15 Miao CY, Tao X, Gong K, Zhang SH, Chu ZX, Su DF. Aterial remodeling in chronic sinoaortic-denervated rats. J Cardiovasc Pharmacol 2001; 37: 6–15.
16 Kimula K, Tojo A, Matsuoka H, Sugimoto T. Renel arteriolar diameters in spontaneously hypertensive rats: Vascular cast study. Hypertension 1991; 18: 101–10.
17 Jin ZJ. About the evaluation of drug combination. Acta Pharmacol Sin 2004; 25: 146–7.
18 Su DF, Xu LP, Miao CY, Xie HH, Shen FM, Jiang YY. Two useful methods for evaluating antihypertensive drugs in conscious freely moving rats. Acta Pharmacol Sin 2004; 25: 148–51.
19 Waeber B, Ruilope LM. Amlodipine and valsartan as components

of a rational and effective fixed-dose combination. Vasc Health Risk Manag 2009; 5: 165–74.
20 Luft FC, Aronoff GR, Sloan RS, Fineberg NS, Weinberger MH. Calcium channel blockade with nitrendipine. Effects on sodium homeostasis, the renin-angiotensin system, and the sympathetic nervous system in humans. Hypertension 1985; 7: 438–42.
21 Gennari C, Nami R, Pavese G, Gragnani S, Bianchini C, Buracchi P. Calcium-channel blockade (nitrendipine) in combination with ACE inhibition (captopril) in the treatment of mild to moderate hypertension. Cardiovasc Drugs Ther 1989; 3: 319–25.
22 Parati G, Pomidossi G, Albini F, Malaspina D, Mancia G. Relationship of 24-hour blood pressure mean and variability to severity of target organ damage in hypertension. J Hypertens 1987; 5: 93–8.
23 Mancia G, Omboni S, Parati G. The importance of blood pressure variability in hypertension. Blood Press Monit 2000; 5: S9–S15.
24 Sander D, Kukla C, Klingelhofer J, Winbeck K, Conrad B. Relationship between circadian blood pressure patterns and progression of early carotid atherosclerosis: A 3-year follow-up study. Circulation 2000; 102: 1536–41.
25 Miao CY, Su DF. The importance of blood pressure variability in rat aortic and left ventricular hypertrophy by sinoaortic denervation. J Hypertens 2002; 20: 1865–72.
26 Parati G, Lantelme P. Blood pressure variability, target organ damage and cardiovascular events. J Hypertens 2002; 20: 1725–9.
27 Bristow JD, Honour AJ, Pickering GW, Sleight P, Smyth HS. Diminished baroreflex sensitivity in high blood pressure. Circulation 1969; 39: 48–54.
28 La Rovere MT, Bigger JT Jr, Marcus FI, Mortara A, Schwartz PJ. Baroreflex sensitivity and heart-rate variability in prediction of total cardiac mortality after myocardial infarction. ATRAMI (Autonomic Tone and Reflexes After Myocardial Infarction) Investigators. Lancet 1998; 351: 478–84.
29 Mortara A, La Rovere MT, Pinna GD, Prpa A, Maestri R, Febo O, *et al*. Arterial baroreflex modulation of heart rate in chronic heart failure: clinical and hemodynamic correlates and prognostic implications. Circulation 1997; 96: 3450–8.
30 Cai GJ, Miao CY, Xie HH, Lu LH, Su DF. Arterial baroreflex dysfunction promotes atherosclerosis in rats. Atherosclerosis 2005; 183: 41–7.
31 Shan ZZ, Dai SM, Su DF. Relationship between baroreceptor reflex function and end-organ damage in spontaneously hypertensive rats. Am J Physiol 1999; 277: H1200–6.
32 Parmer RJ, Cervenka JH, Stone RA. Baroreflex sensitivity and heredity in essential hypertension. Circulation 1992; 85: 497–503.
33 Parmer RJ, Cervenka JH, Stone RA, O'Connor DT. Autonomic function in hypertension: Are there racial difference? Circulation 1990; 81: 1305–11.
34 Brown AM. Receptors under pressure. An update on baroreceptors. Circ Res 1980; 46: 1–10.
35 Matsumura K, Averill DB, Ferrario CM. Angiotensin II acts at AT1 receptors in the nucleus of the solitary tract to attenuate the baroreceptor reflex. Am J Physiol 1998; 275: R1611–9.
36 Nishikawa K. Angiotensin AT_1 receptor antagonism and protection against cardiovascular end-organ damage. J Human Hypertens 1998; 12: 301–9.
37 Murayama S, Hirano T, Sakaue T, Okada K, Ikejiri R, Adachi M. Low-dose candesartan cilexetil prevents early kidney damage in type 2 diabetic patients with mildly elevated blood pressure. Hypertens Res 2003; 26: 453–8.

Acta Pharmacologica Sinica (2011) 32: 1116–1127
 1671-4083/11 $32.00
www.nature.com/aps

Original Article

Proteome reference map and regulation network of neonatal rat cardiomyocyte

Zi-jian LI[1, #], Ning LIU[2, #], Qi-de HAN[1], You-yi ZHANG[1, *]

[1]*Institute of Vascular Medicine, Peking University Third Hospital and Key Laboratory of Cardiovascular Molecular Biology and Regulatory Peptides, Ministry of Health and Key Laboratory of Molecular Cardiology, Ministry of Education, Beijing 100191, China;* [2]*Central Laboratory, Jilin University Second Hospital, Changchun 130041, China*

Aim: To study and establish a proteome reference map and regulation network of neonatal rat cardiomyocyte.
Methods: Cultured cardiomyocytes of neonatal rats were used. All proteins expressed in the cardiomyocytes were separated and identified by two-dimensional polyacrylamide gel electrophoresis (2-DE) and matrix-assisted laser desorption/ionization-time of flight mass spectrometry (MALDI-TOF MS). Biological networks and pathways of the neonatal rat cardiomyocytes were analyzed using the Ingenuity Pathway Analysis (IPA) program (www.ingenuity.com). A 2-DE database was made accessible on-line by Make2ddb package on a web server.
Results: More than 1000 proteins were separated on 2D gels, and 148 proteins were identified. The identified proteins were used for the construction of an extensible markup language-based database. Biological networks and pathways were constructed to analyze the functions associate with cardiomyocyte proteins in the database. The 2-DE database of rat cardiomyocyte proteins can be accessed at http://2d.bjmu.edu.cn.
Conclusion: A proteome reference map and regulation network of the neonatal rat cardiomyocytes have been established, which may serve as an international platform for storage, analysis and visualization of cardiomyocyte proteomic data.

Keywords: proteome; neonatal rat cardiomyocyte; regulation network; 2-DE database

Acta Pharmacologica Sinica (2011) 32: 1116–1127; doi: 10.1038/aps.2011.86; published online 15 Aug 2011

Introduction

Proteomic technology allows for the global analysis of gene products in various cells, tissues and organisms. In parallel with other burgeoning technologies and coupled with the rapidly growing needs of life scientists, proteomics has become one of the most utilized approaches in all of life science research. As the Human Proteome Project is set in place[1], there will be an urgent need to store vast amounts of information in proteomic databases; these databases will become a powerful tool to utilize in the research of human diseases. Heart disease is the leading cause of death in many countries including the United States, England and Canada. Proteomics approaches have clearly grown in potential to provide global and holistic analysis of changes in protein expression during heart disease. The earliest establishment of myocardial two-dimensional gel electrophoresis (2-DE) protein databases, beginning in the 1990s, focused on identifying proteins from human myocardium. In the database from the Jungblut laboratory, N-terminal sequencing, internal sequencing and amino acid analysis were used to identify twelve proteins of the human myocardial 2-DE pattern[2]. During the same year, a database containing approximately fifty proteins from 2-DE gels of human myocardial tissue was characterized by the Baker laboratory[3]. Subsequent studies have succeeded in establishing myocardial 2-DE protein databases in different species, such as rat, mouse, and dog, and thereby enriched myocardial 2-DE protein databases[4–7]. These databases have allowed investigators to compare data and to establish reference standards.

Proteomic technology has been used extensively to study cardiovascular diseases and to identify candidate molecules for diagnosis and therapy in intact live animals. Compared with intact hearts, cell culture models would be very useful to distinguish the differences between myocytes *versus* fibroblasts, to eliminate hemodynamic and hormonal influences and to study cell phenotypes and signaling in more homogeneous populations in a defined environment. However, pro-

# These authors contributed equally to this work.
* To whom correspondence should be addressed.
E-mail zhangyy@bjmu.edu.cn
Received 2010-10-16 Accepted 2011-05-18

teomic investigations of cardiomyocyte are scarce, and a 2-DE protein database for the rat cardiomyocyte has not been developed before. In this work, we have launched a proteomic study of neonatal rat cardiomyocytes and compiled a profile of proteins expressed in these cells 2-DE and matrix-assisted laser desorption/ionization-time of flight mass spectrometry (MALDI-TOF MS). Using immobilized pH gradient isoelectric focusing in a linear gradient from pH 3 to 10 in 12% sodium dodecyl sulfate-polyacrylamide gel electrophoresis (SDS-PAGE), more than 1000 proteins were separated and displayed from cultured cardiomyocytes. Among those, 148 proteins spots have so far been identified and used for the construction of an extensible markup language-based database. In addition to the cardiomyocyte proteins stored in this database, we also characterized interaction-based biological networks of proteins, which allow us to model how proteins work together to mediate biological processes. Moreover, our network analysis has also revealed function maps and pathway maps potentially involved in the neonatal rat cardiomyocyte proteins database.

In summary, with the rapid development of modern proteomics, it is essential that annotated databases are constructed to store all of the vast data generated by these techniques. More important is that these databases can be interrogated effectively both within the laboratory and by other scientists worldwide through the use of the World Wide Web. The database presented in this work will serve as an international platform for the storage, analysis, and visualization of cardiomyocyte proteomic data that can contribute to a more holistic view of heart tissue. This database may contribute to understanding key cardiovascular functions and pathways and may offer the potential for new avenues of future therapeutic intervention.

Materials and methods

Cardiomyocyte culture

Neonatal rat cardiomyocytes were isolated and cultured as previously described[8]. Briefly, cardiomyocytes were dissociated from ventricles of 1- to 2-d old neonatal Sprague-Dawley rats using 0.1% trypsin (Hyclone) and 80 units/mL collagenase (Worthington Biochemical Corp) in a Hank's balanced salt solution (calcium-free; Hyclone). To purify the cardiomyocytes from non-myocytes, isolated cells were pre-plated for 90 min. The enriched cardiomyocyte fractions were seeded into 150-cm culture dishes and cultured in DMEM (Sigma, 4500 mg/L *D*-glucose, and *L*-glutamine, sodium pyruvate) supplemented with 10% heat-inactivated fetal bovine serum for 24 h. The DNA synthesis inhibitor, bromodeoxyuridine (100 μmol/L), was added during the first 48 h to prevent the proliferation of non-cardiomyocytes. The experiments were approved by the Institutional Animal Care and Use Committee of Peking University Health Science Center (LA2010-035) and were adhered to the American Physiological Society's "Guiding Principles in the Care and Use of Vertebrate Animals in Research and Training." All protocols were conducted in accordance with the Guidelines for Animal Experiments, Peking University Health Science Center.

Two-dimensional electrophoresis (2-DE)

Proteins were separated by two-dimensional electrophoresis. Samples containing 200 μg protein for analytical gels or up to 1.0 mg for micropreparative gels were diluted to 300 μL with rehydration solution (6 mol/L urea, 2 mol/L thiourea, 2% CHAPS, 65 mmol/L DTT, 0.5% *v/v* pH 3-10 Bio-lyte, trace bromophenol blue) and applied to IPG strips (Bio-Rad) for 12–14 h in a passive mode. The isoelectric focusing was performed at 20 °C over 24 h for a total of 70 000 V-h. After equilibration of the IPG strips, the second-dimensional SDS electrophoresis was performed on 12% gels at a current setting of 7.5 mA/gel for the initial 2 h and 15 mA/gel until the tracking dye reached the cathode.

Protein visualization and image analysis

After two-dimensional gel electrophoresis, proteins were stained with silver or with G-250 for subsequent mass spectrometry. In order to increase the sensitivity of Coomassie staining, we improved the prescription of Coomassie staining as follows: 20% methanol, 2% phosphoric acid, 10% ammonium sulfate and 0.1% Coomassie Brilliant Blue G-250. Gels were fixed in 12.5% TCA for 60 min and rinsed in Milli-Q water for 20 min. The gels were then stained in the improved Coomassie staining solution for 24 h. After the stained gels were scanned with a high-resolution scanner (Umax 1120), the gel images were analyzed using the PDQuest software (Version 7.1.1; Bio-Rad) according to the protocols provided by the manufacturer.

Identification of protein spots

Protein spots of interest visualized with colloidal Coomassie blue G-250 staining were excised and transferred to 1.5 mL siliconized Eppendorf tubes. The gel spots were then washed and destained by 50% ACN, then dried in a vacuum centrifuge. The dried gel-pieces were incubated in the digestion solution containing 50 mmol/L NH_4HCO_3 and 0.1 g/L TPCK-trypsin for 12 h at 37 °C. The resulting peptides were extracted three times by 50 μL aliquots of 5% trifluoroacetic acid in 60% acetonitrile. Combined extracts were concentrated in a Speed Vac to 3–5 μL.

The concentrated tryptic peptide mixture was mixed with a saturated CHCA matrix solution and vortexed gently. A volume (1 μL) of the mixture containing CHCA matrix was loaded on a 96×2 well hydrophobic plastic surface sample plate (Applied Biosystems) and air-dried. The samples were analyzed with a Voyager DE STR MALDI-TOF MS (Applied Biosystems) fitted with a 337-nm nitrogen laser. Spectra were acquired using the instrument in reflectron mode and calibrated using a standard peptide mixture. Database searching with the monoisotopic peptide masses was performed against the NCBInr database by using the peptide search engine ProFound (http://prowl.rockefeller.edu/cgi-bin/ProFound) by using the following conditions: partial methionine oxidation, complete cysteine carbamidomethylation, mass tolerance of

0.2 Da, and one missing cleavage.

Biological networks and pathway analysis

The biological network data were generated through the use of Ingenuity Pathways Analysis (IPA) software (www.ingenuity.com), a web-delivered application that evaluates biological networks. A data set of proteins from cardiomyocytes was uploaded into IPA. Each protein identifier was mapped to its corresponding protein object in the Ingenuity Pathways Knowledge Base (IPKB). These proteins were then used as the starting point for generating biological networks based upon the identities of the focus proteins and interactions with genes/proteins that were reported in the literature. IPA calculated a significance score for each network. The score was generated using a *P*-value calculation and was displayed as the negative log of that *P*-value, indicating the likelihood that the assembly of a set of focus proteins in a network could be explained by random chance alone. A score of 2 indicates that there is a 1 in 100 chance that the focus proteins are together in a network due to random chance. Therefore, networks with scores of 2 or higher have at least a 99% confidence of not being generated by random chance alone. Biological functions or canonical pathways were then calculated and assigned to each network by using findings that had been extracted from scientific literature and stored in the IPKB. The biological functions assigned to each network were ranked according to the significance of that biological function to the network.

Construction of an on-line database

One 2-DE gel of neonatal rat cardiomyocyte proteins was analyzed by PDQuest software (Version 7.1.1; Bio-Rad). The identified protein spots were stored in a flat file database that was made accessible on-line by the Make2ddb package on a web server with search functions, such as by accession number, description, or author or by clicking on a protein spot. The individual protein entries were hyperlinked to the relevant spots on an image map created from the reference gel.

Results

Data management, analysis, and presentation

A schematic representation of our proteomic informatics approach for the research of neonatal rat cardiomyocytes is illustrated in Figure 1. It mainly consists of three parts: data acquisition, data analysis, and web-accessible data presentation. The laboratory information management system (LIMS) is applied in this study for the acquisition of proteomic data. Results of gel image analysis performed by PDQuest can also be transmitted into the LIMS. A Java graphical user interface (Java-GUI) enables transfer of selected data from the LIMS into the database system consisting of 2D-PAGE, network/function analysis and protein information. The database system is interconnected with public and other knowledge databases. Furthermore, continuative explorative data analysis for significant networks and canonical pathways relevant to the dataset were calculated and analyzed using IPA.

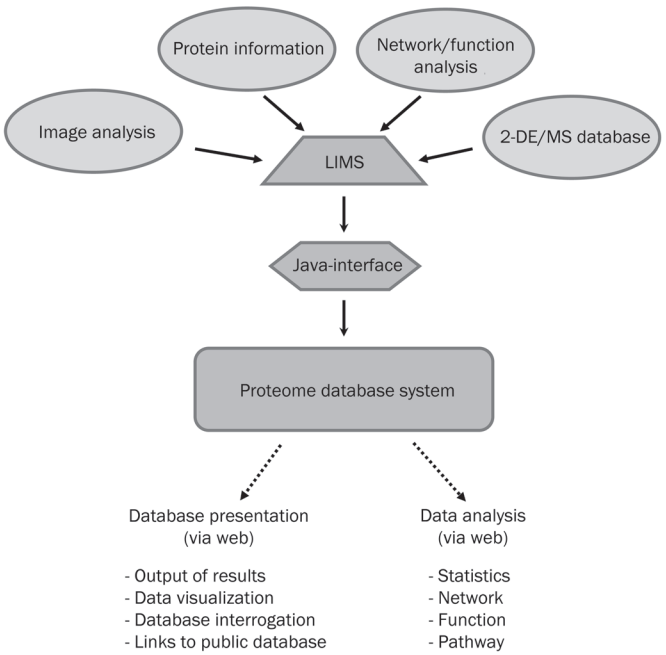

Figure 1. A schematic representation of our proteome informatics approach for the database research of neonatal rat cardiomyocytes.

2-DE pattern of cardiomyocytes

Proteins from cardiomyocytes were resolved by 2-DE methods. IEF was first conducted on a 17 cm, broad range pH 3–10 linear immobilized pH gradient (IPG) strip. However, the results showed that a high resolution 2-DE gel was not obtained due to an insufficient spatial resolution, difficult-to-reveal low copy number proteins in the presence of more abundant proteins and the fact that most of the proteins were distributed in a pH range from 5 to 8. Therefore, in subsequent investigations, we adopted multiple overlapping narrow ranges IPG strips of pH 3–6, pH 5–8, and pH 7–10 in the first dimension (zoom-in gel). In this way, the resolution is greatly improved, and the detection of spots with low intensity can be easily performed (Figure 2A). In addition, Coomassie blue staining was improved as described in Materials and methods. The result showed that the new method possessed the advantages of both Coomassie blue and silver stains, and has sensitivity almost equivalent to silver stain (Figure 2B).

2D-PAGE database

Proteins from cardiomyocytes were separated and stained with the above-mentioned methods. The 2-DE gel was used to create a gel image in the database mentioned above as shown in Figure 3. Protein spots were identified using the PMF method with MALDI-TOF MS. Identified proteins were summarized in Table 1. Furthermore, some selected proteins from the database were confirmed for validity in cardiomyocytes by Western blot (Figure 4). This 2-DE database is fully independent of the platform and can be grafted from one platform to another. The identified protein spots

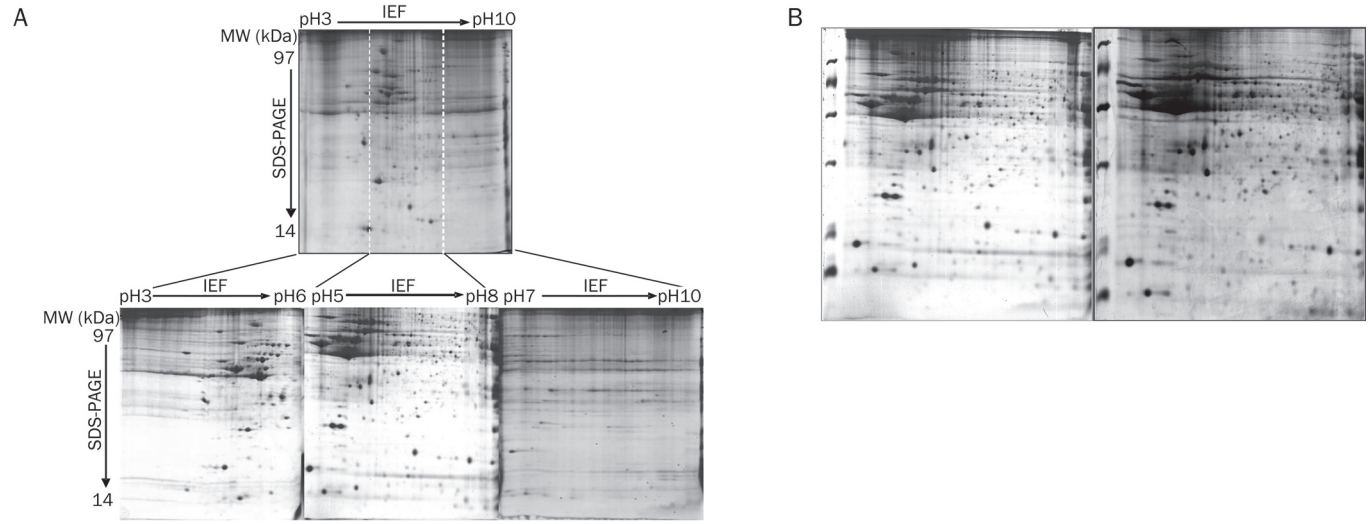

Figure 2. 2-DE proteome map of the cardiomyocytes. (A) Shown are the gel of pI 3–10 (upper) and narrow pI range gels, 3–6, 5–8, and 7–10 (lower). Staining was by colloidal Coomassie blue G-250. (B) Representative 2-DE profiles of neonatal rat cardiomyocytes. Proteins on 2-DE gels were visualized by colloidal Coomassie blue G-250 (left) or silver staining (right).

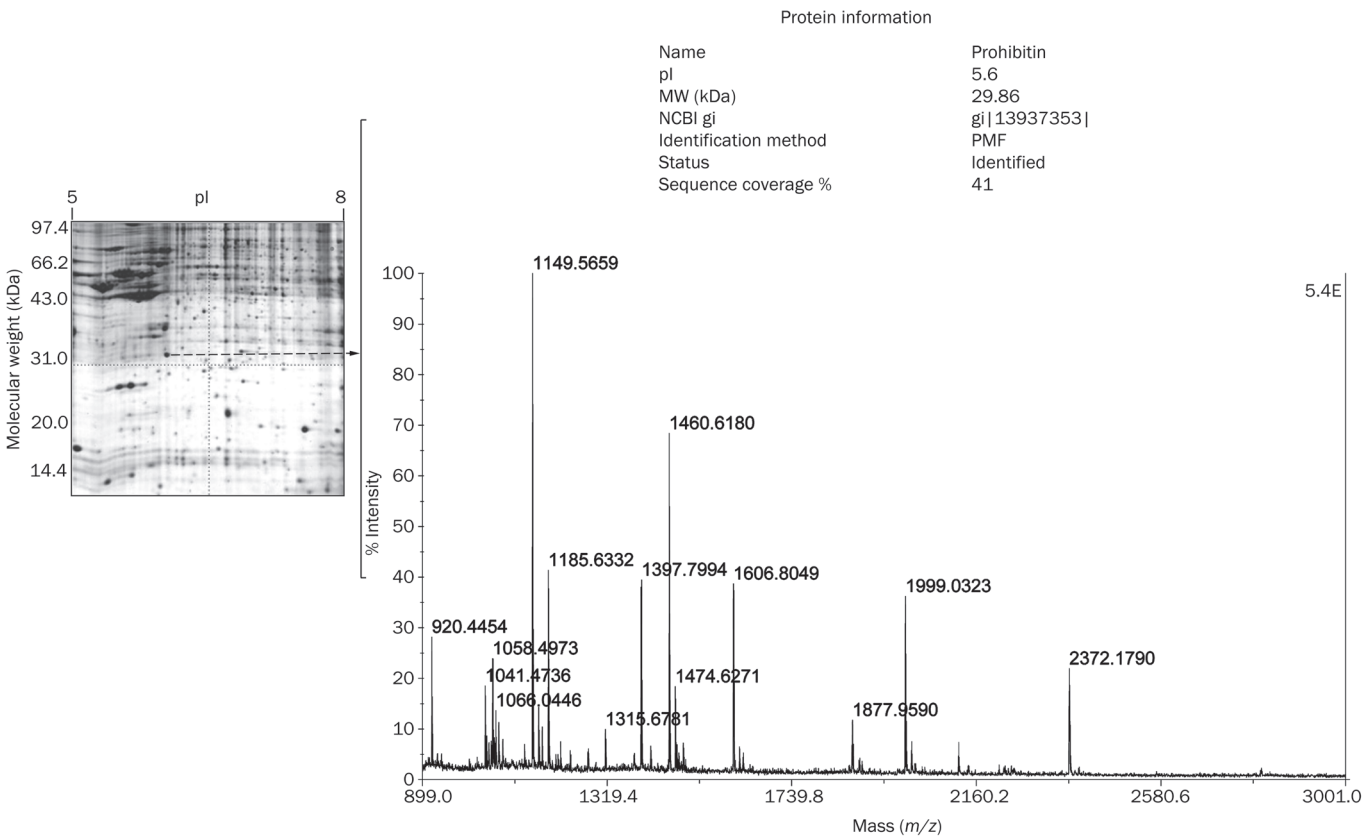

Figure 3. A proteome reference map of neonatal rat cardiomyocytes. Protein spot information (annotation) on prohibitin and generated mass spectrum data.

are hyperlinked to individual protein entries, and the all identification information of each protein entry can be obtained through clickable images. These hyperlinks include protein names, database accession numbers, theoretical molecular mass and pI values. Furthermore, the detailed information of certain protein spots can be obtained through several search-

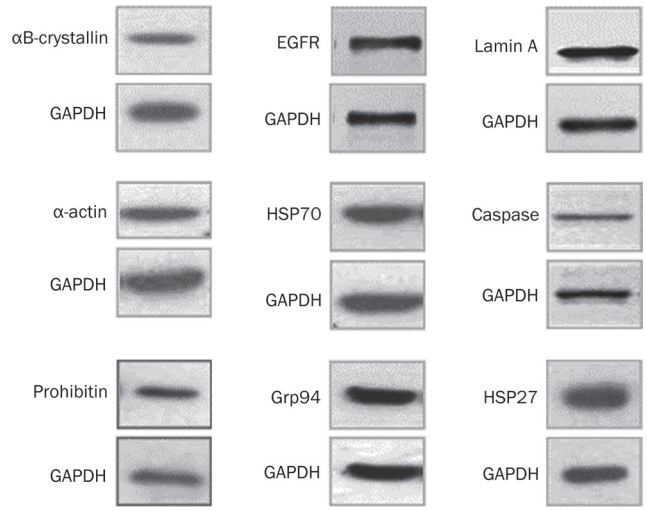

Figure 4. The confirmation of partial proteins from the database in cardiomyocytes by Western blot.

ing tools provided by the database. Besides these, detailed protocols in all the experiments were also provided to ensure the reproducibility of data in the database. Some useful links to other proteomic tools and database can be found throughout the database. For further details of the identified proteins and correspondence of identified proteins to spots in the 2-DE gel image, please refer to our database at http://2d.bjmu.edu.cn.

Data analysis and visualization

In order to futher explore how the cardiomyocyte proteins in the database were related, we used the ingenuity pathway analysis (IPA) program and the Ingenuity Pathways Knowledge Base (IPKB). The IPA program analyzes a large genomic or proteomic data set to find the most significant networks and canonical pathways relevant to the data set based on a calculated probability score. The specificity of connections for each protein was calculated, as defined by the percentage of its direct connections to other proteins showing significant changes. Just as described in Materials and methods, networks with scores of 2 or higher have at least a 99% confidence of not being generated by random chance alone. Therefore, based on the computed scores, four direct networks with scores of 24, 20, 16, and 12 were found to be significant in the database (Figure 5). In addition, high-level functions were calculated and assigned to each direct network if the significance of the association between the network and the biological function had a $P<0.05$ (Table 2). The functions displayed in the table represent the top 4 high-level functions from the local analysis, which provides an overview of the biological functions associated with a given network (A, network 1; B, network 2; C, network 3; and D, network 4). In order to obtain a more comprehensive regulation-relationship map of the cardiomyocyte proteins in the database, a merge network, which included above-mentioned four networks, was created by IPA (Supplementary Figure 1). Not only does the IPA software analysis find novel interconnectivity but the "biological functions and canonical pathways" feature also enables us to further understand biological functions and signaling cascades engaged by each network. The functional analysis for the merge direct network revealed a function map (Supplementary Figure 2A). The top three functions in the network were related to cellular assembly and organization, cardiovascular disease and cell death. Moreover, pathway analysis showed a canonical pathways map (Supplementary Figure 2B). The top three canonical pathways in the network were citrate cycle, glyoxylate and dicarboxylate metabolism and valine, leucine and isoleucine degradation. Beside these, four indirect networks and a merge indirect network with their functional analysis and pathway analysis were also found in the database (Supplementary Figure 3 and 4, and Supplementary Table 1). More detailed information can be found at http://2d.bjmu.edu.cn.

Discussion

Proteomic technology can provide new insights into cellular mechanisms involved in cardiac dysfunction[9–13]. The majority of proteomic investigations still use 2D gel electrophoresis (2-DE) with immobilized pH gradients to separate the proteins in a sample and combine this with mass spectrometry (MS) technologies to identify proteins. In spite of the development of novel gel-free technologies, 2-DE remains the only technique that can be routinely applied to parallel quantitative expression profiling of large sets of complex protein mixtures such as whole cell lysates. Current limitations to this technology include the resolution of the 2-DE and the detection of low-abundance proteins. In the present study, two approaches were explored to solve these drawbacks. The first was to apply multiple overlapping narrow range IPG strips (to increase the resolution of the 2-DE), and the second was to improve protein visualization (to achieve the highly sensitive detection of 2-DE separated proteins). With complex samples such as cardiomyocytes, 2-DE on a single wide-range pH gradient reveals only a small percentage of the whole proteome because of insufficient spatial resolution and difficulty to reveal low-copy proteins in the presence of the most abundant proteins. Our results showed that the resolution of 2-DE with multiple overlapping narrow range IPG strips (pH 3–6, pH 5–8, and pH 7–10) is about 2.5 times that of wide range (pH 3–10). Using these gel systems, more than 1000 proteins were resolved from our model. It was well-accepted that silver staining and Coomassie blue staining are currently the most popular methods of protein detection. Although silver staining, with a sensitivity approximately 10–50 times that of Coomassie blue, is the most sensitive staining method so far reported, there are a number of drawbacks and limitations associated with this method. A high background resulting from a number of variables may cause poor resolution of protein spots. Quantifying protein abundance is also difficult with silver-stained gels due to the poor linearity to protein concentration. In addition, silver stain does greatly interfere with subsequent protein identification by mass

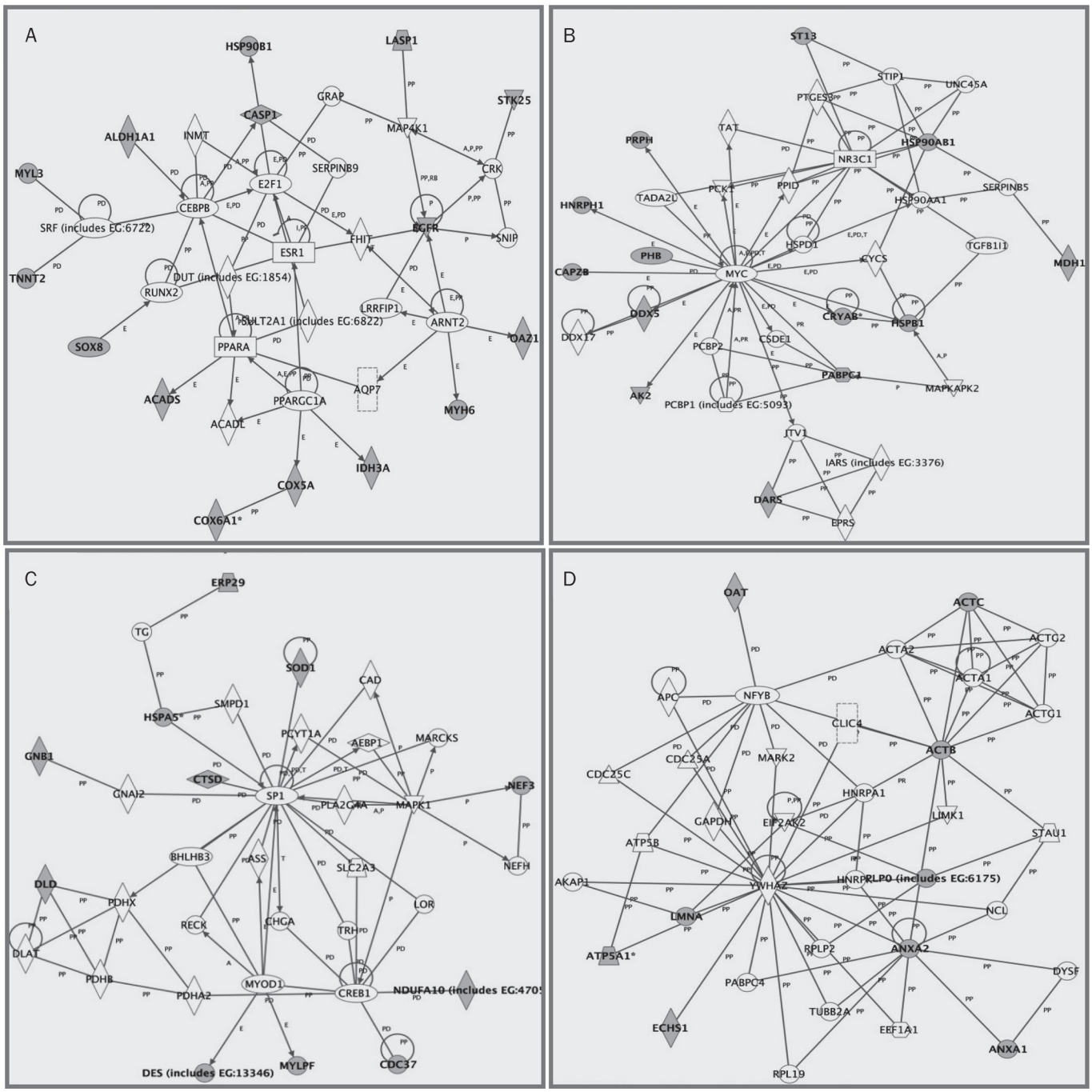

Figure 5. The direct interaction functional networks map of cardiomyocyte proteins in the database. The direct interaction network scores were 24 (A, network 1), 20 (B, network 2), 16 (C, network 3), and 12 (D, network 4), accordingly. Nodes represent proteins, with their shape indicating the functional class of the protein and multiple edges indicating the biological relationships between the nodes. For the functional analyses of networks, see Table 2.

spectrometry. Unlike silver staining, Coomassie blue staining has a good compatibility with subsequent analytical techniques and yields higher dynamic range in determining the changes of protein expression levels. But the major issue of Coomassie staining is that its sensitivity is well below that of silver. In this study, we improved colloidal Coomassie brilliant blue G-250 (Coomassie blue dye) and increased its sensitivity to be almost equivalent to that of silver stain.

As mentioned earlier, the protein database will be important to serve as a basis for further studies of human disease. There are four 2-DE protein databases of cardiac proteins, established by three independent groups, which can be accessed via the World Wide Web[7, 14–16]. These databases facilitate proteomic research into heart diseases containing information

Table 1. Identified proteins of neonatal rat cardiomyocytes.

No	Accession No	Protein information	Z score estimated by profound	Sequence coverage %	pI/ Theoretical MW (kDa)
1	gi|2894106|	Collagen alpha1	2.35	25	5.8/138.9
2	gi|27688933|	Similar to Collagen alpha1	2.43	16	5.8/138.9
3	gi|27688933|	Similar to Collagen alpha1	2.22	16	5.8/138.9
4	gi|58865966|	Tumor rejection antigen gp96	2.42	43	5.02/74.12
5	gi|58865966|	Tumor rejection antigen gp96	2.42	43	5.02/74.12
6	gi|58865966|	Tumor rejection antigen gp96	2.42	43	5.02/74.12
7	gi|38303969|	Heat shock 70 kDa protein 5	2.4	26	5.1/72.50
8	gi|56385|	Hsc70-ps1	2.24	24	5.4/71.14
9	gi|2119726|	DnaK-type molecular chaperone grp75 precursor-rat	2.35	31	5.9/74.01
10	gi|19705459|	poly(A) binding protein, cytoplasmic 1	1.75	15	9.6/70.91
11	gi|227429|	Non muscle caldesmon	2.43	18	6.4/61.76
12	gi|2498205|	Non-muscle caldesmon (CDM) (*L*-caldesmon)	2.43	20	6.3/60.68
13	gi|227429|	Non muscle caldesmon	2.43	24	6.4/61.76
14	gi|10637996	Mitochondrial aconitase	1.83	12	7.87/85.42
15	gi|40538860	Aconitase 2, mitochondrial	2.23	22	7.87/85.38
16	gi|10637996	Mitochondrial aconitase	2.02	16	7.87/85.42
17	gi|10637996	Mitochondrial aconitase	1.93	20	7.87/85.42
18	gi|92654|	Propionyl-CoA carboxylase (EC 6.4.1.3) alpha chain	2.43	12	6.3/78.22
19	gi|129684|	Propionyl-CoA carboxylase alpha chain, mitochondrial	2.08	17	6.3/78.32
20	gi|47938978|	Dars protein	1.72	10	6.0/57.56
21	gi|1346413|	LAMA_RAT Lamin A	2.37	23	6.5/74.59
22	gi|1346413|	LAMA_RAT Lamin A	2.43	26	6.5/74.59
23	gi|1334284|	Unnamed protein product	2.35	21	5.3/58.08
24	gi|90207|	Mitochondrial protein P1 precursor	2.25	32	5.3/58.08
25	gi|51036657|	Prolyl 4-hydroxylase alpha subunit	1.79	18	5.6/61.22
26	gi|56090441	Ddx5	2.03	12	9.06/69.2
27	gi|34874349|	Similar to Dihydropyrimidinase related protein-2 (DRP-2)	2.28	25	6.3/82.08
28	gi|453180|	Lamin A	2.19	21	6.2/71.91
29	gi|1794160|	Lamin C	2.32	37	6.4/65.49
30	gi|51702230|	60 kDa heat shock protein, mitochondrial precursor (Hsp60)	1.94	20	5.35/57.89
31	gi|51702230|	60 kDa heat shock protein, mitochondrial precursor (Hsp60)	2.37	23	5.35/57.89
32	gi|34875806|	Hypothetical protein XP_212759	2.29	24	5.9/61.05
33	gi|34875806|	Hypothetical protein XP_212759	2.40	37	5.9/61.05
34	gi|38197676|	Desmin	2.26	41	5.2/53.46
35	gi|38382858|	Glucose regulated protein, 58 kDa	2.34	21	5.9/57.06
36	gi|38382858|	Glucose regulated protein, 58 kDa	2.43	43	5.9/57.06
37	gi|38382858|	Glucose regulated protein, 58 kDa	2.25	26	5.9/57.06
38	gi|38382858|	Glucose regulated protein, 58 kDa	2.36	20	5.9/57.06
39	gi|38382858|	Glucose regulated protein, 58 kDa	2.43	40	5.9/57.06
40	gi|38303871|	Dihydrolipoamide dehydrogenase	1.93	14	7.96/54
41	gi|34862189|	ATP synthase, H^+ transporting, mitochondrial F1 complex	2.38	26	5.1/56.33
42	gi|34862189|	ATP synthase, H^+ transporting, mitochondrial F1 complex	2.37	36	5.1/56.33
43	gi|34862189|	ATP synthase, H^+ transporting, mitochondrial F1 complex	2.37	36	5.1/56.33
44	gi|25990263	Mitochondrial aldehyde dehydrogenase	2.43	20	5.7/53.29
45	gi|25742617	Epidermal growth factor receptor	1.84	28	6.66/134.8
46	gi|37589940|	Heterogeneous nuclear ribonucleoprotein H1	2.43	25	5.9/49.47
47	gi|50926833|	Eno1 protein	2.43	28	6.2/47.45
48	gi|16073616|	Aldehyde dehydrogenase	2.43	31	6.1/48.65
49	gi|62644240	Dihydrolipoamide branched chain transacylase E2	2.12	24	7.64/33.89
50	gi|6729934	Chain A, Rat Liver F1-Atpase	2.06	20.0	8.28/55.24
51	gi|6729934	Chain A, Rat Liver F1-Atpase	1.83	20.0	8.28/55.24
52	gi|40538742|	ATP synthase, H^+ transporting, mitochondrial F1 complex	1.98	24	9.22/58.79
53	gi|34876531|	Similar to hypothetical protein FLJ10849	2.09	21	6.5/59.16
54	gi|114523	ATP synthase alpha chain, mitochondrial precursor	2.21	24	9.22/58.79

(to be continued)

No	Accession No	Protein information	Z score estimated by profound	Sequence coverage %	pI/ Theoretical MW (kDa)
55	gi|56200|	Unnamed protein product	2.24	23	8.3/61.75
56	gi|6978441|	Actin beta	2.32	26	5.3/42.26
57	gi|71620|	Actin beta	1.82	26	5.2/42.08
58	gi|81890783|	Suclg2_predicted protein (fragment)	1.76	13	7.57/46.75
59	gi|6981112	Isovaleryl coenzyme a dehydrogenase	2.01	15	8.03/46.86
60	gi|11968102	Ornithine aminotransferase	1.82	12	6.53/48.30
61	gi|38181818|	Ornithine aminotransferase	2.31	22	6.5/48.71
62	gi|34859187|	Similar to RIKEN cDNA 2300002G02	2.39	22	7.3/49.9
63	gi|34859187|	Similar to RIKEN cDNA 2300002G02	2.24	34	7.3/49.9
64	gi|34859187|	Similar to RIKEN cDNA 2300002G02	1.83	23	7.3/49.9
65	gi|38303993|	Cathepsin D [rattus norvegicus]	2.43	18	6.7/45.12
66	gi|30171809|	NADH dehydrogenase 1 alpha subcomplex 10-like protein	1.82	15	7.2/40.81
67	gi|20150495|	Chain B, crystal structure of rat short chain acyl-coa dehydrogenase complexed with Acetoacetyl-Coa	1.87	22	6.4/42.44
68	gi|20150495|	Chain B, crystal structure of rat short chain acyl-coa dehydrogenase complexed with Acetoacetyl-Coa	1.90	36	6.4/42.44
69	gi|16758570|	Cell division cycle 37 homolog; CDC37 (cell division cycle 37, *S cerevisiae*, homolog)	2.18	22	5.4/44.87
70	gi|12964644|	NAD^+-specific isocitrate dehydrogenase a-subunit	1.90	31	6.5/40.05
71	gi|38304046|	NADH dehydrogenase (ubiquinone) 1 alpha subcomplex 10	1.85	26	5.4/31.85
72	gi|38541406|	Acidic ribosomal protein P0	2.35	34	5.9/34.37
73	gi|511131|	Alpha-actin cardiac	1.9	26	5.2/42.34
74	gi|145553966|	Voltage-dependent calcium channel alpha 1E	1.82	21	8.25/252.1
75	gi|235879|	Lipocortin I	2.43	13	7.0/39.14
76	gi|15100179|	Malate dehydrogenase 1; Malate dehydrogenase-like enzyme	2.43	15	6.2/36.64
77	gi|38197394|	Annexin 1	2.43	13	7.0/39.15
78	gi|37590235|	Malate dehydrogenase 1	2.29	15	5.9/36.64
79	gi|37590785|	Calpactin I heavy chain	1.7	27	7.7/38.95
80	gi|984553|	G protein beta 1 subunit	2.16	14	5.5/38.17
81	gi|3122930|	3-mercaptopyruvate sulfurtransferase (MST)	1.91	23	5.9/33.21
82	gi|4699609|	Chain C, dienoyl-coa Isomerase	1.81	18	7.1/30.70
83	gi|49903126|	Calcium modulating ligand	1.8	17	7.8/33.06
84	gi|396418|	Actin-capping protein beta chain, splice form 2	2.4	20	5.69/30.95
85	gi|16758848|	Endoplasmic reticulum protein 29	2.25	31	6.2/28.61
86	gi|2119779|	Multidrug resistance protein 3	2.23	17	6.5/27.74
87	gi|13937353|	Prohibitin	1.7	34	5.6/29.86
88	gi|13937353|	Prohibitin	2.37	41	5.6/29.86
89	gi|37590233|	Unknown (protein for MGC:72744)	1.75	25	6.2/31.22
90	gi|37590233|	Unknown (protein for MGC:72744)	1.75	25	6.2/31.22
91	gi|20149810|	Chain F, structure of enoyl-coa hydratase complexed with the substrate dac-coa	2.16	26	6.4/28.31
92	gi|1170367|	Heat-shock protein beta-1 (HspB1) (HSP 27)	2.23	32	6.1/22.93
93	gi|1170367|	Heat-shock protein beta-1 (HspB1) (HSP 27)	2.43	30	6.1/22.93
94	gi|34877098|	Similar to spindlin	1.73	15	6.4/29.72
95	gi|34855918|	Similar to thioether *S*-methyltransferase	2.22	11	5.9/34.79
96	gi|1709429|	Ornithine decarboxylase antizyme (ODC-Az)	2.19	33	6.7/25.67
97	gi|6981240|	Myosin light polypeptide 3 (myosin light chain 1)	2.00	60	5.03/22.26
98	gi|6981240|	Myosin light polypeptide 3 (myosin light chain 1)	2.12	38	5.03/22.01
99	gi|206681	Rieske Fe-S protein precursor	1.8	19	8.9/27.67
100	gi|136708|	Ubiquinol-cytochrome *c* reductase iron-sulfur subunit, mitochondrial precursor (Rieske iron-sulfur protein) (RISP)	2.02	20	9.2/27.96
101	gi|38511598|	Adenylate kinase 2	2.43	18	7.0/26.74
102	gi|30387799|	Alpha B-crystallin	2.43	43	6.8/20.07
103	gi|30387799|	Alpha B-crystallin	2.43	45	6.8/20.07
104	gb|AAB37470.1|	Myosin regulatory light chain 2	2.22	38	4.86/18.74
105	gi|818029|	Dismutase	2.43	32	5.9/15.73
106	gi|30387800|	Alpha B-crystallin	2.43	34	6.8/21.15

(to be continued)

No	Accession No	Protein information	Z score estimated by profound	Sequence coverage %	pI/ Theoretical MW (kDa)
107	gi|34876505|	Similar to RIKEN cDNA 4921537P18	2.24	11	5.9/20.97
108	gi|3790238|	MHC class II RT1D beta1 chain antigen	2.00	31	6.9/14.83
109	gi|34883131|	Similar to RIKEN cDNA 1700081022	2.43	22	7.8/19.17
110	gi|57580|	Alpha B-crystallin	1.81	22	6.9/19.94
111	gi|8393823	Neurofilament 3, medium	1.92	23	9.57/110
112	gi|818021|	Cytochrome *c* oxidase subunit Via (85 AA)	1.82	35	6.3/9.25
113	gi|12055450|	Immunoglobulin heavy chain variable region	1.92	37	8.1/9.25
114	gi|511131|	Alpha-actin cardiac	2.10	28	5.2/42.34
115	gi|1717770|	Troponin T, cardiac muscle isoforms (TnTC) (cTnT)	2.33	24	5/38.81
116	gi|34864883|	Similar to chaperonin containing TCP-1 beta subunit	2.21	39	6/57.78
117	gi|33943091|	Serine/threonine kinase 25	2.05	23	6.3/48.37
118	gi|51948476|	Ubiquinol-cytochrome *c* reductase core protein I	2.42	31	5.6/53.52
119	gi|51948476|	Ubiquinol-cytochrome *c* reductase core protein I	2.25	31	5.6/53.52
120	gi|16758274|	Peroxiredoxin 4	2.43	25	6.2/31.22
121	gi|34870174|	Similar to RIKEN cDNA 0610040B21	1.83	33	6.1/27.37
122	gi|55992|	Cytochrome *c* oxidase subunit Via (AA 1–118)	2.12	41	6.5/12.96
123	gi|38079128|	RIKEN cDNA 4930473A06	2.43	25	5.2/42.69
124	gi|27229195|	RIKEN cDNA 2310032D16; hypothetical glycerophosphoryl diester phosphodiesterase	2.23	22	5.2/51.8
125	gi|2253159|	Peripherin	2.43	18	5.4/52.78
126	gi|6981240|	Myosin light polypeptide 3 (Myosin light chain 1)	2.42	60	5.03/22.26
127	gi|34875200|	Similar to expressed sequence AL022641	2.06	21	5.6/47.02
128	gi|191618|	Alpha cardiac myosin heavy chain	2.42	36	5.57/22.4
129	gi|21707954|	Cytochrome *c* oxidase, subunit Va	1.87	27	6.1/16.31
130	gi|511131|	Alpha-actin cardiac	2.10	28	5.2/42.34
131	gi|5869934|	Hypothetical protein	2.08	25	6.3/145.71
132	gi|33859486|	4-hydroxyphenylpyruvic acid dioxygenase	1.90	21	6.6/45.26
133	gi|1083311|	Protein disulfide-isomerase (EC 5.3.4.1) ERp61 precursor	2.00	22	6.1/56.95
134	gi|13506795|	LASP-1	2.16	23	6.6/30.35
135	gi|31542341|	Caspase 1	2.00	20	4.3/45.8
136	gi|34784670|	Cd1d2 protein	2.11	21	6.4/34.07
137	gi|33563276|	SRY-box containing gene 8	2.43	19	6.6/50.03
138	gi|29468270|	Hemopoietic lineage switch protein 5	2.38	18	6.7/58.64
139	gi|33859486|	4-hydroxyphenylpyruvic acid dioxygenase	2.43	28	6.6/45.26
140	gi|109803|	Phosphopyruvate hydratase (EC 4.2.1.11) alpha	2.43	24	6.4/47.45
141	gi|1717770|	Troponin T, cardiac muscle isoforms (TnTC)	2.33	24	5/38.81
142	gi|1083311|	Protein disulfide-isomerase (EC 5.3.4.1) ERp61 precursor	2.30	27	6.1/56.95
143	gi|12832696|	Unnamed protein product	2.15	43	7.8/13.68
144	gi|6753530|	Crystallin, alpha B; crystallin, alpha 2; alpha B-crystallin	2.42	43	6.8/20.05
145	gi|6753530|	Crystallin, alpha B; crystallin, alpha 2; alpha B-crystallin	2.09	28	6.8/20.05
146	gi|27370092|	RIKEN cDNA 2300002G02	2.43	40	7.3/49.89
147	gi|38075421|	Similar to taxilin	2.43	27	6.1/57.18
148	gi|1346413|	Lamin A	2.38	25	6.5/74.59

on several hundred cardiac proteins that have been identified by protein chemical methods. In addition, 2-DE protein databases and proteomic maps for other mammals are also under construction to support work on animal models of heart disease[17–20].

As we know, cultured cardiac myocytes are attractive models for detailed proteomic investigations of cardiovascular diseases. Unlike the intact heart, cell culture models are very useful to distinguish effects on myocytes *versus* fibroblasts, to eliminate hemodynamic and hormonal influences and especially to analyze and integrate results of high throughput-omic approaches. However, there is not, so far as we know, a proteome database for cardiomyocytes. In this study, a two-dimensional electrophoresis database for rat cardiomyocyte proteins was constructed using our improved methods. Our data show that the largest class of proteins in cardiomyocytes is energy and mass metabolism proteins (20%). For instance, the glucose-regulated proteins play important roles in glucose metabolism. Pyruvate decarboxylase, one of the key enzymes in gluconeogenesis, is closely involved in the process of carbohydrate metabolism. In addition, adenylate kinase also plays a crucial role in maintaining the energy balance in cells. The

Table 2. The top functions table for direct interaction networks.

id	Genes	Score	Focus genes	Top functions
1	ACADL, ACADS, ALDH1A1, AQP7, ARNT2, CASP1, CEBPB, COX5A, COX6A1, CRK, DUT (includes EG:1854), E2F1, EGFR, ESR1, FHIT, GRAP, HSP90B1, IDH3A, INMT, LASP1, LRRFIP1, MAP4K1, MYH6, MYL3, OAZ1, PPARA, PPARGC1A, RUNX2, SERPINB9, SNIP, SOX8, SRF (includes EG:6722), STK25, SULT2A1 (includes EG:6822), TNNT2	24	15	Connective tissue development and function, tissue morphology, cancer
2	AK2, CAPZB, CRYAB, CSDE1, CYCS, DARS, DDX5, DDX17, EPRS, HNRPH1, HSP90AA1, HSP90AB1, HSPB1, HSPD1, IARS (includes EG:3376), JTV1, MAPKAPK2, MDH1, MYC, NR3C1, PABPC1, PCBP2, PCBP1 (includes EG:5093), PCK1, PHB, PPID, PRPH, PTGES3, SERPINB5, ST13, STIP1, TADA2L, TAT, TGFB1I1, UNC45A	20	13	Drug metabolism, endocrine system development and function, lipid metabolism
3	AEBP1, ASS, BHLHB3, CAD, CDC37, CHGA, CREB1, CTSD, DES (includes EG:13346), DLAT, DLD, ERP29, GNAI2, GNB1, HSPA5, LOR, MAPK1, MARCKS, MYLPF, MYOD1, NDUFA10 (includes EG:4705), NEF3, NEFH, PCYT1A, PDHA2, PDHB, PDHX, PLA2G4A, RECK, SLC2A3, SMPD1, SOD1, SP1, TG, TRH	16	11	Genetic disorder, neurological disease, cell morphology
4	ACTA1, ACTA2, ACTB, ACTC, ACTG1, ACTG2, AKAP1, ANXA1, ANXA2, APC, ATP5A1, ATP5B, CDC25A, CDC25C, CLIC4, DYSF, ECHS1, EEF1A1, EIF2AK2, GAPDH, HNRPA1, HNRPK, LIMK1, LMNA, MARK2, NCL, NFYB, OAT, PABPC4, RPL19, RPLP2, RPLP0 (includes EG:6175), STAU1, TUBB2A, YWHAZ	12	9	Cardiovascular system development and function, organ morphology, protein synthesis

other two main groups of proteins are cytoskeletal proteins and oxidative stress proteins/heat shock proteins. The former, including actin, myosin, lamin, *etc*, play a central role in the creation and maintenance of cell shapes in cardiomyocytes. Meanwhile, cytoskeletal proteins also play important roles in both intracellular transport (the movement of vesicles and organelles) and cellular division. In addition, well-known heat-shock proteins and oxidative-stress proteins play pivotal roles during cardiac ischemia, ischemia preconditioning and cardiac hypertrophy. The functions of all those proteins are consistent with a heart that is a myogenic muscular organ.

Based on those identified proteins, this paper describes the creation of an on-line accessible 2-DE reference database for the cardiomyocyte proteome and provides protein identification data for a restricted number of reference spots. Such a 2-DE protein database reduces the need for routine protein identification, which is often difficult to achieve from an organism of which the genome is not sequenced. This Java-based database is fully independent on the platform and can be grafted from one platform to another. The customers can view the information of any protein spots in 2D images simply by clicking them. That is, 2-DE images can be provided on a World Wide Web server and, as a response to a mouse click on any identified spot on the image, the user can obtain the database entry for the corresponding protein. This method allows a user to easily identify proteins on a 2-DE image. At the same time, the detailed information of certain protein spots can also be obtained through several searching tools provided by the database, such as searching by accession number, searching by theoretical molecular weight (kDa) and searching by theoretical pI. In addition, the detailed protocols in all the experiments were also provided to ensure the reproducibility of data in the database and enable other laboratory to repeat the results of those experiments. The database is linked to other databases through active hypertext cross-references; that is to say, the user automatically gets connected to the corresponding web site through a simple mouse click on a cross-reference.

Although it is important to identify the individual proteins expressed in cultured cardiac myocytes, there is an increasing need to move beyond this level of analysis. Cluster and principal component analyses describe overall changes in apparent protein expression but provide few insights into the biological processes and regulatory networks involving in cultured cardiac myocytes. In this study, we combine large-scale analysis of protein expression with knowledge-based functional network analyses. A complex network involved in this database was mapped, and the biological function and biologically meaningful pathways that yield novel, predictive insights were computed and analyzed by IPA. IPA is a software/database search tool for finding function and pathway for specific biological states. It is a web-delivered application that makes use of the Ingenuity Pathways Knowledge Base, the curated database consisting of millions of individually modeled relationships between proteins, genes, complexes, cells, tissues, drugs, and diseases. Sets of interaction data can be viewed as graphs or maps in which each protein is a node and each interaction is a line connecting two nodes. The importance of this view has led to use of the term "interaction map" to refer generically to interaction datasets. The map view provides not only an intuitive interface for biologists to explore the data

but also a formal mathematical framework for computational biologists to explore the properties of interaction networks. These networks include both direct and indirect interactions. Direct interactions are characterized by a well-defined information flow (*eg*, from a transcription factor to the gene it regulates). Indirect interactions do not have an assigned direction (*eg*, mutual binding relationships). Furthermore, as we know, cardiovascular diseases are complicated diseases that are controlled by complex regulation network. In these regulation networks, most proteins function in collaboration with other proteins. In this study, we established, for the first time, a proteome reference map and regulation network of the neonatal rat cardiomyocyte. This is especially useful in understanding dysfunction of complicated diseases. Furthermore, integrated analysis such as that provided by IPA enables analysis of all interactions and may offer additional insights into how such an extensive map contributes to cardiovascular diseases.

In our cardiomyocyte protein database, protein regulatory networks and pathway analysis are created to show how protein–protein interaction may eventually participate in the physiological process of heart. The functional analysis and pathways analysis show that the majority of proteins from ardiomyocytes are involved in cellular assembly and organization, cardiovascular system development, cell morphology, cardiovascular disease and plenty of metabolism pathway and oxidative-stress pathway (such as citrate cycle, glyoxylate and dicarboxylate metabolism, valine and leucine degradation, fat acid metabolism, oxidative phosphorylation and endoplasmic reticulum stress pathway). These results from network analysis also are consistent with the above-mentioned protein components of cardiomyocytes. More importantly, if a user finds certain interesting proteins in this database, the detail regulatory relationship about these proteins can be further found in the protein regulatory network, which will serve as a useful predictive tool for further research.

In conclusion, we have presented an improved methodology for cultured cardiomyocyte proteomics. The on-line database with reference gel and identified proteins serves as a stable framework that facilitates the study of the heart proteome and the exchange of heart proteome data. In addition, biological regulatory networks were for the first time constructed into 2-DE protein databases. Our network analysis has also revealed function and pathway maps potentially involved in the neonatal rat cardiomyocyte protein database. Together, this allowed us to better understand the mechanism, biological processes and specific regulatory networks of the heart. Our study also provides the basis for the development of new therapeutic strategies. Finally, the database we established can serve as an international platform for storage, exchange and analysis of proteomic data. The informational management for experimental data amd the standardization, sharing and integration of this database will certainly provide a basis for further cardiovascular study.

Acknowledgements

This work was supported by grants from Major State Basic Research Development Program of China (973 Program, 2011CB503903), the National Natural Science Foundation of China (81070078 and 81030001) and Beijing Municipal Natural Science Foundation (7102158).

Author contribution

Zi-jian LI designed and performed the research, analyzed the data, and wrote the manuscript; Ning LIU performed the research and analyzed the data; Qi-de HAN designed the research; and You-yi ZHANG designed the research and analyzed the data.

Supplementary information

Supplementary figures are available at Acta Pharmacologica Sinica website of NPG.

References

1 Peters KF, Menaker TJ, Wilson PL, Hadley DW. The Human Genome Project: an update. Cancer Nurs 2001; 24: 287–92.
2 Jungblut P, Otto A, Regitz V, Fleck E, Wittmann-Liebold B. Identification of human myocard proteins separated by two-dimensional electrophoresis. Electrophoresis 1992; 13: 739–41.
3 Baker CS, Corbett JM, May AJ, Yacoub MH, Dunn MJ. A human myocardial two-dimensional electrophoresis database: protein characterisation by microsequencing and immunoblotting. Electrophoresis 1992; 13: 723–6.
4 Dunn MJ, Corbett JM, Wheeler CH. HSC-2DPAGE and the two-dimensional gel electrophoresis database of dog heart proteins. Electrophoresis 1997; 18: 2795–802.
5 Corbett JM, Wheeler CH, Dunn MJ. Coelectrophoresis of cardiac tissue from human, dog, rat and mouse. Towards the establishment of an integrated two-dimensional protein database. Electrophoresis 1995; 16: 1524–9.
6 Pleissner KP, Sander S, Oswald H, Regitz-Zagrosek V, Fleck E. Towards design and comparison of World Wide Web-accessible myocardial two-dimensional gel electrophoresis protein databases. Electrophoresis 1997; 18: 480–3.
7 Li XP, Pleissner KP, Scheler C, Regitz-Zagrosek V, Salnikow J, Jungblut PR. A two dimensional electrophoresis database of rat heart proteins. Electrophoresis 1999; 20: 891–7.
8 Ito H, Hirata Y, Hiroe M, Tsujino M, Adachi S, Takamoto T. Endothelin-1 induces hypertrophy with enhanced expression of muscle-specific genes in cultured neonatal rat cardiomyocytes. Circ Res 1991; 69: 209–15.
9 Kullo IJ, Cooper LT. Early identification of cardiovascular risk using genomics and proteomics. Nat Rev Cardiol 2010; 7: 309–17.
10 Wang J, Bai L, Li J, Sun C, Zhao J, Cui C, *et al*. Proteomic analysis of mitochondria reveals a metabolic switch from fatty acid oxidation to glycolysis in the failing heart. Sci China C Life Sci 2009; 52: 1003–10.
11 Zamilpa R, Lopez EF, Chiao YA, Dai Q, Escobar GP, Hakala K, *et al*. Proteomic analysis identifies *in vivo* candidate matrix metalloproteinase-9 substrates in the left ventricle post-myocardial infarction. Proteomics 2010; 10: 2214–23.
12 Hare JM, Beigi F, Tziomalos K. Nitric oxide and cardiobiology-methods for intact hearts and isolated myocytes. Methods Enzymol 2008; 441: 369–92.
13 Didangelos A, Simper D, Monaco C, Mayr M. Proteomics of acute coronary syndromes. Curr Atheroscler Rep 2009; 11: 188–95.
14 Evans G, Wheeler CH, Corbett JM, Dunn MJ. Construction of HSC-

2DPAGE: a two-dimensional gel electrophoresis database of heart proteins. Electrophoresis 1997; 18: 471– 9.

15 Muller EC, Thiede B, Zimny-Arndt U, Scheler C, Prehm J, Muller-Werdan U, *et al*. High-performance human myocardial two-dimensional electrophoresis database: edition 1996. Electrophoresis 1996; 17: 1700–12.

16 Pleissner KP, Sander S, Oswald H, Regitz-Zagrosek V, Fleck E. The construction of the World Wide Web-accessible myocardial twodimensional gel electrophoresis protein database "HEART-2DPAGE": a practical approach. Electrophoresis 1996; 17: 1386–92.

17 McGregor E, Dunn MJ. Proteomics of the heart: unraveling disease. Circ Res 2006; 98: 309–21.

18. Raddatz K, Albrecht D, Hochgräfe F, Hecker M, Gotthardt M. A proteome map of murine heart and skeletal muscle. Proteomics 2008; 8: 1885–97.

19 Robichaud S, Lalu M, Udenberg T, Schulz R, Sawicki G. Proteomics analysis of changes in myocardial proteins during endotoxemia. J Proteomics 2009; 72: 648–55.

20 Lam L, Arthur J, Semsarian C. Proteome map of the normal murine ventricular myocardium. Proteomics 2007; 7: 3629–33.

Acta Pharmacologica Sinica (2011) 32: 1128–1137
 1671-4083/11 $32.00
www.nature.com/aps

Original Article

Effects of the histamine H_1 receptor antagonist hydroxyzine on hERG K^+ channels and cardiac action potential duration

Byung Hoon LEE[1, 2], Seung Ho LEE[3], Daehyun CHU[4], Jin Won HYUN[5], Han CHOE[4, *], Bok Hee CHOI[3, *], Su-Hyun JO[1, *]

[1]*Department of Physiology, Institute of Bioscience and Biotechnology, Kangwon National University School of Medicine, Chuncheon 200–701, Korea;* [2]*Department of Radiology, Ilsan Paik Hospital, Inje University School of Medicine, Goyang 411–706, Korea;* [3]*Department of Pharmacology, Institute for Medical Sciences, Chonbuk National University Medical School, Jeonju, Jeonbuk 561–180, Korea;* [4]*Department of Physiology, Bio-Medical Institute of Technology, University of Ulsan College of Medicine, Seoul 138–736, Korea;* [5]*Department of Biochemistry, School of Medicine, Jeju National University, Jeju 690–756, Korea*

Aim: To investigate the effects of hydroxyzine on human *ether-a-go-go*-related gene (hERG) channels to determine the electrolphysiological basis for its proarrhythmic effects.
Methods: hERG channels were expressed in *Xenopus oocytes* and HEK293 cells, and the effects of hydroxyzine on the channels were examined using two-microelectrode voltage-clamp and patch-clamp techniques, respectively. The effects of hydroxyzine on action potential duration were examined in guinea pig ventricular myocytes using current clamp.
Results: Hydroxyzine (0.2 and 2 μmol/L) significantly increased the action potential duration at 90% repolarization (APD_{90}) in both concentration- and time-dependent manners. Hydroxyzine (0.03–3 μmol/L) blocked both the steady-state and tail hERG currents. The block was voltage-dependent, and the values of IC_{50} for blocking the steady-state and tail currents at +20 mV was 0.18±0.02 μmol/L and 0.16±0.01 μmol/L, respectively, in HEK293 cells. Hydroxyzine (5 μmol/L) affected both the activated and the inactivated states of the channels, but not the closed state. The S6 domain mutation Y652A attenuated the blocking of hERG current by ~6-fold.
Conclusion: The results suggest that hydroxyzine could block hERG channels and prolong APD. The tyrosine at position 652 in the channel may be responsible for the proarrhythmic effects of hydroxyzine.

Keywords: histamine antagonists; hydroxyzine; cardiomyocytes; hERG channels; K^+ channel; proarrhythmic effects

Acta Pharmacologica Sinica (2011) 32: 1128–1137; doi: 10.1038/aps.2011.66

Introduction

The cardiac action potential is composed of five distinct phases that are designated phases 0–4[1]. The precise shape of the action potential is determined by the coordinated activity of many various ion channels. The action potential is also responsible for the propagation of excitation information from cell to cell and allows the heart to function as a syncytium. The initial upstroke (phase 0) is due to inward Na^+ current (I_{Na}) through fast-activating voltage-gated Na^+ channels. The initial rapid repolarization phase (phase 1) results from rapid voltage-dependent inactivation of the fast inward I_{Na} and the activation of a transient outward current (I_{to}) and the ultrarapid components of the delayed rectifier K^+ current (I_{Kur}). During phase 2, inward depolarizing currents through Na^+ and L-type Ca^{2+} channels are balanced by the various components of the delayed rectifier K^+ current, such as I_{Kur}, the rapidly activating delayed rectifier K^+ current (I_{Kr}), and the slowly activating delayed rectifier K^+ current (I_{Ks}). The terminal phase 3 of repolarization is due to increasing conductance of the channels that carry I_{Kr}, I_{Ks}, and inwardly rectifying K^+ currents (I_{Kir})[2].

Several ion currents such as inward Na^+ and Ca^{2+} currents and outward K^+ currents contribute to the duration of the cardiac action potential. However, the most common mechanism of delayed repolarization—which results in a prolonged QT interval—is by blocking one or more outward K^+ currents[3]. Among the various cardiac K^+ currents, I_{Kr} is the most critical current for terminating the cardiac action potential, and this

* To whom correspondence should be addressed.
E-mail suhyunjo@kangwon.ac.kr (Su-Hyun JO);
bhchoi@jbnu.ac.kr (Bok Hee CHOI);
hchoe@amc.seoul.kr (Han CHOE).
Received 2011-01-13 Accepted 2011-04-22

current determines the shape of the repolarization phase[4]. The pore-forming α subunit of the I_{Kr} channel is the human *ether-a-go-go*-related gene (hERG) protein. In the heart, I_{Kr} contributes prominently to terminal repolarization in humans[5].

The mechanism that is often proposed for drug-induced QT interval prolongation is the direct block of hERG channels[6]. Thus, the inhibition of K^+ currents through hERG can result in a prolongation of the cardiac action potential duration, *torsades de pointes* and sudden cardiac death. Long QT syndrome is characterized by a prolongation of the QT interval on the electrocardiogram. This lengthening of the QT interval usually indicates delayed repolarization of the action potential in ventricular myocytes[3]. In addition, QT interval prolongation is a risk factor for *torsades de pointes*, a potentially fatal form of ventricular arrhythmia.

Hydroxyzine is a first generation sedating antihistamine commonly used for treating a variety of conditions. It is one of the most potent histamine 1 (H_1) receptor antagonists[7]. Abnormal ventricular repolarization[8, 9] and sinus tachycardia[9, 10] have been shown to underlie the cardiac toxicity that can occur with hydroxyzine use. The second generation antihistamines terfenadine and astemizole produce cardiac toxicity primarily in the form of an increased risk for *torsades de pointes*[7]. Both terfenadine and astemizole are H_1-receptor antagonists that also block hERG channels[11].

The purpose of this study was to investigate the acute effects of hydroxyzine on both cardiac action potentials in guinea pig ventricular myocytes and recombinant hERG channels expressed in *Xenopus laevis* oocytes and HEK cells to determine the electrophysiological basis for hydroxyzine's proarrhythmic effects. In addition, we examined the molecular basis of this block using a mutant (Y652A) hERG channel. Finally, a virtual docking simulation was used to propose a hydroxyzine-blocking mode of the hERG channel using the KvAP channel structure as a template.

Materials and methods

Ventricular myocyte isolation

Single ventricular myocytes were isolated from guinea pig hearts using a method that was described previously[12]. In brief, guinea pigs (300–500 g) were anesthetized with pentobarbital (~50 mg/kg, ip) and the heart was quickly excised. The heart was retrogradely perfused sequentially at 37 °C with a 750 μmol/L Ca^{2+} solution, a Ca^{2+}-free solution, and one containing 150 μmol/L Ca^{2+}, collagenase type I and protease type XIV. The heart was then flushed with a 150 μmol/L Ca^{2+} solution. The ventricles were removed and chopped into small pieces, which were then shaken in a flask containing a 150 μmol/L Ca^{2+} solution. The cells in suspension were then allowed to sediment, and the supernatant was replaced with a 500 μmol/L Ca^{2+} solution. The cells were kept at room temperature. These experiments were conducted with the approval of the Research Guidelines of Kangwon National University IACUC.

Solutions and action potential recordings from myocytes

Myocytes in the experimental chamber were continuously superfused at room temperature (24–26 °C) with Tyrode's solution containing 10 mmol/L glucose, 5 mmol/L HEPES, 140 mmol/L NaCl, 4 mmol/L KCl, 1 mmol/L $MgCl_2$, and 1.8 mmol/L $CaCl_2$, titrated to pH 7.4 with 4 mol/L NaOH. The experimental chamber held a volume of 150 μL, and the flow rate of the Tyrode's solution was 2 mL/min. Miniature solenoid valves (LFAA1201618H; Lee Products, Bucks, UK) were used to control the solution entering the chamber, and the superfusate within the chamber could be changed within 5 s. The solution level in the chamber was controlled with a suction system. The chamber and solenoid valves were mounted on the sliding stage of a microscope (Diaphot, Nikon, Japan) that sat on an antivibration table (Newport, USA).

Protease type XIV, dimethyl sulfoxide (DMSO), tetraethylammonium chloride (TEA-Cl) (all from Sigma, St Louis, MO, USA), and collagenase type 1 (Worthington Biochemical, Freehold, NJ, USA) were used in the form of stock solutions or test solutions. The H_1 antihistamine hydroxyzine and all other reagents were purchased from Sigma (St Louis, MO, USA). A stock solution of hydroxyzine was prepared in distilled water and added to the external solutions at suitable concentrations shortly before each experiment.

Membrane potential measurements were performed using conventional patch pipettes pulled from filamented thin wall glass tubing of 1.5-mm outer diameter and 1.2-mm inner diameter (World Precision Instruments, USA); when filled with 300 mmol/L KCl, the electrodes had a resistance of 25–40 MΩ. After patching onto a myocyte in the whole-cell configuration, the membrane potential was measured with an Axoclamp 900A amplifier (Axon Instruments, USA). Action potentials were elicited at 0.33 Hz by 2-ms depolarizing current pulses that were passed through the microelectrode. We selected rod shaped myocytes with clear cross striations and rejected the records with noisy or drifting baselines. Data acquisition was performed with a digital computer, analog data acquisition equipment (National Instruments, Austin, TX, USA), and the software WCP (written and supplied by John Dempster of Strathclyde University) on-line.

Expression of hERG channels in oocytes

hERG (accession No U04270) cRNA was synthesized by *in vitro* transcription of 1 μg of linearized cDNA using the mMESSAGE mMACHINE T7 Kit (Ambion, Austin, TX, USA) and stored in 10 mmol/L Tris-HCl (pH 7.4) at -80 °C. Stage V–VI oocytes were surgically removed from female *Xenopus laevis* (Nasco, Modesto, CA, USA) that were anesthetized with 0.17% tricane methanesulfonate (Sigma, St Louis, MO, USA). Using fine forceps, the theca and follicle layers were manually removed from the oocytes, and then each oocyte was injected with 40 nL of cRNA (0.1–0.5 μg/μL). The injected oocytes were maintained in modified Barth's solution containing (in mmol/L): 88 NaCl, 1 KCl, 0.4 $CaCl_2$, 0.33 $Ca(NO_3)_2$, 1 $MgSO_4$, 2.4 $NaHCO_3$, 10 HEPES (pH 7.4), and 50 μg/mL gentami-

cin sulfate. The currents were measured two to seven days after injection. These experiments were conducted with the approval of the Research Guidelines of Kangwon National University IACUC.

Solutions and voltage clamp recordings from oocytes

Normal Ringer's solution contained 96 mmol/L NaCl, 2 mmol/L KCl, 1.8 mmol/L $CaCl_2$, 1 mmol/L $MgCl_2$, and 10 mmol/L HEPES (pH adjusted to 7.4 with NaOH). The antihistamine drug hydroxyzine and all reagents were purchased from Sigma (St Louis, MO, USA). A stock solution of hydroxyzine was prepared in distilled water and added to the external solutions at suitable concentrations shortly before each experiment. The solutions were applied to the oocytes by continuous perfusion of the recording chamber. Solution exchanges were completed within 3 min, and the hERG currents were recorded 5 min after the solution exchange. The effects of several concentrations of hydroxyzine on the hERG current were measured, and the effects were fully reversible by washing with normal Ringer's Solution. In general, each oocyte was treated with four to seven concentrations of hydroxyzine. The currents were measured at room temperature (20–23 °C) with a two-microelectrode voltage-clamp amplifier (Warner Instruments, Hamden, CT, USA). The electrodes were filled with 3 mol/L KCl and had a resistance of 2–4 MΩ for the voltage-recording electrodes and 0.6–1 MΩ for the current-passing electrodes. Stimulation and data acquisition were controlled with an AD-DA converter (Digidata 1200, Axon Instruments) and pCLAMP software (v 5.1, Axon Instruments).

Pulse protocols and analysis

To obtain concentration-response curves in the presence of hydroxyzine, dose-dependent inhibition was fitted with the equation:

$$I_{tail}=I_{tail\cdot max}/[1+(IC_{50}/D)^n],$$

where I_{tail} indicates the peak tail current, $I_{tail\cdot max}$ is the maximum peak tail current, D is the concentration of hydroxyzine. n is the Hill coefficient, and IC_{50} is the concentration at which the half–maximal peak tail currents were inhibited.

HEK cell culture and transfection

HEK293 cells stably expressing HERG channels, a kind gift from Dr C JANUARY, were used for electrophysiological recordings[13]. The method for establishing HERG channel expression in HEK293 cells is briefly described as follows. HERG cDNA was cloned into the plasmid expression vector pCDNA3 vector (Invitrogen Corporation, San Diego, CA, USA). HEK293 cells were stably transfected with HERG cDNA using a calcium phosphate precipitate method (Invitrogen) or Lipofectamine (Invitrogen). The transfected cells were cultured in minimum essential medium (MEM) supplemented with 10% fetal bovine serum, 1 mmol/L sodium pyruvate, 0.1 mmol/L non-essential amino acid solution, 100 units/mL penicillin, and 100 μg/mL streptomycin sulfate. The cultures were passaged every 4–5 d with a brief trypsin-EDTA treatment followed by seeding onto 12-mm diameter glass coverslips (Fisher Scientific, Pittsburgh, PA, USA) in a Petri dish. After 12–24 h, the cell-attached coverslips were used for electrophysiological recordings.

Electrophysiology of HEK cells

HERG currents were recorded from HEK293 cells using the whole-cell patch-clamp technique at room temperature (22–23 °C)[14]. The patch pipettes were fabricated from glass capillary pipettes (PG10165-4; World Precision Instruments, Sarasota, FL, USA) with a double-stage vertical puller (PC-10; Narishige, Tokyo) and had a tip resistance of 2–3 MΩ when filled with the pipette solution. Whole-cell currents were amplified with an Axopatch 1D amplifier (Molecular Devices, Sunnyvale, CA, USA), digitized with a Digidata 1200A (Molecular Devices) at 5 kHz and low-pass filtered with a four-pole Bessel filter at 2 kHz. Capacitive currents were canceled and series resistance was compensated by 80% with the amplifier, and leak subtraction was not applied. The generation of voltage commands and the acquisition of data were controlled with pClamp 6.05 software (Molecular Devices) running on an IBM-compatible Pentium computer. The recording chamber (RC-13, Warner Instruments Corporation, Hamden, CT, USA) was continuously perfused with bath solution (see below for composition) at a rate of 1 mL/min.

The external solution contained 137 mmol/L NaCl, 4 mmol/L KCl, 1.8 mmol/L $CaCl_2$, 1 mmol/L $MgCl_2$, 10 mmol/L glucose and 10 mmol/L HEPES (adjusted to pH 7.4 with NaOH). The intracellular solution contained 130 mmol/L KCl, 1 mmol/L $MgCl_2$, 5 mmol/L EGTA, 5 mmol/L MgATP and 10 mmol/L HEPES (adjusted to pH 7.4 with KOH). Hydroxyzine (Sigma Chemical Co, St Louis, MO, USA) was dissolved in distilled water at 100 mmol/L and further diluted into the bath solution.

Virtual docking

A homology model of the hERG potassium channel was built on the basis of the 1.7-Å crystal structure (PDB ID code: 1R3J) of the KvAP channel[15] using the homology modeling program MODELLER v8.0[16]. A 25-residue stretch of amino acids (M579 to G603) in the third extracellular loop of the hERG channel was not included in the model because this region was not present in the template structure and does not appear to be involved in the drug-induced inhibition of the hERG channel. The 3D energy-minimized conformation of hydroxyzine was generated using LigPrep version 2.0 (Schrödinger LLC, New York, NY). In the LigPrep operation, the ionization state was calculated at pH 7.4 without additional generation of the tautomer forms. The virtual docking of hydroxyzine was performed using GLIDE version 4.0 (Schrödinger LLC, New York, NY)[17]. The extra-precision (XP) mode of GLIDE was used to achieve an accurate pose prediction. The GLIDE XP mode utilizes an improved scoring function, including a water desolvation energy term and protein–ligand structural motifs that result in enhanced binding affinity[18]. For docking, the receptor structures were preprocessed using protein refinement

components in the GLIDE docking package. A restrained minimization using the OPLS-AA force field was performed for the refinement of the hERG channel structure. This minimization continued until the average RMS deviation of the non-hydrogen atoms reached the specified limit of 0.3 Å. To assign the candidate docking site, a grid center was defined as a centroid of the Y652 and F656 residues in the four monomers that comprised the whole hERG homology model. The grid box size was set to 15Å from the grid center. The PoseView program (BioSolveIT GmbH, Sankt Augustin, Germany) was used to investigate the interactions of the hydroxyzine molecule with the HERG channel. All structural figures were prepared using PyMOL v1.2 (DeLano Scientific LLC, San Francisco, CA) and ChemDraw Ultra 11.0 (CambridgeSoft, Cambridge, MA).

Statistical analysis

All summary data are expressed as means±SEM. Unpaired or paired Student's *t* tests or ANOVA were used for statistical comparisons as appropriate, and differences were considered significant at $P<0.05$.

Results

The effects of hydroxyzine on action potentials in guinea pig ventricular myocytes

In this study we examined the effects of hydroxyzine on action potentials in guinea pig ventricular myocytes. The control action potential duration at 90% (APD_{90}) of myocytes was 576±45 ms (n=9). Figure 1A shows superimposed traces of the action potentials recorded before and during exposure to hydroxyzine at varying concentrations and exposure times. At 0.2 μmol/L, the hydroxyzine-induced lengthening of APD_{90} was positively correlated with application time, such that APD_{90} was longer after exposure for 10 min than after 5 min. This effect was more pronounced with 2 μmol/L hydroxyzine, which exerted its maximum effect on APD_{90} within 5 min. Therefore, hydroxyzine increases APD_{90} in both concentration- and time-dependent manners.

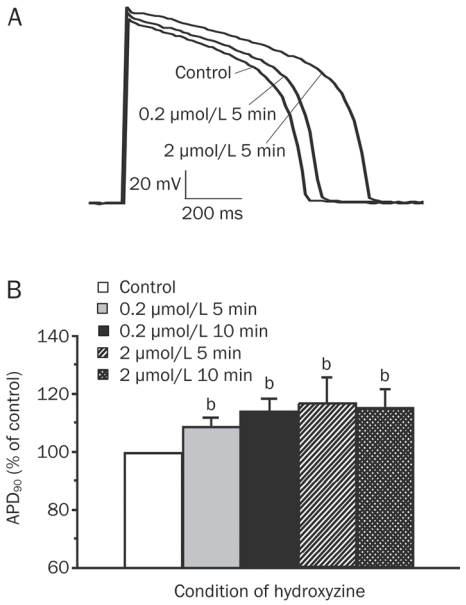

Figure 1. The effect of hydroxyzine on action potentials in isolated guinea pig ventricular myocytes. (A) Superimposed action potentials recorded before and after exposure to various concentrations of hydroxyzine. (B) Concentration- and time-dependent prolongation of action potential duration at 90% (APD_{90}). At each experimental condition (after exposure to 0.2 μmol/L for 5 min, 0.2 μmol/L for 10 min, 2 μmol/L for 5 min, and 2 μmol/L for 10 min), the APD_{90} values were normalized to control APD_{90} (obtained in the absence of drug). $^bP<0.05$. n=4–9.

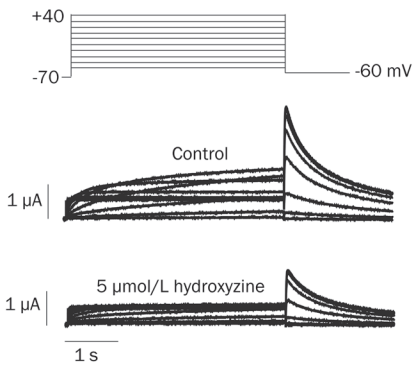

Figure 2. The effect of hydroxyzine on human *ether-a-go-go*-related gene (hERG) currents (I_{HERG}) elicited by depolarizing voltage pulses in *Xenopus* oocytes. Superimposed current traces elicited by depolarizing voltage pulses (4 s) in 10 mV increments from a holding potential of -70 mV (upper panel) in the absence of hydroxyzine (control, center panel) and presence of 5 μmol/L hydroxyzine (lower panel).

Concentration-dependence of WT hERG channel block by hydroxyzine in *Xenopus* oocytes

We next examined the effect of hydroxyzine on hERG currents using the *Xenopus* oocyte expression system. Throughout these experiments, the holding potential was maintained at -70 mV, and tail currents (I_{tail}) were recorded at -60 mV following step depolarizing pulses from -50 through +40 mV. Figure 2 shows an example of a voltage-clamp recording of a *Xenopus* oocyte and the representative current traces both under control conditions and after exposure to 5 μmol/L hydroxyzine. The amplitude of the outward currents measured near the end of the pulse (I_{HERG}) increased with increasingly positive voltage steps and reached maximum amplitude at -10 mV (Figure 3A). The I_{HERG} amplitude was normalized to the maximum I_{HERG} amplitude under control conditions and plotted against the membrane potential during the step depolarization ($I_{HERG, nor}$, Figure 3B). Increasing concentrations of hydroxyzine caused increasing inhibition of $I_{HERG\ (Norm)}$, which is consistent with a concentration-dependent effect.

After the depolarizing step, repolarization to -60 mV elicited an outward I_{tail} with an amplitude that was even larger than that of I_{HERG} during depolarization, which is due to rapid recovery from inactivation coupled with a slow deactivation mechanism[13, 19]. When 5 μmol/L hydroxyzine was added to the perfusate, both I_{HERG} and I_{tail} were reduced (Figure 2).

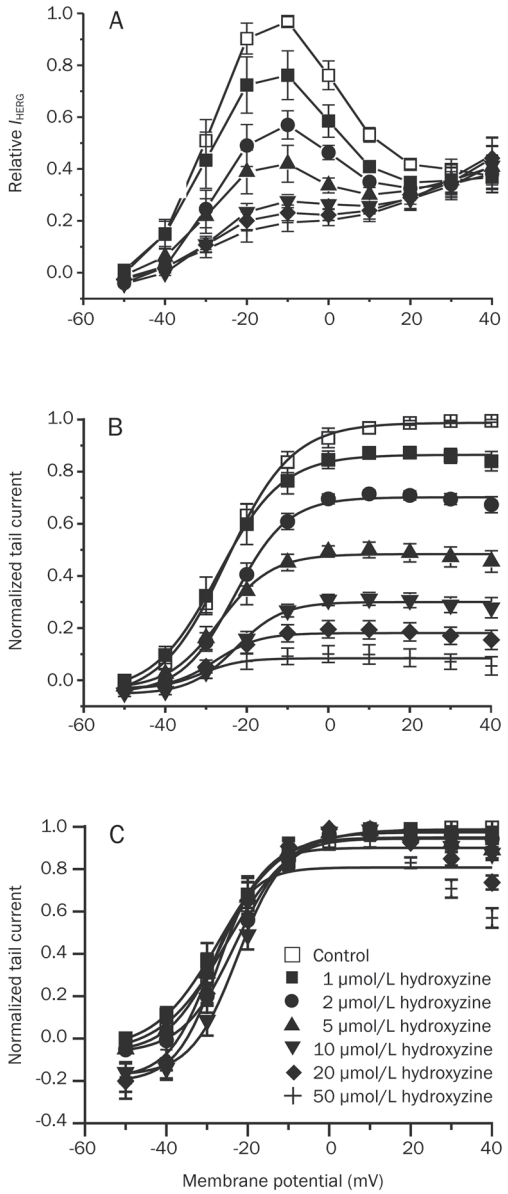

Figure 3. The effect of hydroxyzine on hERG channels expressed in *Xenopus* oocytes. (A) Plot of the normalized hERG current measured at the end of the depolarizing pulse (I_{hERG}) against pulse potential in control and hydroxyzine conditions. The maximal amplitude of the I_{hERG} in control solution was normalized to 1. (B) Plot of the normalized tail current measured at its peak following repolarization. The peak amplitude of the tail current in control solution was normalized to 1. The control data were fitted with the following Boltzmann equation, $y=1/\{1+\exp[(-V+V_{1/2})/dx]\}$, yielding a $V_{1/2}$ of -19.2 mV. (C) Activation curves with the values normalized to their respective maximum for each concentration of hydroxyzine. n=3–5.

The amplitude of I_{tail} was normalized to the peak amplitude obtained under control conditions at maximum depolarization and plotted against the membrane potential during the step depolarization (Figure 3B). The data obtained under control conditions were well fitted by a Boltzmann equation with half-maximal activation ($V_{1/2}$) at -19.2 mV. The peak I_{tail} amplitude decreased with increasing hydroxyzine concentrations, indicating that the conductance of the hERG channels was decreased by hydroxyzine. In addition, in the presence of hydroxyzine, I_{tail} did not reach a steady-state level but continued to decrease at increasingly positive potentials, indicating that the blockade is more pronounced at more positive potentials.

The data presented in Figure 3B were normalized to their respective maximum values at each concentration of hydroxyzine to determine whether hydroxyzine shifts activation of hERG channels (Figure 3C). The activation curve measured in control oocytes was similar to those of oocytes treated with 1−50 μmol/L hydroxyzine. The $V_{1/2}$ values are consistent with this finding, yielding values of -25.0±0.42, -27.0±0.59, -22.9±0.61, -26.7±0.96, -22.7±0.97, -27.8±1.71 and -31.1±3.40 mV in control and 1, 2, 5, 10, 20, and 50 μmol/L hydroxyzine-treated groups, respectively (n=3–5, P>0.05, ANOVA). Therefore, the $V_{1/2}$ values in the presence of 1–50 μmol/L hydroxyzine were similar, indicating that hydroxyzine does not alter the voltage dependence of activation for hERG channels in this concentration range.

Hydroxyzine blocks WT hERG currents in HEK cells

The IC_{50} values of many hERG channel blockers have been shown to differ depending on whether the hERG channels are expressed in *Xenopus* oocytes or mammalian cells, an effect that is probably due to the sequestration of blockers in the large ooplasm of the oocytes[12]. We therefore tested the effect of hydroxyzine on hERG channels expressed in HEK293 cells at 36 °C (Figure 4). As shown in Figure 4A, whole-cell currents were elicited with 4-s depolarizing steps to +20 mV from a holding potential of -80 mV, and tail currents were recorded at -60 mV for 6 s. Bath-applied hydroxyzine reduced I_{HERG} in a concentration-dependent manner. The dose-dependent inhibition of the steady-state current measured at the end of a pulse to +20 mV and the peak tail current were analyzed quantitatively (Figure 4B). A nonlinear least-squares fit of dose-response plots with the Hill equation yielded an IC_{50} and Hill coefficient of 0.18±0.02 μmol/L and 1.05±0.11 (n=5), respectively, for the steady-state current and 0.16±0.01 μmol/L and 1.23±0.12 (n=5), respectively, for the peak tail current. Thus, hydroxyzine is ~30-fold more effective at inhibiting hERG channels expressed in HEK293 cells than in *Xenopus* oocytes.

Voltage-dependent block of WT hERG channel by hydroxyzine

We examined the hydroxyzine-induced decrease in I_{tail} at different potentials to determine whether the effect of hydroxyzine on hERG channels in oocytes was voltage dependent (Figure 5A). Dose–response relationships were measured at -20, +10, and +40 mV. The percent inhibition of the hERG current by 5 μmol/L hydroxyzine at these voltages was 44.0%±8.95%, 47.6%±4.73%, and 54.2%±4.04%, respectively (Figure 5B). This suggests that hydroxyzine-induced block of hERG channels progressively increases with increasing depolarization.

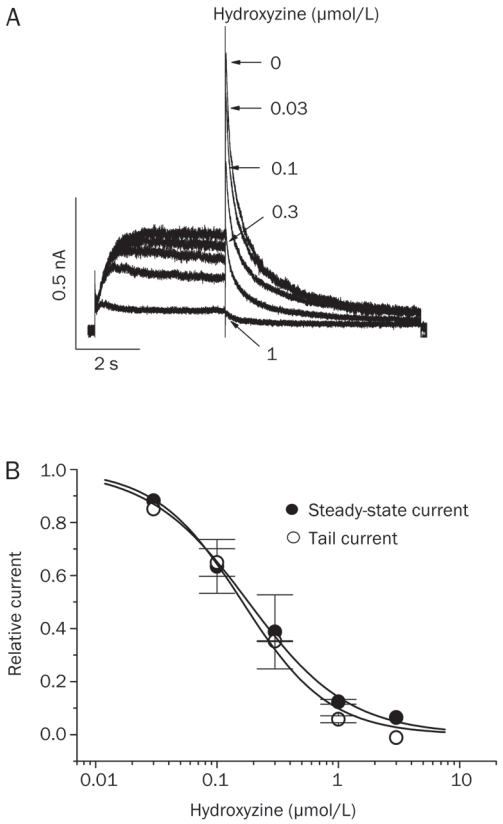

Figure 4. The concentration dependence of hydroxyzine-induced inhibition of hERG channels stably expressed in HEK293 cells. (A) Superimposed I_{HERG} traces were elicited with 4-s depolarizations to +20 mV from a holding potential of –80 mV, and the tail current was recorded at -60 mV for 6 s in the absence or presence of 0.03, 0.1, 0.3, and 1 μmol/L hydroxyzine, as indicated. The voltage protocol was applied every 15 s. The dotted line represents zero current. (B) Concentration dependence curve of inhibition by hydroxyzine for steady-state currents measured at the end of the depolarizing pulse to +20 mV or peak tail currents. The respective normalized currents were plotted against the various concentrations of hydroxyzine. The solid lines are fits of the data points using the Hill equation (see Methods).

Time-dependence of WT hERG channel block by hydroxyzine

Next we activated the current using a protocol that consisted of a single depolarizing step to 0 mV for 8 s to determine whether the channel is blocked in the closed or activated (ie, open and/or inactivated) state using the oocyte expression system (Figure 6A). After recording control currents, 5 μmol/L hydroxyzine was applied and currents were again recorded. Figure 6B shows the relative current (ie, normalized to the control current amplitude) of a representative cell. An analysis of the test pulse in the presence of hydroxyzine revealed a time-dependent block that reached 56% at 2 s (Fig-

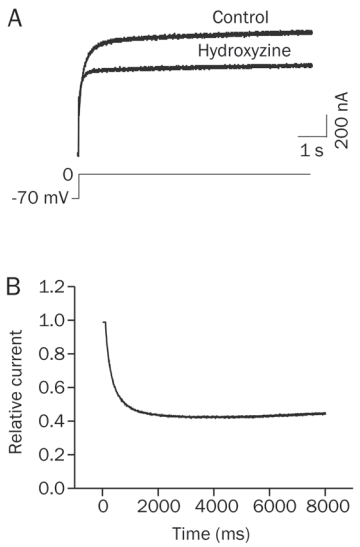

Figure 6. Relative changes in sustained hERG currents in response to hydroxyzine in *Xenopus* oocytes. (A) An example recording of currents under control conditions (control) and after application of 5 μmol/L hydroxyzine (for 7 min without any intervening test pulses). (B) Relative current obtained by dividing the current in 5 μmol/L hydroxyzine by the control current shown in in panel A. Current inhibition increased with depolarization time to 56% at 2 s in this representative cell, indicating that primarily open and/or inactivated channels were blocked.

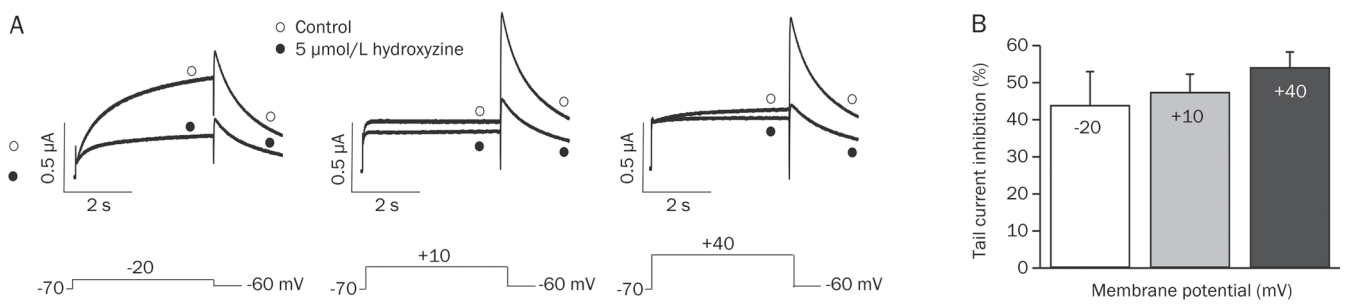

Figure 5. Voltage dependence of hydroxyzine-induced blockade of hERG channels expressed in *Xenopus* oocytes. (A) Current traces from a cell depolarized to -20 mV (left panel), +10 mV (middle panel), or +40 mV (right panel) before and after application of 5 μmol/L hydroxyzine, showing increased blockade of hERG current at more positive potentials. The protocol consisted of 4 s depolarizing steps to -20 mV, +10 mV, or +40 mV from a holding potential of -70 mV, followed by repolarization to -60 mV. (B) Hydroxyzine-induced hERG current inhibition at various voltages. At each depolarizing voltage step (-20, +10, or +40 mV), the tail currents in the presence of 5 μmol/L hydroxyzine were normalized to the tail current obtained in the absence of drug. *n*=4.

ure 6B). In contrast, at the beginning of the pulse, the normalized currents were 95%±3% of control currents (n=4), which indicates that the hERG channels were only slightly blocked by hydroxyzine while at the holding potential (ie, while the channels were in the closed state). In this series of experiments, 5 μmol/L hydroxyzine reduced the hERG outward current at the end of the 0 mV pulse by 48.0%±7.2% (n=4).

In order to address the question of whether the hERG channels are also blocked by hydroxyzine in the inactivated state, a long (4 s) test pulse to +80 mV was applied to inactivate the channels, and this was followed by a second voltage step (to 0 mV for 3.5 s) to re-open the hERG channels that were not inactivated by the first test pulse; these experiments were performed in *Xenopus* oocytes (n=3). Figure 7A shows typical current traces under control conditions and in the presence of 5 μmol/L hydroxyzine. Figure 7B shows the percent inhibition [ie (1-hydroxyzine current/control current)×100 (in %)upon channel opening during the second voltage pulse (to 0 mV)], indicating that pronounced inhibition of the hERG channels had already occurred during the previous inactivating pulse to +80 mV. No additional time-dependent block of the open channels was observed during the pulse to 0 mV. The currents at the end of the second voltage step (to 0 mV) were decreased by 49.1%±12.3% (n=3). Thus, the inhibition of hERG channels occurs primarily in the open and inactivated states but not in the closed state.

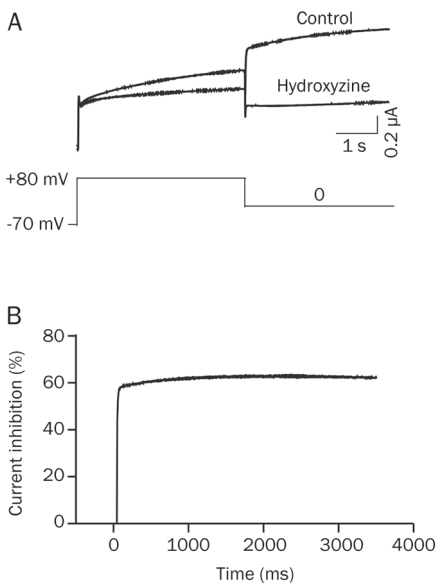

Figure 7. Blocking of inactivated hERG channels by hydroxyzine in *Xenopus* oocytes. (A) Inhibition of inactivated channels by 5 μmol/L hydroxyzine. hERG channels were inactivated by an initial voltage-step to +80 mV, followed by channel opening at 0 mV. (B) The corresponding relative block during the 0 mV step is shown. Maximum inhibition was achieved in the inactivated state during the first step, and no additional time-dependent inhibition occurred upon channel opening during the second voltage step.

The Y652A mutation in the S6 domain attenuates hydroxyzine-mediated block of hERG channels

Tyr-652 is located in the S6 domain and faces the pore cavity of the channel, both of which are important components of the binding site for a number of compounds[19, 20]. The potency of channel block by hydroxyzine for wild type and a mutant (Y652A) hERG channel was compared in *Xenopus* oocytes to determine whether this key residue is also important in hydroxyzine-induced block of hERG channels (Figure 8). The degree of hERG current block by 50 μmol/L hydroxyzine was dramatically decreased by the Y652A mutation (Figure 8A). The IC_{50} values were 5.9±1.5 μmol/L (n=3) and 35.1±50.5 μmol/L (n=4) in WT and Y652A mutant channels, respectively (Figure 8B). This indicates that Tyr-652 is an important residue for mediating hydroxyzine-induced block of hERG channels.

Virtual docking simulation

We next performed a virtual docking simulation to elucidate

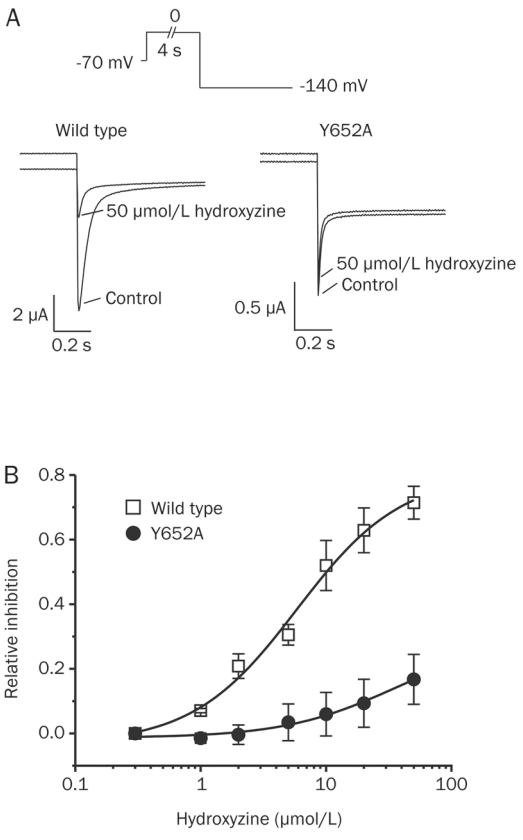

Figure 8. Concentration-dependent inhibition of WT and Y652A mutant hERG channels expressed in *Xenopus* oocytes. (A) Representative traces of WT and mutant hERG currents in the presence and absence of the indicated concentrations of hydroxyzine. The effects of the drug on WT and Y652A tail currents were recorded at -140 mV (instead of -60 mV as above) following a 4 s activating pulse. (B) The concentration-response curves were fitted with a logistic dose-response equation to yield IC_{50} values of 5.9±1.5 μmol/L (n=3) and 35.1±50.5 μmol/L (n=4) for WT and Y652A hERG channels, respectively.

the blocking mode of the hERG channel by hydroxyzine. Because the crystal structure of the hERG channel is not yet known, we made a homology model of the hERG channel using the K_{vAP} channel structure as the template.

The crystal structure of the K_{vAP} channel was presumably obtained in the closed state[15]. The virtual docking was then performed by designating Tyr-652 and Phe-656 as active sites using the GLIDE program. Hydroxyzine carries a net positive charge at pH 7.4 (Figure 9A). The PoseView analysis of the highest score result showed that one of the protonated nitrogens forms a hydrogen bond with the carbonyl oxygen of Thr-623 in monomer I (Figure 9B, 9C). The etheric oxygen of hydroxyzine also makes a hydrogen bond with the hydroxyl group of Ser-649 in monomer IV. In addition to these hydrogen bonds, the aromatic group of hydroxyzine makes interactions with the side chain of aromatic rings of hERG residues Tyr-652 in monomer III and the non-aromatic side chains of Thr-623 in monomer I, Met-645 in monomer IV, Leu-646 in monomer IV and Ser-649 in monomer IV.

Discussion

Long QT syndrome can be acquired as a side effect of treatment with commonly used medications[20]. Both cardiac and noncardiac agents cause acquired (drug induced) long QT syndrome[21] through their inhibition of hERG channel currents[22]. Antihistamines are widely used to treat a variety of conditions such as skin allergies, pruritus and urticaria[7, 23]; however, some antihistamines cause QT prolongation and ventricular tachyarrhythmias[23]. Long QT syndrome is the result of abnormal cardiac repolarization that can degenerate into ventricular fibrillation and cause sudden cardiac death[20]. An antihistamine overdose can cause cardiac arrhythmia by directly inhibiting cardiac K^+ currents. Among the various cardiac K^+ currents, I_{Kr} is important for the termination of the cardiac action potential[4]. The inhibition of hERG channels has been implicated in drug-induced prolongation of the QT interval and *torsades de pointes*[24].

Hydroxyzine, a first generation H_1-receptor antagonist, has both cardiovascular and CNS adverse effects in humans. Hydroxyzine toxicity in the CNS can manifest as generalized seizures[9, 10]. This drug has also been implicated in cardiac adverse effects such as abnormal ventricular repolarization[8, 9], sinus tachycardia[9, 10] and an increased risk of dysrhythmias and sudden death[8, 9]. In the isolated, perfused feline heart model, hydroxyzine acts directly on the heart to slow repolarization and prolong the QT interval[8]. In our study, hydroxyzine inhibits recombinant hERG K^+ currents with an IC_{50} value of 0.16 μmol/L in HEK cells, which is similar to the value obtained after single dose oral (0.7 mg/kg)[25]. We also found that hydroxyzine at 0.2–2 μmol/L prolonged APD_{90} in mammalian myocytes and inhibited hERG channels in concentration-, voltage-, time-, and state-dependent manners. Therefore, the hydroxyzine-induced cardiac adverse effects such as abnormal ventricular repolarization and increased risk of sudden death might be attributed to the drug's direct block of hERG channels, possibly by hydrogen bonds and hydrophobic

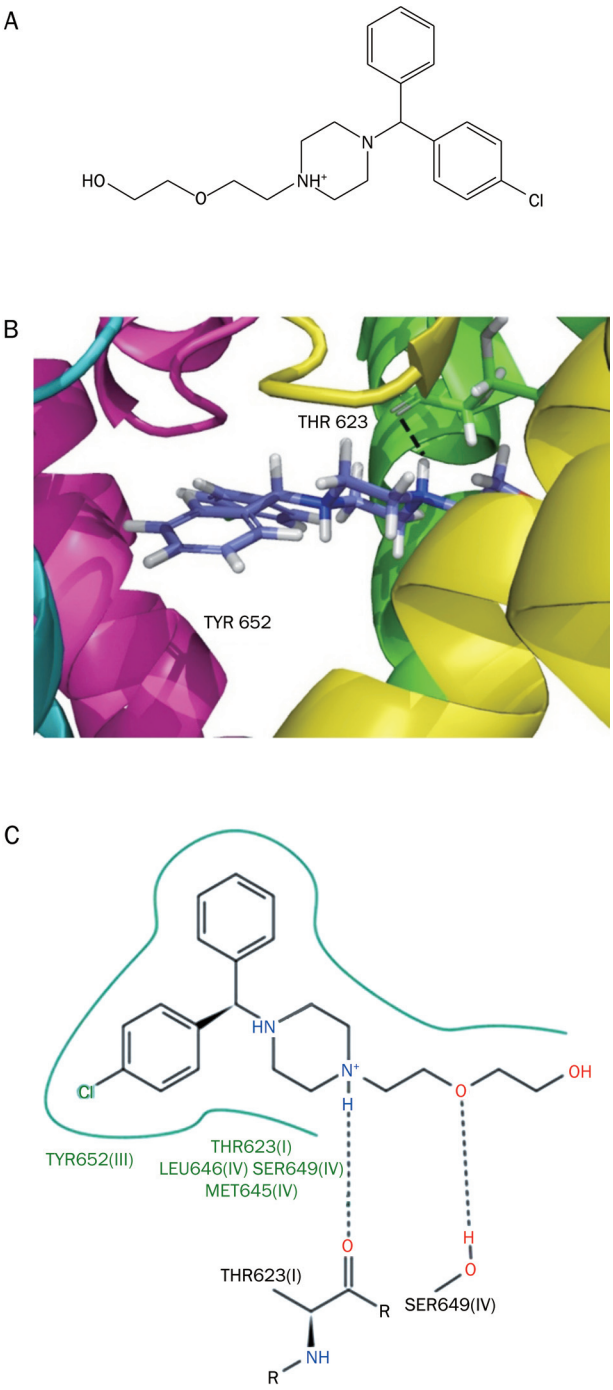

Figure 9. Docking of hydroxyzine within the inner cavity of a HERG channel homology model. (A) The major microspecies of hydroxyzine protonation at pH 7.4. (B) Inner view of hydroxyzine docked to the ligand binding site in the HERG channel. Hydroxyzine is shown in stick form and the dotted line indicates a hydrogen bond between the blocker and channel. The HERG channel inhibitor hydroxyzine shows interactions with THR623 (subunit A) and TYR652 (subunit C). (C) PoseView analysis of protein-ligand interactions. Hydrogen bonding is depicted as a dotted line between the participating atoms. The green lines with residue names and numbers indicate hydrophobic interactions between the drug and channel. Note the hydrogen bond between the hydrogen atom of the protonated nitrogen (in the hydroxyzine molecule) and the carbonyl oxygen atom of THR623(I).

interactions between the drug and the channel (Figure 9).

In the heart, the hERG gene encodes the pore-forming subunit of the rapidly activating delayed rectifier K^+ channel (I_{Kr})[26]. Mutations in hERG reduce I_{Kr} and cause the inherited form of type 2 long QT syndrome[27], and the acquired long QT syndrome can occur in patients who are treated with commonly used medications[20]. In one patient, the combination of a genetic mutation (A614V) and treatment with hydroxyzine appeared to cause severe cardiac pathophysiology that included syncope due to *torsade de pointes*[28]. hERG channels have several putative binding sites for blocking agents[20]. The mechanism that has been proposed for the most direct block of I_{Kr} involves the drug binding to specific amino acid residues in the pore-lining S6 region of the hERG channel[20]. In the present study, the mutation Y652A in the S6 domain attenuated the hERG current block by about 6-fold; the IC_{50} of hydroxyzine-dependent hERG block increased from 5.9 μmol/L to 35.1 μmol/L with the Y652A mutation (Figure 8). This result is consistent with our docking model, which shows that the aromatic group of hydroxyzine makes interactions with the side chain of aromatic rings of TYR652(III) in the hERG channel. In this context, the present study suggests that hydroxyzine is a direct and potent blocker of hERG channels and provide a molecular mechanism for the drug-induced arrhythmogenic adverse effects.

In our virtual docking simulation of the blocking mode of hERG channels by hydroxyzine, there was no interaction between the drug and F656, the amino acid that is involved in drug inhibition (Figure 9). Nonetheless, our results are consistent with our previous hERG channel blocking model in which i) a protonated nitrogen in the blocker forms a hydrogen bond with the carbonyl oxygen of residues THR623 or SER624, ii) an aromatic moiety in the blocker makes a π-π interaction with the aromatic ring of residue TYR652, and iii) a hydrophobic group in the blocker makes a hydrophobic interaction with the benzene ring of residue PHE656[29].

In conclusion, we found that the histamine H_1-receptor antagonist hydroxyzine directly inhibits hERG channels and the I_{Kr} currents carried by these channels, thereby resulting in a prolongation of the cardiac action potential. These results help explain the mechanisms that underlie drug-induced cardiac arrhythmia.

Acknowledgements

This study was supported by a grant (08172KFDA465) from the Korea Food & Drug Administration and a grant (A100096) of the Korea Healthcare technology R&D Project, Ministry for Health, Welfare & Family Affairs, Republic of Korea.

Author contribution

Bok Hee CHOI, Han CHOE, Jin Won HYUN, and Su-Hyun JO designed the research; Byung Hoon LEE, Seung Ho LEE, Daehyun CHU, Han CHOE, and Su-Hyun JO performed the experiments; Dae-hyun CHU, Seung Ho LEE, Han CHOE, Bok Hee CHOI, and Su-hyun JO analyzed the data; Byung Hoon LEE, Seung Ho LEE, Han CHOE, Bok Hee CHOI, and Su-Hyun JO wrote the paper.

References

1 Grunnet M. Repolarization of the cardiac action potential. Does an increase in repolarization capacity constitute a new anti-arrhythmic principle? Acta Physiol (Oxf) 2010; 198 (Suppl 676): 1–48.
2 Tamargo J, Caballero R, Gomez R, Valenzuela C, Delpon E. Pharmacology of cardiac potassium channels. Cardiovasc Res 2004; 62: 9–33.
3 Jo SH, Hong HK, Chong SH, Choe H. Protriptyline block of the human *ether-a-go-go*-related gene (HERG) K^+ channel. Life Sci 2008; 82: 331–40.
4 Hong HK, Jo SH. Block of HERG K channel by classic histamine h(1) receptor antagonist chlorpheniramine. Korean J Physiol Pharmacol 2009; 13: 215–20.
5 Dennis A, Wang L, Wan X, Ficker E. hERG channel trafficking: novel targets in drug-induced long QT syndrome. Biochem Soc Trans 2007; 35: 1060–3.
6 Rajamani S, Eckhardt LL, Valdivia CR, Klemens CA, Gillman BM, Anderson CL, *et al*. Drug-induced long QT syndrome: hERG K^+ channel block and disruption of protein trafficking by fluoxetine and norfluoxetine. Br J Pharmacol 2006; 149: 481–9.
7 Wong AR, Rasool AH. Hydroxyzine-induced supraventricular tachycardia in a nine-year-old child. Singapore Med J 2004; 45: 90–2.
8 Wang WX, Ebert SN, Liu XK, Chen YW, Drici MD, Woosley RL. "Conventional" antihistamines slow cardiac repolarization in isolated perfused (Langendorff) feline hearts. J Cardiovasc Pharmacol 1998; 32: 123–8.
9 Taglialatela M, Timmerman H, Annunziato L. Cardiotoxic potential and CNS effects of first-generation antihistamines. Trends Pharmacol Sci 2000; 21: 52–6.
10 Magera BE, Betlach CJ, Sweatt AP, Derrick CW Jr. Hydroxyzine intoxication in a 13-month-old child. Pediatrics 1981; 67: 280–3.
11 Suessbrich H, Waldegger S, Lang F, Busch AE. Blockade of HERG channels expressed in *Xenopus* oocytes by the histamine receptor antagonists terfenadine and astemizole. FEBS Lett 1996; 385: 77–80.
12 Choi SY, Koh YS, Jo SH. Inhibition of human *ether-a-go-go*-related gene K^+ channel and I_{Kr} of guinea pig cardiomyocytes by antipsychotic drug trifluoperazine. J Pharmacol Exp Ther 2005; 313: 888–95.
13 Zhou Z, Gong Q, Ye B, Fan Z, Makielski JC, Robertson GA, *et al*. Properties of HERG channels stably expressed in HEK 293 cells studied at physiological temperature. Biophys J 1998; 74: 230–41.
14 Hamill OP, Marty A, Neher E, Sakmann B, Sigworth FJ. Improved patch-clamp techniques for high-resolution current recording from cells and cell-free membrane patches. Pflugers Arch 1981; 391: 85–100.
15 Zhou Y, MacKinnon R. The occupancy of ions in the K^+ selectivity filter: charge balance and coupling of ion binding to a protein conformational change underlie high conduction rates. J Mol Biol 2003; 333: 965–75.
16 Sali A, Blundell TL. Comparative protein modelling by satisfaction of spatial restraints. J Mol Biol 1993; 234: 779–815.
17 Friesner RA, Banks JL, Murphy RB, Halgren TA, Klicic JJ, Mainz DT, *et al*. Glide: a new approach for rapid, accurate docking and scoring. 1. Method and assessment of docking accuracy. J Med Chem 2004; 47: 1739–49.
18 Friesner RA, Murphy RB, Repasky MP, Frye LL, Greenwood JR, Halgren TA, *et al*. Extra precision glide: docking and scoring incorporating a

model of hydrophobic enclosure for protein-ligand complexes. J Med Chem 2006; 49: 6177–96.
19 Sanchez-Chapula JA, Navarro-Polanco RA, Culberson C, Chen J, Sanguinetti MC. Molecular determinants of voltage-dependent human *ether-a-go-go* related gene (hERG) K^+ channel block. J Biol Chem 2002; 277: 23587–95.
20 Mitcheson JS, Chen J, Lin M, Culberson C, Sanguinetti MC. A structural basis for drug-induced long QT syndrome. Proc Natl Acad Sci U S A 2000; 97: 12329–33.
21 Witchel HJ, Hancox JC. Familial and acquired long QT syndrome and the cardiac rapid delayed rectifier potassium current. Clin Exp Pharmacol Physiol 2000; 27: 753–66.
22 Taglialatela M, Castaldo P, Pannaccione A, Giorgio G, Annunziato L. Human *ether-a-go-go*-related gene (HERG) K^+ channels as pharmacological targets: present and future implications. Biochem Pharmacol 1998; 55: 1741–6.
23 Yap YG, Camm AJ. Potential cardiac toxicity of H1-antihistamines. Clin Allergy Immunol 2002; 17: 389–419.
24 Roden DM. Drug-induced prolongation of the QT interval. N Engl J Med 2004; 350: 1013–22.
25 Simons FE, Simons KJ, Frith EM. The pharmacokinetics and antihistaminic of the H1 receptor antagonist hydroxyzine. J Allergy Clin Immunol 1984; 73: 69–75.
26 Sanguinetti MC, Jiang C, Curran ME, Keating MT. A mechanistic link between an inherited and an acquired cardiac arrhythmia: hERG encodes the I_{kr} potassium channel. Cell 1996; 81: 299–307.
27 Keating MT, Sanguinetti MC. Molecular and cellular mechanisms of cardiac arrhythmias. Cell 2001; 104: 569–80.
28 Sakaguchi T, Itoh H, Ding WG, Tsuji K, Nagaoka I, Oka Y, *et al*. Hydroxyzine, a first generation H(1)-receptor antagonist, inhibits human *ether-a-go-go*-related gene (HERG) current and causes syncope in a patient with the HERG mutation. J Pharmacol Sci 2008; 108: 462–71.
29 Choe H, Nah KH, Lee SN, Lee HS, Jo SH, Leem CH, *et al*. A novel hypothesis for the binding mode of HERG channel blockers. Biochem Biophys Res Commun 2006; 344: 72–8.

Acta Pharmacologica Sinica (2011) 32: 1138–1147
 1671-4083/11 $32.00
www.nature.com/aps

Original Article

Activating transcription factor 6 protects insulin receptor from ER stress-stimulated desensitization via p42/44 ERK pathway

Xuan TANG[1], Hong SHEN[1], Jing CHEN[1, *], Xu WANG[2], Yu ZHANG[1], Li-li CHEN[1], Vatcharin RUKACHAISIRIKUL[3], Hua-liang JIANG[1], Xu SHEN[1]

[1]State Key Laboratory of Drug Research, Shanghai Institute of Materia Medica, Chinese Academy of Sciences, Shanghai 201203, China; [2]Department of Oral and Maxillofacial Surgery, Ninth People's Hospital, Shanghai Jiao Tong University School of Medicine, Shanghai Key Laboratory of Stomatology, Shanghai 200011, China; [3]Department of Chemistry and Center for Innovation in Chemistry, Faculty of Science, Prince of Songkla University, Thailand

Aim: Activating transcription factor 6 (ATF6) is a key signal transducer of endoplasmic reticulum stress (ER stress). This study was conducted to clarify the potential role of ATF6 in the insulin signaling pathway under chronic ER stress.
Methods: ER stress of HEK293 cells was induced with tunicamycin (2 μg/mL). The cells were transfected with ATF6α or ATF6β. The phosphorylation level of insulin receptor (IR) was analyzed using Western blot. The changes in ER stress and ERK signaling pathways were explored using Western blot and quantitative real-time PCR.
Results: Tunicamycin-induced chronic ER stress attenuated IR tyrosine phosphorylation in a time-dependent manner, whereas over-expression of ATF6 protected IR from desensitization. ATF6 modulation of IR suppression was associated with insulin-stimulated extracellular signal-regulated kinase (ERK) phosphorylation. The treatment of the cells with a specific ERK inhibitor U0126 (10 μmol/L) mimicked the effect of ATF6 over-expression and restored the insulin-stimulated IR phosphorylation. The treatment of the cells with the ERK activator epidermal growth factor (EGF, 200 ng/mL) decreased the protection effect of ATF6 on IR.
Conclusion: Our results demonstrate that ATF6 may serve as a potential therapeutic target for the treatment of insulin resistance and type 2 diabetes.

Keywords: activating transcription factor 6; ER stress; insulin receptor; MEK/ERK pathway; type 2 diabetes

Acta Pharmacologica Sinica (2011) 32: 1138–1147; doi: 10.1038/aps.2011.75; published online 15 Aug 2011

Introduction

Type 2 diabetes is a severe threat to worldwide public health. Its main features include relative insulin deficiency, insulin resistance and hyperglycemia[1]. Over the past few years, tremendous progress has been made in elucidating the molecular mechanisms involved in the origin and development of insulin resistance, although many gaps still remain to be filled.

The endoplasmic reticulum (ER) is an organelle where protein folding, post-translational modification and oligomerization take place. This reticulum system senses alterations of intracellular homeostasis provoked by stimuli, subsequently inducing an unfolded protein response (UPR)[2]. The UPR decreases protein translation, increases chaperone expression and accelerates the degradation of misfolded proteins via three main signal transducers to alleviate cellular stress and restore ER homeostasis. These transducers include inositol-requiring enzyme-1α (IRE-1α), PKR-like ER kinase (PERK), and activating transcription factor 6 (ATF6). When ER stress fails to be attenuated, apoptosis will be activated and cells are subjected to chronic stimulation[2].

Recently, there has been a special interest in ER stress because of its central role in the pathogenesis of type 2 diabetes, and valuable results have been discovered[3–6]. For example, it was found that molecular indicators of ER stress, such as PERK, eukaryotic initiation factor 2α (eIF2α) and glucose-regulated protein 78 (GRP78), increased in liver and adipose tissues of dietary and genetic murine obesity models. In addition, administration of tunicamycin, an ER stress inducer, results in suppression of insulin receptor signaling (insulin receptor substrate 1 (IRS-1) tyrosine and AKT serine phos-

* To whom correspondence should be addressed.
E-mail jingchen@mail.shcnc.ac.cn
Received 2010-12-10 Accepted 2011-05-08

phorylation) in liver cells[3]. ER stress was also discovered to repress the insulin signaling pathway through activation of the IRE-1α and c-Jun N-terminal kinase (JNK) pathways[3, 7, 8]. Over-expression of X-box binding protein 1 (XBP-1), another important ER stress signal transducer, down-regulates JNK activity, enhances insulin receptor signaling pathway activity and restores glucose homeostasis[3]. The attenuation of ER stress by chemical chaperone [*eg*, 4-phenyl butyric acid (PBA) and taurine-conjugated derivative (TUDCA)] treatment or oxygen-regulated protein 150 kDa (Orp150) over-expression has been confirmed effective in increasing insulin sensitivity and ameliorating diabetes *in vivo*[4–6]. Although targeting ER stress has been hinted at as a promising therapeutic strategy for anti-diabetic agent discovery, further investigations should remain in consideration of the complexity of the ER stress network.

Activating transcription factor 6 (ATF6) is a 90-kDa ER-anchoring protein with cytoplasmic and transmembrane domains. The cytoplasmic domain contains a transcriptional activation domain (TAD) and a b-ZIP DNA binding motif[9, 10]. Two isoforms of ATF6 have been determined to date, ATF6α and ATF6β. Although the N-terminals of these two isoforms share conserved b-ZIP domains, ATF6α and ATF6β differ greatly in their transcriptional abilities. This is because of their dissimilar transcriptional activation domains[11], which leads to different functions on target genes[12, 13]. When unfolded proteins accumulate in the ER by chemical stimulation or in physiopathological conditions[14, 15], ATF6 is released from the ER lumen by sequential cleavage of Site 1 (S1P) and Site 2 proteases (S2P)[9]. This produces a 50-kDa fragment that moves to the nucleus to activate chaperone genes, such as GRP78, GRP94 and protein disulfide isomerase (PDI), thus ameliorating ER stress[16].

Regarding the potent involvement of ER stress in the pathogenesis of type 2 diabetes[17–19] and the determined function of ATF6 in the management of cell homeostasis[15, 16], we attempted to clarify the potential role of ATF6 in the insulin signaling pathway. We discovered that both ATF6α and ATF6β attenuate tunicamycin stimulated IR desensitization through an ERK-related pathway. It is expected that members of the ATF6 family could be potential therapeutic targets for anti-obesity and type 2 diabetes drug discovery.

Materials and methods

Materials

Restriction enzymes were purchased from New England Biolabs, NJ, USA. Cell culture plastic ware was from Corning Inc, MA, USA. DMEM culture medium and fetal bovine serum were from Invitrogen, CA, USA. Tunicamycin, insulin, epidermal growth factor, U0126, MTT [3-(4,5-dimethyl-2-yl)-2,5-diphenyl tetrazolium bromide] and SB203580 were obtained from Sigma, USA. RNAiso, RT reagent Kit and SYRB Premix Ex Taq were purchased from TaKaRa, Japan. Anti-ATF6α (full and cleavage) antibody was from Imgenex Corp, San Diego, USA. Anti-IR, anti-phospho-IGF-I receptor β (Tyr1135/1136)/insulin receptor β (Tyr1150/1151), anti-AKT, anti-phospho-AKT (Ser473), anti-p44/42 Erk1/2, anti-phospho-p44/42 Erk1/2 (Thr202/Tyr204), anti-SAPK/JNK, anti-phospho-SAPK/JNK (Thr183/Tyr185), anti-p38 MAPK, anti-phospho-p38 MAPK (Thr180/Tyr182), anti-GRP78/Bip, anti-GAPDH, anti-eIF2α-pSer51 and anti-IRE1α-pSer74 antibodies were purchased from Cell Signaling Technology, MA, USA. Plasmids pcDNA3.1-hATF6α and β were kindly provided by Prof Kazutoshi MORI (Department of Biophysics, Graduate School of Science, Kyoto University, Kyoto, Japan).

Plasmid constructs

ATF6α and ATF6β genes were amplified by Pfu polymerase (Tiangen) from the plasmids pcDNA3.1-hATF6α and pcDNA3.1-hATF6β. The genes were then ligated into *Xho* I/*Hin*d III-digested and *Xho* I/*Eco*R I-digested pEYFP-C1 vectors, respectively.

Stable transfection

HEK293 cells were plated into 3.5 cm plates and transfected with 3 μg pEYFP-C1/pEYFP-C1-hATF6α/pEYFP-C1-hATF6β by using 8 μL Lipofectamine™ 2000 (Invitrogen Inc, California, USA). Medium was changed after 5 h. On the next day, cells were harvested and plated into 10-cm plates in the ratio of 1:400 and incubated in 10% DMEM/FBS. Medium was refreshed every 2 d. After 2 weeks, resistant foci of clones were selected, verified and maintained for further study.

Western blot analysis

Supernatants of the whole cell extracts were fractionated by SDS-PAGE and transferred to Hybond-c nitrocellulose membrane (Amersham Bioscience, Sweden). The membranes were blocked for 1 h at room temperature and then incubated overnight at 4 °C in TBST buffer (5% milk) containing antibody. On the next day, the membranes were incubated for an hour at room temperature in TBST buffer (5% milk) containing anti-rabbit IgG or anti-mouse IgG (Jackson-ImmunoResearch, West Grove, PA, USA). Blots were visualized by incubation with SuperSignal West Dura chemiluminescence kit (Pierce Biotechnology, Rockford, USA) and exposed to light-sensitive film. The experiments were performed in triplicate, and bands were quantified using Image-Pro Plus software and statistically analyzed. Each band was calculated as "intensity×area" using the Image-Pro Plus software (MediaCybernetics, Micromecanique, France). SD was calculated from the three replications of the experiment.

RNA preparation and quantitative real-time PCR

Total RNA was extracted from transiently transfected HEK293 cells or stable cell lines (6-well) using RNAiso (TaKaRa, Japan) reagent according to the kit instruction. Complementary DNA was synthesized using an RT reagent kit (TaKaRa, Japan). Real-time PCR was performed using SYBR Premix Ex Taq (TaKaRa, Japan) on DNA Engene Opticon™ 2 System (MJ Research, Waltham, MA, USA). The PCR cycle was 95 °C for 10 s, 58 °C for 45 s, and 72 °C for 30 s. The primers are listed in Table 1.

Table 1. Primer sequences of selected genes for quantitative real-time PCR.

Gene	Primer sequence
ATF6α	sense 5′-TCAACTCAGCACGTTCCTGAGG-3′
	antisense 5′-GCACATTCACCACATGGTTAGG-3′
ATF6β	sense 5′-ATCCAGCGAGGCTCTTGGGGTAGG-3′
	antisense 5′-TGGCATTGGGACAGTGGTTAGCAC-3′
β-actin	sense 5′-GATGAGATTGGCATGGCTTT-3′
	antisense 5′-GAGAAGTGGGGTGGCTT-3′
GRP94	sense 5'-ATGTTTCCCGCGAGACTCTTC-3′
	antisense 5′-GAGTGGTCTTCAATCACACCAA-3′
PDI	sense 5′-GACGGAGTACCCTACGCTCAA-3′
	antisense 5′-AGAAGCCAATGACCACTAGGT-3′
ERdj4	sense 5′-GGTGTGCCAAAATCGGCATC-3′
	antisense 5′-GCACTGTGTCCAAGTGTATCATA-3′

MTT assay

Stable cell lines were plated in 96-well culture plates (10 000 cells/well). After overnight culture, the cells were treated with tunicamycin (0, 2, 5, and 10 μg/mL) for 12 h. MTT stock solution was added at a final concentration of 0.5 mg/mL. Cells were then cultured for another 4 h. The resulting formazan crystals were dissolved in dimethylsulfoxide (DMSO, 200 μL) for 10 min. Absorbance was then recorded at 490 nm on a microplate spectrophotometer (Bio-Rad, USA). The effect of tunicamycin on cell viability was assessed as percentage of cell viability compared to DMSO-treated control cells, which were arbitrarily assigned as 100% viable.

Statistical analysis

All data are shown as mean±standard deviation (SD). Data were analyzed using either a one-way ANOVA with an appropriate *post hoc* test comparison of multiple groups or an unpaired student's *t* test for comparison of two groups as described in the figure legends (Graphpad Prism software).

Results

Excessive ER stress desensitized insulin receptor signaling

As reported, the ER stress inducer tunicamycin significantly inhibited insulin signal transduction by suppression of insulin-induced IRS-1 and AKT phosphorylation in Fao liver cells[3]. Here we examined the potential effects of tunicamycin on the insulin receptor in the HEK293 cell line. This cell line is often used as a model cell line in preliminary investigations related to ER stress, MAPK and insulin signaling pathways[20, 21]. Compared with the DMSO-treated group, short-term (2–4 h) stimulation with tunicamycin increased insulin-induced IR (Tyr1150/1151) phosphorylation. Prolonged tunicamycin treatment (8–12 h) attenuated such insulin-induced IR activities (Figure 1A). In addition, we also observed that the total amount of IR decreased after long-term tunicamycin treatment. These results indicate that short-term stimulation with tunicamycin could activate IR signaling, whereas excessive ER stress will desensitize this signaling in HEK293 cells.

ATF6 protected the insulin pathway from ER stress-induced desensitization

ATF6 optimized long-term ER stress and protected cells from damage through regulating a number of genes responsible for protein folding and degradation[22–24]. Bearing that in mind, we thus investigated whether members of the ATF6 family could protect IR activity from excessive ER stress. For this assay, after transiently transfected with pcDNA3.1-ATF6α/ATF6β, HEK293 cells were treated with tunicamycin for 4–12 h. The over-expression efficiency is shown in panels B and D of Figure 1. As shown in panels C and E of Figure 1, IR phosphorylation was highly responsive to insulin stimulation from 8 h in ATF6α-transfected cells and from 12 h in ATF6β-transfected cells. To further confirm that ATF6α/ATF6β protection of IR phosphorylation in response to insulin induction only appeared under long-term ER stress stimulation, IR phosphorylation in ATF6α/ATF6β overexpressing cells without tunicamycin treatment were examined at 4, 8, and 12 h. As shown in Figure 1F, ATF6α/ATF6β overexpression failed to alter IR phosphorylation without tunicamycin treatment. Moreover, tunicamycin markedly decreased the total IR, while over expression of ATF6α (or ATF6β) failed to prohibit IR degradation (Figure 1C and 1E). To further verify this result, an ATF6α (or ATF6β) stable cell line with EYFP-C1 as a control was constructed and phosphorylation of IR was examined. The over-expression efficiency is shown in Figure 1G and 1I. As indicated in Figure 1H and 1J, obvious increase of IR phosphorylation induced by insulin was shown from 8-h tunicamycin stimulation in the ATF6α stable cell line and from 4-h tunicamycin supplementation in the ATF6β stable cell line. Compared with the transiently transfected cells, the protection of IR phosphorylation from degradation appeared at an earlier time in the ATF6 stable cell lines. This might be caused by a more efficient response to tunicamycin stimulation in stable cell lines with persistent ATF6 expression.

Therefore, all of our results suggest that the ATF6 family could protect IR activity from long-term ER stress stimulation, while such an effect may not be associated with the regulation of total IR protein level.

ATF6 protection against insulin resistance did not merely link with its function in ER stress

ATF6 is one of the three main transducers in UPR that up-regulate a series of genes to relieve the overload of unfolded protein in the ER, thus ameliorating long-term ER stress damage[24–27]. Here, expression of three ATF6 target genes (GRP78, GRP94 and PDI) was examined in tunicamycin stimulated HEK293 stable cell lines. The results in Figure 2A–2D and Figure S1 indicate that the stable over-expressing ATF6α (or ATF6β) cells respond to tunicamycin stimulation potently as reflected by the increased expression levels of these genes as early as 4 h after stimulation. Additionally, we also examined whether the PERK-eIF2α and IRE1α-XBP-1 pathways could be modulated by ATF6 over-expression. As shown in Figure 2A and 2B, the PERK-phosphorylated eIF2α phosphorylation did not differ in the stable cells with ATF6α or ATF6β over-expres-

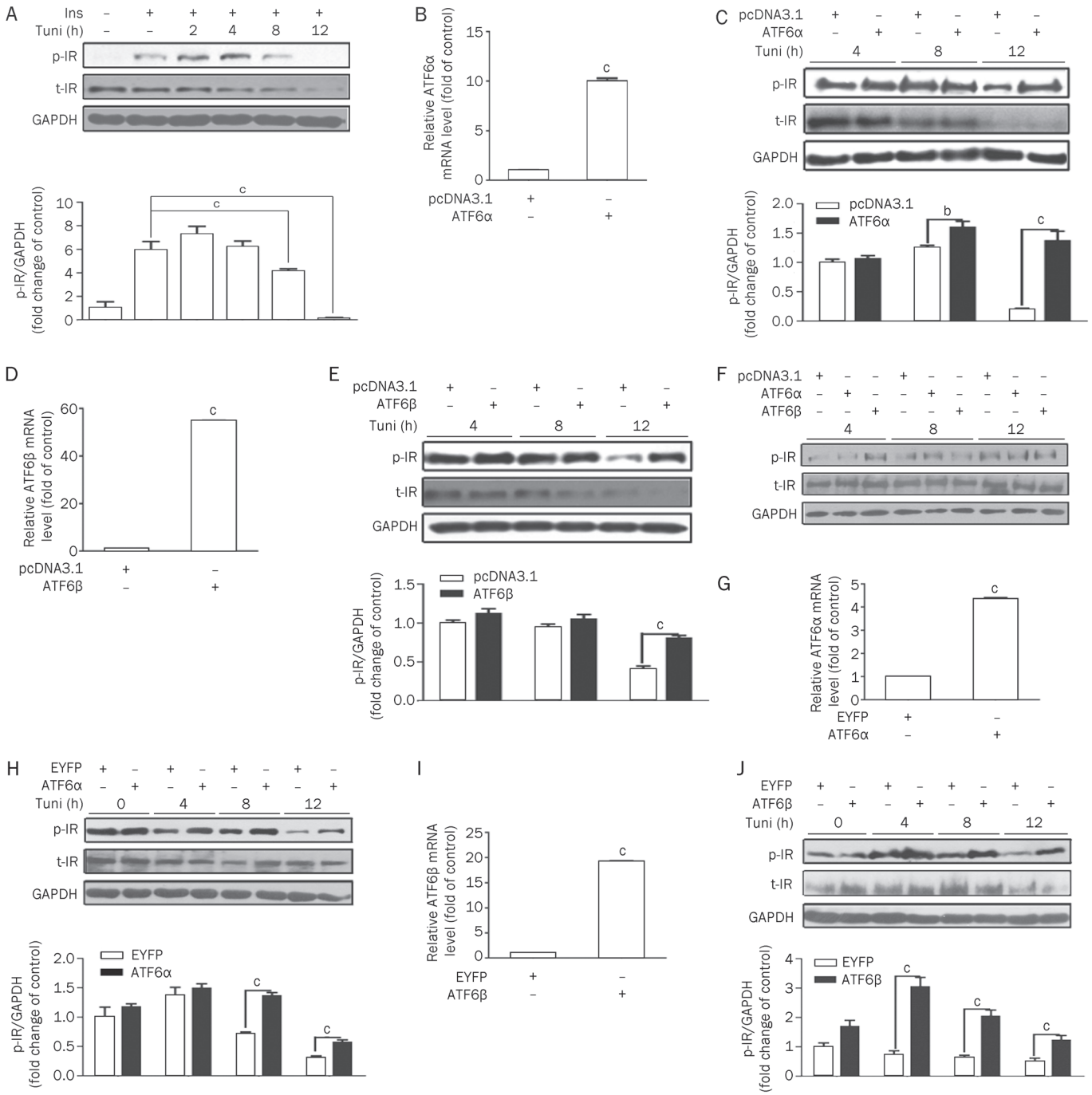

Figure 1. ATF6 protects the insulin pathway from ER-stress induced desensitization. (A) Excessive ER stress-desensitized insulin receptor signaling. When confluence reached 80%, HEK293 cells were refreshed with serum-free DMEM supplemented with tunicamycin (2 μg/mL) for the time indicated before 5-min insulin (167 nmol/L) stimulation. (B and D) The transient over-expression efficiency of ATF6α (B)/β (D). HEK293 cells were transiently transfected with pcDNA3.1 or pcDNA3.1-hATF6α/β. After 5 h, cells were refreshed with 10% DMEM/FBS and then harvested for real-time RT-PCR on the next day. (C and E) ATF6α (C)/β (E) transient over-expression protected the insulin pathway from ER stress-induced desensitization. HEK293 cells were transiently transfected with pcDNA3.1 or pcDNA3.1-hATF6α/β for 5 h and then refreshed with serum-free DMEM supplemented with tunicamycin (2 μg/mL) for the indicated time before 5-min insulin (167 nmol/L) stimulation. The cells were harvested to analyze the phosphorylated and total IR. (F) ATF6α/β's effect on the insulin pathway without tunicamycin treatment. HEK293 cells were transiently transfected with pcDNA3.1 or pcDNA3.1-hATF6α/β. After 5 h, cells were refreshed with serum-free DMEM for 4, 8, and 12 h before 5-min insulin (167 nmol/L) stimulation. (G and I) The stable over-expression efficiency of ATF6α (G)/β (I). ATF6 over-expression stable cell lines (HEK293-EYFP-C1-ATF6α and HEK293-EYFP-C1-ATF6β) and control cells (HEK293-EYFP-C1) were plated into 6-well culture plates (100 000 cells/well) and then harvested for real-time PCR on the third day. (H and J) ATF6α (H)/β (J) stable over-expression protects the insulin pathway against ER stress-induced desensitization. HEK293 (EYFP-C1), HEK293 (EYFP-C1-ATF6α) and HEK293 (EYFP-C1-ATF6β) were separately treated with tunicamycin (2 μg/mL) and then stimulated for 5 min with insulin (167 nmol/L). The phosphorylated and total IR were analyzed. $^{b}P<0.05$; $^{c}P<0.01$.

sion. Phosphor-IRE1α and mRNA levels of ERdj4 (one of the IRE1α-XBP-1 downstream genes) were up-regulated (Figure 2A, 2B, and 2E) at 12 h. These results are consistent with previously reported results[28]. Therefore, we propose that ATF6 function in the insulin pathway might be associated with resistance to ER stress. Considering that the cell death induced by ER stress could act as an assessment to evaluate sensitivity to ER stress[29], we applied an MTT assay in stable ATF6α (or ATF6β) over-expressing cells. The results indicate that ATF6 over-expressing cells failed to counteract tunicamycin-induced cell death in HEK293 cells within 12 h (Figure 2F). Therefore, all of the above-mentioned results suggest that the regulation of the ATF6 family on IR activity might not solely depend on its modulation of UPR.

ATF6 failed to attenuate tunicamycin-induced JNK pathway activation

As reported, the JNK pathway plays a central role in connecting ER stress with type 2 diabetes. Upon activation by ER stress through IRE1α[30], JNK can directly phosphorylate IRS-1 at Ser307 leading to the reduction of insulin-induced IRS-1 tyrosine phosphorylation and a decrease in activity of the insulin pathway[31, 32]. Given that ATF6 might protect the insulin pathway by attenuating JNK pathway activity, the related

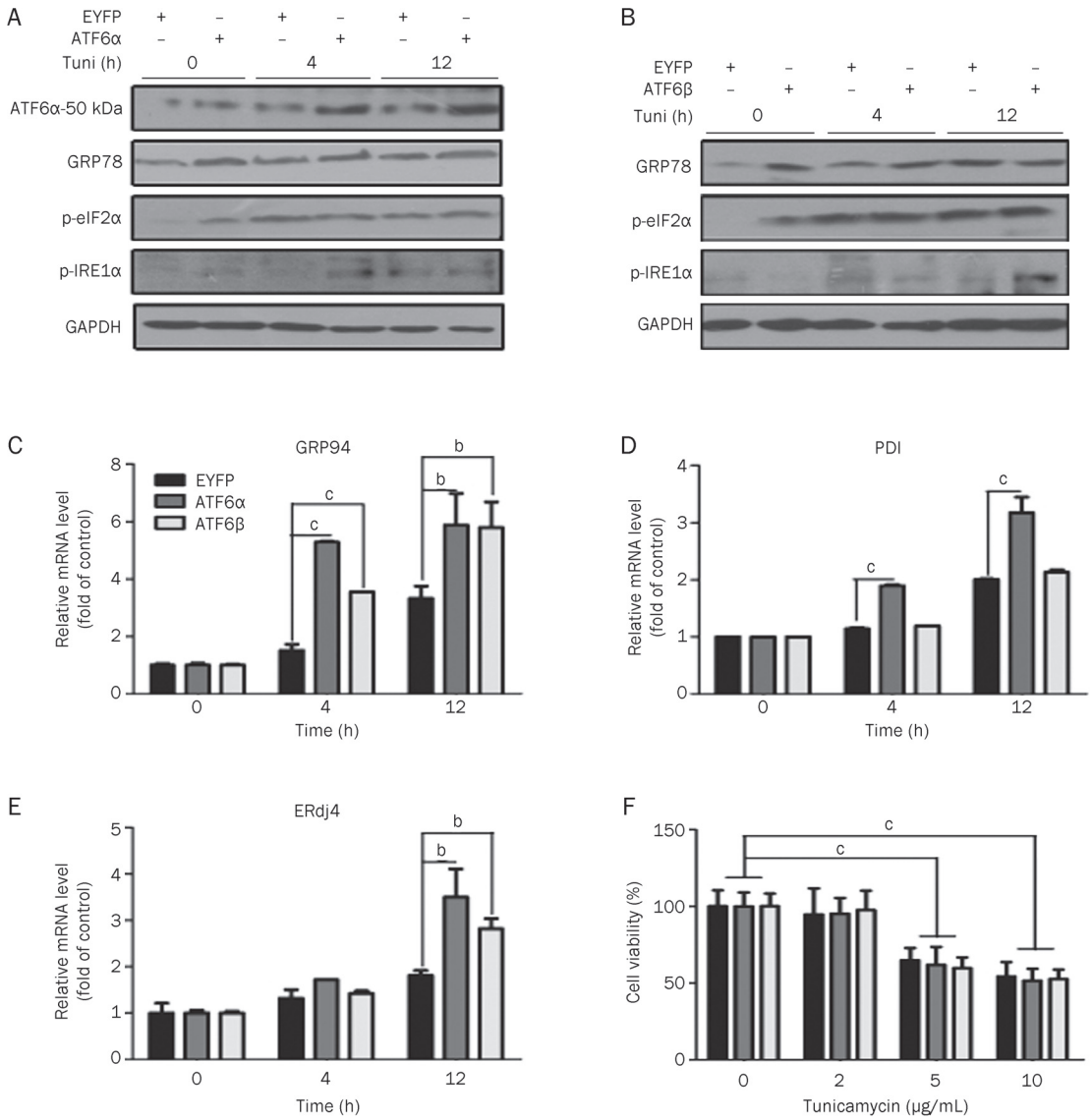

Figure 2. ATF6 regulation on IR was not solely dependent on its protective role in ER stress. (A and B) HEK293 (EYFP-C1), HEK293 (EYFP-C1-ATF6α), and HEK293 (EYFP-C1-ATF6β) were cultured with tunicamycin for the indicated time before harvest. The ATF6α-50 kDa (cleavage form of ATF6α), GRP78, phosphorylated eIF2α and IRE1α were then analyzed. (C–E) HEK293 (EYFP-C1), HEK293 (EYFP-C1-ATF6α), and HEK293 (EYFP-C1-ATF6β) were cultured in 6-well plates and stimulated with tunicamycin (2 μg/mL) for the indicated time before harvest. Total RNA extraction and mRNA quantification of GRP94 (C), PDI (D), and ERdj4 (E) were performed as described in "Materials and methods". (F) MTT assays were applied to HEK293 (EYFP-C1), HEK293 (EYFP-C1-ATF6α), and HEK293 (EYFP-C1-ATF6β) as described in "Materials and methods". $^{b}P<0.05$, $^{c}P<0.01$.

assays were performed. The results in Figure 3A indicate that stimulation with tunicamycin for 4–8 h strongly elevated JNK phosphorylation, while ATF6α could not reverse such elevation. These results suggest that ATF6α might not participate in the regulation of JNK signaling.

ATF6 protection on IR phosphorylation from excessive tunicamycin stimulation is not connected with the p38 pathway

Besides the JNK pathway, the MKK3/6-p38 and MEK1/2-ERK pathways are also associated with several key proteins within the insulin receptor signaling pathway (*eg*, IR, IRS, and AKT)[33–37]. We thereby hypothesized that the ERK or p38 pathways might be involved in ATF6's protection on insulin signaling from excessive ER stress stimulation. To evaluate this hypothesis, basal and insulin-stimulated p38 phosphorylation were tested in control or ATF6α transfected HEK293 cells with 4–12 h incubation with tunicamycin. An obvious increase in p38 phosphorylation was observed in ATF6α-transfected cells treated with tunicamycin. There were no apparent differences in p38 activity found between control and ATF6α transfected cells with insulin stimulation (Figures 3B and 3C). In addition, SB203580 (specific p38 inhibitor) did not alter the phosphorylation of IR with long-term tunicamycin treatment -(Figure 3D). These results indicate that the p38 signaling pathway might not contribute to the protective effects of ATF6. Similar results were also obtained by over-expressing ATF6β (data not shown).

ATF6 regulation against insulin receptor signaling is associated with the ERK pathway

To further explore the potential signaling pathway for ATF6 regulation of the insulin receptor, basal and insulin-stimulated ERK phosphorylation were tested in control or ATF6α transfected HEK293 cells incubated with tunicamycin for 0–24 h.

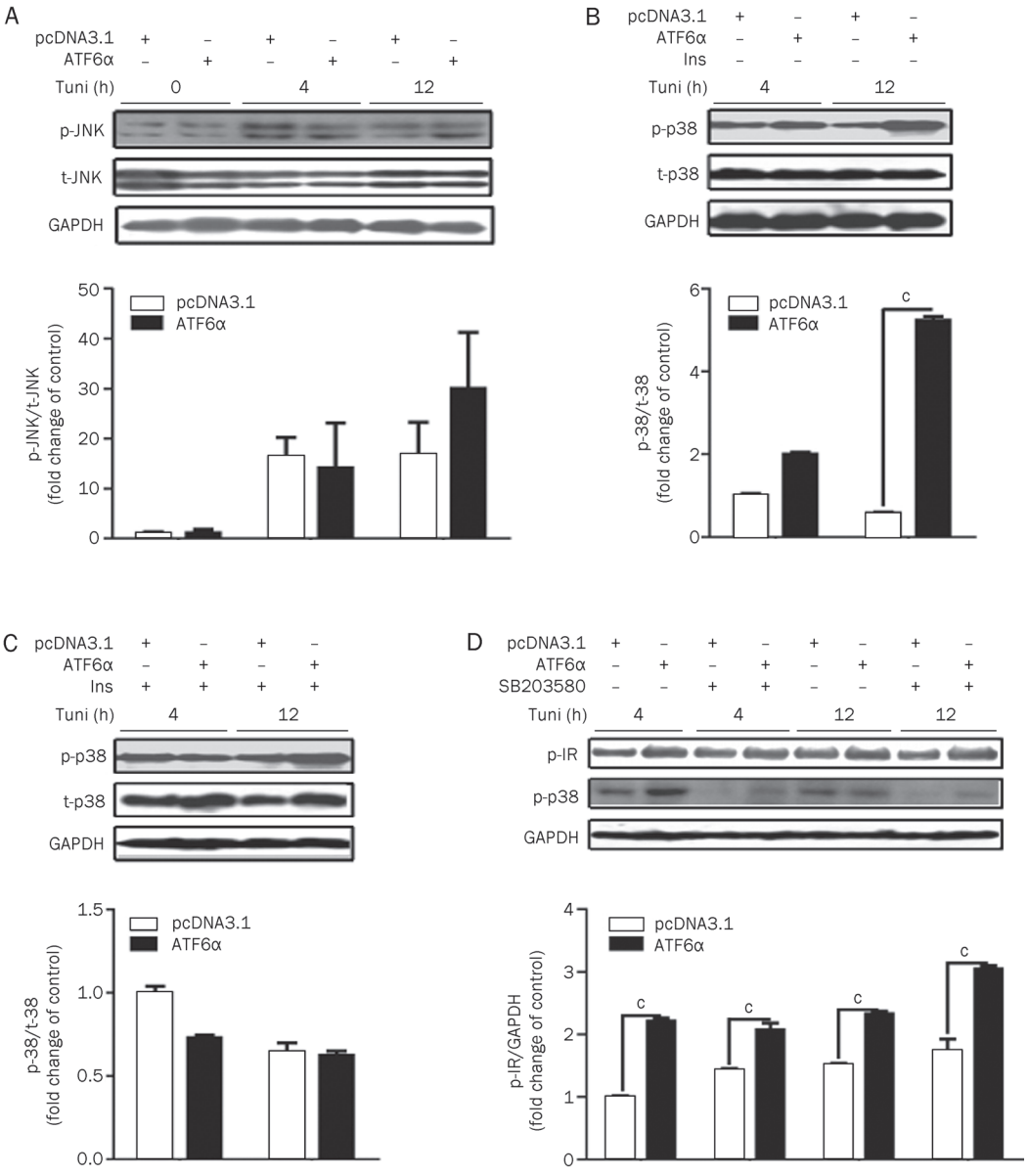

Figure 3. ATF6 protection was not involved in the JNK and p38 signaling pathways. (A) HEK293 cells were transiently transfected with pcDNA3.1/pcDNA3.1-hATF6α. After tunicamycin (2 μg/mL) treatment for the indicated time, the total/phosphorylated JNK was analyzed. (B and C) HEK293 cells were transiently transfected with pcDNA3.1/pcDNA3.1-hATF6α. After tunicamycin (2 μg/mL) treatment with (C) or without (B) insulin (167 nmol/L) stimulation for 5 min, the phosphorylated and total p38 were analyzed. (D) After transfection, HEK293 cells were treated with tunicamycin (2 μg/mL) together with SB203580 (5 μmol/L) for the indicated time and insulin (167 nmol/L) for 5 min. Then, the phosphorylated IR was analyzed. $^{c}P<0.01$.

The results indicate that insulin-stimulated ERK phosphorylation was significantly attenuated in cells exposed to tunicamycin at 12 h (Figure 4A), while its sensitivity in ATF6α-overexpressing cells maintained stability except with 24 h tunicamycin incubation (Figure 4B). Furthermore, the basal level of ERK phosphorylation was largely inhibited in ATF6α-overexpressing cells as compared with control cells (Figure 4C), whereas ATF6α was able to enhance the level of insulin-induced ERK phosphorylation (Figure 4D) with tunicamycin treatment. Therefore, our findings demonstrate that ATF6 modulates ERK activity induced by tunicamycin stimulation. To further confirm the role of ERK in ATF6 effects on IR, the IR activity was then evaluated in control and ATF6α transient transfected cells with or without U0126 (specific ERK inhibitor) treatment. As shown in Figure 5A, IR phosphorylation was greatly dampened by long-term tunicamycin incubation in control but not in ATF6α transient transfected cells. As expected, U0126 treatment almost completely inhibited ERK activity and restored the insulin-stimulated IR phosphorylation in control cells. On the contrary, epidermal growth factor (EGF, ERK activator) treatment together with tunicamycin stimulation largely decreased the protective effects of ATF6α on IR (Figure 5B). However, the results shown in Figure 5C are without tunicamycin treatment and suggest that the above ERK-associated hypothesis was tenable under the instance of tunicamycin stimulation. Similar results were also obtained by over-expressing ATF6β (data not shown). Accordingly, our results imply that ATF6 protects IR activity through attenuation of basal ERK activity (at 4–12 h) that is subject to excessive ER stress stimulation.

Discussion

In recent years, accumulating evidence has demonstrated that the ER may serve as an "interpreter" by sensing a number of exogenous or endogenous stimuli such as inflammatory cytokines[38, 39], abnormal energy fluxes[15] and oxidative stimuli[40]. The ER is a complicated and systemic network, and excessive ER stress may result in insulin resistance[3, 41, 42] and islet β-cell dysfunction[43]. Currently, increasing chaperones has been reported to help improve insulin resistance[6]. Here we focused on ATF6 for its potent service as a critical signal transducer in the ER stress system. ATF6 is responsible for up-regulating main chaperone systems[27] and plays a pivotal role in XBP-1 generation[44], which is essential to normal insulin signaling pathway functioning and glucose homeostasis[3]. In addition, the genetic report has even identified ATF6 as a

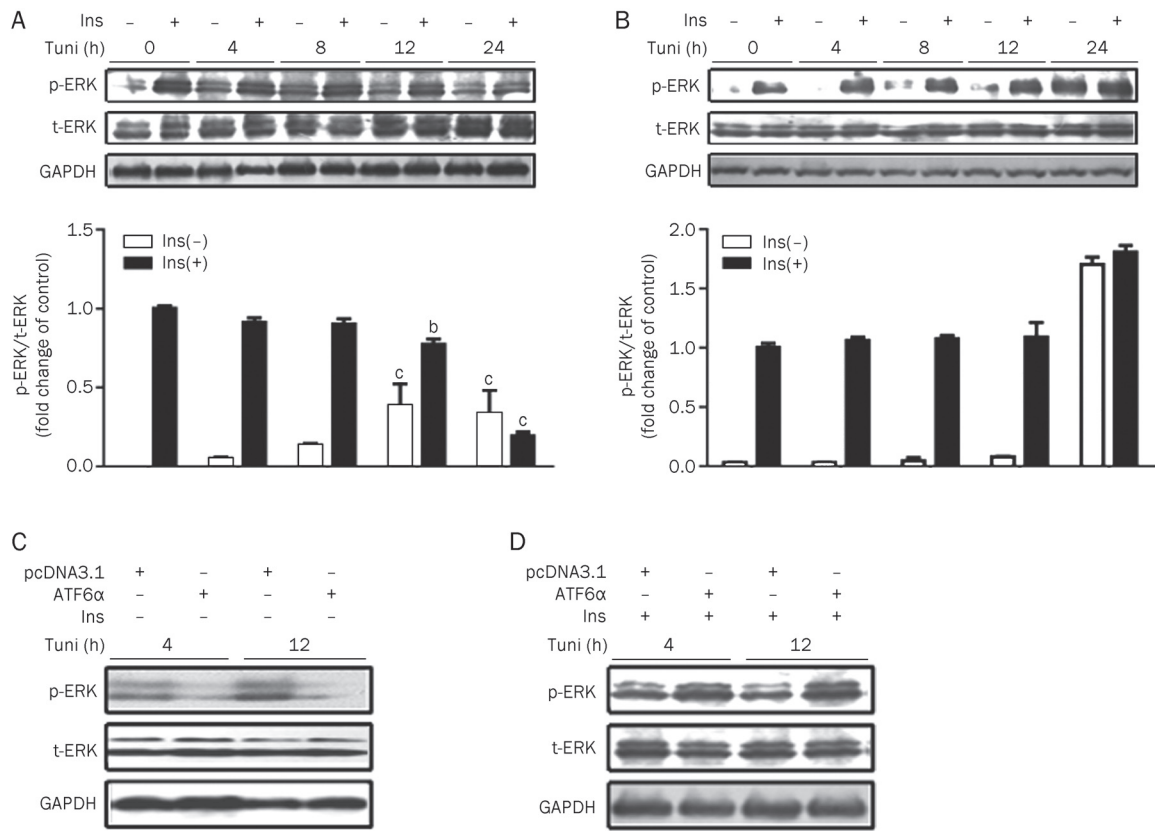

Figure 4. ATF6 could modulate ERK activity induced by tunicamycin simulation. (A and B) HEK293 cells were transiently transfected with pcDNA3.1 (A)/pcDNA3.1-hATF6α (B). After tunicamycin (2 μg/mL) treatment with or without insulin (167 nmol/L) stimulation for 5 min, phosphorylated and total ERK were analyzed. (C and D) After transfection, tunicamycin (2 μg/mL) treated HEK293 cells were stimulated with (D) or without (C) insulin (167 nmol/L). Then, phosphorylated and total ERK were analyzed. $^{b}P<0.05$, $^{c}P<0.01$ compared with control groups (0 h) with or without insulin stimulation, respectively.

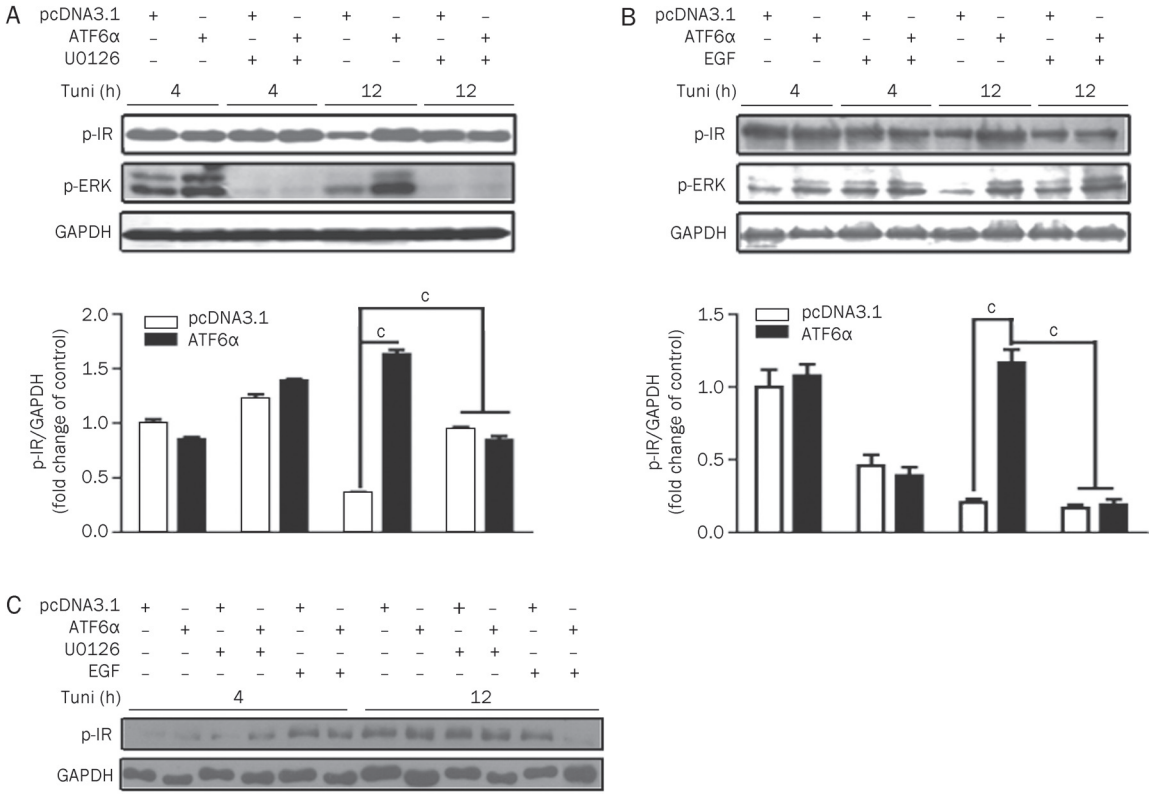

Figure 5. ATF6 regulation of IR signaling pathway activity is associated with ERK pathway. (A and B) After transfection, HEK293 cells were treated with tunicamycin (2 μg/mL) together with U0126 (10 μmol/L) (A) or EGF (200 ng/mL) (B) for the indicated time and insulin for 5 min (167 nmol/L). Then, the phosphorylated IR was analyzed. (C) HEK293 cells were transiently transfected with pcDNA3.1/pcDNA3.1-hATF6α. After 5 h, cells were refreshed and incubated with U0126 (10 μmol/L) or EGF (200 ng/mL) in serum-free DMEM for 4, 8, and 12 h without tunicamycin stimulation before 5-min insulin (167 nmol/L) stimulation. $^{c}P<0.01$.

susceptibility gene of type 2 diabetes in Pima Indians[45].

As previously published[43, 46], short-term (from 0 to 4 h) ER stress stimulation could increase AKT activity, while long-term (from 8 to 12 h) stimulation could suppress AKT activity. This reflects the dual character of ER stress: the adaptive/moderate level stress (featured by increased chaperone proteins and decreased misfolded proteins) and the destructive/excessive level stress (featured by activating JNK, apoptosis signal-regulating kinase (ASK))[2, 3, 30, 47]. We found that tyrosine-phosphorylated IR was first elevated and then decreased when stimulated with tunicamycin, while total IR decreased after tunicamycin incubation (Figure 1A) based on the results of p-IR/GAPDH ratio quantification instead of the p-IR/t-IR ratio because t-IR was too weak to quantify in 12 h. IR is an important upstream regulator of AKT and its change may partly account for the variation of AKT activity. We discovered that the ATF6 family could protect IR activity from tunicamycin stimulation. To further investigate whether ATF6 protection on IR could affect its downstream molecules, phosphorylation of AKT was examined. As shown in Figure S2, ATF6 also protects AKT from phosphorylation degradation induced by tunicamycin.

The contribution of ER stress transducer and related genes were evaluated in HEK293 cell lines to investigate the mechanism of ATF6 protection on the insulin pathway. Although the phosphorylation of IRE1α and cleavage of ATF6 could be modulated in ATF6 over-expressing cells, we failed to find any differences between ATF6 over-expression and control cells in the MTT assay. These results suggest that ATF6 over-expression does not improve cell sensitivity to ER stress and regulation of the ATF6 family on IR activity might not be dependent on its protective roles in ER stress. Recently, more new target genes of the ATF6 family have been discovered, including ER-stress related genes (*eg*, GRP78, GRP94, PDI, XBP-1[21]) and others [*eg*, Sterol regulatory element binding protein 2 (SREBP2)[48]]. It is reported that 250 genes could be up-regulated by tunicamycin treatment and at least 45 were ATF6α-dependent, although most of these genes have not yet been fully investigated[23].

The MAPK signaling pathways MKK4/7-SAPK/JNK, MKK3/6-p38, and MEK1/2-ERK have been reported to play key roles in insulin resistance induced by excessive ER stress[33–38]. Therefore, the phosphorylation of JNK, p38 and ERK were examined in ATF6 over-expressing cells. Our results indicate that the MEK1/2-ERK pathway is associated with the ATF6 protection mechanism. Before our investigation, several studies reported that MEK exerted negative effects on the insulin signaling pathway via down-regulation

of the expression of IR/IRS, decreasing tyrosine phosphorylation of IR/IRS, increasing serine phosphorylation of IRS and inhibiting the subsequent activations of PI3K and AKT[33–35]. Several diabetes-inducing agents have also been demonstrated as causing insulin resistance in a MEK-dependent manner[35, 20]. ER stress was also reported to induce activation of ERK[46], and ATF6 was shown to counteract the effects of ER stress[23, 24]. Based on this prior evidence and our results (Figures 4 and 5), it could be concluded that excessive ER stress could increase the basal, but decrease the insulin-induced, activity of ERK. We thus propose the potential effects of ATF6 to be as follows. Long-time ER stress stimulation could induce a constant "basal" activation of the ERK pathway, which might have a negative feedback causing the desensitization of IR activity. ATF6 could counteract this negative process through down-regulation of the basal ERK activity and up-regulation of insulin-induced ERK activity until 12 h, leading to the restoration of insulin signaling pathway activity. Although our results also showed that ATF6 could enhance p38 activity, it seems that p38 is not involved in ATF6 modulation of IR phosphorylation (Figure 3). This is consistent with the finding that p38 stimulates insulin-induced glucose uptake through GLUT4 activation instead of IR/IRS/AKT-dependent transporter translocation[36, 37].

As reported, ATF6 family members exhibit different influences on GRP78 transcription with a hypothetical mechanism that ATF6α, as a strong but labile transcription factor, and ATF6β, as a weak but stable transcription factor, work collaboratively to address different ER stress signals[11, 12]. However, we found that ATF6α and ATF6β demonstrated almost the same effects on IR activity. Thus, we hypothesized that no matter what characteristics they possess, these two isotypes might have similar influences on ER quality and cellular physiology in the process of adaptation to long-time stress since chronic stimulation would fully induce their activities.

Contrary to the opinion that the ATF6 family contributes to alleviating cellular stress[9, 16, 24], the studies by Seo *et al* suggest that ATF6 plays an important role in the development of β-cell dysfunction[49]. Although ATF6 was shown to suppress insulin gene expression in INS-1 cells, this process might be a feedback to prevent hyperinsulinmia *in vivo*. In addition, this report also indicated that ATF6 expression was increased in the pancreatic islets of diabetic rats compared with non-diabetic counterparts. However, this study did not confirm that the increase in ATF6 expression might cause or aggregate diabetes. Based on our current work, we suggest that ATF6 family members could be up-regulated in response to cellular stress to counteract the diabetic stress.

Recently, more studies have suggested that the signaling pathway involved in ER stress could be used as a potential target for anti-type 2 diabetes drug design[4–6, 38, 39]. Here we discovered that ATF6 family members protect the insulin receptor pathway from long-term tunicamycin treatment (4–12 h) that mimics the effects of chronic ER stress, implying that ATF6 could be a potential target for increasing insulin sensitivity. However, further investigations need to be carried out to clarify the underlying mechanism by which ATF6 regulates ERK activity and other diabetes-related pathways.

Acknowledgements

We gratefully acknowledge Prof Kazutoshi MORI for the plasmids of pcDNA3.1-hATF6α and pcDNA3.1-hATF6β. This work was supported by the State Key Program of Basic Research of China (No 2010CB912501 and 2007CB914304), the National Natural Science Foundation of China (No 90713046 and 30890044), Shanghai Basic Research Project from the Shanghai Science and Technology Commission (No 11ZR1444500) and Open Research Fund of the Key Laboratory of Biotherapy, West China Hospital, West China Medicine School, Sichuan University (No SKLB200901).

Author contribution

Xu SHEN, Hua-liang JIANG, Jing CHEN, and Vatcharin RUKACHAISIRIKUL designed the research; Hong SHEN, Yu ZHANG, Li-li CHEN, and Xu WANG performed experiments in investigating the effect of tunicamycin on IR; Xuan TANG and Hong SHEN studied the effect of ATF6 on IR under long-term ER stress by transient transfection and stable transfection with ATF6, and they also performed related assays to reveal the potential molecular mechanisms; Xu SHEN, Hua-liang JIANG, and Jing CHEN supervised the project; and Xu SHEN, Jing CHEN, Hong SHEN, and Xuan TANG contributed to the manuscript writing.

Supplementary information

Supplementary figures are available at Acta Pharmacologica Sinica website of NPG.

References

1 Saltiel AR, Kahn CR. Insulin signalling and the regulation of glucose and lipid metabolism. Nature 2001; 414: 799–806.
2 Kaufman RJ. Stress signaling from the lumen of the endoplasmic reticulum: coordination of gene transcriptional and translational controls. Genes Dev 1999; 13: 1211–33.
3 Ozcan U, Cao Q, Yilmaz E, Lee AH, Iwakoshi NN, Ozdelen E, *et al*. Endoplasmic reticulum stress links obesity, insulin action, and type 2 diabetes. Science 2004; 306: 457–61.
4 Ozcan U, Yilmaz E, Ozcan L, Furuhashi M, Vaillancourt E, Smith RO, *et al*. Chemical chaperones reduce ER stress and restore glucose homeostasis in a mouse model of type 2 diabetes. Science 2006; 313: 1137–40.
5 Ozawa K, Miyazaki M, Matsuhisa M, Takano K, Nakatani Y, Hatazaki M, *et al*. The endoplasmic reticulum chaperone improves insulin resistance in type 2 diabetes. Diabetes 2005; 54: 657–63.
6 Nakatani Y, Kaneto H, Kawamori D, Yoshiuchi K, Hatazaki M, Matsuoka TA, *et al*. Involvement of endoplasmic reticulum stress in insulin resistance and diabetes. J Biol Chem 2005; 280: 847–51.
7 Gao Z, Zhang X, Zuberi A, Hwang D, Quon MJ, Lefevre M, *et al*. Inhibition of insulin sensitivity by free fatty acids requires activation of multiple serine kinases in 3T3-L1 adipocytes. Mol Endocrinol 2004; 18: 2024–34.
8 Herschkovitz A, Liu YF, Ilan E, Ronen D, Boura-Halfon S, Zick Y. Common inhibitory serine sites phosphorylated by IRS-1 kinases, triggered by insulin and inducers of insulin resistance. J Biol Chem 2007; 282: 18018–27.
9 Ye J, Rawson RB, Komuro R, Chen X, Davé UP, Prywes R, *et al*. ER

stress induces cleavage of membrane-bound ATF6 by the same proteases that process SREBPs. Mol Cell 2000; 6: 1355–64.
10 Shen J, Chen X, Hendershot L, Prywes R. ER stressregulation of ATF6 localization by dissociation of BiP/GRP78 binding and unmasking of Golgi localization signals. Dev Cell 2002; 3: 99–111.
11 Thuerauf DJ, Morrison LE, Hoover H, Glembotski CC. Coordination of ATF6–mediated transcription and ATF6 degradation by a domain that is shared with the viral transcription factor, VP16. J Biol Chem 2002; 277: 20734–9.
12 Thuerauf DJ, Morrison L, Glembotski C. Opposing roles for ATF6alpha and ATF6beta in endoplasmic reticulum stress response gene induction. J Biol Chem 2004; 279: 21078–84.
13 Thuerauf DJ, Marcinko M, Belmont PJ, Glembotski CC. Effects of the isoform-specific characteristics of ATF6 alpha and ATF6 beta on endoplasmic reticulum stress response gene expression and cell viability. J Biol Chem 2007; 282: 22865–78.
14 Salminen A, Kauppinen A, Suuronen T, Kaamiranta K, Ojala J. ER stress in Alzheimer's disease: a novel neuronal trigger for inflammation and Alzheimer's pathology. J Neuroinflammation 2009; 6: 41.
15 Kapoor A, Sanyal AJ. Endoplasmic reticulum stress and the unfolded protein response. Clin Liver Dis 2009; 13: 581–90.
16 Dobson CM. Principles of protein folding, misfolding and aggregation. Semin Cell Dev Biol 2004; 15: 3–16.
17 Kammoun HL, Hainault I, Ferré P, Foufelle F. Nutritional related liver disease: targeting the endoplasmic reticulum stress. Curr Opin Clin Nutr Metab Care 2009; 12: 575–82.
18 Fonseca SG, Burcin M, Gromada J, Urano F. Endoplasmin reticulum stress in beta-cells and development of diabetes. Curr Opin Pharmacol 2009; 9: 763–70.
19 Scheuner D, Kaufman RJ. The unfolded protein response: a pathway that links insulin demand with beta-cell failure and diabetes. Endocr Rev 2008; 29: 317–33.
20 Izawa Y, Yoshizumi M, Fujita Y, Ali N, Kanematsu Y, Ishizawa K, *et al*. ERK1/2 activation by angiotensin II inhibits insulin-induced glucose uptake in vascular smooth muscle cells. Exp Cell Res 2005; 308: 291–9.
21 Yoshida H, Okada T, Haze K, Yanagi H, Yura T, Negishi M, *et al*. ATF6 activated by proteolysis binds in the presence of NF-Y (CBF) directly to the *cis*-acting element responsible for the mammalian unfolded protein response. Mol Cell Biol 2000; 20: 6755–67.
22 Morris JA, Dorner AJ, Edwards CA, Hendershot LM, Kaufman RJ. Immunoglobulin binding protein (BiP) function is required to protect cells from endoplasmic reticulum stress but is not required for the secretion of selective proteins. J Biol Chem 1997; 272: 4327–34.
23 Wu J, Rutkowski DT, Dubois M, Swathirajan J, Saunders T, Wang J, *et al*. ATF6alpha optimizes long-term endoplasmic reticulum function to protect cells from chronic stress. Dev Cell 2007; 13: 351–64.
24 Yamamoto K, Sato T, Matsui T, Sato M, Okada T, Yoshida H, *et al*. Transcriptional induction of mammalian ER quality control proteins is mediated by single or combined action of ATF6alpha and XBP1. Dev Cell 2007; 13: 365–76.
25 Yoshida H, Haze K, Yanagi H, Yura T, Mori K. Identification of the *cis*-acting endoplasmic reticulum stress response element responsible for transcriptional induction of mammalian glucose-regulated proteins. Involvement of basic leucine zipper transcription factors. J Biol Chem 1998; 273: 33741–9.
26 Haze K, Yoshida H, Yanagi H, Yura T, Mori K. Mammalian transcription factor ATF6 is synthesized as a transmembrane protein and activated by proteolysis in response to endoplasmic reticulum stress. Mol Biol Cell 1999; 10: 3787–99.
27 Ni M, Lee AS. ER chaperones in mammalian development and human diseases. FEBS Lett 2007; 581: 3641–51.
28 Ji C, Kaplowitz N. ER stress: Can the liver cope? J Hepatol 2006; 45: 321–33.
29 Nakayaa H, Zhao J, Ei-Fakhrany A, Isosaki M, Satoh H, Kyotani Y, *et al*. Neuroprotective effects of praipexole against tunicaycin-induced cell death in PC12 cells. Clin Exp Pharacol Physiol 2009; 36: 1183–5.
30 Urano F, Wang X, Bertolotti A, Zhang Y, Chung P, Harding HP, *et al*. Coupling of stress in the ER to activation of JNK protein kinases by transmembrane protein kinase IRE1. Science 2000; 287: 664–6.
31 Hirosumi J, Tuncman G, Chang L, Görgün CZ, Uysal KT, Maeda K, *et al*. A central role for JNK in obesity and insulin resistance. Nature 2002; 420: 333–6.
32 Aguirre V, Uchida T, Yenush L, Davis R, White MF. The c-Jun NH_2-terminal kinase promotes insulin resistance during association with insulin receptor substrate-1 and phosphorylation of Ser(307). J Biol Chem 2000; 275: 9047–54.
33 Fujishiro M, Gotoh Y, Katagiri H, Sakoda H, Ogihara T, Anai M, *et al*. Three mitogen-activated protein kinases inhibit insulin signaling by different mechanisms in 3T3-L1 adipocytes. Mol Endocrinol 2003; 17: 487–97.
34 De Fea K, Roth RA. Modulation of insulin receptor substrate-1 tyrosine phosphorylation and function by mitogen-activated protein kinase. J Biol Chem 1997; 272: 31400–6.
35 Engelman JA, Berg AH, Lewis RY, Lisanti MP, Scherer PE. Tumor necrosis factor alpha-mediated insulin resistance, but not dedifferentiation, is abrogated by MEK1/2 inhibitors in 3T3-L1 adipocytes. Mol Endocrinol 2000; 14: 1557–69.
36 Sweeney G, Somwar R, Ramlal T, Volchuk A, Ueyama A, Klip A. An inhibitor of p38 mitogen-activated protein kinase prevents insulin-stimulated glucose transport but not glucose transporter translocation in 3T3-L1 adipocytes and L6 myotubes. J Biol Chem 1999; 274: 10071–8.
37 Somwar R, Kim DY, Sweeney G, Huang C, Niu W, Lador C, *et al*. GLUT4 translocation precedes the stimulation of glucose uptake by insulin in muscle cells: potential activation of GLUT4 via p38 mitogen-activated protein kinase. Biochem J 2001; 359: 639–49.
38 Hotamisligil GS. Inflammation and endoplasmic reticulum stress in obesity and diabetes. Int J Obes (Lond) 2008; 32: S52–4.
39 Hotamisligil GS. Endoplasmic reticulum stress and the inflammatory basis of metabolic disease. Cell 2010; 140: 900–17.
40 Wu RF, Terada LS. Focal oxidant and Ras signaling on the ER surface activates autophagy. Autophagy 2010; 6: 828–9.
41 Hotamisligil G. Role of endoplasmic reticulum stress and c-Jun NH_2-terminal kinase pathways in inflammation and origin of obesity and diabetes. Diabetes 2005; 54: S73–8.
42 Hotamisligil GS, Shargill NS, Spiegelman BM. Adipose expression of tumor necrosis factor-alpha: direct role in obesity-linked insulin resistance. Science 1993; 259: 87–91.
43 Srinivasan S, Ohsugi M, Liu Z, Fatrai S, Bernal-Mizrachi E, Permutt MA. Endoplasmic reticulum stress-induced apoptosis is partly mediated by reduced insulin signaling through phosphatidylinositol 3-kinase/Akt and increased glycogen synthase kinase-3beta in mouse insulinoma cells. Diabetes 2005; 54: 968–75.
44 Lee K, Tirasophon W, Shen X, Michalak M, Prywes R, Okada T, *et al*. IRE1-mediated unconventional mRNA splicing and S2P-mediated ATF6 cleavage merge to regulate XBP1 in signaling the unfolded protein response. Genes Dev 2002; 16: 452–66.
45 Thameem F, Farook VS, Bogardus C, Prochazka M. Association of amino acid variants in the activating transcription factor 6 gene (ATF6) on 1q21-q23 with type 2 diabetes in Pima Indians. Diabetes 2006; 55: 839–42.
46 Hu P, Han Z, Couvillon AD, Exton JH. Critical role of endogenous Akt/IAPs and MEK1/ERK pathways in counteracting endoplasmic reticulum stress-induced cell death. J Biol Chem 2004; 279: 49420–9.
47 Nishitoh H, Matsuzawa A, Tobiume K, Saegusa K, Takeda K, Inoue K, *et al*. ASK1 is essential for endoplasmic reticulum stress–induced neuronal cell death triggered by expanded polyglutamine repeats. Genes Dev 2002; 16: 1345–55.
48 Zeng L, Lu M, Mori K, Luo S, Lee AS, Zhu Y, *et al*. ATF6 modulates SREBP2-mediated lipogenesis. EMBO J 2004; 23: 950–8.
49 Seo HY, Kim YD, Lee KM, Min AK, Kim MK, Kim HS, *et al*. Endoplasmic reticulum stress-induced activation of activating transcription factor 6 decreases insulin gene expression via up-regulation of orphan nuclear receptor small heterodimer partner. Endocrinology 2008; 149: 3832–41.

Acta Pharmacologica Sinica (2011) 32: 1148–1158
 1671-4083/11 $32.00
www.nature.com/aps

Original Article

Novel selective cannabinoid CB_1 receptor antagonist MJ08 with potent *in vivo* bioactivity and inverse agonistic effects

Wei CHEN[1, #], Cheng XU[2, #], Hong-ying LIU[1], Long LONG[1], Wei ZHANG[1], Zhi-bing ZHENG[1], Yun-de XIE[1], Li-li WANG[1, *], Song LI[1]

[1]*Beijing Institute of Pharmacology and Toxicology, Beijing 100850, China;* [2]*Department of physiology, Pharmaceutical University of Shenyang, Shenyang 110016, China*

Aim: To characterize the biological profiles of MJ08, a novel selective CB_1 receptor antagonist.
Methods: Radioligand binding assays were performed using rat brain and spleen membrane preparations. CB_1 and CB_2 receptor redistribution and intracellular Ca^{2+} ($[Ca^{2+}]_i$) assays were performed with IN CELL Analyzer. Inverse agonism was studied using intracellular cAMP assays, and in guinea-pig ileum and mouse vas deferens smooth muscle preparations. *In vivo* pharmacologic profile was assessed in diet-induced obesity (DIO) mice.
Results: In radioligand binding assay, MJ08 selectively antagonized CB_1 receptor (IC_{50}=99.9 nmol/L). In EGFP-CB_1_U2OS cells, its IC_{50} value against CB_1 receptor activation was 30.23 nmol/L (SR141716A: 32.16 nmol/L). WIN 55,212-2 (1 μmol/L) increased $[Ca^{2+}]_i$ in the primary cultured hippocampal neuronal cells and decreased cAMP accumulation in CHO-hCB_1 cells. MJ08 (10 nmol/L–10 μmol/L) blocked both the WIN 55,212-2-induced effects. Furthermore, MJ08 reversed the inhibition of electrically evoked twitches of mouse vas deferens by WIN 55,212-2 (pA_2=10.29±1.05). MJ08 and SR141716A both showed an inverse agonism activity by markedly promoting the contraction force and frequency of guinea pig ileum muscle. MJ08 significantly increased the cAMP level in CHO-hCB_1 cells with an EC_{50} value of 78.6 nmol/L, which was lower than the EC_{50} value for SR141716A (159.2 nmol/L). Besides the more potent pharmacological effects of cannabinoid CB_1 receptor antagonism in DIO mice, such as reducing food intake, decreasing body weight, and ameliorating dyslipidemia, MJ08 (10 mg/kg) unexpectedly raised the fasted blood glucose *in vivo*.
Conclusion: MJ08 is a novel, potent and selective CB_1 receptor antagonist/inverse agonist with potent bioactive responses *in vitro* and *in vivo* that may be useful for disclosure the versatile nature of CB_1 receptors.

Keywords: MJ08; CB_1 receptor; antagonist; inverse agonist; obesity; dyslipidemia

Acta Pharmacologica Sinica (2011) 32: 1148–1158; doi: 10.1038/aps.2011.80; published online 15 Aug 2011

Introduction

Cannabinoid CB_1 receptors are widely expressed in both the central and peripheral nervous systems, and they display numerous physiological effects such as behavioral, neuroprotective, immunosuppressive, and metabolic functions[1–3]. In the past decade, the metabolic homeostasis regulated by the cannabinoid CB_1 receptor has been the focus of intensive studies. Striking advances were made in developing high affinity selective cannabinoid CB_1 receptor antagonists and/or inverse agonists as therapeutic agents for obesity, diabetes and metabolic syndrome. Some selective antagonists of the cannabinoid CB_1 receptor have been developed and reached various stages of clinical trials. These new chemical entities also provided useful tools for understanding the sophisticated physiological mechanism of this receptor[4–6]. Among them, the most representative selective antagonist/inverse agonist of the cannabinoid CB_1 receptor is rimonabant (SR141716A). It was developed by Sanofi-Aventis and approved for treatment of obesity in Europe in June of 2006. Unfortunately, psychiatric side effects delayed its approval in the United States, which also led to subsequent market withdrawal of the drug in the European Union in late 2008. Hence, to circumvent the problems that have beset the current agents, some strategies such as developing non-brain penetrating and peripheral restrictive CB_1 receptor antagonists or focusing on allosteric modulation

# These two authors contributed equally to this work.
* To whom correspondence should be addressed.
E-mail wangll63@yahoo.com.cn
Received 2011-03-11 Accepted 2011-05-18

of CB_1 receptors are being used at present[7, 8].

Previously reported cannabinoid CB_1 receptor selective antagonists exhibited mainly two types of behavior[9, 10]. One type, expressed by SR141716A and Imidazole 24b, has effects in the opposite direction to those produced by the cannabinoid receptor agonists, *ie*, they are cannabinoid CB_1 receptor inverse agonists[11, 12]. The other type is expressed by the cannabinoid CB_1 receptor neutral antagonist, such as AM4113, with no intrinsic activity[13]. It was presumed that the inverse agonist and neutral antagonist may involve different signal transduction mechanisms. However, aside from their structural differences, the related pharmacological and toxicological effects produced by the different types of cannabinoid CB_1 receptor antagonists are still not completely known.

Novel drug candidates acting against cannabinoid CB_1 receptors, such as MJ08 and MJ15, were discovered in our laboratory through a series of *in-vitro, ex-vivo*, and *in-vivo* biological screenings and evaluations. Both compounds behaved as highly potent selective cannabinoid CB_1 receptor antagonists. Although they have similar molecular formulas, the substitution with piperidin-1-yl at the N atom of the pyrazol 3 site (N-pyridin-3-methyl for MJ15) characterizes MJ08 (patent No CN101062919A) with different receptor-binding characteristics and bioactivities[14]. MJ08 exhibits an inverse agonism activity even stronger than that of SR141716A in functional assays; however, it has a relatively lower affinity than SR141716A in radioligand competitive binding analysis. In addition to its significant weight loss effect, MJ08 increases fasting blood glucose in diet-induced obesity (DIO) mice. The *in vitro* and *in vivo* pharmacological profiles of MJ08 were described in this paper.

Materials and methods

Drugs and Chemicals

Forskolin, CP55, 940 (CB_1/CB_2 agonist), WIN 55,212-2 (CB_1/CB_2 agonist), and Fluo-3 were purchased from Sigma. [^{3}H]-SR141716A and [^{3}H]-WIN 55,212-2 were purchased from Amersham. SR141716A and MJ08 were synthesized and prepared by the New Drug Design Center of Beijing Institute of Pharmacology and Toxicology. The purity and structure of these two compounds were confirmed by high-performance liquid chromatography, mass spectrometry and ^{1}H-nuclear magnetic resonance (NMR). The structure of MJ08 {[5-(4-chlorophenyl)-1-(2,4-dichlorophenyl)-4-methyl-1*H*-pyrazol-3-yl](piperidin-1-yl)methanone} is shown in Figure 1.

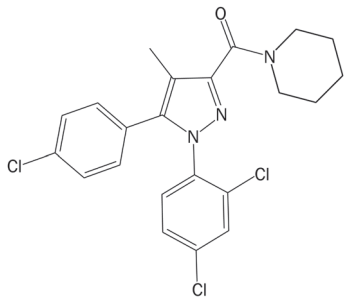

Figure 1. Structure of MJ08 [5-(4-chlorophenyl)-1-(2,4-dichlorophenyl)-4-methyl-1*H*-pyrazol-3-yl](piperidin-1-yl)methanone.

Membrane preparations and radioligand competitive binding analysis

The cannabinoid CB_1 and CB_2 receptor membranes were prepared from rat brain and spleen, respectively, as reported in our previous paper, and stored at -80 °C until use[14]. Competitive binding analysis was conducted by incubating 50 μg of membrane and competing ligand (2.4 nmol/L [^{3}H]-SR141716A for CB_1 and 6.4 nmol/L [^{3}H]-WIN 55,212-2 for CB_2) in Tris-HCl (50 mmol/L, pH 7.4) at 30 °C for 1 h. Competitive binding inhibition curves were generated with different concentrations of SR141716A or MJ08. The radioactivity bound to the filters was counted with 1 mL of Biofluor liquid scintillant (New England Nuclear Corp, UK) in a LS6500 counter. Non-specific binding was determined in the presence of 25 μmol/L non-radioactive SR141716A for CB_1 and CP55 940 for the CB_2 receptor. The affinity of MJ08 to the CB_1 or CB_2 receptor was expressed as a K_i value or an inhibition of the specific binding of radioactive [^{3}H]-SR141716A to the CB_1 receptor or [^{3}H]-WIN 55,212-2 to the CB_2 receptor. Each competitive binding inhibition curve was generated from the data pooled from three independent experiments conducted in duplicate.

Assay of cannabinoid receptor antagonism at the cellular level

Thermo scientific CB_1 and CB_2 redistribution assays (Themo Fisher Bioimage ApS, Soeborg, Denmark) were used to analyze the antagonistic effects and the selectivity of MJ08 with SR141716A as the reference compound. The assay was performed as previously reported[14]. The cannabinoid CB_1 and CB_2 antagonist redistribution assay formats were specially designed cell models to screen agonists or antagonists of CB_1 and CB_2 receptors, respectively. The assay was validated with an average Z'=0.55±0.21 (CB_1) and Z'=0.34±0.1 (CB_2) and was suitable for both high content screening and profiling applications (Thermo scientific cannabinoid CB_1 and CB_2 redistribution assay specifications).

Before each experiment, the culture medium was changed to assay buffer [F12 culture medium containing 1 μmol/L Hoechst 33342 (Invitrogen, Oregon, USA)] and incubated at 37 °C for 20 min before different concentrations (10 nmol/L, 100 nmol/L, 1 μmol/L, and 10 μmol/L) of SR141716A or MJ08 combined with 1 μmol/L WIN 55,212-2 [the maximally active concentration on the EGFP-CB_U2OS cells (EGFP, enhanced green fluorescent protein)] was added. After further incubation at 37 °C for 2 h, the cells were imaged on the IN Cell Analyzer 1000 (20×objective), and the pictures were analyzed with the Granularity Analysis Module of IN Cell. DMSO (0.1%) was used as the vehicle control. The inhibition ratio of a test compound was expressed as percent inhibition of the internalization induced by the reference agonist WIN 55,212-2. The corresponding IC_{50} values were calculated from the inhibition ratios. The results were obtained from three independent experiments performed in triplicate.

Hippocampal neurons and Fluo-3/AM Ca^{2+} imaging

Intracellular Ca^{2+} assays were conducted in hippocampal neurons as previously described[14]. After being washed with HBS solution (130 mmol/L NaCl, 5.4 mmol/L KCl, 1.8 mmol/L $CaCl_2$, 1 mmol/L $MgCl_2$, 10 mmol/L HEPEs, and 25 mmol/L *D*-glucose, pH 7.4), the cells were incubated for 60 min with 10 μmol/L fluorescent Ca^{2+} indicator, fluoro-3 acetoxymethyl ester (Fluo-3/AM), and then pluronic acid F-127 (Cambridge Bioscience, Cambridge, UK) was added. Subsequently, the cells were washed again three times with HBS and challenged with 0.1% DMSO (vehicle control), or SR141716A or MJ08 at different concentrations (10 nmol/L, 100 nmol/L, 1 μmol/L, or 10 μmol/L). An application of 1 μmol/L WIN 55,212-2 was administered 1 min later. Fluorescence was monitored and imaged with the IN Cell Analyzer 1000 (GE Healthcare, NJ, USA) at 3 s intervals, and then analyzed with the Object Intensity Analysis Module of IN Cell. Background levels of fluorescence were subtracted at the beginning of the experiments. The time courses of $[Ca^{2+}]_i$ change were plotted by recording the relative fluorescence intensity per cell *vs* time.

Intracellular cAMP assays

Stable Chinese hamster ovary (CHO) cells expressing the human cannabinoid CB_1 and CB_2 (CHO-hCB_1 and CHO-hCB_2, respectively) receptors were established in our previous work[14]. Functional antagonism of the cannabinoid CB_1 receptor agonist response was measured by incubating the recombinant cannabinoid CHO cells with various concentrations of test ligands and 200 μmol/L 3-isobutyl-1-methylxanthine (IBMX, phosphodiesterase inhibitor) in the assay buffer at room temperature for 30 min. The intrinsic inverse agonism was tested in the presence of 1 μmol/L forskolin in CHO-hCB_1 and CHO-hCB_2 cells as above. Intracellular cAMP was assayed with the LANCE cAMP 384 kit (AD0262, PerkinElmer, CA, USA) according to the manufacturer's specifications. Briefly, cells were harvested with versene, washed with Hank's Balanced Salt Solutions (HBSS) and re-suspended in stimulation buffer at a concentration of 1.7×10^6/mL. Six μL of the cell suspension (containing the Alexa-labeled antibodies) were added into one well of white OptiPlate-384, and then 6 μL of different compound dilutions was added. After incubation for 30 min at room temperature, 12 μL of detection mix was added and further incubated for 60 min. The fluorescence was read on EnVision Multilabel Plate Readers (PerkinElmer, CA, USA) with 475 nm excitation and 665 nm emission. The amounts of cAMP produced in the stimulated cells were determined according to the cAMP standard curves. In the inverse agonism assay, 10 μmol/L MJ08-enhanced, forskolin-stimulated cAMP production was used to define 100% efficacy, and the correspondent IC_{50} values were calculated from the curve.

Tissue preparations and contraction studies

Male Kun-ming mice (25–30 g) and guinea-pigs (350–400 g) from Laboratory Animal Center of Pharmaceutical University of Shenyang, China, were humanely killed by decapitation following CO_2 asphyxiation. The vas deferens and ileum were excised according to the method in the literature[15–17] and placed in Krebs' physiological salt solution [pH 7.4, composition (mmol/L): NaCl 119, KCl 4.69, KH_2PO_4 1.18, glucose 11, $NaHCO_3$ 25, $CaCl_2$ 2.5, EDTA 0.026], gassed with 95% O_2/5% CO_2 and maintained at 37 °C. Each vas deferens or ileum was mounted in a 30-mL organ bath and connected to an isometric transducer (RM6240CD, Chengdu, China). The vas deferens was subsequently equilibrated for 30 min and stimulated with trains of 10 pulses of 40 V for 0.5-ms duration at intervals of 50 ms. Contraction data were registered on a polygraph recorder before and after incubation with 10^{-7} mol/L SR14716A, 10^{-7} mol/L MJ08 or the vehicle (0.1% DMSO) for 30 min. The cannabinoid agonist WIN 55,212-2 was then added at 30-min intervals to construct an inhibitory cumulative concentration-response curve. The inhibition rate of the tested compounds was calculated with the following equation: $(A_n–A_0)/A_0\times100\%$, where A_0 and A_n denote the twitch amplitude of the tested compounds before and after the administration of different concentrations of WIN 55,212-2, respectively. The pA_2 values were determined using the method of Arunlakshan and Schild, *ie*, pA_2=log (E′/E–1)–logB, where E′ is the ED_{50} of the agonist under the presence of the antagonist, E is the ED_{50} of the agonist in the absence of the antagonist and B is the concentration of the antagonist.

Meanwhile, the specific effects of the test compounds on the contraction of the vas deferens smooth muscle and guinea-pig ileum were also observed. After equilibration for 30 min, the vas deferens was stimulated as described above, and a recording of the contraction amplitude was begun before administration of SR141716A or MJ08 for 30 min at ten-fold increments using 30-min intervals to construct a cumulative concentration-response curve. For the ileum, contraction data were recorded for 2 min before and after treatments, and cumulative concentration-response curves were generated.

Animals and treatment

Animals were obtained from Laboratory Animal Center of Beijing Institute of Pharmacology and Toxicology, unless otherwise stated. All animal experiments were performed strictly in accordance with the Guide for the Care and Use of Laboratory Animals of the National Institutes of Health and were approved by the Institutional Animal Care and Use Committee of the Beijing Institute of Pharmacology and Toxicology. Male Wistar rats (220–240 g) and their neonates (1 d) were used for radioligand competitive binding studies and primary cultures of hippocampus cells, respectively.

Male C57BL/6J mice (6 weeks old), maintained under controlled illumination (12/12-h light/dark cycle) and temperature (22±1 °C), were fed a high-fat diet (45% fat, 18% protein, 37% carbohydrate) for 16 weeks to obtain a DIO mouse model. Age-matched lean mice were used as normal controls. The DIO mice were randomly divided into three groups based on their initial body weights. SR141716A (10 $mg\cdot kg^{-1}\cdot d^{-1}$), MJ08 (10 $mg\cdot kg^{-1}\cdot d^{-1}$) or the vehicle (1% DMSO) were administered by gavage once daily for 40 d. Individual body weight and cage food consumption were measured every day. At the end

of the experimental period, the mice were fasted overnight, and blood samples were collected for the assessment of serum glucose, triglycerides (TG) and total cholesterol (TC) levels as previously described[18].

Statistical analysis

All results are expressed as the mean±SD. For multiple comparisons, the statistical analysis was performed using one-way ANOVA followed by Tukey's multiple comparison tests with SPSS 11.5. $P<0.05$ was considered to be statistically significant.

Results

Selective interaction of MJ08 with the cannabinoid CB_1 receptor at the molecular level

Figure 2 showed that [^{3}H]-SR141716A can specifically bind to the cannabinoid CB_1 receptor of rat brain membranes, and such interaction can be replaced by unlabeled SR141716A or MJ08 in a concentration-dependent manner. However, it is noted that the competitive binding inhibition curves of SR141716A or MJ08 are different in slope and shape. SR141716A exhibited a sharply competitive effect from 10^{-11} to 10^{-9} mol/L; nevertheless, MJ08 gradually inhibited [^{3}H]-SR141716A binding from 10^{-14} to 10^{-4} mol/L. The concentration-response curves gave K_i and IC_{50} values of 25.4 and 99.9 nmol/L, respectively, for MJ08, and 22.9 and 99.3 pmol/L, respectively, for SR141716A. In contrast, both SR141716A and MJ08 showed very low affinity to the CB_2 receptor expressed in rat spleen preparations; even at a higher concentration (about 34% inhibition at 10 μmol/L for both compounds, n=6), they could not compete with the binding of [^{3}H]-WIN 55,212-2 to the CB_2 receptor. However, the cannabinoid CB_1/CB_2 receptor agonist CP55,940 could antagonize this effect under the same conditions, with more than 90% inhibition to the CB_2 receptor at 100 nmol/L (data not shown). These results indicate that MJ08 is a selective cannabinoid CB_1 (not CB_2) ligand but that it has relatively lower affinity than SR141716A at an *in vitro* molecular level.

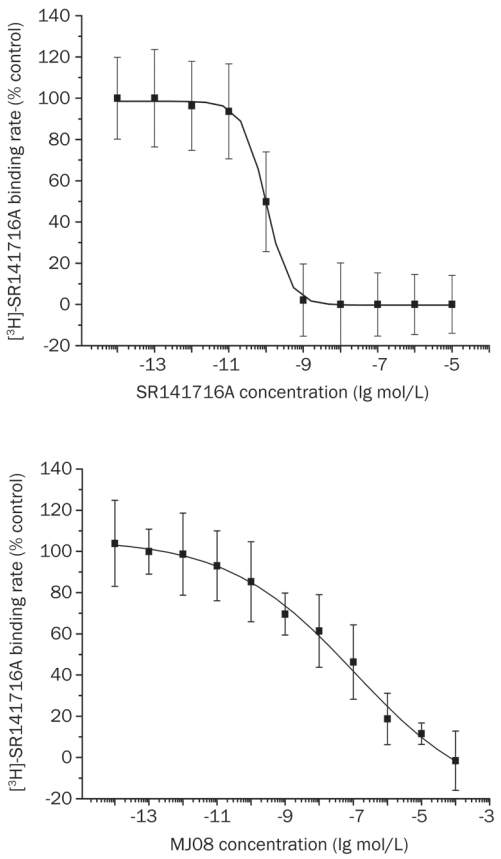

Figure 2. The competitive inhibition of [^{3}H]-SR141716A binding to the CB_1 receptor by MJ08 and SR141716A. The specific binding rate of 2.4 nmol/L [^{3}H]-SR141716A was defined as 1; other values of [^{3}H]-SR141716A binding under different concentrations of SR141716A or MJ08 were relative to that. Values are the mean±SD.

MJ08 antagonized the activation of the cannabinoid CB_1 receptor at the cellular level

As a $G_{i/s}$-coupled G-protein-coupled receptor (GPCR), the cannabinoid receptor is rapidly internalized following agonist binding and receptor activation[19]. Recombinant U2OS cells stably express human cannabinoid CB_1 or CB_2 receptors fused to the N-terminus of EGFP. The cannabinoid CB_1 or CB_2 receptor internalization assay is available for the screening of agonists or antagonists of the cannabinoid CB_1 and CB_2 receptors. Figure 3A shows that 1 μmol/L CB_1/CB_2 receptor agonist WIN 55,212-2 markedly induced the internalization of the membrane-localized CB_1-EGFP fusion protein to the endosomes; the agonistic potency was 2.59 times that of the vehicle control. However, when co-administered with MJ08, it dose-dependently antagonized the internalization of the CB_1-EGFP fusion protein, and the IC_{50} calculated from the concentration-response curve was 30.23±6.41 nmol/L, which was comparable to the value of SR141716A (32.16±6.72 nmol/L) in the same experiment (Figure 3B). However, both SR141716A and MJ08 exhibited weak antagonism towards the cannabinoid CB_2 receptor activation and internalization induced by WIN 55,212-2 in EGFP-CB_2_U2OS cells, with only approximately 25% to 35% inhibition by 10 μmol/L of MJ08 or SR141716A (data not shown). Therefore, MJ08 is macroscopically demonstrated to be equally potent and selective as a CB_1 receptor antagonist as SR141716A in the cellular assay.

MJ08 antagonized the elevation and oscillation of $[Ca^{2+}]_i$ induced by the cannabinoid CB_1 receptor agonist

$[Ca^{2+}]_i$ was measured in hippocampal neurons using the fluorescent dye Fluo3/AM as an indicator. It had been shown that cannabinoid CB_1, rather than the CB_2 receptor, is predominantly expressed in hippocampal tissue, and cannabinoid CB_1 receptor activation increases $[Ca^{2+}]_i$[20]. In cultured rat hippocampal cells, 1 μmol/L CB_1/CB_2 receptor agonist WIN 55,212-2 significantly increased $[Ca^{2+}]_i$ (Figure 4); the $[Ca^{2+}]_i$ signal showed an initial rise, slow decay, and sustained elevated phase with oscillations. SR141716A and MJ08 both (10 nmol/L to 10 μmol/L) blocked the activation of the cannabinoid CB_1 receptor by WIN 55,212-2 and the following induced elevation and oscillations of intracellular Ca^{2+} (Figure 4B).

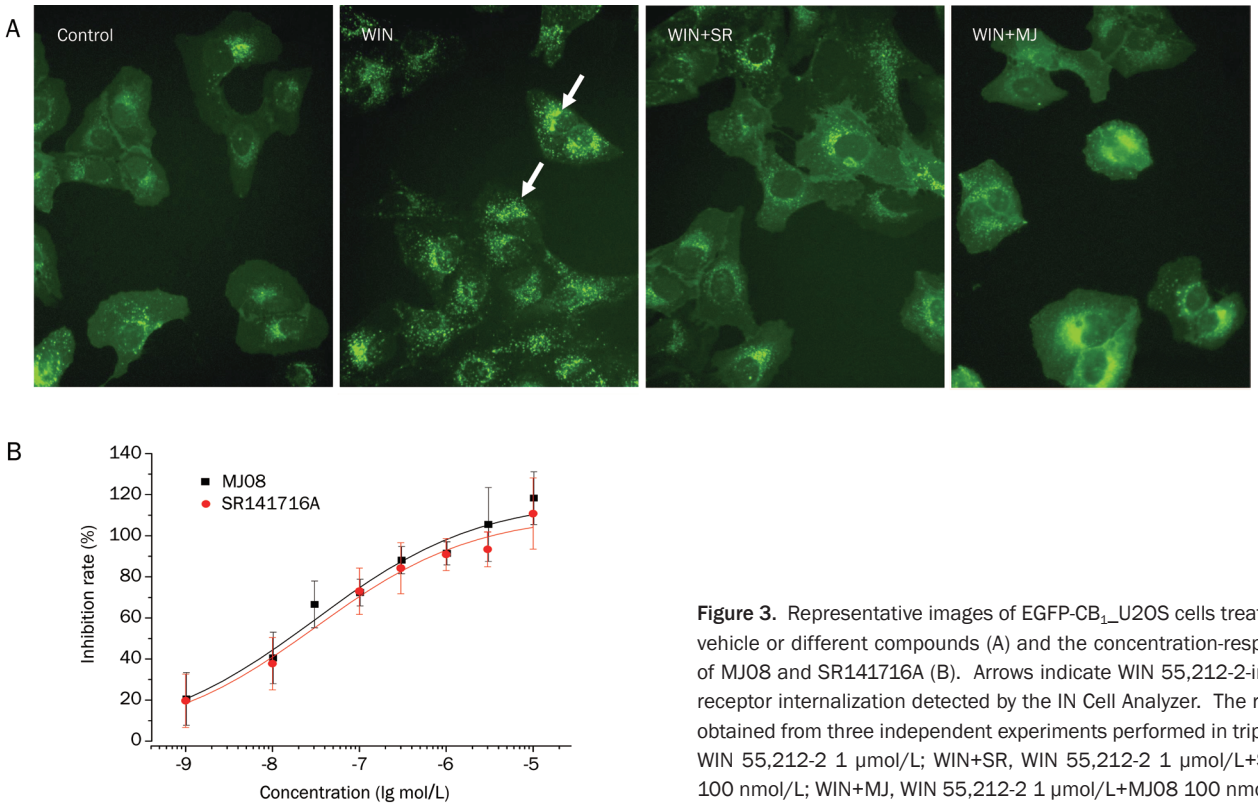

Figure 3. Representative images of EGFP-CB_1_U2OS cells treated with the vehicle or different compounds (A) and the concentration-response curve of MJ08 and SR141716A (B). Arrows indicate WIN 55,212-2-induced CB_1 receptor internalization detected by the IN Cell Analyzer. The results were obtained from three independent experiments performed in triplicate: WIN, WIN 55,212-2 1 μmol/L; WIN+SR, WIN 55,212-2 1 μmol/L+SR141716A 100 nmol/L; WIN+MJ, WIN 55,212-2 1 μmol/L+MJ08 100 nmol/L.

This result indicates that MJ08 may antagonize the second messenger molecules of cannabinoid CB_1 receptor activation.

Antagonism on intracellular cAMP and inverse agonism of MJ08

The effect of MJ08 on the agonist-mediated decrease of cAMP level in CHO cells expressing human cannabinoid CB_1 receptor was examined. Like SR141716A, MJ08 (0.1 and 1 μmol/L) also significantly and dose-dependently reversed the WIN 55,212-2-induced inhibition of forskolin-stimulated cAMP accumulation, and intracellular cAMP contents at higher doses even exceeded that induced by forskolin alone; this suggests that MJ08 may also possess the inverse agonism property (Figure 5A). Neutral antagonists and inverse agonists can be well differentiated by the intracellular cAMP assay when the agonist is absent. Therefore, to further verify its functional inverse agonism, MJ08 was tested by the cAMP assays in both CHO-hCB_1 and CHO-hCB_2 cells. Figure 5B showed that 1 nmol/L of MJ08 can further increase cAMP levels in CHO-hCB_1 cells in the presence of 1 μmol/L forskolin, and the four-fold increase of the E_{max} (maximal effect) was obtained at 10 μmol/L with the EC_{50} of 78.6 nmol/L. However, an antagonizing effect of SR141716A was observed at 1 nmol/L under the same conditions. Inverse agonism was displayed above 10 nmol/L, and the E_{max} value was significantly lower than that of MJ08 (P<0.05), which corresponds to that of MJ08 at 1 μmol/L. The EC_{50} in this assay was 159.2 nmol/L, about two-fold that of MJ08. However, MJ08 and SR141716A did not influence intracellular cAMP in CHO-hCB_2 cells, even at 10 μmol/L. These data indicate that MJ08 possesses more potent intrinsic inverse agonistic activity to CB_1 receptors than SR141716A in the absence of the receptor agonist.

The effects of MJ08 on the contraction of guinea pig ileum and mouse vas deferens smooth muscle

At concentrations of 10^{-6} and 10^{-5} mol/L, SR141716A markedly increased the contraction intensity of guinea pig ileum smooth muscle, but its potency tended to decrease in a time-dependent manner (Figure 6A). The contraction frequency was only significantly increased at 10^{-5} mol/L at 60 and 120 s after the administration (Figure 6C). MJ08 demonstrated a similar promotion effect. It remarkably increased the contraction force and frequency. However, a more significant effect was observed on frequency, which was strikingly enhanced by MJ08 and without attenuation over time, even at 10^{-9} mol/L at 60 s (Figure 6B, 6D).

The electrically-stimulated vas deferens bioassay was reported to be a preferable approach for the determination of the antagonist potency[17]. Without pretreatment with the antagonist, the cannabinoid CB_1/CB_2 receptor agonist WIN 55,212-2 elicited a concentration-dependent inhibition of the twitches of mouse vas deferens (IC_{50}=0.44 nmol/L), and a nearly completed inhibition appeared at 10^{-6} mol/L (Figure 7A and B). At 10^{-7} mol/L, both SR141716A and MJ08 significantly antagonized the inhibitory effect of WIN 55,212-2 (P<0.01 for both) and induced dextral displacements of the agonist's dose-responsive curve with IC_{50} values of 0.206 and 3.31 μmol/L, respectively (Figure 7A). The competitive interaction between the antagonist and agonist signified that SR141716A and

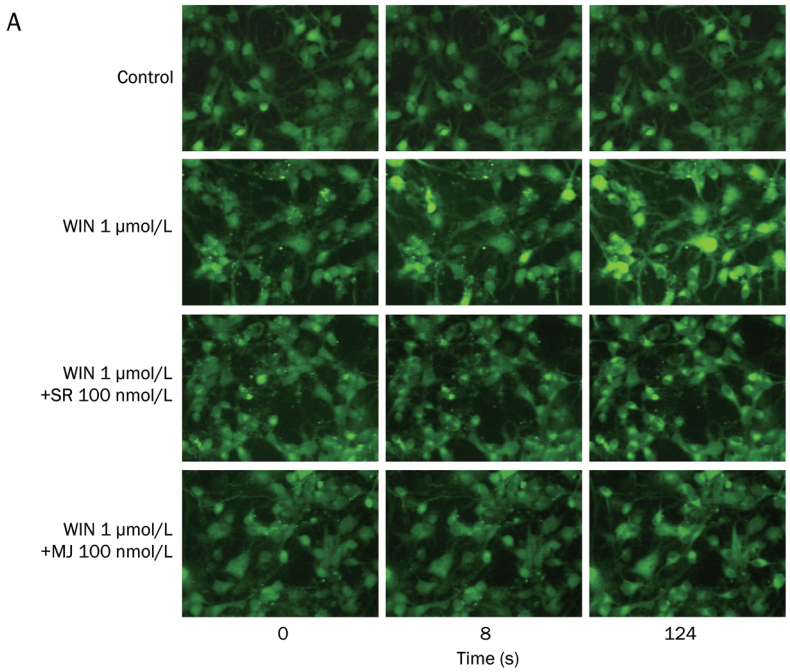

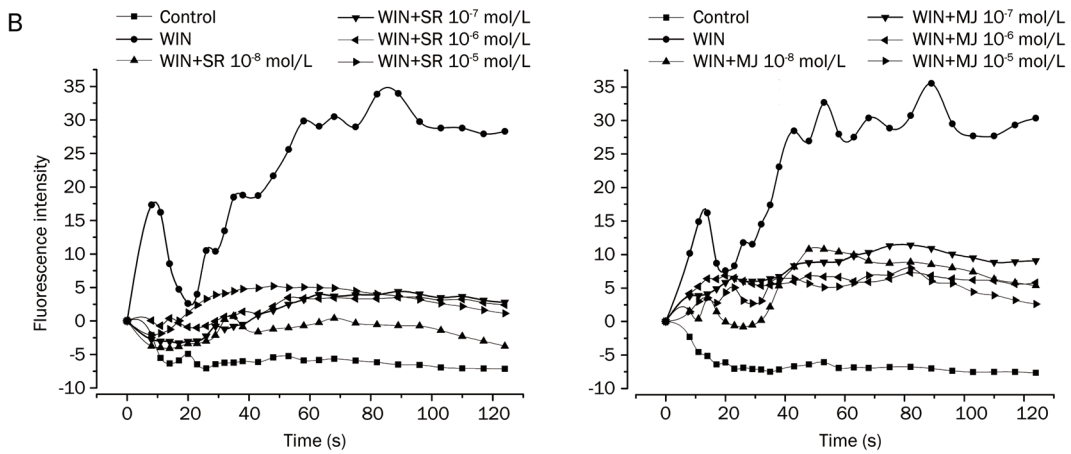

Figure 4. Intracellular free Ca^{2+} $[Ca^{2+}]_i$ measured by Ca^{2+} indicators in hippocampal cells. (A) Representative micrographs showing intracellular $[Ca^{2+}]_i$ in hippocampal cells. (B) The dynamic course of different concentrations of SR141716A (SR) or MJ08 (MJ) antagonizing WIN 55,212-2-induced elevation and pulse oscillation of intracellular $[Ca^{2+}]_i$.

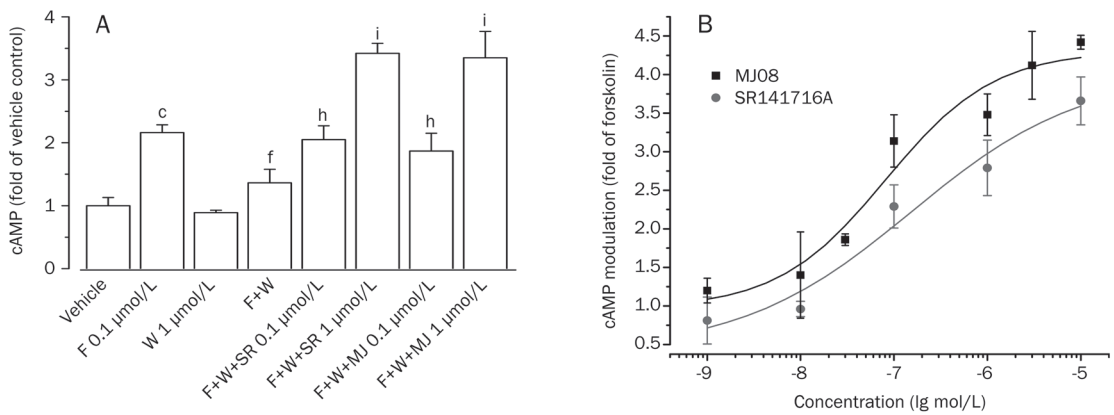

Figure 5. Effect of MJ08 on 1 μmol/L WIN 55,212-2 induced inhibition of cAMP accumulation stimulated by 0.1 μmol/L forskolin (A) and inverse agonism property of MJ08 in CHO-hCB_1 cells (B). The data were derived from a cell-based assay measuring the intracellular cAMP level with the LANCE cAMP kits. Fos (F), forskolin; WIN (W), WIN 55,212-2; values are the mean±SD. $^{c}P<0.01$ versus vehicle; $^{f}P<0.01$ versus forskolin; $^{h}P<0.05$, $^{i}P<0.01$ versus F+W.

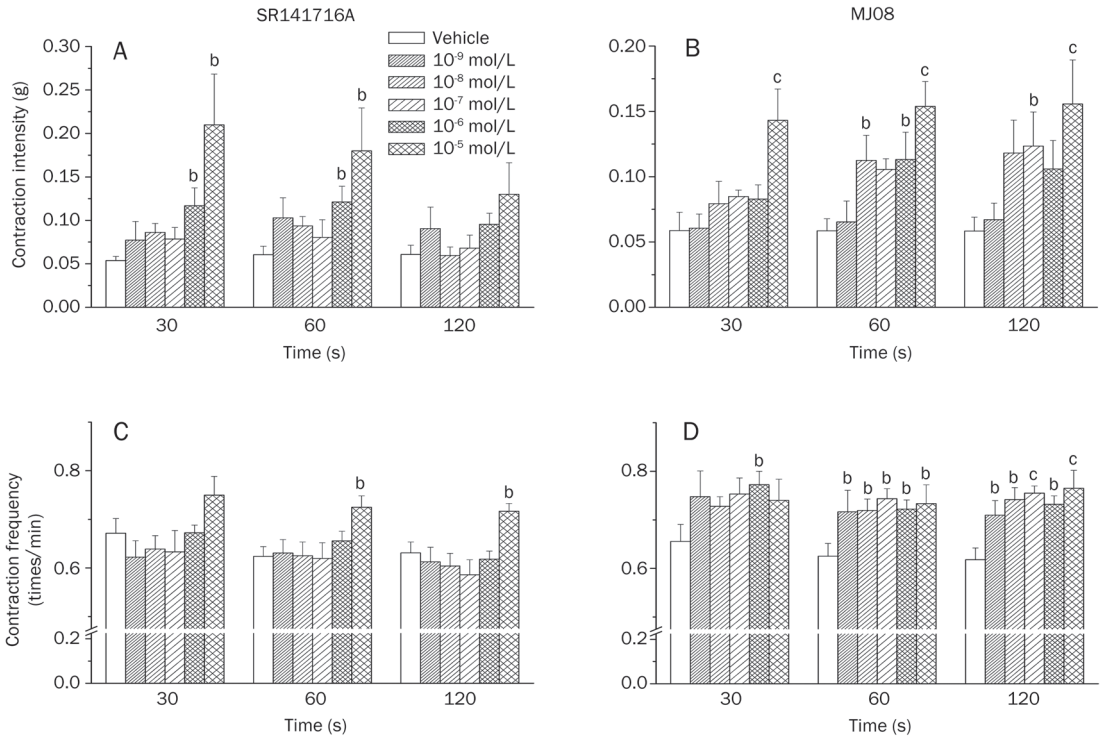

Figure 6. Effect of MJ08 and SR141716A on the contractions of the guinea pig ileum measured 2 min after compound administration. (A) and (B) SR141716A and MJ08 promoted the contraction amplitude. (C) and (D) SR141716A and MJ08 promoted the contraction frequency. Values are the mean±SD (n=6). ^bP<0.05, ^cP<0.01, versus vehicle.

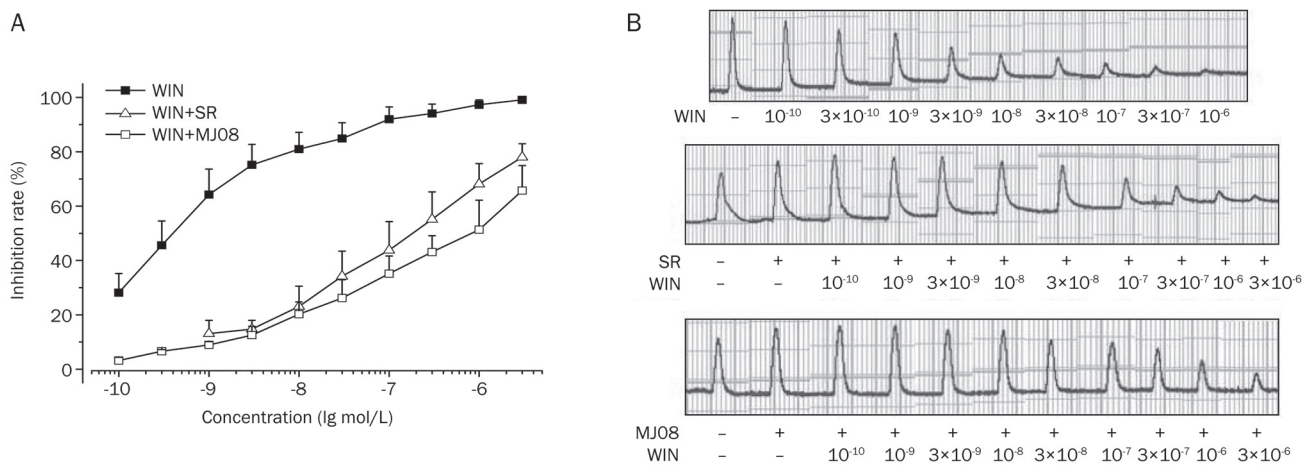

Figure 7. Effect of MJ08 and SR141716A on electrically-evoked twitches of the mouse vas deferens measured 30 min after drug administration. (A) The antagonistic effect on inhibiting the contraction induced by WIN 55,212-2. 10^{-7} mol/L SR141716A or MJ08 were added to the bath solutions 30 min before the agonist. (B) Representative records of mouse vas deferens' contraction. Values are the mean±SD (n=5–6).

MJ08 were competitive antagonists of WIN 55,212-2. The calculated pA_2 values for SR141716A and MJ08 were 9.47±0.73 and 10.29±1.05, respectively, indicating that the antagonistic potency of MJ08 was comparable to that of SR141716A. However, when the concentration of WIN 55,212-2 increased to 3 μmol/L, SR141716A (0.1 μmol/L) nearly lost its antagonism, whereas MJ08 (0.1 μmol/L) still preserved the contract ability of the muscle (Figure 7B). Furthermore, MJ08 and SR141716A both had trends towards promoting the electrically-evoked twitches of the mouse vas deferens even at a concentration of 1 nmol/L in absence of the agonist, although without apparent dose-response relationships (data not shown). These results indicate that MJ08 is not only a selective and competitive CB_1 receptor antagonist but also a cannabinoid CB_1 receptor

inverse agonist with equal or more potency than SR141716A.

Effect of MJ08 in DIO mice

Adverse effects on animal behavior or obvious signs of toxicity were not observed at any point in the experiment for any treatment group. The body weight of DIO mice was significantly higher than that of normal mice (32.02±0.83 g *vs* 24.3±0.29 g, $P<0.01$) at the beginning of the experiment. Sequential monitoring showed that both SR141716A and MJ08 decreased the body weight of the DIO mice throughout the experiment. On average, the body weight of MJ08-treated mice was relatively lower than that of SR141716A-treated mice during the first 25 d of treatment (Figure 8A). The impact of food intake was similar between the two testing compounds, which was reduced only in the first 10 d of administration and then relapsed to the consumption amount of the model group (Figure 8B). Meanwhile, both SR141716A and MJ08 dramatically decreased the hypertriglyceridemia ($P<0.05$) and the intra-abdominal adipose tissue ($P<0.05$) in DIO mice (Table 1). However, different from SR141716A, MJ08 also markedly lowered serum TC levels ($P<0.05$). Unexpectedly, the fasting blood glucose of the DIO mice was significantly increased by MJ08 after 35 d of treatment ($P<0.01$), yet it was decreased by SR141716A. However, the increased fasting blood glucose soon recovered to normal once MJ08 was withdrawn (the FBG were 5.04±1.09 mmol/L and 4.57±0.91 mmol/L at 5 and 10 d after discontinuation, respectively).

Table 1. Serum lipid and blood glucose analysis in DIO mice.

	Normal	Model	SR141716A	MJ08
TG (mmol/L)	1.25±0.12	1.81±0.22[c]	1.41±0.23[e]	0.77±0.07[f]
TC (mmol/L)	2.55±0.21	3.56±0.22[b]	3.34±0.12	2.26±0.56[e]
FBG (mmol/L)	4.58±0.72	5.77±0.66[b]	4.63±0.62[e]	13.28±2.12[f]

Compounds were given to the DIO mice by gavage for 40 d as described in the 'Methods' section. TG, triglyceride; TC, total cholesterol; FBG, fasting blood glucose; Values are the mean±SD of 10–12 animals per group. [b]$P<0.05$, [c]$P<0.01$ versus normal, [e]$P<0.05$, [f]$P<0.01$ versus model.

Discussion

As a new chemical entity targeting the cannabinoid CB_1 receptor, the pharmacological properties of MJ08 were evaluated in various *in vitro* and *in vivo* experimental systems in the present study. MJ08 exhibited selective and potent antagonism to the cannabinoid CB_1 receptor. Although *in vitro* competitive binding analysis revealed that its affinity was lower than that of SR141716A at the molecular level, the cellular cannabinoid receptor activation and transposition assay, $[Ca^{2+}]_i$ and cAMP measurements in mammalian cells functionally demonstrated the equivalent efficiency of MJ08 in selectively antagonizing the cannabinoid CB_1 receptor compared with SR141716A. Furthermore, more potent or equivalent cannabinoid CB_1 recep-

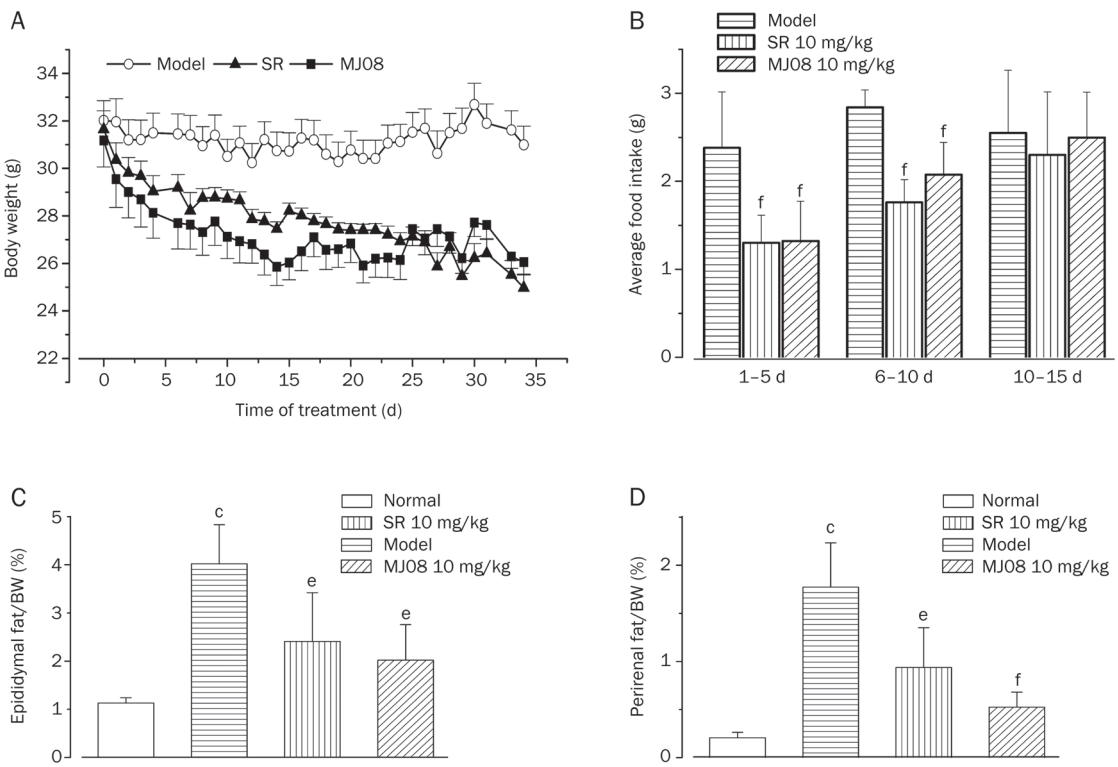

Figure 8. Effects of MJ08 on body weight, food intake and white adipose weight in DIO mice. (A) Body weight change, which was calculated for individual mouse and then averaged. (B) Food intake, which was calculated every day and then averaged. (C) Epididymal fat weight and (D) Perirenal fat weight index. SR, SR141716A. Values are the mean±SD of 10–12 animals per group. [c]$P<0.01$ versus normal; [e]$P<0.05$, [f]$P<0.01$ versus model.

tor inverse agonistic effects of MJ08 relative to SR141716A were revealed by directly increasing intracellular cAMP and promoting the contraction of guinea pig ileum and mouse vas deferens smooth muscles in isolated tissues at *in vitro* and *ex vivo* tests. Additionally, the results from DIO mice further confirmed its oral bioactivity and *in vivo* potency.

Receptor competitive binding analysis is a classical method for the evaluation of binding characteristics of ligands. Rat cerebellum and spleen (CB_1 and CB_2 receptor-rich tissues, respectively) membrane preparations were used here to analyze the receptor binding activity and characteristics of MJ08. The radioligand displacement curves showed that, similar to the well-known cannabinoid CB_1 receptor selective antagonist SR141716A, MJ08 dose dependently displaced [^{3}H]-SR141716A binding to rat cerebellum membranes, and its selectivity to the CB_1 receptor against the CB_2 receptor was more than 100-fold. However, the binding affinity of MJ08 to the CB_1 receptor was about 500–1000 times less potent than that of SR141716A. It was noted that the slope of the displacement curve was steeper for SR141716A than MJ08, SR141716A exhibited a sharp competitive effect from 10^{-11} to 10^{-9} mol/L, but MJ08 gradually inhibited [^{3}H]-SR141716A's binding from 10^{-14} to 10^{-4} mol/L. This result indicates that the binding mode of MJ08 is somewhat different from that of SR141716A. MJ08 showed more potent affinity to the CB_1 receptor at a lower concentration in the molecular test.

Recently, functional assays of receptor activation in living cells were widely used in screening and in the evaluation of novel ligands for receptors. Compared with molecular-level assays, living cell assays reflect both receptor binding and the functional activity of a ligand. In this study, the CB_1/CB_2 redistribution assay (commercial EGFP-CB_1/CB_2_U2OS cell model, specially designed for screening of agonists or antagonists of cannabinoid CB_1/CB_2 receptor with High Content Assay) was used. Both MJ08 and SR141716A antagonized the internalization of the membrane-located CB_1-EGFP fusion protein induced by the agonist (WIN 55,212-2) without significant impact to WIN 55,212-2-induced internalization of the membrane-located CB_2-EGFP fusion protein; this signified that they selectively antagonized the cannabinoid CB_1 receptor activation in the cellular model. Moreover, in contrast to the receptor binding test at the molecular level, MJ08 displayed an equivalent antagonistic effect to SR141716A in the living cell assay suggesting that MJ08 may be more suitable for binding to CB_1 receptor in living cells.

Intracellular Ca^{2+} and adenylyl cyclase are considered to be important signaling molecules of cannabinoid CB_1 receptors[20–22]. To confirm the functional antagonistic activities of MJ08 toward the cannabinoid CB_1 receptor, the effects of MJ08 on cannabinoid CB_1 receptor agonist-induced responses, including intracellular Ca^{2+} ($[Ca^{2+}]_i$) and cAMP content, were observed in hippocampal neurons (abundance of CB_1 receptor) and CHO-hCB_1 cells, respectively. It has been documented that the cannabinoid CB_1/CB_2 receptor agonist WIN 55,212-2 increases intracellular Ca^{2+} via CB_1 coupling to $G_{q/11}$ G proteins[20]. In our experiment, similar to SR141716A and other reported antagonists[23, 24], the increase of $[Ca^{2+}]_i$ induced by WIN 55,212-2 was absent in hippocampal neurons after the incorporation of MJ08 (from 10^{-8} to 10^{-5} mol/L) with comparable efficiency to SR141716A. Additionally, as CB-coupled $G_{i/o}$ proteins, cAMP is the key molecule in reflecting cannabinoid CB_1 receptor activation or antagonism. Our results revealed that MJ08 significantly reversed WIN 55,212-2-induced inhibition of forskolin-stimulated cyclic AMP accumulation in a dose-dependent manner in CHO-hCB_1 cells. Taken together, the $[Ca^{2+}]_i$ and cAMP assays demonstrated that MJ08 acts as a cannabinoid CB_1 receptor antagonist of second messenger signaling in mammalian cells with similar efficacy to SR141716A. Additionally, both SR141716A and MJ08 significantly antagonized the inhibition by WIN 55,212-2 of the contraction of mouse vas deferens smooth muscle with electrical stimulation. The relatively higher pA_2 value of MJ08 than SR141716A in this assay indicates its stronger or comparable antagonism. Therefore, the above results suggest that MJ08 is a potent and highly selective cannabinoid CB_1 receptor antagonist.

On the other hand, MJ08 also displayed inverse agonist properties, *ie*, inhibiting CB_1 receptor activity in the absence of an agonist, which includes directly increasing cAMP accumulation in CHO-hCB_1 cells and promoting contractions of isolated preparations of guinea pig ileum and mouse vas deferens. In CHO-hCB_1 cells, MJ08 not only enhanced cAMP accumulation in the presence of forskolin (its efficacy was about 5 to 10 times of SR141716A) but also markedly evoked the increase of intracellular cAMP in the absence of forskolin at higher concentrations. The efficacy of 1 μmol/L of MJ08 also corresponds to the efficacy of 10 μmol/L of SR141716A (data not shown). This result indicates that MJ08 is a more potent inverse agonist of the cannabinoid CB_1 receptor than SR141716A. SR141716A has been shown to enhance the contraction force of guinea pig ileum smooth muscle in isolated guinea pig ileum tests, but we found that it displayed a time-dependent decreasing trend, with the maximum effect at 30 s. The contraction frequency was increased 1.16 times by 10^{-5} mol/L SR141716A at 60 s, whereas MJ08 significantly enhanced both the contraction force and frequency under the same conditions without attenuation with time. The contraction frequency was significantly increased by MJ08 even at 10^{-9} mol/L at 60 s and reached to 1.24 times with 10^{-5} mol/L MJ08. In the isolated mouse vas deferens experiment, similar to known inverse agonists, SR141716A or and MJ08 also both promoted the electrically-evoked contractions of the mouse vas deferens at concentrations ranging from 10^{-10} to 10^{-6} mol/L, although the contraction amplitude was only slightly increased. This phenomenon corresponded with the point that the inverse agonist exhibited greater potency in producing opposing effects induced by the cannabinoid CB_1 receptor agonists[9]. As MJ08 did not interact directly with the muscarinic receptor or adrenergic receptor α (data not shown), the mechanisms by which MJ08 promotes muscle contraction and the electrically-evoked contractions of the mouse vas deferens are likely to be cannabinoid CB_1 receptor mediated rather than through non-specific interactions with other receptors. Therefore, MJ08 is a selective antagonist

and inverse agonist of the cannabinoid CB_1 receptor.

Previously, an increasing body of evidence has demonstrated the roles of the endogenous cannabinoid system (ECs), including CB_1 receptor, endocannabinoids, and related metabolic enzymes, in the regulation of food consumption and body weight in animals and humans[25, 26]. Hyperphagic effects are closely related to the hyperactivity of the ECs, and thus the endocannabinoid system had been a valuable therapeutic target for obesity[27, 28]. Correspondingly, the cannabinoid CB_1 receptor antagonist had been shown to attenuate food intake and increase body energy expenditure in DIO mice and genetic obese animals[26, 29, 30]. Thus, in the present study, high-fat diet-induced obese mice were used to evaluate the *in vivo* pharmacodynamic effects of MJ08. Compared with SR141716A, chronic treatment with MJ08 displayed a higher efficacy in inducing weight loss (although without statistical difference), correcting dyslipidemia, and in lowering retroperitoneal adipose tissue in DIO mice. This effect suggests that MJ08 is an orally active cannabinoid CB_1 receptor antagonist. Additionally, a significant increase in FBG in DIO mice by MJ08 was surprisingly found after 40 d of treatment; however, the FBG values returned to normal soon after compound withdrawal. Similarly, during the preparation of our manuscript, another CB_1 receptor inverse agonist AM251 was also reported to increase the serum glucose level in 24-h fasted obese rats, but the author attributed it to heavy insulin resistance produced by hypercaloric diets[31]. However, this conclusion seems inappropriate because the serum insulin and glucose levels of the obese rats were both lower than that of the standard diet rats; the levels of the other two hormones (adiponectin and leptin) relating to glucose homeostasis were also comparable to the non-obese rats in their study[31]. Here, we considered two reasons may be responsible for this FBG increasing effect of a cannabinoid CB_1 receptor antagonist/inverse agonist MJ08: first, it may be related to the activation of the sympathoadrenal system and the release of noradrenaline, which had been recently demonstrated in the diet-induced obese rats by Molhoj *et al*[32]; and secondly, MJ08 itself markedly increased intracellular cAMP, which may have promoted gluconeogenesis and/or glycogenolysis via increasing phosphorylation of phosphoenolpyruvate carboxykinase (PEPCK) and glucose-6-phosphate (G6P), respectively. Therefore, the more potent inverse agonistic characteristic of MJ08 may be partially related to this FBG increasing effect, although the detailed mechanisms still need further study. However, if this is a category response of some CB_1 receptor inverse agonists can't be completely excluded.

Additionally, it was also observed that the bioactivities of MJ08 became more potent as the experimental system advanced from the *in vitro* molecular level to the cellular level and then to the *in vivo* experiments; a significant enhancement was particularly seen between the molecular and cellular systems. First, we think that the incomplete, identical binding modes of MJ08 and SR141716A and the minute conformational change of the cannabinoid CB_1 receptor in cell membrane preparations and living cells may be responsible for the phenomenon. When considering the cannabinoid CB_1 receptor to be a well-defined but dynamic receptor protein, changes in the receptor steric conformation under different circumstances will likely affect its response to exogenous ligands. Secondly, the complex pharmacological regulations depend on the particular profile of the used ligand; the minute difference in structure of MJ08 may be key because the compound's conformation or conformational freedom is crucial for the receptor's affinity, selectivity, and efficacy[33]. Different small-molecule antagonists and inverse agonists bind in very different modes into the funnel of the main ligand-binding pocket GPCRs. In fact, MJ08 has a different amide in the 3 site of the pyrazole compared with SR141716A; when calculated with ChemOffice 2008, the LogP of MJ08 (7.04) is higher than that of SR141716A (6.28). This indicates that SR141716A is more hydrophilic than MJ08 and may thus display higher affinity at the *in vitro* molecular level, which is also confirmed by their different behaviors in the thin-layer chromatography assay. Certainly, the involved mechanisms need to be studied in further detail.

In conclusion, MJ08 is a structurally novel, potent and selective cannabinoid CB_1 receptor antagonist with many specialized pharmacologic effects on different experimental systems. It exhibits potent inverse agonism and *in vivo* bioactivity. MJ08 may be used as a novel pharmacological tool to characterize the versatile nature and complexity of the cannabinoid signaling pathway.

Acknowledgements

We gratefully acknowledge Prof Hua LI for her critical reading of the manuscript. This work was funded by Chinese National Hi-tech Research and Development Grants '863' (No 2003AA235010), the National Key Technologies R&D Program for New Drug of China (No 2009ZX09301-002) and the National Science and Technology Major Project of the Ministry of Science and Technology of China (No 2009ZX09501-031).

Author contribution

Wei CHEN analyzed the data, wrote the manuscript and performed the experiments; Cheng XU analyzed the data and performed the experiments; Li-li WANG and Song LI designed the research and revised the paper; Hong-ying LIU, Long LONG, Wei ZHANG, Zhi-bing ZHENG, and Yun-de XIE performed the experiments.

Abbreviations

CHO, Chinese hamster ovary; DMSO, dimethyl sulphoxide; CP55,940, {5-(1,1-dimethylheptyl)-2-[5-hydroxy-2-(3-hydroxypropyl) cyclohexyl] phenol}; WIN 55,212-2, {[2, 3-Dihydro-5-methyl-3-[(morpholinyl)methyl]pyrrolo[1,2,3-de]-1,4-benzoxazinyl]-(1-naphthalenyl)methanone}; SR141716A, [N-Piperidino-5-(4-chlorophenyl)-1-(2, 4-dichlorophenyl)-4-methylpyrazole-3-carboxamide].

References

1 Xie S, Furjanic MA, Ferrara JJ, McAndrew NR, Ardino EL, Ngondara A, *et al*. The endocannabinoid system and rimonabant: a new drug

with a novel mechanism of action involving cannabinoid CB1 receptor antagonism — or inverse agonism — as potential obesity treatment and other therapeutic use. J Clin Pharm Ther 2007; 32: 209–31.
2 Janero DR, Makriyannis A. Cannabinoid receptor antagonists: pharmacological opportunities, clinical experience, and translational prognosis. Expert Opin Emerg Drugs 2009; 14: 43–65.
3 Pertwee RG. Emerging strategies for exploiting cannabinoid receptor agonists as medicines. Br J Pharmacol 2009; 156: 397–411.
4 Di Marzo V, Szallasi A. Rimonabant in rats with a metabolic syndrome: good news after the depression. Br J Pharmacol 2008; 154: 915–7.
5 Scheen AJ, Paquot N. Use of cannabinoid CB1 receptor antagonists for the treatment of metabolic disorders. Best Pract Res Clin Endocrinol Metab 2009; 23: 103–16.
6 Nisoli E, Carruba MO. Emerging aspects of pharmacotherapy for obesity and metabolic syndrome. Pharmacol Res 2004; 50: 453–69.
7 Lee HK, Choi EB, Pak CS. The current status and future perspectives of studies of cannabinoid receptor 1 antagonists as anti-obesity agents. Curr Top Med Chem 2009; 9: 482–503.
8 Receveur JM, Murray A, Linget JM, Norregaard PK, Cooper M, Bjurling E, *et al*. Conversion of 4-cyanomethyl-pyrazole-3-carboxamides into CB1 antagonists with lowered propensity to pass the blood-brain-barrier. Bioorg Med Chem Lett 2010; 20: 453–7.
9 Pertwee RG. Inverse agonism and neutral antagonism at cannabinoid CB1 receptors. Life Sci 2005; 76: 1307–24.
10 Fong TM, Heymsfield SB. Cannabinoid-1 receptor inverse agonists: current understanding of mechanism of action and unanswered questions. Int J Obes (Lond) 2009; 33: 947–55.
11 Rinaldi-Carmona M, Barth F, Heaulme M, Shire D, Calandra B, Congy C, *et al*. SR141716A, a potent and selective antagonist of the brain cannabinoid receptor. FEBS Lett 1994; 350: 240–4.
12 Shearman LP, Stribling DS, Camacho RE, Rosko KM, Wang JY, Tong S, *et al*. Characterization of a novel and selective cannabinoid CB1 receptor inverse agonist, Imidazole 24b, in rodents. Eur J Pharmacol 2008; 579: 215–24.
13 Sink KS, McLaughlin PJ, Wood JA, Brown C, Fan P, Vemuri VK, *et al*. The novel cannabinoid CB1 receptor neutral antagonist AM4113 suppresses food intake and food-reinforced behavior but does not induce signs of nausea in rats. Neuropsychopharmacology 2008; 33: 946–55.
14 Chen W, Tang H, Liu H, Long L, Gong Z, Zheng J, *et al*. Novel selective antagonist of the cannabinoid CB1 receptor, MJ15, with prominent anti-obesity effect in rodent models. Eur J Pharmacol 2010; 637: 178–85.
15 Jagerovic N, Hernandez-Folgado L, Alkorta I, Goya P, Navarro M, Serrano A, *et al*. Discovery of 5-(4-chlorophenyl)-1-(2,4-dichlorophenyl)-3-hexyl-1h-1,2,4-triazole, a novel *in vivo* cannabinoid antagonist containing a 1,2,4-triazole motif. J Med Chem 2004; 47: 2939–42.
16 Pertwee RG, Joe-Adigwe G, Hawksworth GM. Further evidence for the presence of cannabinoid CB1 receptors in mouse vas deferens. Eur J Pharmacol 1996; 296: 169–72.
17 Christopoulos A, Coles P, Lay L, Lew MJ, Angus JA. Pharmacological analysis of cannabinoid receptor activity in the rat vas deferens. Br J Pharmacol 2001; 132: 1281–91.
18 Chen W, Zhou XB, Liu HY, Xu C, Wang LL, Li S. P633H, a novel dual agonist at peroxisome proliferator-activated receptors alpha and gamma, with different anti-diabetic effects in *db/db* and KK-Ay mice. Br J Pharmacol 2009; 157: 724–35.
19 Hsieh C, Brown S, Derleth C, Mackie K. Internalization and recycling of the CB_1 cannabinoid receptor. J Neurochem 1999; 73: 493–501.
20 Lauckner JE, Hille B, Mackie K. The cannabinoid agonist WIN55,212-2 increases intracellular calcium via CB1 receptor coupling to Gq/11 G proteins. Proc Natl Acad Sci U S A 2005; 102: 19144–9.
21 Wang H, Dey SK, Maccarrone M. Jekyll and hyde: two faces of cannabinoid signaling in male and female fertility. Endocr Rev 2006; 27: 427–48.
22 Bosier B, Muccioli GG, Hermans E, Lambert DM. Functionally selective cannabinoid receptor signalling: therapeutic implications and opportunities. Biochem Pharmacol 2010; 80: 1–12.
23 Drysdale AJ, Ryan D, Pertwee RG, Platt B. Cannabidiol-induced intracellular Ca^{2+} elevations in hippocampal cells. Neuropharmacology 2006; 50: 621–31.
24 Sugiura T, Kodaka T, Kondo S, Tonegawa T, Nakane S, Kishimoto S, *et al*. 2-arachidonoylglycerol, a putative endogenous cannabinoid receptor ligand, induces rapid, transient elevation of intracellular free Ca^{2+} in neuroblastoma X glioma hybrid NG108-15 cells. Biochem Biophys Res Commun 1996; 229: 58–64.
25 Di Marzo V, Capasso R, Matias I, Aviello G, Petrosino S, Borrelli F, *et al*. The role of endocannabinoids in the regulation of gastric emptying: alterations in mice fed a high-fat diet. Br J Pharmacol 2008; 153: 1272–80.
26 Hildebrandt AL, Kelly-Sullivan DM, Black SC. Antiobesity effects of chronic cannabinoid CB1 receptor antagonist treatment in diet-induced obese mice. Eur J Pharmacol 2003; 462: 125–32.
27 Di Marzo V. The endocannabinoid system: its general strategy of action, tools for its pharmacological manipulation and potential therapeutic exploitation. Pharmacol Res 2009; 60: 77–84.
28 Di Marzo V, Matias I. Endocannabinoid control of food intake and energy balance. Nat Neurosci 2005; 8: 585–9.
29 Griffith DA, Hadcock JR, Black SC, Iredale PA, Carpino PA, DaSilva-Jardine P, *et al*. Discovery of 1-[9-(4-chlorophenyl)-8-(2-chlorophenyl)-9H-purin-6-yl]-4-ethylaminopiperi dine-4-carboxylic acid amide hydrochloride (CP-945,598), a novel, potent, and selective cannabinoid type 1 receptor antagonist. J Med Chem 2009; 52: 234–7.
30 Di Marzo V, Goparaju SK, Wang L, Liu J, Batkai S, Jarai Z, *et al*. Leptin-regulated endocannabinoids are involved in maintaining food intake. Nature 2001; 410: 822–5.
31 Rivera P, Romero-Zerbo Y, Pavon FJ, Serrano A, Lopez-Avalos MD, Cifuentes M, *et al*. Obesity-dependent cannabinoid modulation of proliferation in adult neurogenic regions. Eur J Neurosci 2011; 33: 1577–86.
32 Molhoj S, Hansen HS, Schweiger M, Zimmermann R, Johansen T, Malmlof K. Effect of the cannabinoid receptor-1 antagonist rimonabant on lipolysis in rats. Eur J Pharmacol 2010; 646: 38–45.
33 Thomas BF, Zhang Y, Brackeen M, Page KM, Mascarella SW, Seltzman HH. Conformational characteristics of the interaction of SR141716A with the CB1 cannabinoid receptor as determined through the use of conformationally constrained analogs. AAPS J 2006; 8: E665–71.

Acta Pharmacologica Sinica (2011) 32: 1159–1164
 1671-4083/11 $32.00
www.nature.com/aps

Original Article

Negative regulation of cyclin D3 expression by transcription factor c-Ets1 in umbilical cord hematopoietic cells

Fan-kai MENG, Han-ying SUN, Xi-you TAN[§], Chun-rui LI, Jian-feng ZHOU, Wen-li LIU*

Department of Hematology, Tongji Hospital, Tongji Medical College, Huazhong University of Science and Technology, Wuhan 430030, China

Aim: To investigate the role of transcription factor c-Ets1 in cyclin D3 expression and its effects on the proliferation of umbilical cord hematopoietic cells.
Methods: Cyclin D3 promoter deletion constructs were generated and transfected into $CD34^+$ cells. Dual luciferase reporter assays and TFSEARCH software were used to identify negative regulatory domains and to predict putative transcription factors involved in cyclin D3 downregulation. Expression of c-Ets1 in $CD34^+$ cells was detected using electrophoretic mobility shift and super shift assays. Point mutants of c-Ets1 binding sites were constructed. The wild-type c-Ets1 and the mutant promoter constructs were co-transfected into $CD34^+$ cells to determine the promoter activity. The impact of c-Ets1 expression on the proliferation of $CD34^+$ cells was assessed using MTT assay.
Results: Nine cyclin D3 promoter deletion constructs were generated. A negative regulatory domain containing c-Ets1 binding sites was identified between -439 bp and -362 bp. Transfection of the promoter deletion constructs containing mutant c-Ets1 binding sites enhanced cyclin D3 promoter activity. However, the opposite results were observed when $CD34^+$ cells were co-transfected with wildtype c-Ets1 and its promoter deletion constructs. The overexpression of c-Ets1 could suppress cyclin D3 mRNA and protein levels. In addition, it inhibits the proliferation of $CD34^+$ cells.
Conclusion: c-Ets1 functions as a negative transcription factor, down-regulating the expression of cyclin D3, which leads to inhibition of $CD34^+$ cell proliferation.

Keywords: transcription factor c-Ets1; cyclins; hematopoietic stem cells; $CD34^+$ cells; gene regulation; cell cycle; point mutation

Acta Pharmacologica Sinica (2011) 32: 1159–1164; doi: 10.1038/aps.2011.41; published online 15 Aug 2011

Introduction

Hematopoiesis is a continuous process of blood production that begins with the self-renewal and differentiation of hematopoietic stem cells (HSCs). HSCs are mainly in a quiescent state; only small amounts of HSCs enter the cell cycle to proliferate and differentiate into mature blood cells. During this process, many regulators control the balance between cycling and quiescence as well as between proliferation and differentiation. When this balance is broken, hematological diseases result. One example of this is leukemia, whereby leukemic cells become transformed, gaining the ability to proliferate but losing the ability to effectively differentiate. The molecular regulators of this balancing act are the subject of intense study in the field of hematopoiesis[1].

The cell cycle is controlled by cyclins, cyclin-dependent kinases (CDKs) and CDK inhibitors. Cyclin D is the first cyclin expressed in the cell cycle after stimulation by mitogenic signals. The complex of cyclin D and CDK 4/6 stimulates cells to enter the cell cycle and complete the G_1/S phase transition. Once a cell passes this checkpoint, the cell can go through the whole cell cycle and division irrevocably[2, 3]. Cyclin E is the other cyclin involved in the G_1/S phase transition. However, constitutive expression of cyclin E2 cannot bypass arrest at the G_1 phase induced by cyclin D1 degradation[4]. This indicates that cyclin D is the most important cyclin in the cell cycle. The dominant isoform, cyclin D3, is uniquely required for the proliferation of HSCs and is regulated mainly at the transcriptional level in these cells[2, 5]. Transcription factors bind to the promoter of cyclin D3, regulating the expression of the cyclin

[§] Now in *Department of Bone Marrow Transplantation, Shanghai Daopei Hospital, Shanghai 200240, China*.
*To whom correspondence should be addressed.
E-mail liuwenlitj@163.com
Received 2010-12-24 Accepted 2011-04-13

D3 gene. Both positive and negative regulators could theoretically be involved in this regulation[6]. However, most studies have focused on the positive regulators, with characterization of negative regulators seldom reported in the literature.

The transcription factor c-Ets1 is a member of the Ets family of transcription factors, commonly involved in the regulation of development, differentiation and proliferation[7]. c-Ets1 is expressed in hematopoietic cells and contributes to their cellular differentiation. It plays an essential role in lymphoid cell differentiation and also promotes megakaryocytic and early erythroid differentiation[8-12]. In general, the proliferative ability of hematopoietic cells declines along with the cell's differentiation to a more mature cell stage. Because c-Ets1 promotes differentiation, it may also limit the proliferation of hematopoietic cells. We found a negative regulatory region in the promoter of cyclin D3 and a c-Ets1-binding motif in this region. As previously discussed, c-Ets1 may play a negative role in the expression of cyclin D3.

Umbilical cord HSCs possess common characteristics of human HSCs and have the advantages of being easily procured with a low risk to donors. For these reasons, these cells have become an alternative source of HSCs for experimental and clinical studies[13]. In these experiments, umbilical cord HSCs were utilized to explore the underlying mechanism in the regulation of cyclin D3 by c-Ets1.

Materials and methods

Cell culture

Human $CD34^+$ cells were obtained from umbilical cord blood of healthy donors. $CD34^+$ cells were isolated using MidiMACS technology (Miltenyi Biotec, Germany) according to the manufacturer's instructions. Briefly, 50 mL of umbilical cord blood was treated with Ficoll-Paque™ PLUS to isolate mononuclear cells. To prevent coagulation, 0.6% ACD-A was added. $CD34^+$ cells were purified twice with the MidiMACS. The purified cells were seeded at 1×10^5 cells/mL in 24-well plates and maintained in Iscove's modified Dulbecco's medium (IMDM) supplemented with 25% fetal bovine serum (FBS), penicillin (100 IU/mL), stem cell factor (SCF) (100 ng/mL), FLt3-L (100 ng/mL), IL-3 (50 ng/mL), IL-6 (50 ng/mL) and thrombopoietin (TPO) (2 U/mL) in a humidified atmosphere at 5% CO_2 and 37 °C. The medium was refreshed on the third day and cells were harvested on the sixth day. The harvested cells were utilized for all subsequent experiments. After harvesting, cells were stained with mouse anti-CD34-FITC antibodies, with mouse IgG_1 (BD Biosciences, USA) used as a negative control. Cells were incubated at 4°C in the dark for 30 min, washed with PBS, fixed with 1% paraformaldehyde and subsequently analyzed by flow cytometry (Becton Dickinson, USA) to measure the proportion of $CD34^+$ cells present. The results were obtained from three independent samples.

Plasmid constructs

To generate the cyclin D3 promoter deletion constructs, the restriction endonuclease sites of the full-length sequence of human cyclin D3 promoter were predicted by Webcutter 2.0 software. Using human blood lymphocyte genomic DNA as a template, cyclin D3 promoter deletions of different lengths were amplified by polymerase chain reaction (PCR). The primers utilized were as follows: sense primers (containing *Kpn* I sites) were:

PA1 (*Kpn* I -1042): 5′-CGG GGT ACC ggg agg tgg aag aaa tgc-3′,

PA2 (*Kpn* I -924): 5′-CGG GGT ACC ggg ctt gtc caa acc tag-3′,

PA3 (*Kpn* I -764): 5′-CGG GGT ACC gag agt ctg cat ttc taa cc-3′,

PA4 (*Kpn* I -686): 5′-CGG GGT ACC ggt gta gaa cac aga atc tg-3′,

PA5 (*Kpn* I -549): 5′-CGG GGT ACC gca gcg ttc act aag aac-3′,

PA6 (*Kpn* I -436): 5′-CGG GGT ACC att gtt tcc tgg gtg act ag-3′,

PA7 (*Kpn* I -380): 5′-CGG GGT ACC aag ttc tct gca ccc ggt gg-3′,

PA8 (*Kpn* I -262): 5′-CGG GGT ACC gct cag cca acc ctt tcc-3′ and

PA9 (*Kpn* I -195): 5′-CGG GGT ACC att cca cgg ttg cta cat c-3′;

and the antisense primer (containing *Smal* I sites) was

PB (~ + 2): 5′-TCC CCC GGG ata ctc ggg cag cga aca-3′.

PCR conditions (Table 1) varied according to expected product lengths. PCR fragments were inserted into pGEM-T Easy vectors (Promega, USA) between the *Kpn* I and *Bam* I sites. Subcloning of the amplified fragments into the luciferase expression vector pGL3-Basic (Promega, USA) was performed via *Kpn* I and *Bgl* II sites (*Bam* I and *Bgl* II sites are compatible). The constructs were designated as pD3-Δ, where Δ refers to the number of base pairs in the upstream 5′-flanking sequence with respect to the start codon of cyclin D3.

Table 1. PCR conditions for application of various promoter deletion fragments.

Promoter sequence	Denaturation	Anneal	Extension	Cycles
pA1B, pA2B	94 °C 1 min	55 °C	72 °C 2 min	30
pA3B	the first cycle 5 min	1 min	the last cycle 8 min	
pA4B, pA5B	94 °C 1 min	56 °C	72 °C 2 min	30
pA6B	the first cycle 5 min	1 min	the last cycle 8 min	
pA7B, pA8B	94 °C 1 min	56 °C	72 °C 1 min	30
pA9B	the first cycle 5 min	45 s	the last cycle 8 min	

pA1B is the full-length promoter. *Kpn* I and *Smal* I sites are respectively included in sense and anti-sense primers.

Liposomal transient transfection and luciferase assay

The harvested cells (5×10^5 cells/mL) were transiently transfected using Lipofectamine 2000 (Invitrogen, USA) according to the manufacturer's instructions. Briefly, cells were plated in 24-well plates in IMDM with 15% FBS and transfected using

0.8 μg of the luciferase reporter plasmid (pD3-Δ or pD3-Basic vector), with 0.1 ng of pRL-CMV as an internal control in each well. The cells were harvested 36 h later, and lysates were assayed with the dual luciferase reporter system (Promega, USA) on a SIRIUS Luminometer V3.1 (Berthold, Germany) to determine the promoter activity. The negative regulatory domain was identified based on the results from five independent experiments.

Electrophoretic mobility shift assay (EMSA)

c-Ets1 was selected as a candidate transcription factor that might bind the negative regulatory domain of cyclin D3 with the assistance of TFSEARCH 1.3v software[14]. Nuclear extracts were prepared to determine the expression of c-Ets1 in $CD34^+$ cells using an EMSA kit (Panomics, USA) according to the manufacturer's instructions. The DNA sequence of the c-Ets1 probe was 5′-GGA GGA GGG CTG CTT GAG GAA GTA TAA GAA T-3′. Nuclear extracts (15 μg) were co-incubated with biotin-labeled specific DNA probes and c-Ets1 antibodies (Santa Cruz, CA), subjected to 6% SDS-PAGE and transferred to membranes. Bands were visualized with ECL (Amersham, UK).

Point mutant constructs

The core-binding motif of c-Ets1 is GAAG (CTTC on the antisense chain). To confirm that c-Ets1 could bind to the CTTC motif present in the cyclin D3 promoter, a point mutant construct was generated by PCR with primers P1 (5′-GGG AAG CTT TTT GCA AAA GCC TAG GCC TCC-3′) and P2 (5′-TTT GGT ACC ATT GTT CTT CGG GTG ACT AGA GTC CGA GAA G-3′). *Hind* III and *Kpn* I restriction sites are underlined and were designed in order to convert the sequence TCCT to CTTC (dotted). Using human blood lymphocyte genomic DNA as a template, PCR was conducted as follows: 94°C for 5 min (first cycle), followed by 30 cycles of 94°C for 1 min, 55°C for 1 min and 72°C for 1 min, followed by a final extension at 72°C for 10 min. PCR products were inserted into pUcm-T vectors for amplification and sub-cloned into the pGL3-Basic vector. $CD34^+$ cells were transfected either with a promoter construct or its corresponding mutant and incubated for 36 h before luciferase activity was determined.

Western blot

$CD34^+$ cells were harvested 36 h after being transfected with either pSG5-Ets1 or pSG5 vectors. The pSG5-Ets1 expression vector was kindly provided by Prof J CHEN of Tzu Chi University, Taiwan, China. Total protein was extracted, subjected to SDS-PAGE, transferred to the membrane and successively incubated with cyclin D3 and β-actin (internal control) antibodies followed by corresponding secondary antibodies. Cyclin D3 and β-actin bands were visualized with ECL.

RT-PCR

$CD34^+$ cells were harvested 36 h after transfection with either pSG5-Ets1 or pSG5 vectors. Semi-quantitative RT-PCR was employed to examine mRNA expression. The primers 5′-GAG GGG GAA TAG TCT AGA TG-3′ (sense) and 5′-TAC AGT AGG ATG ATG GT CCT-3′ (antisense) were utilized for the cyclin D3 gene (515 bp). The PCR conditions were as follows: 94°C for 5 min (first cycle), 28 cycles of 94°C for 1 min, 56°C for 1 min and 72°C for 1 min, followed by a final extension at 72°C for 8 min. For GAPDH (340 bp), the primers 5′-CCT TGC CTC TCA GAC AAT GC-3′ (sense) and 5′-CCA CGA CAT ACT CAG CAC-3′ (antisense) were used under the same PCR conditions. An aliquot of each reaction mixture was analyzed by electrophoresis on 1% agarose gel, and the band density was determined.

Methyl thiazolyl tetrazolium (MTT) assay

$CD34^+$ cells were separated into two groups and transfected with either pSG5-Ets1 or pSG5 vectors. The proliferation of these cells was determined by MTT (Sigma, USA) assay. The transfected cells were seeded into 96-well plates (5×10^3 cells/well) and incubated for 36 h in triplicate. Fifty microliters of MTT solution (1 mg/mL) was added to each well for 4 h at 37°C. Subsequently, 100 μL of DMSO (Sigma, USA) was added to each well for 10 min at 37°C. Optical density (*OD*) values of each well were measured in a microplate reader at 490 nm (A_{490}). The experiment was repeated three times.

Statistical analysis

Results are presented as the mean±standard deviation (SD). Student's *t*-test for paired data was used to determine significant differences between the two groups. Differences were considered significant when the *P* value was less than 0.05.

Results

Isolation and confirmation of $CD34^+$ cells

Purification of 85.06%±3.02% $CD34^+$ cells was achieved from umbilical cord blood after two rounds of purification with Midi-MACS (Figure 1A). Additionally, 60%±4.31% of cells were $CD34^+$ after 6 d of culture and proliferation (Figure 1B).

Construction of promoter deletion plasmids for cyclin D3

Nine cyclin D3 promoter deletion fragments were generated by PCR and inserted into the pGL3-Basic vector (pD3-Δ) that contained the luciferase reporter gene. The results of restriction enzyme digestion patterns and nucleic acid sequencing confirmed the contents of the constructs.

Promoter activity in $CD34^+$ cells

The $CD34^+$ cells exhibited various levels of luciferase activity when transiently transfected with either pD3-Δ or pD3-Basic vectors. The relative activity of the promoter was defined as the ratio of the luciferase activity value of promoter deletion constructs (pD3-Δ) to that of the complete promoter sequence (pD3-1044) (Figure 2). According to our results, the promoter activity of pD3-362 was greatly enhanced compared with that of pD3-439 ($P<0.01$), which indicated that a negative regulatory sequence was located between -439 bp and -362 bp.

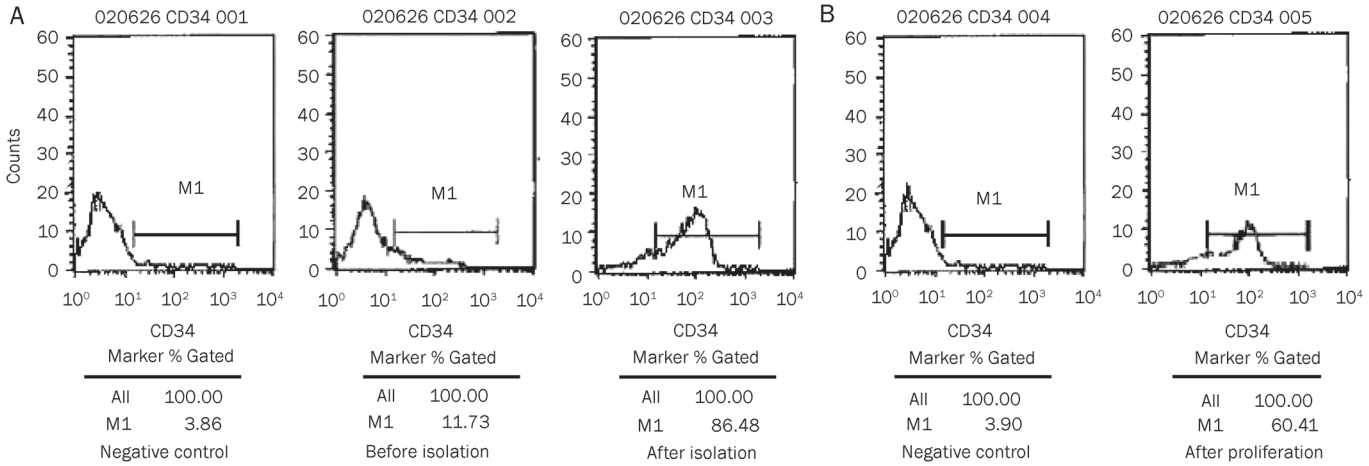

Figure 1. Flow cytometry analysis of CD34$^+$ cells. Cells were isolated from umbilical cord blood and stained mouse anti-CD34-FITC antibody, with mouse IgG1 as negative control and analyzed with flow cytometry. (B) Proportion of CD34$^+$ cells after a 6-d proliferation.

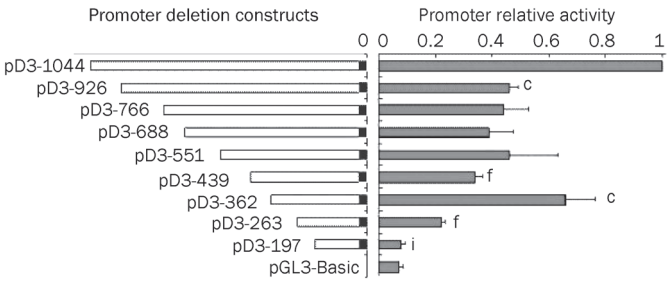

Figure 2. The function analysis of cyclin D3 promoter. CD34$^+$ cells transfected with pD3-Δ or pD3-Basic were harvested 36 h later and lysates were subjected to Dual Luciferase reporter system to determine the promoter activity. n=6. Mean±SD. $^c P<0.01$ *vs* pD3-1044. $^e P<0.05$, $^f P<0.01$ *vs* pD3-362. $^i P<0.01$ *vs* pD3-263.

c-Ets1 is a candidate to negatively regulate cyclin D3 transcription

Based on the results above, we utilized TFSEARCH 1.3 to search for transcription factor binding sites over the regulatory region between -439 bp and -362 bp. We found binding sites for USF, c-Ets, HNF-3b, N-Myc and Lyf-1. Excluding putative transcriptional activators and those not involved in hematopoiesis, we speculated that c-Ets1, which was widely expressed in hematopoietic cells, was a good candidate involved in the negative regulation of cyclin D3[5–11]. To test this hypothesis, we performed EMSA and super shift assays to determine the nuclear expression of c-Ets1 in CD34$^+$ cells. As shown in Figure 3A, c-Ets1 was detected with specific oligonucleotide probes and antibodies, confirming that c-Ets1 was expressed in the nuclei of CD34$^+$ cells.

c-Ets1 binds to an AGGA core sequence in the regulatory domain of cyclin D3

We generated the point mutant pD3-439m to further analyze the binding sites of c-Ets1 to the negative regulatory domain of the cyclin D3 promoter. The dual luciferase assay indicated that pD3-439m transfected cells had increased relative promoter activity (0.58±0.06) compared with those transfected with wild-type pD3-439 (0.36±0.09), with a P value less than 0.05. We speculate that c-Ets1 binds to the AGGA core sequence on the negative regulatory region.

c-Ets1 expression suppresses the activity of the cyclin D3 promoter

To further confirm the negative effects of c-Ets1 on cyclin D3 expression, CD34$^+$ cells were transfected with the c-Ets1 expression plasmid pSG5-Ets1 or the empty vector pSG5. Western blot results confirmed that c-Ets1 was overexpressed in CD34$^+$ cells after transfection (Figure 3B). Furthermore, we co-transfected the CD34$^+$ cells with pSG5-Est1 (or pSG5) and the promoter deletion constructs pD3-1044, pD3-926, pD3-439, pD3-362, pD3-263 or pGL3-Basic. Luciferase assays indicated that c-Ets1 significantly inhibited the activity of pD3-1044, pD3-439 and pD3-362 transfected cells (Figure 3C) (P<0.05), which confirmed that c-Ets1 was negatively regulating the cyclin D3 promoter.

c-Ets1 suppresses cyclin D3 expression in CD34$^+$ cells

Finally, we investigated the effects of c-Ets1 on the expression of cyclin D3 in CD34$^+$ cells. The expression of both cyclin D3 mRNA (Figure 4A) and protein levels (Figure 4B) was down-regulated by overexpressing c-Ets1.

c-Ets1 inhibits the proliferation of CD34$^+$ cells

Compared with the pSG5 vector group (1.623±0.086), the *OD* value of the pSG5-Ets1 group (1.336±0.107) was lower (P<0.05). The inhibition rate was 17.76%±2.24%. These data showed that c-Ets1 could inhibit the proliferation of CD34$^+$ cells.

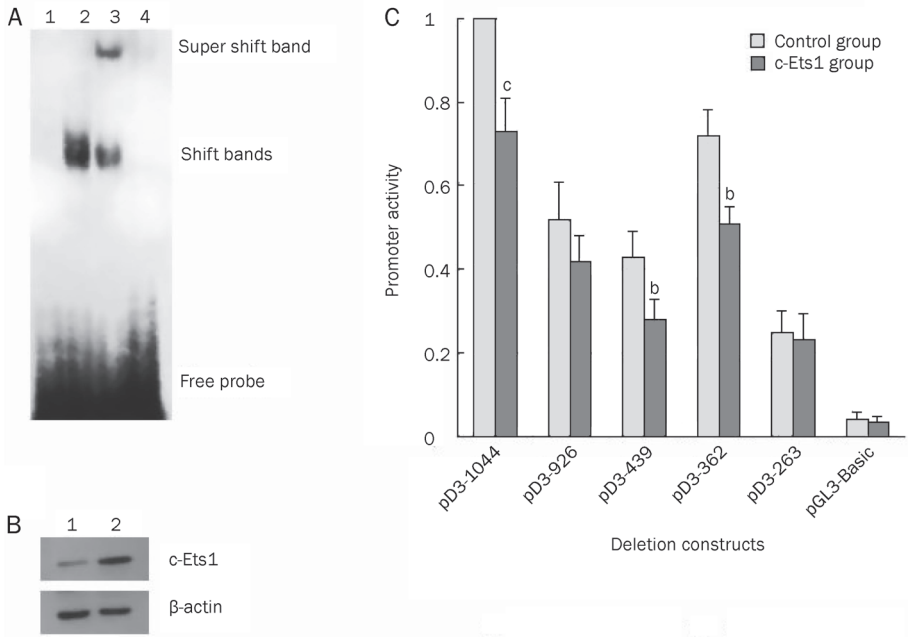

Figure 3. The effects of c-Ets1 on activity of cyclin D3 promoter. EMSA and Super shift assay detected c-Ets1 in $CD34^+$ cells. lane 1, free probe; lane 2, nuclear extract+labeled probe; lane 3, nuclear extract+labeled probe+antibody; lane 4, nuclear extract+labeled probe+cold probe. (B) $CD34^+$ cells transfected with pSG5–Ets1 (lane 2) or vector alone (lane 1) were collected after 36 h incubation. Western blot was applied to detect the expression of c-Ets1 in $CD34^+$ cells transfected with pSG5-Ets1 cells. (C) $CD34^+$ cells were co-transfected with the pSG5-Est1 (or pSG5) and the promoter deletion constructs pD3-1044, pD3-926, pD3-439, pD3-362, pD3-263 or pGL3-Basic respectively. Dual Luciferase assay system was used to determine the effects of c–Ets1 on the cyclin D3 promoter activity. n=6. Mean±SD. $^bP<0.05$, $^cP<0.01$ *vs* control.

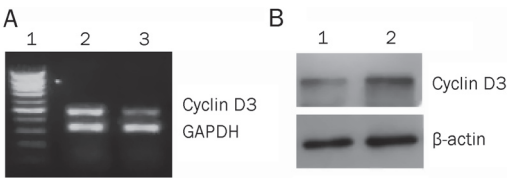

Figure 4. The effects of c-Ets1 on cyclin D3 expression. (A) $CD34^+$ cells were transfected with pSG5-Est1 or pSG5 vector and cyclin D3 mRNA expression was determined using semi-quantitative RT-PCR. Lane 1, marker; lane 2, pSG5 vector (control) group; lane 3, pSG5-Est1 group. (B) After CD34+cells were transfected with pSG5–Est1 or pSG5 vector, cyclin D3 protein was determined by Western blot. Lane 1, pSG5-Est1 group; lane 2, pSG5 vector (control) group.

Discussion

The initiation of cell cycle progression is crucial to the differentiation and proliferation of HSCs. Especially important is the G_1 phase, as extracellular signals during this interval may signal cells to commit to progression to the next phase. Cyclin D proteins, which are expressed before cyclin E at the initial stage of the cell cycle, are essential G_1-phase regulators. With the stimulation of mitogenic signals (such as growth factors), HSCs synthesize cyclin D proteins, which form a complex with CDK4 and CDK6, leading to the phosphorylation of Rb protein and the successive activation of downstream genes. In this way, cells pass the G_1/S checkpoint and enter the S phase. Once this checkpoint is overridden, cells can progress through the whole cell cycle, even in the absence of growth factors[2, 12].

At present, three isoforms of cyclin D have been identified that display tissue-specific expression patterns. Cyclin D3 is a dominant regulator in HSCs and is regulated mainly at the transcriptional level[3, 5]. Transcription factors bind to the promoter region of cyclin D3 and regulate the activity of promoters and, thus, the transcription of the target gene. Both positive and negative regulatory elements are involved in the modulation of cyclin D3 transcription[6]. To date, most studies concerning cyclin D3 transcription have focused on the positive regulators, with few reports discussing negative regulators.

To explore the mechanism underlying cyclin D3 transcription regulation, we cloned promoter deletion sequences, transfecting them into $CD34^+$ cells after short-term expansion. The CD34 antigen is a generally accepted marker of human HSCs and early progenitor cells. The amount of $CD34^+$ cells after short term expansion was more than 60%, indicating that more than half of the expanded cells retained their stem and progenitor cell characteristics. Furthermore, most of the expanded cells were in the cell cycle and could be transfected easily. As a result, we discovered a negative regulatory region between -439 bp and -361 bp in the promoter of cyclin D3. Further analysis indicated that binding sites of many transcription factors such as USF, c-Ets1, HNF-3b, N-Myc and Lyf-1 were also present in this region. USF is a positive transcription factor and can up-regulate the activity of various promoters[15]. Additionally, HNF-3b is expressed mainly in liver and is responsible for the modulation of genes involved in glucose and lipid metabolism during hepatocyte differentiation[16]. Some laboratories have demonstrated that N-Myc is a positive transcriptional regulator and involved in carcinogenesis, especially in the nervous system[17]. Lyf-1 is expressed in lymphoid cells and involved in the transcription of some lymphoid-specific genes[18]. The transcription factor c-Ets1 is expressed in HSCs and the megakaryocytic, myeloid and lymphoid lineages, where it plays a crucial role in differentiation and proliferation[8–12]. Based on all this evidence, we speculated that c-Ets1 was probably a negative transcription factor

for cyclin D3 transcription.

Utilizing EMSA and super shift assays, we found that c-Ets1 was expressed in the nucleus of $CD34^+$ cells and that it bound to the negative regulatory domain of the cyclin D3 promoter. Transient expression of c-Ets1 in $CD34^+$ cells suppressed promoter activity, decreased the mRNA and protein level of cyclin D3, and inhibited the proliferation of $CD34^+$ cells. Our results indicate that c-Ets1 can repress cyclin D3 promoter activity and is thus a negative regulator of cyclin D3.

The Ets protein family is one of the largest signal-dependent transcription factor families. Ets1, present on human chromosome 11q23 and encoding a 54 kDa protein, is a widely expressed transcription factor implicated in cell proliferation, differentiation and apoptosis, but its role varies depending on cell type and differentiation stage[7–12]. Our results demonstrate that c-Ets1 is expressed in $CD34^+$ cells and specifically binds to the cyclin D3 promoter. Furthermore, c-Ets1 inhibits cyclin D3 activity, consequently decreasing its transcription and expression. Because cyclin D3 plays a key role in modulating the proliferation of $CD34^+$ cells, c-Ets1 is a potential target for inhibiting the growth of $CD34^+$ cells. Our results help in clarifying the mechanism underlying hematopoietic diseases, providing possible targets for clinical treatments.

Acknowledgements

This work was supported by the National Natural Science Foundation of China (No 30070326).

Author contribution

Jian-feng ZHOU, Han-ying SUN and Wen-li LIU designed the research; Fan-kai MENG, Xi-you TAN and Chun-rui LI performed the research; Fan-kai MENG and Xi-you TAN analyzed the data; and Fan-kai MENG and Han-ying SUN wrote the paper.

References

1 Jude CD, Gaudet JJ, Speck NA, Ernst P. Leukemia and hematopoietic stem cells: balancing proliferation and quiescence. Cell Cycle 2008; 7: 586–91.

2 Della Ragione F, Borriello A, Mastropietro S, Della Pietra V, Monno F, Gabutti V, *et al*. Expression of G_1-phase cell cycle genes during hematopoietic lineage. Biochem Biophys Res Commun 1997; 231: 73–6.

3 Ma Y, Yuan J, Huang M, Jove R, Cress WD. Regulation of the cyclin D3 promoter by E2F1. J Biol Chem 2003; 278: 16770–6.

4 Masamha CP, Benbrook DM. Cyclin D1 degradation is sufficient to induce G_1 cell cycle arrest despite constitutive expression of cyclin E2 in ovarian cancer cells. Cancer Res 2009; 69: 6565–72.

5 Kozar K, Ciemerych MA, Rebel VI, Shigematsu H, Zagozdzon A, Sicinska E, *et al*. Mouse development and cell proliferation in the absence of *D*-cyclins. Cell 2004; 118: 477–91.

6 Ando K, Ajchenbaum-Cymbalista F, Griffin JD. Regulation of G_1/S transition by cyclins D2 and D3 in hematopoietic cells. Proc Natl Acad Sci U S A 1993; 90: 9571–5.

7 Dittmer J. The biology of the Ets1 proto-oncogene. Mol Cancer 2003; 2: 29.

8 Eyquem S, Chemin K, Fasseu M, Chopin M, Sigaux F, Cumano A, *et al*. The development of early and mature B cells is impaired in mice deficient for the Ets-1 transcription factor. Eur J Immunol 2004; 34: 3187–96.

9 Jackers P, Szalai G, Moussa O, Watson DK. Ets-dependent regulation of target gene expression during megakaryopoiesis. J Biol Chem 2004; 279: 52183–90.

10 Marziali G, Perrotti E, Ilari R, Lulli V, Coccia EM, Mazzeo S. Role of Ets–1 in erythroid differentiation. Blood Cells Mol Dis 2002; 29: 553–61.

11 Lulli V, Romania P, Riccioni R, Boe A, Lo-Coco F, Testa U, *et al*. Transcriptional silencing of the ETS1 oncogene contributes to human granulocytic differentiation. Haematologica 2010; 95: 1633–41.

12 Lulli V, Romania P, Morsilli O, Gabbianelli M, Pagliuca A, Mazzeo S, *et al*. Overexpression of Ets-1 in human hematopoietic progenitor cells blocks erythroid and promotes megakaryocytic differentiation. Cell Death Differ 2006; 13: 1064–74.

13 Lee MW, Jang IK, Yoo KH, Sung KW, Koo HH. Stem and progenitor cells in human umbilical cord blood. Int J Hematol 2010; 92: 45–51.

14 Kast C, Wang M, Whiteway M. The ERK/MAPK pathway regulates the activity of the human tissue factor pathway inhibitor-2 promoter. J Biol Chem 2003; 278: 6787–94.

15 Makaula S, Adam T, Essop MF. Upstream stimulatory factor 1 transactivates the human gene promoter of the cardiac isoform of acetyl-CoA carboxylase. Arch Biochem Biophys 2006; 446: 91–100.

16 Kanda S, Shiroi A, Ouji Y, Birumachi J, Ueda S, Fukui H, *et al*. *In vitro* differentiation of hepatocyte-like cells from embryonic stem cells promoted by gene transfer of hepatocyte nuclear factor 3 beta. Hepatol Res 2003; 26: 225–31.

17 Nesbit CE, Tersak JM, Prochownik EV. MYC oncogenes and human neoplastic disease. Oncogene 1999; 18: 3004–16.

18 Hahm K, Ernst P, Lo K, Kim GS, Turck C, Smale ST. The lymphoid transcription factor LyF-1 is encoded by specific, alternatively spliced mRNAs derived from the Ikaros gene. Mol Cell Biol 1994; 14: 7111–23.

Acta Pharmacologica Sinica (2011) 32: 1165–1172
 1671-4083/11 $32.00
www.nature.com/aps

Original Article

Cross-regulation between protein *L*-isoaspartyl *O*-methyltransferase and ERK in epithelial mesenchymal transition of MDA-MB-231 cells

Jiyeon RYU, Jihyeok SONG, Jieun HEO, Yongwoo JUNG, Sang-Jin LEE, Sungyoul HONG*, Jae Youl CHO*

Department of Genetic Engineering, Sungkyunkwan University, Suwon 440-746, Korea

Aim: Protein *L*-isoaspartyl *O*-methyltransferase (PIMT) regulates cell adhesion in various cancer cell lines through activation of integrin αv and the PI3K pathway. The epithelial mesenchymal transition (EMT) enables epithelial cells to acquire the characteristics of mesenchymal cells, and to allow them to migrate for metastasis. Here, we examined the relationship between PIMT and EMT with attached or detached MDA-MB 231 cells.
Methods: Human breast cancer cell line MDA-MB-231 cells were maintained in a suspension on poly-HEMA in the presence or absence of PIMT siRNA or ERK inhibitor PD98059. The mRNAs and proteins were analyzed using RT-PCR and immunoblotting, respectively.
Results: During cellular incubation under detached conditions, PIMT, integrin αv and EMT proteins, such as Snail, Slug and matrix metalloproteinase 2 (MMP-2), were significantly increased in correlation with the phosphorylation of ERK1/2. The ERK inhibitor PD98059 (25 μmol/L) strongly suppressed the expression of the proteins and PIMT. Interestingly, PIMT siRNA blocked the phosphorylation of ERK and the expression of the EMT proteins. Additionally, PIMT and ERK phosphorylation were both co-activated by treatment with TGF-β (10 ng/mL) and TNF-α (10 ng/mL).
Conclusion: A tight cross-regulation exists between ERK and PIMT in regards to their activation and expression during the EMT.

Keywords: protein *L*-isoaspartyl *O*-methyltransferase (PIMT); breast cancer; metastasis; epithelial mesenchymal transition; extracellular signal-regulated kinase (ERK); siRNA

Acta Pharmacologica Sinica (2011) 32: 1165–1172; doi: 10.1038/aps.2011.94; published online 15 Aug 2011

Introduction

The epithelial mesenchymal transition (EMT) is an essential component of tumor progression and also plays a normal role in embryonic development, tissue remodeling and wound repair[1]. The occurrence of the EMT during tumor progression allows benign tumor cells to acquire three major changes in cellular phenotype. These include morphological changes from the cobblestone-like morphology of epithelial cells into spindle-shaped mesenchymal cells, changes in differentiation markers, where cytokeratin intermediate filaments become vimentin filaments, fibronectin or certain integrins, and the conversion of stationary cells to motile cells capable of invading through the extracellular matrix (ECM)[2, 3]. The breakdown of epithelial cells that ultimately leads to aggressive cancer progression is correlated with a loss of epithelial characteristics and the acquisition of a migratory phenotype[4]. In addition to reorganization through translocation during metastasis, additional aspects of EMT biology, such as resistance to anoikis, enhanced survival, genomic instability, and resistance to chemotherapies, have also been recently identified[5].

Protein *L*-isoaspartyl *O*-methyltransferase (PIMT, EC2.1.1.77) is a widely distributed enzyme that catalyzes the transfer of an active methyl group from *S*-adenosyl-*L*-methionine (SAM) to the α-carboxyl group of atypical *L*-isoaspartyl and *D*-aspartyl residues that are generated during the aging process. This enzyme does not catalyze this transfer to normal *L*-aspartyl residues contained in peptides or proteins[6, 7]. The functional role of PIMT in cancer cell migration has not been clearly elucidated. The reduced motility of cells on aged type-I collagen has been shown to be alleviated by PIMT-treated repaired collagen by up to 72%[8]. It is thus clear that the detachment and attachment of tumor cells can be regulated by PIMT expression. Furthermore, functional activation of integrins and integrin binding to fibronectin-I_5 has been reported to regulate PIMT expression and to be relevant in the formation of isoaspartyl residues in the extracellular matrix[9].

* To whom correspondence should be addressed.
E-mail jaecho@skku.edu (Jae Youl CHO);
syhong@skku.edu (Sungyoul HONG)
Received 2011-01-13 Accepted 2011-06-08

Because the role of PIMT in the EMT and metastatic processes remains unclear, in this study, we explored the involvement of PIMT in the regulation of the detachment and attachment of the anoikis-resistant cell line MDA-MB-231, an aggressive breast cancer cell line with a highly invasive, migrative, and metastatic characters[10], by culturing the cells in poly-HEMA (2-hydroxyethylmethacrylate)-coated dishes and introducing siRNA specific for PIMT.

Materials and methods

Materials

LiCl and poly-HEMA were purchased from Sigma-Aldrich (St Louis, MO, USA). Dulbecco's modified Eagle's medium (DMEM), penicillin/streptomycin solution (10 000 unit/mL and 10 mg/mL, respectively), fetal bovine serum (FBS) and Dulbecco's phosphate-buffered saline (DPBS) were purchased from Gibco BRL (Gaithersburg, MD, USA). MDA-MB 231 cells were obtained from American Type Culture Collection (Manassas, VA, USA). Moloney murine leukemia virus (M-MLV) reverse transcriptase, polymerase chain reaction (PCR) premix, and Sapphire Super Taq were purchased from Rexgene Biotech Co, Ltd (Ochang, Korea). All primers used for PCR were purchased from Bioneer (Taejeon, Korea). A mixture of Stealth™/siRNA duplex oligoribonucleotides against PIMT and Lipofectamine™ RNAiMAX was purchased from Invitrogen (Carlsbad, CA, USA). Rabbit anti-PIMT antiserum was produced against recombinant PIMT proteins of porcine brain as previously described (Koh and Hong, unpublished data). Antibodies against MAPK, MMP-2, MMP-9, N-cadherin, integrin αv, phospho-GSK3 ($Tyr^{279/216}$), phospho-ERK1/2 (Thr^{202}/Tyr^{204}), phospho-MEK1 ($Ser^{218/222}$)/MEK2 ($Ser^{222/226}$), phospho-Akt1/PkBα (Ser^{473}) and phospho-p90RSK (Ser^{380}) were obtained from Millipore (Bedford, MA, USA). β-actin antibody was obtained from Santa Cruz Biotechnology (Santa Cruz, CA, USA). The ERK kinase inhibitor PD98059 was purchased from CalBiochem (La Jolla, CA, USA).

Cell culture

MDA-MB 231 cells (poorly differentiated adenocarcinoma, grade III), a human breast cancer cell line, appearing phenotypically as spindle shaped cells exhibiting highly invasive phenotype[10, 11] and differentiation markers such as E-cadherin and keratin, β-catenin, and vimentin[12], were grown in DMEM with 10% fetal bovine serum and 1% penicillin/streptomycin at 37 °C in a humidified atmosphere under 5% CO_2. Cells were collected and passaged using a 0.05% trypsin-0.02% ethylenediamine tetra-acetic acid (EDTA) solution, and cell counts were performed in triplicate using a hemocytometer.

Quantitative analysis of EMT

Detached (d) MDA-MB-231 cells (10^6 cells/well ×6 wells) were maintained in suspension on poly-HEMA or were allowed to attach (a) to culture dishes in serum-free media for 24 h. The cells were then treated with 0.025% trypsin/0.02 mmol/L EDTA and re-attached to the culture plates. The images were taken by a digital camera at the indicated time after seeding. The numbers of round and total cells were counted in a hemocytometer, as reported previously[13]. The percentage of cells morphologically changed was determined by the following equation: % of cells in aggregates=[(total cells−round cells)/total cells]×100. All values, expressed as mean±SEM, were obtained from 3 to 6 replicate cultures.

Reverse transcriptase-polymerase chain reaction analysis

Cells were plated at a density of 1×10^6 cells/well in 6-well tissue culture plates. After treatment with each of the indicated reagents, total RNA was obtained with an assayBLUE™ total RNA extraction reagent (Intron Biotechnology, Sungnam, Korea). After determination of the amounts of the total RNA in each sample followed by electrophoresis on a formaldehyde-agarose gel, cDNA synthesis was performed using M-MLV reverse transcriptase (Rexgene, Ochang, Korea) as reported previously[14]. Polymerase chain reaction (PCR) was then conducted using Premix (Rexgene, Ochang, Korea) in a 20 μL reaction that contained 2 μL of reaction buffer, 1 μL of 5 mmol/L dNTPs, 1 μL of forward and reverse primer and 1 μL of cDNA as the template, as reported previously[15]. The primer sequences are shown in Table 1.

Immunoblotting

Cells were lysed in PRO-PREP (Intron Biotechnology, Sungnam, Korea), after which the protein concentrations were quantified using a Bio-Rad protein assay (Bio-Rad, Hercules, CA, USA). Next, the lysates were boiled for 5 min, after which 20 μg of each total protein was subjected to SDS-polyacrylamide gel electrophoresis (PAGE) on 12% slab gels. The proteins were then transferred to polyvinylidene difluoride membranes (PVDF, Millipore, Bedford, MA, USA), which were subse-

Table 1. The sequence of primers used.

Gene		Sequences
GAPDH	F	5′-AAGGGTCATCATCTCTGCCC-3′
	R	5′-GTGATGGCATGGACTGTGGT-3′
PIMT	F	5′-TCAGGAAGGACGATCCAACA-3′
	R	5′-TCCTCCGGGCTTTAACTGAT-3′
Fibronectin	F	5′-ATTCCGGGTGGAATATGAGC-3′
	R	5′-CTGCTCCAGCGAACAACAAT-3′
TGF-β1	F	5′-GAGGGGAAATTGAGGGCTTT-3′
	R	5′-CGGTAGTGAACCCGTTGATC-3′
MMP-2	F	5′-AATGCCATCCCCGATAACC-3′
	R	5′-AAACTTCACGCTCTTCAGAC-3′
MMP-9	F	5′-TCTTCCAGTACCGAGAGAAA-3′
	R	5′-AGGATGTCATAGGTCATAGGT-3′
Snail	F	5′-GGGCAGGTATGGAGAGGAAG-3′
	R	5′-TTCTTCTGCGCTACTGCTGC-3′
Slug	F	5′-CCTGGTCAAGAAGCATTTCA-3′
	R	5′-GCCCCAAAGATGAGGAGTAT-3′
Integrin αv	F	5′-GTTGGGAGATTAGACAGAGG-3′
	R	5′-CAAAACAGCCAGTAGCAACA-3′
E-cadherin	F	5′-CAGCACGTACACAGCCCTAA-3′
	R	5′-GCTGGCTCAAGTCAAAGTCC-3′

quently blocked for 2 h in TBS containing 0.5% Tween-20 and 5% (*w/v*) dry skim milk powder and then incubated overnight with primary antibodies as reported previously[16, 17]. The membranes were then washed with TBS-T and incubated for 2 h with HRP-linked anti-rabbit IgG (Millipore, Bedford, MA, USA) or HRP-linked anti-mouse IgG (Millipore, Bedford, MA, USA) secondary antibody. For chemiluminescence detection, the probed blots were incubated for 5 min with Immobilon Western HRP substrate (Millipore, Bedford, MA, USA) as reported previously[18, 19].

siRNA transfection

To conduct PIMT siRNA transfection, 4×10^5 cells per well were seeded in 6-well plates and then incubated for 48 h at 37 °C in medium containing serum, which allowed the cells to become approximately 80% confluent. A mixture of PIMT siRNA and Lipofectamine™ RNAiMAX (Invitrogen, Carlsbad, CA, USA) was prepared prior to treatment as reported previously[20]. Briefly, the Lipofectamine™ RNAiMAX was incubated with siRNA in OPTI-MEM (Gibco, Gaithersburg, MD, USA) at room temperature for 30 min. The cells were then incubated in this mixture for 48 h at 37 °C in a fresh culture medium containing serum.

Gelatin zymography

Gelatin zymography was performed for semiquantitative analysis of the gelatinase activities of conditioned media secreted from detached human breast cancer cells as previously described by Gottschall and Yu[21], with slight modifications[22]. Briefly, samples of the culture media were mixed with non-reducing sample buffer [5% *w/v* SDS, 20% glycerol, 0.5 mol/L Tris-HCl (pH 6.8) and 1% bromophenol blue] and then separated by electrophoresis for 1 h at 150 V on 7.5% to 10% polyacrylamide gel containing 0.1% SDS and 1.5 mg/mL gelatin. Next, the gels were washed twice with 2.5% Triton X-100 for 30 min to remove the SDS and then incubated for 24 h at 37 °C with developing buffer (50 mmol/L Tris-HCl, 5 mmol/L $CaCl_2$, pH 7.6). The gels were then stained with Coomassie Brilliant Blue R-250 (0.1% Coomassie Brilliant Blue, 40% (*v/v*) methanol, and 10% (*v/v*) acetic acid) for 30 to 60 min, after which the gels were destained with 10% (*v/v*) acetic acid /20% (*v/v*) methanol. The gelatinolytic activities were then visualized as a white band against to the uniformly stained background.

Wound healing assay

The method for our wound closure assay was modified as reported previously[23, 24]. Briefly, cells were grown to confluence in 24-well-plates. A control group was cultured in DMEM supplemented with 10% FBS, and the experimental group was transfected with PIMT siRNA. After the cells grew into full confluency, the medium was aspirated, and a wound was scraped on the cell monolayer using a 200 μL micropipette tip. The wounded culture plates were then incubated for 24 h at 37 °C. The migration of cells into the scraped area was evaluated using a bright field microscope and then photographed by digital photography (Canon, Japan).

Statistical analysis

A student's *t*-test and a one–way ANOVA were used to determine the statistical significance of differences between values for the various experimental and control groups. Data are expressed as mean±standard errors (SEM) and the results are taken from at least three independent experiments performed in triplicate. *P* values of 0.05 or less were considered to be statistically significant.

Results

Cell detachment leads to EMT-like changes of MDA-MB 231 cells

Cell detachment from the ECM suppresses anoikis, allowing these tumor cells to survive and proliferate in the body; however, these cells must eventually resettle in the substratum at a different site[25]. Indeed, detached cells (d) reattached to the culture dish at a much faster rate than attached cells (a) and exhibited a spindle-like morphology (Figure 1A). Indeed, detached-reattached cells exhibited morphologically changed pattern at 1 h incubation up to 4-fold (Figure 1A, right panel). To determine if the change in the morphology of the detached cancer cells represents EMT, the mRNA and protein levels of several EMT-specific proteins were evaluated. The expression levels of integrin αv, fibronectin, TGF-β1, and MMP-2 were all strikingly increased (Figure 1B and 1C). Furthermore, the transcription factors Snail and Slug, known to repress E-cadherin, a suppressor of invasion during carcinoma progression[26], were highly upregulated in the detached cells up to 3 to 10 folds (Figure 1B). In agreement with expression level tests, MMP-2 activity (72 kDa) occurred prominently only in detached cells grown in conditioned media (CM).

ERK is a critical enzyme involved in the regulation of EMT proteins in MDA-MB 231 cells

To evaluate a regulatory pathway controlling EMT and EMT protein expression, the activated (phosphorylated) forms of several enzymes were investigated using detached cells. Of tested proteins, the levels of phospho-ERK1/2 and phospho-MEK1/2 were increased in a time-dependent manner, while phospho-AKT1 appeared at 1 h and was maintained at similar levels for up to 6 h. Additionally, the levels of phospho-GSK3 decreased in a time-dependent manner (Figure 2A, left panel).

To confirm this pattern, selective inhibitors of ERK kinase (PD98059, 25 μmol/L) and the activator of GSK3 (LiCl, 2 μmol/L) were employed, and the mRNA levels of EMT proteins or EMT-regulatory proteins were then determined. As Figure 2B shows, LiCl enhanced phospho-GSK3 levels, and PD98059 blocked the phosphorylation of ERK1/2, indicating that the drugs were functioning. As expected, PD98059 suppressed the mRNA expression of the EMT proteins. In contrast, the induction effect by LiCl was only observed in fibronectin expression assays. PD98059 also suppressed the activity of MMP-2 (Figure 2D).

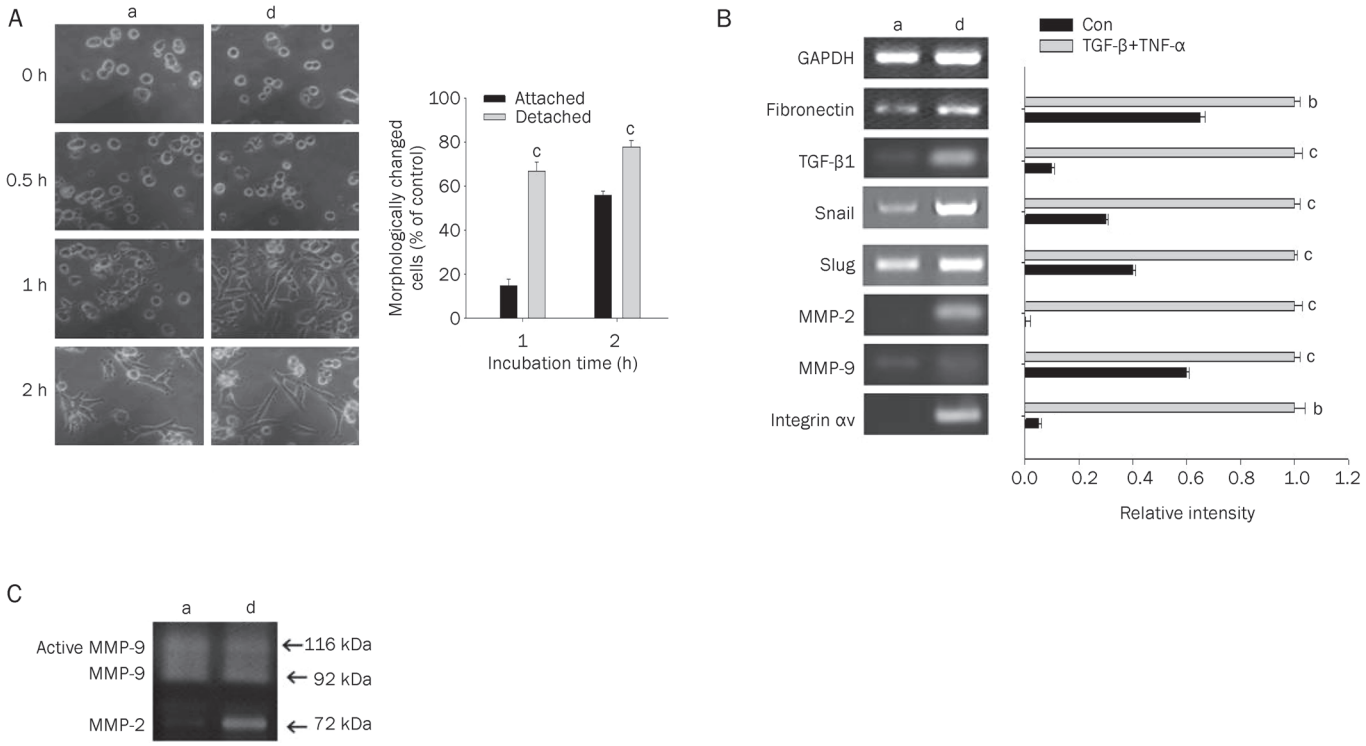

Figure 1. Cell detachment led to an EMT-like change and increased PIMT expression. (A) Detached (d) MDA-MB-231 cells (10^6 cells/well×6 wells) were maintained in suspension on poly-HEMA or were allowed to attach (a) to culture dishes in serum-free media for 24 h. The cells were then treated with 0.025% trypsin/0.02 mmol/L EDTA and re-attached to the culture plates. The images were taken by a digital camera at the indicated time after seeding. (B) Effect of detachment on the mRNA expression of the mesenchymal markers fibronectin, TGF-β1, Snail, Slug, MMP-2, MMP-9, and integrin αv in MDA-MB-231 cells were examined by RT-PCR. (C) Effect of detachment on the activity of MMPs from human breast cancer cells. Attached and detached cells were incubated for 24 h, and the conditioned media (CM) from each group was harvested after one day of incubation in serum-free media. The relative intensity of individual bands was calculated by using Syngene gel image analysis software. $^bP<0.05$, $^cP<0.01$ represent significant difference compared to each control group.

PIMT is a critical enzyme involved in the regulation of EMT proteins in MDA-MB 231 cells

To examine the importance of PIMT in the EMT, the expression of PIMT was measured. As Figure 3A shows, the mRNA and protein levels of PIMT were markedly increased in cells cultured on poly-HEMA-coated dishes compared to cells adhered to uncoated plastic dishes. Interestingly, levels of PIMT were clearly reduced by PD98059 treatment, whereas LiCl enhanced PIMT mRNA and protein levels (Figure 3B). These data suggest that ERK acts as a positive regulator, while GSK3 acts as a negative one, as reported previously[27].

Knockdown of PIMT is linked to the suppression of EMT protein expression in MDA-MB 231 cells

To determine whether PIMT influences the expression of EMT proteins, siRNA targeting PIMT was introduced to detached MDA-MB-231 human breast cancer cells. Intriguingly, knockdown of PIMT led to blockade of the EMT-like transformation as well as suppression of the mRNA levels of PIMT, integrin αv, fibronectin, and TGF-β1 (Figure 4A). Conversely, RT-PCR revealed that E-cadherin expression occurred in PIMT-knockdown MDA-MB-231 cells (Figure 4A). Interestingly, PIMT depletion also induced the suppression of phospho-ERK levels and the phosphorylation of p90RSK, a downstream enzyme of ERK, indicating that there may be a cross-regulation between the PIMT and ERK pathways that affects the expression of these proteins in EMT.

Finally, to determine if PIMT is important for the conversion of stationary cells into motile cells capable of invasion through the ECM[2], a wound healing migration assay was employed. As Figure 4C shows, PIMT siRNA-treated cells displayed a clear reduction in cell migration, suggesting that PIMT is indeed linked to cancer cell migration and invasion.

PIMT is up-regulated during the EMT of MDA-MB-231 cells triggered by cotreatment with TGF-β and TNF-α

During siRNA analysis, we found that PIMT expression was required for the EMT phenotype of MDA-MB-231 breast cancer cells in poly-HEMA-coated dishes. As such, we sought to determine if PIMT expression is up-regulated during the induction of EMT by TGF-β and TNF-α. Previously, treatment with a combination of TGF-β and TNF-α was shown to induce EMT in some cell types[28]. Indeed, when MDA-MB-231 breast cancer cells were treated with TGF-β/TNF-α, a morphological change from an epithelial-like to a mesenchymal-like appearance was induced (Figure 5A). Additionally, TGF-β/

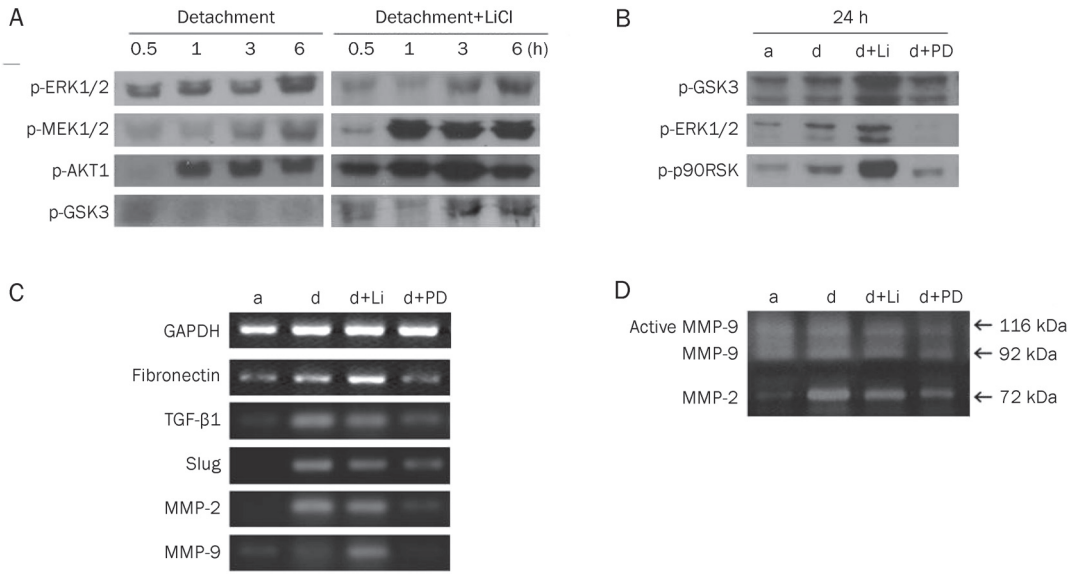

Figure 2. The ERK inhibitor PD98059 alters the expression of PIMT and EMT proteins. (A, B, and C) Detached (d) MDA-MB-231 cells (10^6 cells/well ×6 wells) were maintained in suspension on poly-HEMA in serum-free media for indicated times in media containing PD98059 (PD, 25 μmol/L) or LiCl (Li, 2 μmol/L). After preparing whole lysates, the phosphorylation levels of ERK, MEK, Akt1, and GSK3 were analyzed by immunoblotting. (B) The phosphorylation levels of GSK3, ERK1/2, and p90RSK were determined by immunoblotting analysis of detached MDA-MB-231 cells (10^6 cells/well ×6 wells) cultured on poly-HEMA in the presence or absence of PD98059 (25 μmol/L) or LiCl (2 μmol/L) for 24 h. (C) The mRNA levels of fibronectin, TGF-β1, Slug, MMP-2, and MMP-9 were analyzed by RT-PCR using detached MDA-MB-231 cells (10^6 cells/well x 6 wells) cultured on poly-HEMA in the presence or absence of PD98059 (25 μmol/L) or LiCl (2 μmol/L) for 24 h. (D) The activity of MMP-2 and MMP-9 was examined by gelatin zymography using detached MDA-MB-231 cells (10^6 cells/well x 6 wells) cultured on poly-HEMA in the presence or absence of PD98059 (25 μmol/L) or LiCl (2 μmol/L) for 24 h.

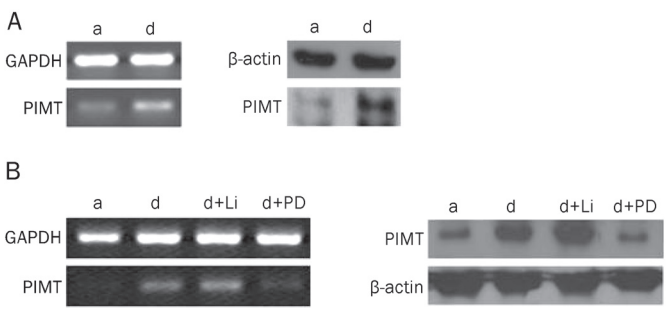

Figure 3. ERK1/2 activation regulates PIMT expression. (A) Detached (d) MDA-MB-231 cells (10^6 cells/well×6 wells) were maintained in a suspension on poly-HEMA or were allowed to attach (a) to culture dishes in serum free media for 24 h. The mRNA and protein levels of PIMT were analyzed by RT-PCR and immunoblotting. (B) The mRNA and protein levels of PIMT were determined by RT-PCR and immunoblotting analysis of detached MDA-MB-231 cells (10^6 cells/well x 6 wells) cultured on poly-HEMA in the presence or absence of PD98059 (PD, 25 μmol/L) or LiCl (Li, 2 μmol/L) for 24 h.

TNF-α-treated MDA-MB-231 cells showed increased mRNA expression of EMT proteins such as integrin αv, fibronectin, Snail, Slug, MMP-2, and MMP-9 as well as PIMT, up to 2 to 5 folds (Figure 5B). The protein levels of PIMT, integrin αv, MMP-2, N-cadherin, phospho (p)-ERK, and p-GSK3 were also significantly upregulated by 2 to 5 folds during TGF-β/TNF-α-induced EMT (Figure 5C).

Discussion

At the cellular level, one requirement of metastasis is that cells detach from their primary site and then migrate to the lymphatic and circulatory systems. In the absence of ECM attachment, cells undergo a form of apoptosis known as anoikis[29]. It is thought that anoikis-resistant cells contribute to the epithelial-mesenchymal transition (EMT), which is one of the metastatic components that lead to a more flexible and migratory phenotype[30]. In an attempt to gain further insight into the biochemical features underlying the EMT, we selected anoikis-resistant cells by culturing the breast cancer cell line MDA-MB-231 on poly-HEMA-coated tissue culture plates. We found that detached MDA-MB-231 cells exhibited spindles and a lengthened morphology compared to attached cells (Figure 1A). This is phenotypically characteristic of the EMT. During this transition, mesenchymal cells acquire a morphology that is appropriate for both migration in an extracellular environment and interactions between epithelial and mesenchymal cells[31]. Our results also showed that detached MDA-MB-231 cells expressed increased levels of metastatic factors such as integrin αv and EMT proteins such as TGF-β1, Snail, Slug, and MMP-2 (Figure 1B and 1C). All of these factors are important for tumor progression and metastasis, as they facilitate cell migration[32].

It has been reported that ERK plays a critical role in the

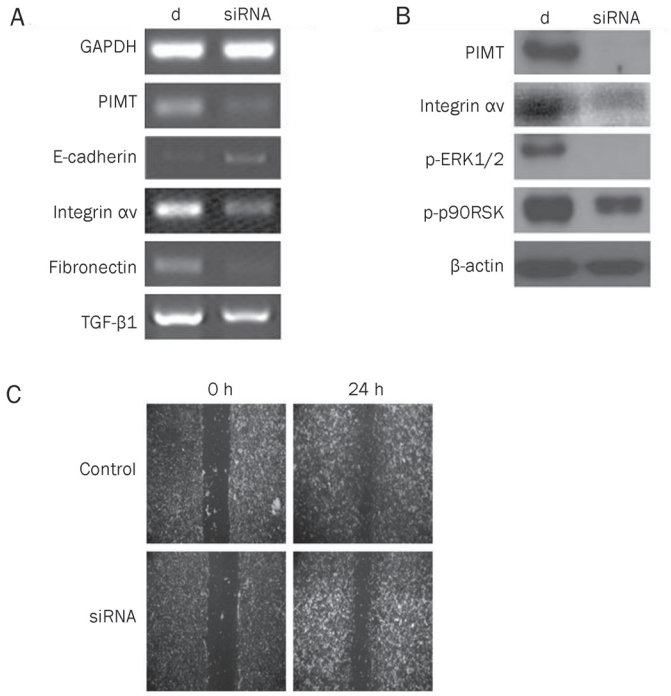

Figure 4. Depletion of PIMT results in the up-regulation of E-cadherin and the down-regulation of integrin αv and EMT proteins and inhibits cell migration. (A) Detached cells (4×10^5 cells/well ×6 wells) were transfected with the indicated siRNA constructs for 48 h. After preparing mRNA, the levels of PIMT, E-cadherin, integrin αv, fibronectin, TGF-β1, and GAPDH were determined by RT-PCR. (B) The phospho- or total levels of integrin αv, ERK1/2, p90RSK, and β-actin were determined by immunoblotting analysis using PIMT siRNA-transfected cells after 48 h. (C) After transient transfection of PIMT siRNA, wounds were introduced with 200 μL micropipette tips. After 24 h of incubation in 5% CO_2 atmosphere at 37 °C in a humidified incubator, the amount of wound recovery was photographed using a light microscope with 400× magnification for each group.

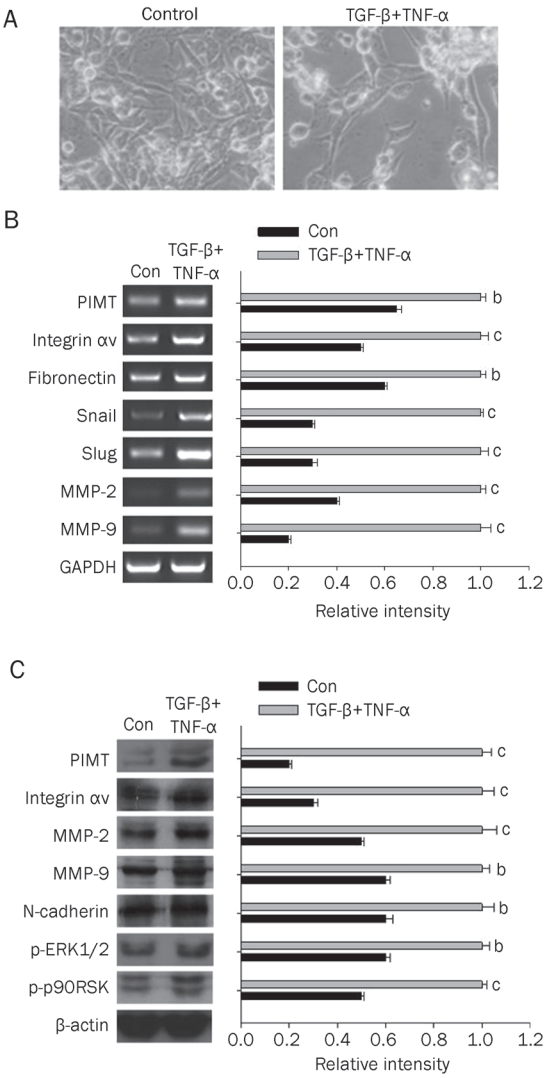

Figure 5. TGF-β/TNF-α treatment increases ERK1/2 phosphorylation and PIMT expression. (A) Cells were treated with a combination of TGF-β (10 ng/mL) and TNF-α (10 ng/mL) for 48 h and then examined by phase-contrast microscopy. (B and C) MDA-MB-231 cells were incubated for 48 h with TGF-β/TNF-α, and the mRNA and protein levels of PIMT, integrin αv, fibronectin, Snail, Slug, MMP-2, MMP-9, N-cadherin, p-ERK1/2, and p-p90RSK were determined by RT-PCR and immunoblotting analysis. The relative intensity of individual bands was calculated by using Syngene gel image analysis software. $^bP<0.05$,$^cP<0.01$ represent significant difference compared to each control group.

process of EMT[33, 34]. During the course of our assays, phosphorylation of MEK1/2 and ERK was found to be increased in detached MDA-MB-231 cells (Figure 2A). The critical role of ERK in EMT process has been illustrated by treating cells with PD98059, a specific ERK inhibitor (Figure 2B). This compound strongly inhibited the expression of EMT proteins such as integrin αv, fibronectin, Snail, Slug, and MMP-2 (Figure 2C), suggesting that ERK is crucial for the EMT. Although it is well known that ERK is functionally important for the survival of detached cells[35], our results and those of others suggest that this enzyme plays a critical role throughout the entire EMT, promoting morphological changes, migration, and adhesiveness. In addition, ERK inhibition has been reported to strongly suppress the migration of various cancer cells and the homotypic cell-cell adhesion induced by integrins[13, 36, 37].

Under our conditions, PIMT expression was also markedly increased in detached cells compared to attached MDA-MB-231 cells (Figure 3A). Similar findings have been reported in other nonattached HUVEC, Caki-1, and U-87 cells[9]. Interestingly, the protein and mRNA levels of PIMT were reduced upon exposure to the ERK inhibitor PD98059 (Figure 3B), indicating that ERK is biochemically important for PIMT synthesis. Interestingly, siRNA targeting PIMT suppressed various EMT proteins in addition to ERK phosphorylation, suggesting that PIMT possesses a critical function in the biochemical regulation of EMT proteins. Furthermore, PIMT siRNA treatment also resulted in diminished cell migration, as assessed by a wound healing assay (Figure 4C). Up-regulation of PIMT was also observed in TGF-β/TNF-α-stimulated EMT

conditions exhibiting enhanced levels of integrin αv, Snail, Slug, MMP-2, and MMP-9 (Figure 5), up to 2 to 5 folds, as reported previously[38]. Additionally, it has been reported that PIMT possesses a potential anti-apoptotic function in Bax-overexpressing cells[39]. Considering these findings, enhanced levels of PIMT appear to be essential for the survival of detached cells. This protein likely influences the early events of anoikis and migration, both of which are regulated by EMT proteins and ERK activity. We cannot, however, rule out the possibility that PIMT is functioning as a repair enzyme[40], although the involvement or appearance of aged proteins or isoaspartyl residues in the signaling cascade required for EMT protein synthesis was not verified. Surprisingly, it has been observed that valproic acid and lithium, used for the treatment of epileptic seizures and mania in bipolar disorder, have both been shown to simultaneously upregulate the ERK pathway and PIMT induction[27, 41]. These results suggest that the activation and expression of ERK pathway members and PIMT could be tightly associated. As it remains unclear how ERK and PIMT co-regulate the EMT, our future experiments will focus on understanding this cross-regulation mechanism.

Numerous lines of evidence indicate that EMT is able to impose cancer cells into self-renewal cancer stem-like cells to spawn macroscopic metastases[42, 43]. EMT-based tumor metastatic events include cell migration requiring for embryonic development and wound healing managed by adult stem cells[44]. Therefore, it could be interesting to determine whether our EMT conditions are capable of transforming MDA-MB-231 cells into highly metastatic stem-like cells. To do this, phenotype of these cells will be determined by measuring the surface levels of CD44/CD24[45].

Taken together, the results presented here provide *in vitro* support for the idea that PIMT and ERK are tightly expressed and activated in EMT conditions generated during the detachment of MDA-MB-231 cells from poly-HEMA coated dishes and by TGF-β/TNF-α stimulation, as summarized in Figure 6. These findings suggest that the development of specific inhibitors of PIMT may lead to a novel route of inhibition of the EMT and metastasis.

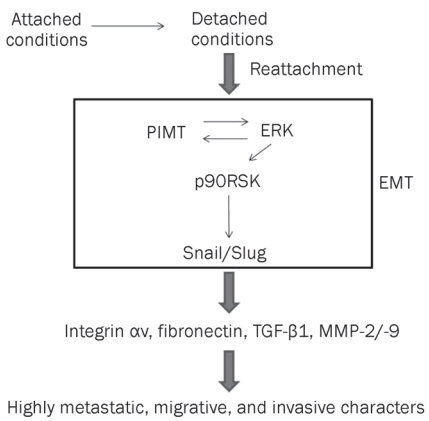

Figure 6. Schematic diagram of EMT process of MDA-MD-231 cells induced by detachment and reattachment conditions.

Abbreviations

ECM, extracellular matrix; EMT, epithelial-mesenchymal transition; ERK1/2, extracellular signal-regulated kinase; GSK3, glycogen synthase kinase 3; MAPK, mitogen-activated protein kinase; MMP, matrix metalloproteinase; PIMT, protein *L*-isoaspartyl *O*-methyltransferase; PI3K, phosphoinositide 3-kinase; TGF-β, transforming growth factor-beta; TNF-α, tumor necrosis factor-alpha.

Acknowledgements

This research was supported by Technology Development Program for Agriculture and Forestry, Ministry for Food, Agriculture, Forestry and Fisheries, Republic of Korea.

Author contribution

Jiyeon RYU and Sungyoul HONG designed research; Jiyeon RYU, Jihyeok SONG, Jieun HEO and Yongwoo JUNG performed research; Jiyeon RYU, Sang-Jin LEE, Jae Youl CHO, and Sungyoul HONG analyzed data; Jae Youl CHO and Sungyoul HONG wrote the paper.

References

1 Creighton CJ, Chang JC, Rosen JM. Epithelial-mesenchymal transition (EMT) in tumor-initiating cells and its clinical implications in breast cancer. J Mammary Gland Biol Neoplasia 2010; 15: 253–60.
2 Yang J, Weinberg RA. Epithelial-mesenchymal transition: at the crossroads of development and tumor metastasis. Dev Cell 2008; 14: 818–29.
3 Do Kwon Y, Bin Noh H, Ahn HJ, Lee WJ, Kwack K. The molecular signature of *in vitro* senescence in human mesenchymal stem cells. Genes Genom 2010; 32: 87–93.
4 Gotzmann J, Mikula M, Eger A, Schulte-Hermann R, Foisner R, Beug H, *et al*. Molecular aspects of epithelial cell plasticity: implications for local tumor invasion and metastasis. Mutat Res 2004; 566: 9–20.
5 Smalley KS, Brafford PA, Herlyn M. Selective evolutionary pressure from the tissue microenvironment drives tumor progression. Semin Cancer Biol 2005; 15: 451–9.
6 Shimizu T, Matsuoka Y, Shirasawa T. Biological significance of isoaspartate and its repair system. Biol Pharm Bull 2005; 28: 1590–6.
7 Reissner KJ, Aswad DW. Deamidation and isoaspartate formation in proteins: unwanted alterations or surreptitious signals? Cell Mol Life Sci 2003; 60: 1281–95.
8 Lanthier J, Desrosiers RR. Protein *L*-isoaspartyl methyltransferase repairs abnormal aspartyl residues accumulated *in vivo* in type-I collagen and restores cell migration. Exp Cell Res 2004; 293: 96–105.
9 Lanthier J, Desrosiers RR. Regulation of protein *L*-isoaspartyl methyltransferase by cell-matrix interactions: involvement of integrin alphavbeta3, PI3-kinase, and the proteasome. Biochem Cell Biol 2006; 84: 684–94.
10 Johnson-Holiday C, Singh R, Johnson E, Singh S, Stockard CR, Grizzle WE, *et al*. CCL25 mediates migration, invasion and matrix metalloproteinase expression by breast cancer cells in a CCR9-dependent fashion. Int J Oncol 2011; 38: 1279–85.
11 Garrido T, Riese HH, Aracil M, Perez-Aranda A. Endothelial cell differentiation into capillary-like structures in response to tumour cell conditioned medium: a modified chemotaxis chamber assay. Br J Cancer 1995; 71: 770–5.

12 Hunakova L, Sedlakova O, Cholujova D, Gronesova P, Duraj J, Sedlak J. Modulation of markers associated with aggressive phenotype in MDA-MB-231 breast carcinoma cells by sulforaphane. Neoplasma 2009; 56: 548–56.
13 Cho JY, Fox DA, Horejsi V, Sagawa K, Skubitz KM, Katz DR, *et al*. The functional interactions between CD98, beta1-integrins, and CD147 in the induction of U937 homotypic aggregation. Blood 2001; 98: 374–82.
14 Rhee DK, Kim EH, Lee MJ, Kim IH, Pyo S, Choi KT. Anti-apoptotic effects of red ginseng on oxidative stress induced by hydrogen peroxide in SK-N-SH cells. J Ginseng Res 2010; 34: 138–44.
15 Lee YH, Hong JK, Kim JS, Kim JA, Lee SI, Lim MH, *et al*. Identification and characterization of *SHI* family genes from *Brassica rapa* L ssp pekinensis. Genes Genom 2010; 32: 309–17.
16 Xing P, Li JG, Jin F, Zhao TT, Liu Q, Dong HT, *et al*. Fascin, an actin-bundling protein, promotes breast cancer progression *in vitro*. Cell Biochem Funct 2011; 29: 303–10.
17 Park JK, Do Kim H, Ha SE, Kang JR. Effect of Korean red ginseng extract on cell death responses in peroxynitrite-treated keratinocytes. J Ginseng Res 2010; 34: 205–11.
18 Tsuchiyama J, Imajo K, Yoshino T, Nanba N, Toyota A, Yoshida C, *et al*. High-dose chemotherapy and autologous peripheral blood stem cell transplantation for treatment of unspecified peripheral T-cell lymphoma presented with hepatosplenomegaly and hypercytokinemia syndrome: report of three cases. Ann Hematol 2002; 81: 588–92.
19 Chun YJ, Shim JH, Choi CS, Lee EC, Kim MY. Tamoxifen suppresses clusterin level through Akt inactivation and proteasome degradation in human prostate cancer cells. Biomol Ther 2009; 17: 25–31.
20 Chun YJ, Lee HM, Surh BY. Roles of neutral sphingomyelinase 1 on CD95-mediated apoptosis in human Jurkat T lymphocytes. Biomol Ther 2010; 18: 262–70.
21 Gottschall PE, Yu X. Cytokines regulate gelatinase A and B (matrix metalloproteinase 2 and 9) activity in cultured rat astrocytes. J Neurochem 1995; 64: 1513–20.
22 Moon A, Kim JS. Fibronectin induces Pro-MMP-2 activation and enhances invasion in H-Ras-transformed human breast epithelial cells. Biomol Ther 2009; 17: 288–92.
23 Nobes CD, Hall A. Rho GTPases control polarity, protrusion, and adhesion during cell movement. J Cell Biol 1999; 144: 1235–44.
24 Kang TJ, Lee GS, Choi JY, Choi YJ, Yim DS, Cheong JH. The wound healing effect of *Hydnocarpi Semen* extract on ulcer in diabetic mice. Biomol Ther 2010; 18: 329–35.
25 Haraguchi M, Okubo T, Miyashita Y, Miyamoto Y, Hayashi M, Crotti TN, *et al*. Snail regulates cell-matrix adhesion by regulation of the expression of integrins and basement membrane proteins. J Biol Chem 2008; 283: 23514–23.
26 Larriba MJ, Martin-Villar E, Garcia JM, Pereira F, Pena C, de Herreros AG, *et al*. Snail2 cooperates with Snail1 in the repression of vitamin D receptor in colon cancer. Carcinogenesis 2009; 30: 1459–68.
27 Lamarre M, Desrosiers RR. Up-regulation of protein *L*-isoaspartyl methyltransferase expression by lithium is mediated by glycogen synthase kinase-3 inactivation and beta-catenin stabilization. Neuropharmacology 2008; 55: 669–76.
28 Arima Y, Inoue Y, Shibata T, Hayashi H, Nagano O, Saya H, *et al*. Rb depletion results in deregulation of E-cadherin and induction of cellular phenotypic changes that are characteristic of the epithelial-to-mesenchymal transition. Cancer Res 2008; 68: 5104–12.
29 Kim JB, Yu JH, Ko E, Lee KW, Song AK, Park SY, *et al*. The alkaloid berberine inhibits the growth of Anoikis-resistant MCF-7 and MDA-MB-231 breast cancer cell lines by inducing cell cycle arrest. Phytomedicine 2010; 17: 436–40.
30 Savagner P. The epithelial-mesenchymal transition (EMT) phenomenon. Ann Oncol 2010; 21: vii89–vii92.
31 Thiery JP. Epithelial-mesenchymal transitions in tumour progression. Nat Rev Cancer 2002; 2: 442–54.
32 Manes T, Zheng DQ, Tognin S, Woodard AS, Marchisio PC, Languino LR. Alpha(v)beta3 integrin expression up-regulates cdc2, which modulates cell migration. J Cell Biol 2003; 161: 817–26.
33 Chou TY, Chen WC, Lee AC, Hung SM, Shih NY, Chen MY. Clusterin silencing in human lung adenocarcinoma cells induces a mesenchymal-to-epithelial transition through modulating the ERK/Slug pathway. Cell Signal 2009; 21: 704–11.
34 Kuo PL, Chen YH, Chen TC, Shen KH, Hsu YL. CXCL5/ENA78 increased cell migration and epithelial-to-mesenchymal transition of hormone-independent prostate cancer by early growth response-1/Snail signaling pathway. J Cell Physiol 2010; 226: 1224–31.
35 Gollob JA, Wilhelm S, Carter C, Kelley SL. Role of Raf kinase in cancer: therapeutic potential of targeting the Raf/MEK/ERK signal transduction pathway. Semin Oncol 2006; 33: 392–406.
36 Cho JY, Skubitz KM, Katz DR, Chain BM. CD98-dependent homotypic aggregation is associated with translocation of protein kinase Cdelta and activation of mitogen-activated protein kinases. Exp Cell Res 2003; 286: 1–11.
37 Stahle M, Veit C, Bachfischer U, Schierling K, Skripczynski B, Hall A, *et al*. Mechanisms in LPA-induced tumor cell migration: critical role of phosphorylated ERK. J Cell Sci 2003; 116: 3835–46.
38 Gal A, Sjoblom T, Fedorova L, Imreh S, Beug H, Moustakas A. Sustained TGF beta exposure suppresses Smad and non-Smad signalling in mammary epithelial cells, leading to EMT and inhibition of growth arrest and apoptosis. Oncogene 2008; 27: 1218–30.
39 Huebscher KJ, Lee J, Rovelli G, Ludin B, Matus A, Stauffer D, *et al*. Protein isoaspartyl methyltransferase protects from Bax-induced apoptosis. Gene 1999; 240: 333–41.
40 Furuchi T, Sakurako K, Katane M, Sekine M, Homma H. The role of protein *L*-isoaspartyl/*D*-aspartyl *O*-methyltransferase (PIMT) in intracellular signal transduction. Chem Biodivers 2010; 7: 1337–48.
41 Cournoyer P, Desrosiers RR. Valproic acid enhances protein *L*-isoaspartyl methyltransferase expression by stimulating extracellular signal-regulated kinase signaling pathway. Neuropharmacology 2009; 56: 839–48.
42 Alison MR, Lim SM, Nicholson LJ. Cancer stem cells: problems for therapy? J Pathol 2011; 223: 147–61.
43 Kong D, Banerjee S, Ahmad A, Li Y, Wang Z, Sethi S, *et al*. Epithelial to mesenchymal transition is mechanistically linked with stem cell signatures in prostate cancer cells. PLoS One 2010; 5: e12445.
44 Kondo M, Wagers AJ, Manz MG, Prohaska SS, Scherer DC, Beilhack GF, *et al*. Biology of hematopoietic stem cells and progenitors: implications for clinical application. Annu Rev Immunol 2003; 21: 759–806.
45 Bhat-Nakshatri P, Appaiah H, Ballas C, Pick-Franke P, Goulet R Jr, Badve S, *et al*. SLUG/SNAI2 and tumor necrosis factor generate breast cells with $CD44^+/CD24^-$ phenotype. BMC Cancer 2010; 10: 411.

Acta Pharmacologica Sinica (2011) 32: 1173–1180
 1671-4083/11 $32.00
www.nature.com/aps

Original Article

Hepatitis B virus X protein promotes hepatoma cell proliferation via upregulation of MEKK2

Guang-yao KONG[1], Jun-ping ZHANG[1], Shuai ZHANG[1], Chang-liang SHAN[1], Li-hong YE[2, *], Xiao-dong ZHANG[1, *]

Department of [1]Cancer Research, Key Laboratory of Molecular Microbiology and Technology of Ministry of Education, Institute for Molecular Biology and [2]Biochemistry, College of Life Sciences, Nankai University, Tianjin 300071, China

Aim: To investigate the mechanism underlying the increase of hepatoma cell proliferation by hepatitis B virus X protein (HBx).
Methods: HepG2, H7402 and HepG2.2.15 cells, which constitutively replicated hepatitis B virus were used. The effects of HBx on hepatoma cell proliferation were examined using 5-ethynyl-2-deoxyuridine (EdU) incorporation assay and MTT assay. The expression level of MEKK2 was measured using RT-PCR, Western blot and luciferase reporter gene assay. The activity of activator protein 1 (AP-1) was detected using luciferase reporter gene assay. The phosphorylation levels of JNK and c-Jun were measured using Western blot. The expression levels of HBx and MEKK2 in 11 clinical hepatocellular carcinoma (HCC) tissues were measured using real time PCR and Western blot. In addition, the expression of MEKK2 in 95 clinical HCC tissues was examined using immunohistochemistry.
Results: HBx significantly enhanced HepG2-X cell proliferation. In HepG2-X, H7402-X and HepG2.2.15 cells, the expression level of MEKK2 was remarkably increased. In HepG2.2.15 cells, HBx was found to activate JNK and AP-1, which were the downstream effectors of MEKK2 in HepG2-X and HepG2.2.15 cells. In 11 clinical HCC tissues, both HBx and MEKK2 expression levels were remarkably increased, as compared to those in the corresponding peritumor tissues. In 95 clinical HCC tissues, the rate of detection of MEKK2 was 85.3%.
Conclusion: HBx promotes hepatoma cell proliferation via upregulating MEKK2, which may be involved in hepatocarcinogenesis.

Keywords: hepatitis B; hepatocellular carcinoma; hepatitis B virus X protein; MEKK2; activator protein 1; c-jun N-terminal kinase

Acta Pharmacologica Sinica (2011) 32: 1173–1180; doi: 10.1038/aps.2011.52; published online 1 Aug 2011

Introduction

Infection with the hepatitis B virus (HBV) is a major cause of acute hepatitis, fulminant hepatitis, and chronic hepatitis. Chronic infection is closely associated with the development of liver cirrhosis and hepatocellular carcinoma (HCC)[1, 2]. The HBV X protein (HBx) is involved in the pathogenesis of HBV-associated liver diseases by affecting gene expression, apoptosis, cell cycle and cell proliferation[3–5]. The expression of HBx induced the transformation of human liver cells and caused the development of hepatocellular carcinoma in certain strains of transgenic mice[6, 7]. In addition, HBx is involved in many cell signaling transduction pathways, such as the mitogen-activated protein kinase (MAPK), c-jun N-terminal kinase (JNK), phosphatidylinositol 3-kinase (PI 3-kinase), and JAK/STAT pathways[8–11]. Our laboratory has focused on the investigation of HBx-mediated hepatocarcinogenesis. Our findings show that arachidonic acid metabolism, extracellular signal-related kinases (ERK1/2), sterol regulatory element binding protein 1c, 5-lipoxygenase and fatty acid synthase are involved in HBx-induced cell proliferation[5, 12, 13]. However, the underlying mechanisms that mediate the effects of HBx on cell proliferation require further investigation.

MAPK family members consist of at least four groups, including ERK1/2, JNK1/2/3, p38 proteins (p38a/b/c/d), and ERK3/5/7[14]. In response to different external stimuli, these MAPKs are activated via a module that uses a MAPKKK-MAPKK-MAPK pathway. Mitogen-activated protein kinase kinase kinase 2 (MEKK2), which is a member of the MAPK signaling pathway, activates JNK and ERK5[15, 16]. MEKK2 knockout mouse studies have identified important functions for MEKK2 in the T-cell receptor, epidermal growth factor (EGF) and fibroblast growth factor 2 (FGF-2) signaling pathways[15, 17, 18]. MEKK2 is involved in osteoblast activity, bone homeostasis and rheumatoid arthritis[19, 20]. HBx activates AP-1 through ERK and JNK does so through MEKK1[21]. Although MEKK2 and MEKK1 are from the same mitogen-activated protein kinase kinase kinase (MAP3K) family, MEKK2,

* To whom correspondence should be addressed.
E-mail zhangxd@nankai.edu.cn (Xiao-dong ZHANG);
yelihong@nankai.edu.cn (Li-hong YE)
Received 2011-01-14 Accepted 2011-04-08

and MEKK1 are involved in different signaling pathways. For example, growth factor-induced urokinase-type plasminogen activator (uPA) expression requires MEKK1 and not MEKK2[22]. Conversely, MEKK2, but not MEKK1, is required for mast cell tyrosine kinase receptor signaling[23]. Moreover, a recent study orthogonally confirmed the ability of MEKK2 to discriminate tumor cells from normal cells[24]. However, there are no data investigating the role of MEKK2 in HBx-mediated hepatocarcinogenesis. Therefore, we are interested in the role of MEKK2 in HBx-induced growth of hepatoma cells.

In the current study, we investigated the mechanism of increased cell proliferation, which is promoted by HBx. Our results show that HBx enhances the growth of hepatoma cells through upregulation of MEKK2. Our findings provide new insights into the mechanism that is employed by HBx to promote the proliferation of hepatoma cells.

Materials and methods

Cell culture

The cells of HepG2, H7402, and HepG2.2.15, which constitutively replicated HBV[12], were maintained in Dulbecco's modified Eagle's medium (Life Technologies, Inc, Gaithersburg, MD, USA) supplemented with 10% fetal calf serum (Life Technologies). Cultures were incubated at 37 °C in a humidified atmosphere with 5% CO_2. The engineered cells of HepG2-X/H7402-X (stably transfected with the pCMV-HBx plasmid), and HepG2-P/H7402-P (stably transfected with the empty pcDNA3.0 vector plasmid) were generated in HepG2 and H7402 cells, respectively, using the Lipofectamine 2000 reagent (Invitrogen, Carlsbad, CA, USA) according to the manufacturer's protocol, as previously described[12].

Cell proliferation assay

HepG2 cells were seeded onto 96 well plates (1000 cells/well) for 24 h before transfection. MTT assays were used to assess cell proliferation every day from the first day until the fifth day after transfection. The MTT assay was performed as follows: 20 μL of MTT (5 mg/mL) was added to each well and the plates were incubated at 37 °C for 4 h. The MTT medium mixture was then removed and 150 μL of dimethyl sulfoxide (DMSO) was added to each well. The absorbance was measured at 570 nm using a multiwell spectrophotometer. The 5-ethynyl-2-deoxyuridine (EdU) incorporation assay was performed using the Cell-Light EdU imaging detecting kit according to the manufacturer's instructions (RiboBio, Guangzhou, China). EdU is a thymidine analog that is used in a similar manner as BrdU to label cells undergoing DNA replication[25].

RNA extraction, reverse transcription PCR and real time PCR analysis

Total cellular RNA was extracted using the Trizol reagent (Invitrogen) from cells 48 h after treatment. cDNA was synthesized using the M-MLV RTase cDNA Synthesis Kit (TaKaRa Bio, Dalian, China) according to the manufacturer's protocol. To examine the expression of MEKK2 and HBx, we used specific primers for each gene as follows: MEKK2 gene (forward primer, 5′-TTTCCTCAAACGGATTT-3′ and reverse primer, 5′-TGTCTTCCCATCGTCA-3′) and HBx gene (forward primer, 5′-ATGGCTGCTAGGGTGTGCTG-3′ and reverse primer, 5′-CTAGGCAGAGGTGAAAAAGTTGC-3′). As a control, GAPDH was amplified using specific primers (forward, 5′-CATCACCATCTTCCAGGAGCG-3′ and reverse, 5′-TGACCTTGCCCACAGCCTTG-3′). Real-time PCR was performed using double-stranded DNA specific SYBR Green (TaKaRa Bio) and a Bio-Rad sequence detection system according to the manufacturer's instructions. Relative expression was determined by the comparative Ct method using $2^{-\Delta\Delta Ct}$ [26].

Western blot analysis

Cells were washed in PBS, and cellular proteins were extracted in RIPA buffer (Biomed, Beijing, China) for 30 min at 4 °C. Lysates were cleared by centrifugation, and proteins were separated by gel electrophoresis. For tissue protein extraction, frozen tissues were quickly ground into a fine powder using a mortar and pestle under liquid nitrogen and prepared for Western blot analysis as described above. Membranes were blocked in PBS containing 0.1% Tween20 (PBS-T) and 5% (*w/v*) milk for 1 h at room temperature. Membranes were then incubated with primary antibodies diluted in PBS-T for 2 h at room temperature. Subsequently, membranes were washed with PBS-T and incubated with peroxidase-conjugated secondary antibody that was diluted in PBS-T at room temperature for 1 h. Membranes were washed in PBS-T and bound antibody was detected using the enhanced chemiluminescence system ECL-plus Reagents (Amersham Biosciences, Buckinghamshire, UK). After 48 h of transfection, Western blot analysis was performed as described above. The primary antibodies were mouse anti-MEKK2 (Santa Cruz, CA, USA), anti-HBx (Abcam, Cambridge, UK), anti-diphosphorylated JNK (Sigma, St Louis, MO, USA), anti-JNK (Sigma), anti-phosphorylated c-Jun (Cell signaling, Danvers, MA, USA) and mouse anti-β-actin (Sigma).

RNA interference

pSilencer-HBx (pSi-HBx) was used to produce small interfering RNAs (siRNAs) to target HBx mRNA, and pSilencer-control (pSi-con) was used as a negative control[27, 28]. siRNA duplexes targeting human MEKK2 were synthesized and purified by RiboBio (Guangzhou, China)[29]. siRNA duplexes containing non-specific sequences were used as a negative control (NC). Different siRNAs were transfected separately into cells using the Lipofectamine 2000 (Invitrogen) reagent, and the medium was replaced 6 h after transfection.

Construction of the human MEKK2 promoter

To generate a clone of the MEKK2 promoter in a pGL3 basic vector (Promega, Madison, WI, USA), a ~1800-bp region of the putative promoter (from +83 to -1814 nt) was amplified from HepG2 genomic DNA by PCR using specific primers (forward primer, 5′-CCGCTCGAGCTGTAGTCCCATCTACTCGG-3′ and reverse primer, 5′-CCCAAGCTTTTAGTTTGAACTCACCCATT-3′ and was cloned into the pGL3-basic vector.

Luciferase reporter gene assay

Transfected cells were harvested after 36 h. Luciferase activity was determined using the Dual-Luciferase Reporter Assay System (Promega) according to the manufacturer's instructions. The firefly luciferase activity was normalized to Renilla luciferase expression for each sample. All experiments were performed at least three times. pAP1-Luc (Clontech, Plano Alto, CA, USA) is a firefly luciferase reporter gene vector that contains AP-1 binding sites.

Patient samples

The 11 clinical HBV-positive HCC tissues and their corresponding nearby noncancerous livers that were used in this study were obtained from patients who underwent radical resection at Tianjin First Center Hospital (Tianjin, China). All of the tumor samples were immediately frozen after surgical resection and stored in liquid nitrogen until analysis. Written consent, which approved the use of their tissues for research purposes after the operation, was obtained from the patients. The study was approved by the Institute Research Ethics Committee at the Nankai University.

Immunohistochemistry

The hepatocellular carcinoma tissue microarrays were obtained from the Xi-an Aomei Biotechnology Co, Ltd (Xi-an, China). These microarrays were composed of 95 hepatocellular carcinoma (HCC) tissue samples (18 females, 77 males, average age 61 years), which included duplicate core biopsies (1 mm in diameter) from fixed, paraffin-embedded tumors. The immunohistochemical staining of samples was performed as previously reported[27]. The primary antibody of mouse anti-MEKK2 was used (1:50, Abcam). Immunostained slides were evaluated under the microscope. The percentage of cells showing positive nuclear and/or cytoplasmic staining for MEKK2 was calculated by reviewing the entire slide. Based on the percentage of cells with positive nuclear and/or cytoplasmic staining, staining patterns were classified using a six-grade scale as follows: 0, the absence of cell nuclear and/or cytoplasmic staining; 1+, <10% cells with positive nuclear and/or cytoplasmic staining; 2+, 10%–25% positive cells; 3+, 26%–50% positive cells; 4+, 51%–75% positive cells; 5+, >75% positive cells. For statistical analysis, HCC patients were subgrouped into MEKK2-negative staining (scale 0) and MEKK2 positive-staining (scale 1–5) groups. The categorization of immunostaining intensity was performed by three independent observers. The negative control, which lacked incubation with the primary antibody, was treated as described above.

Statistical analysis

All data were expressed as the mean±SD. Statistical analysis was performed using student's *t* test. $P<0.05$ was indicated to be statistically significant.

Results

HBx enhances the proliferation of hepatoma cells

Previously, we established two engineered cell lines, namely HepG2-X, which was stably transfected with HBx, and HepG2-P, which was stably transfected with an empty pcDNA3.0 vector[13]. We examined the growth of HepG2-X cells using the EdU incorporation assay and MTT assay. The results showed that HepG2-X cells grew faster than HepG2-P or HepG2 cells (Figures 1A and 1B). In addition, RNA interference (RNAi) targeting HBx mRNA abolished HBx-induced growth of HepG2 cells. Therefore, the results confirm that HBx enhances the proliferation of hepatoma cells.

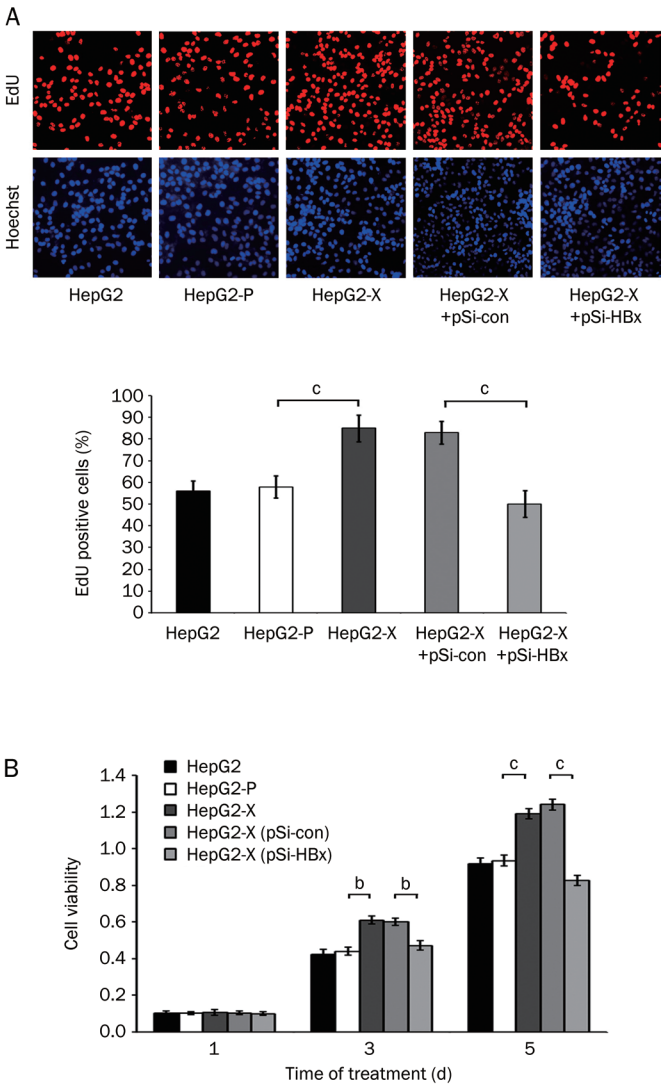

Figure 1. HBx enhances the proliferation of HepG2-X cells. (A, B) The proliferation ability of hepatoma cells was tested using the 5-ethynyl-2-deoxyuridine (EdU) incorporation and MTT assays. Results are representative of three independent experiments. Values represent mean±SD. $^bP<0.05$, $^cP<0.01$, student's *t* test.

HBx upregulates the expression of MEKK2

Previously, we showed using cDNA microarrays that a broad range of genes show aberrant expression in hepatoma cells that overexpress HBx, the results of which included MEKK2

upregulation[30]. To investigate whether MEKK2 is involved in the HBx-mediated growth of hepatoma cells, we further confirmed the effect of HBx on expression of MEKK2. The results show that MEKK2 is significantly upregulated in HepG2-X (or H7402-X) cells at the levels of mRNA and protein, as assessed by RT-PCR and immunoblot analysis (Figure 2A). Meanwhile, we examined the changes of MEKK2 expression after RNA-mediated knockdown of the HBx expression. As expected, the expression level of MEKK2 was decreased in a dose-dependent manner (Figure 2A). Moreover, Western blot analysis showed that MEKK2 was upregulated in HepG2.2.15 cells compared with HepG2 cells (Figure 2B). To investigate the effect of HBx on the promoter activity of MEKK2, we generated a MEKK2 promoter luciferase reporter, which was termed pGL3-MEKK2 pro. Additionally, transient transfection was performed in HepG2 and H7402 cells using the pGL3-MEKK2 promoter plasmid. The promoter activity of MEKK2 was examined in HepG2/H7402 cell lines using luciferase reporter gene assays. The data confirmed the successful construction of the plasmid (Figure 2C). The promoter activity of MEKK2 was remarkably enhanced in HepG2-X/H7402-X cells relative to that in HepG2/H7402 cells (Figure 2D). Meanwhile, the luciferase reporter gene assay showed that HBx RNAi abolished the enhancement of MEKK2 promoter activity in HepG2-X/H7402-X/HepG2.2.15 cells in a dose-dependent manner (Figure 2E).

It has been reported that MEKK2 is involved in the activation of AP-1 and JNK[15, 16, 19]. To further confirm the HBx-mediated regulation of MEKK2, we examined the downstream effectors of MEKK2, such as AP-1 and JNK, in HepG2.2.15 cells. The luciferase report gene assay showed that the activity of AP-1 was decreased in the cells that were treated with HBx RNAi (Figure 3A). AP-1 activation is induced in part by the phosphorylation of c-Jun[31]. To further confirm the luciferase report gene assay result, the phosphorylation level of c-Jun was examined. The Western blot analysis showed that the protein level of MEKK2 and the phosphorylation levels of JNK and c-Jun were decreased (Figure 3B). We silenced the expression of MEKK2 in HepG2.2.15 cells. The data revealed that the knockdown of MEKK2 reduced the activity of AP-1 (Figure 3C). Meanwhile, the phosphorylation levels of JNK and c-Jun were decreased (Figure 3D). Therefore, we conclude that HBx upregulates MEKK2.

MEKK2 contributes to HBx-mediated growth of hepatoma cells

The function of MEKK2 in hepatoma cells is unclear. To elucidate the function of MEKK2, we silenced the expression of MEKK2 in HepG2-X cells using specific siRNAs. The cell proliferation was then measured using EdU incorporation assay and MTT assay. Our results demonstrate that the growth of HepG2-X cell was inhibited by MEKK2 siRNAs (Figure 4A and 4B). Similar effects were observed in HepG2.2.15 cells (Figure 4C and 4D). These results suggest that MEKK2 is involved in HBx-mediated growth of hepatoma cells.

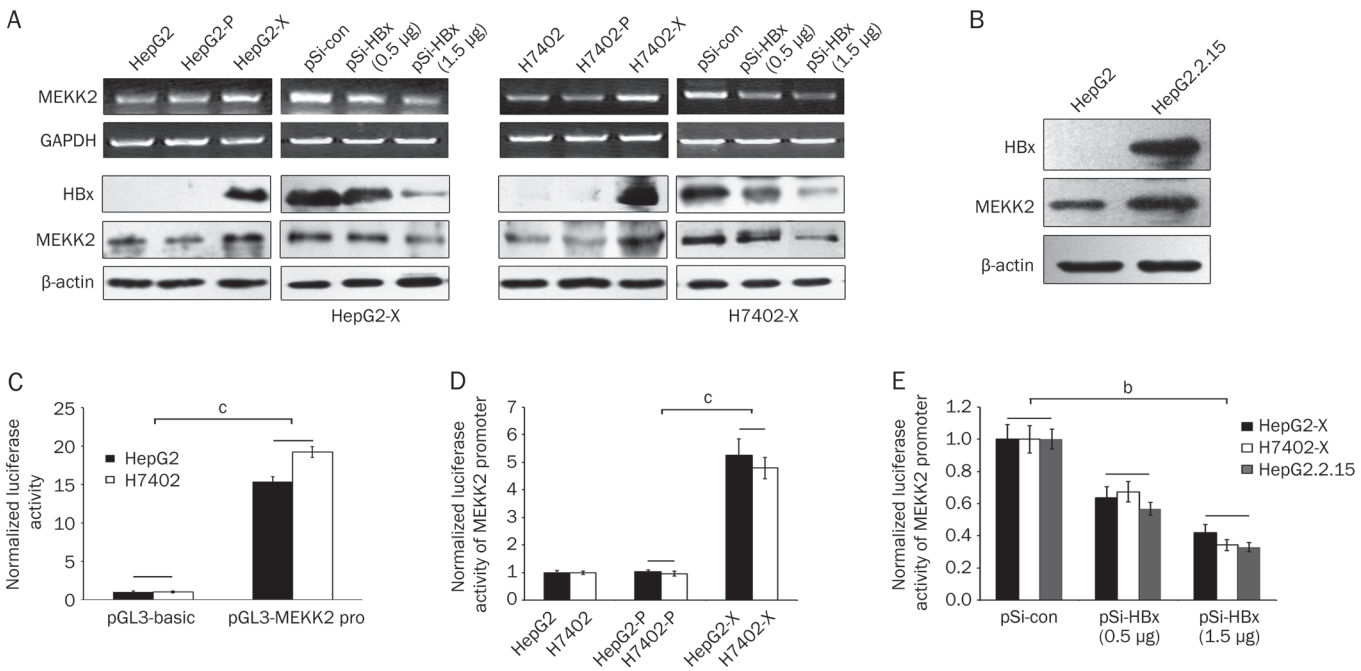

Figure 2. HBx upregulates the expression of MEKK2. (A) The levels of MEKK2 and HBx were detected using RT-PCR and immunoblot analysis. GAPDH and β-actin were used as internal controls. (B) The levels of MEKK2 and HBx were detected in HepG2.2.15 cells using immunoblot analysis. (C) The plasmids of pGL3-MEKK2 pro and pGL3 basic vector were transfected into HepG2 and H7402 cells, respectively. The relative luciferase activity was tested using the luciferase reporter gene assay. (D) The promoter activities of MEKK2 were examined in HepG2-X/H7402-X cells. (E) The promoter activities of MEKK2 were measured after treatment with RNAi that targeted HBx mRNA in HepG2-X/H7402-X/HepG2.2.15 cells in a dose-dependent manner. Results are representative of three independent experiments. Values represent mean±SD. $^{b}P<0.05$, $^{c}P<0.01$, student's *t* test.

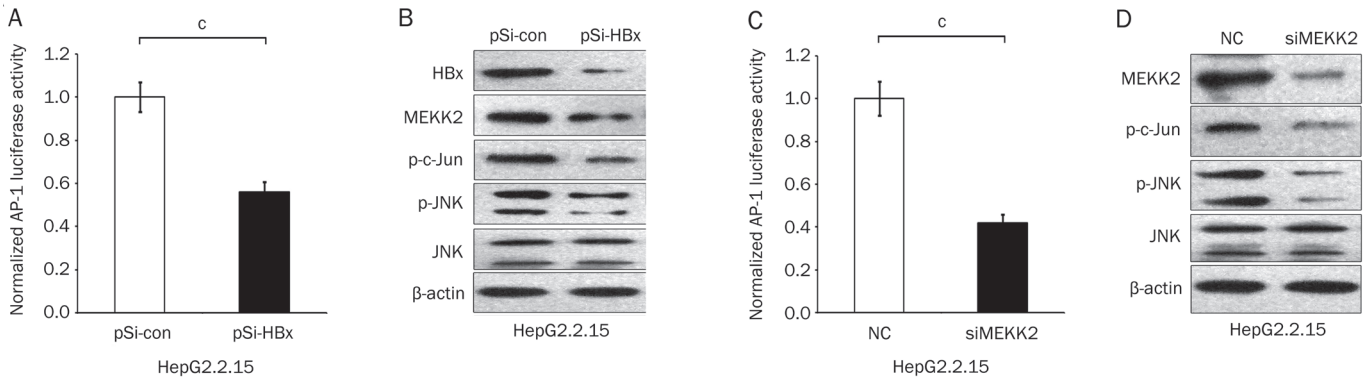

Figure 3. HBx upregulates the expression of MEKK2 to mediate AP-1 and JNK activation. (A) The activity of AP-1 was determined in HepG2.2.15 cells using the luciferase reporter gene assay after HBx RNAi treatment. (B) The phosphorylation levels of JNK and c-Jun were determined using immunoblot analysis. (C) The activity of AP-1 was determined in HepG2.2.15 cells using the luciferase reporter gene assay after MEKK2 RNAi treatment. (D) The phosphorylation levels of JNK and c-Jun were determined using immunoblot analysis. The results are representative of three independent experiments. Values represent mean±SD. $^{c}P<0.01$, student's *t* test.

MEKK2 is overexpressed in clinical HCC tissues

We examined the expression level of MEKK2 in 11 cases of human liver cancer tissues with HBV infection at the mRNA and protein levels using real time PCR and Western blot analysis. Real time PCR analysis revealed that all 11 clinical HCC tissues and their respective peritumor tissues were positive for HBx expression. The expression level of HBx was higher in HCC tissues relative to that in their respective peritumor tissues (Figure 5A). The expression level of MEKK2 was also higher in tumor tissues relative to their peritumor tissues (Figure 5B). Consistent with the results from real time PCR, Western blot analysis revealed that HBx was upregulated in 8 of 11 cases of HCC tissues, whereas MEKK2 was upregulated in 7 of 11 cases (Figure 5C). The clinical data strongly support the conclusion that MEKK2 expression is positively correlated with HBx expression in carcinogenesis. The expression of MEKK2 was assessed using immunohistochemical staining on a tissue microarray that contained 95 cases of HCC tissues. The data showed that the percentage of MEKK2 positivity was 85.3% (81/95 cases) in HCC tissues (Figure 5D).

Discussion

HBx is an essential viral protein that is involved in viral pathogenesis and carcinogenesis. HBx strongly enhances the growth of hepatoma cells in a system of stable transfection[5, 12, 13, 32]. In the current study, we further investigated the mechanism that HBx employs to enhance the proliferation of hepatoma cells. Previously, we examined the expression profiles in stably HBx-transfected hepatoma H7402 (H7402-X) cells using cDNA microarrays[30]. We determined that MEKK2 was one of the upregulated genes. Therefore, we further investigated the role of MEKK2 in HBx-mediated hepatocarcinogenesis.

Previous studies have shown that HBx exhibits either apoptotic or proliferative activities in a context-dependent manner[33, 34]. HBx promotes proliferation in stably transfected cells[5, 12, 13, 32]. Therefore, we investigated the HBx-mediated proliferation in a model of stably HBx-transfected hepatoma HepG2-X cells. We confirmed our previous findings that HBx enhances the proliferation of hepatoma cells in our system (Figure 1). We demonstrated that HBx upregulated MEKK2 at the mRNA and protein level (Figure 2A and 2B). The transcriptional regulation that is mediated by the promoter is a key event in the regulation of gene expression. We demonstrated that HBx activated the promoter activity of MEKK2 in hepatoma cells (Figure 2D). HBx activates AP-1 via a pathway that is mediated by the activation of ERK and JNK[21, 35]. AP-1 and JNK are downstream effectors of MEKK2[15, 16, 19]. To further validate that HBx upregulated MEKK2, we examined the activation of AP-1 and JNK by silencing the expression of HBx or MEKK2 in HepG2.2.15 cells. Our results demonstrate that activation of AP-1 and JNK was inhibited in the cells after siRNA treatment (Figure 3) and support the conclusion that HBx upregulates MEKK2.

At present, few studies have investigated MEKK2 function, even though MEKK2 is involved in osteoblast activity, bone homeostasis and rheumatoid arthritis[19, 20]. In the current study, we demonstrated the function of MEKK2 in hepatoma cells. Our results show that MEKK2 promotes the growth of hepatoma HepG2-X cells and HepG2.2.15 cells, which was characterized using the EdU incorporation and MTT assays (Figure 4). These results suggest that MEKK2 is involved in HBx-mediated proliferation in hepatoma cells. Previously, the clinical significance of MEKK2 in hepatoma tissues has not been elucidated. Therefore, we examined the levels of MEKK2 in 11 cases of clinical HBx-positive hepatoma tissues using real time PCR and Western blot analysis (Figure 5A). Interestingly, we found that the levels of HBx and MEKK2 expression were higher in tumor tissues compared to that in peritumor tissues (Figure 5B). These results suggest that the expression of MEKK2 is positively correlated with HBx expression in carcinogenesis. We are the first to report that the percentage of MEKK2-positive staining is very high (85.3%) in HCC tissues (Figure 5D). This result suggests that MEKK2 is potentially

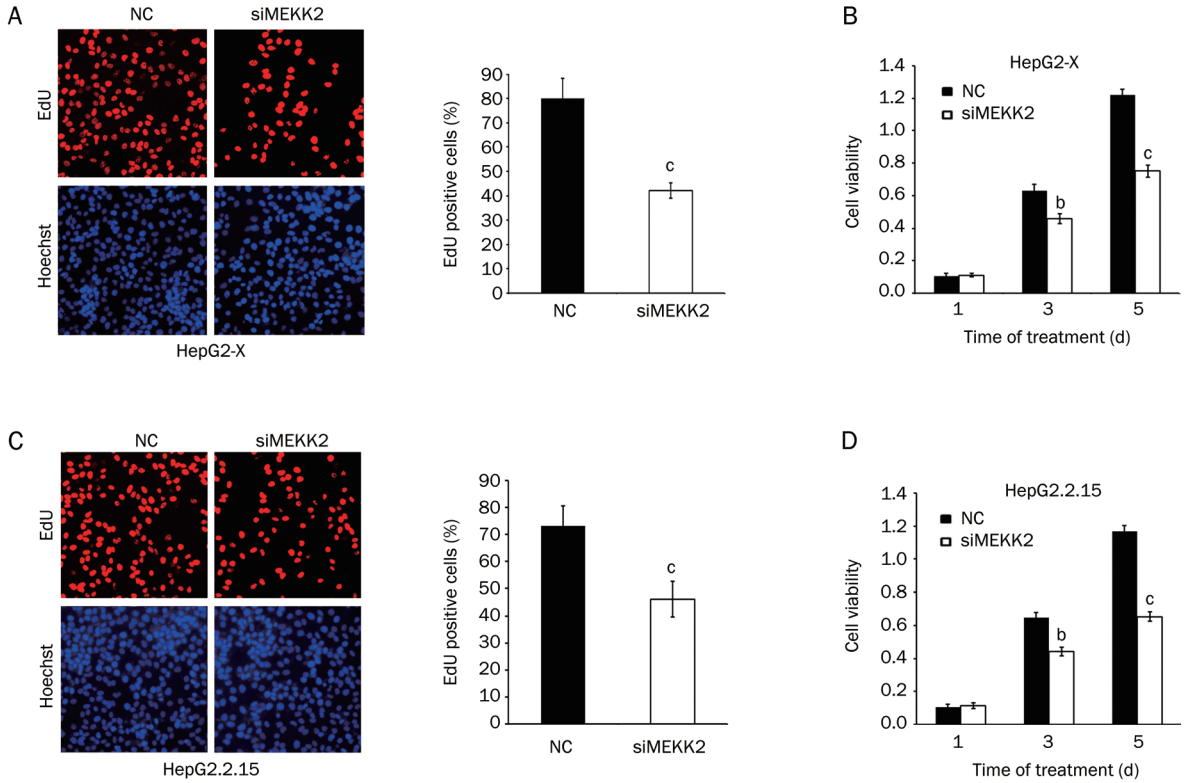

Figure 4. MEKK2 contributes to HBx-mediated growth of hepatoma cells. (A, B) The proliferation ability of HepG2-X cells was tested using the EdU incorporation and MTT assays after MEKK2 siRNA treatment. (C, D) The proliferation ability of HepG2.2.15 cells was tested using the EdU incorporation and MTT assays after MEKK2 siRNA treatment. Results are representative of three independent experiments. Values represent mean±SD. [b]*P*<0.05, [c]*P*<0.01 *vs* NC, student's *t* test.

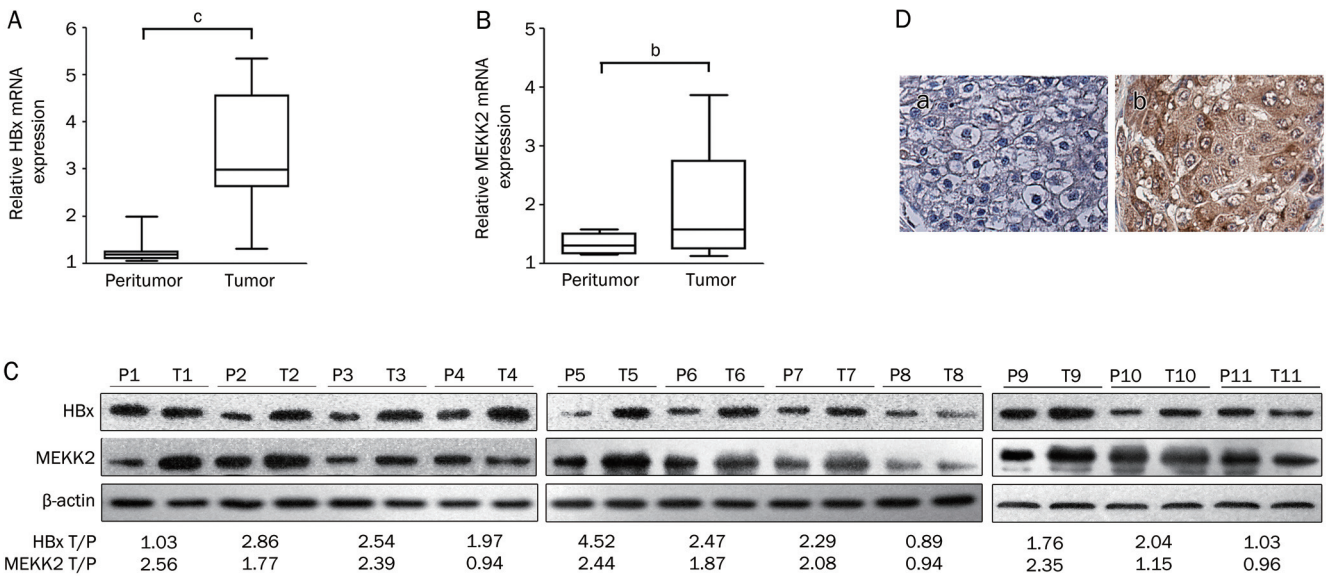

Figure 5. MEKK2 is overexpressed in clinical HCC tissues. (A, B) The relative mRNA expression levels of HBx and MEKK2 were examined in clinical HBx-positive HCC tissues using real time PCR. Values represent mean±SD. [b]*P*<0.05, [c]*P*<0.01, Student's *t* test. (C) The expression levels of HBx and MEKK2 were examined in HCC patients using Western blot analysis. Protein bands were quantified using Quantity One software (Bio-Rad). The value under each pair of samples (T/P), represents the ratio of HBx or MEKK2 expression in the HCC tissue to that in its corresponding peritumor tissue and indicates the fold change in the protein level in HCC. P, peritumor tissue; T, HCC tissue. (D) Immunohistochemical staining showed the expression levels of MEKK2 in HCC tissues using a tissue microarray. (a) Negative control; (b) MEKK2-positive staining. Imaged at 200× magnification.

involved in hepatocarcinogenesis.

In summary, we conclude that HBx upregulates the expression of MEKK2 and that MEKK2 is involved in the promotion of hepatoma cell proliferation, which is mediated by HBx. Our finding suggests that MEKK2 may play important roles in the hepatocarcinogenesis mediated by HBx.

Acknowledgements

This work was supported by grants from the National Basic Research Program of China (973 Program, No 2007CB914802, 2007CB914804 and 2009CB521702) and the National Natural Science Foundation of China (81071624).

Author contribution

Xiao-dong ZHANG, Guang-yao KONG, and Li-hong YE designed the research; Guang-yao KONG, Jun-ping ZHANG, Shuai ZHANG, and Chang-liang SHAN performed the research; Xiao-dong ZHANG, Guang-yao KONG, and Li-hong YE analyzed the data and wrote the paper.

References

1 Koike K. Hepatitis B virus X gene is implicated in liver carcinogenesis. Cancer Lett 2009; 286: 60–8.
2 Zhang X, Zhang H, Ye L. Effects of hepatitis B virus X protein on the development of liver cancer. J Lab Clin Med 2006; 147: 58–66.
3 Liang X, Liu Y, Zhang Q, Gao L, Han L, Ma C, *et al.* Hepatitis B virus sensitizes hepatocytes to TRAIL-induced apoptosis through Bax. J Immunol 2007; 178: 503–10.
4 Mukherji A, Janbandhu VC, Kumar V. HBx-dependent cell cycle deregulation involves interaction with cyclin E/A-cdk2 complex and destabilization of p27Kip1. Biochem J 2007; 401: 247–56.
5 Shan C, Xu F, Zhang S, You J, You X, Qiu L, *et al.* Hepatitis B virus X protein promotes liver cell proliferation via a positive cascade loop involving arachidonic acid metabolism and p-ERK1/2. Cell Res 2010; 20: 563–75.
6 Zhang WY, Cai N, Ye LH, Zhang XD. Transformation of human liver L-02 cells mediated by stable HBx transfection. Acta Pharmacol Sin 2009; 30: 1153–61.
7 Kim CM, Koike K, Saito I, Miyamura T, Jay G. HBx gene of hepatitis B virus induces liver cancer in transgenic mice. Nature 1991; 351: 317–20.
8 Kekule AS, Lauer U, Weiss L, Luber B, Hofschneider PH. Hepatitis B virus transactivator HBx uses a tumour promoter signalling pathway. Nature 1993; 361: 742–5.
9 Natoli G, Avantaggiati ML, Chirillo P, De Marzio E, Collepardo D, Falco M, *et al.* Modulation of intracellular signal transduction pathways by the hepatitis B virus transactivator pX. J Hepatol 1995; 22: 14–20.
10 Lee YH, Yun Y. HBx protein of hepatitis B virus activates Jak1-STAT signaling. J Biol Chem 1998; 273: 25510–5.
11 Diao J, Khine AA, Sarangi F, Hsu E, Iorio C, Tibbles LA, *et al.* X protein of hepatitis B virus inhibits Fas-mediated apoptosis and is associated with up-regulation of the SAPK/JNK pathway. J Biol Chem 2001; 276: 8328–40.
12 Wang Q, Zhang WY, Ye LH, Zhang XD. A mutant of HBx (HBxDelta127) promotes hepatoma cell growth via sterol regulatory element binding protein 1c involving 5-lipoxygenase. Acta Pharmacol Sin 2010; 31: 367–74.
13 Wang Q, Zhang W, Liu Q, Zhang X, Lv N, Ye L, *et al*. A mutant of hepatitis B virus X protein (HBxDelta127) promotes cell growth through a positive feedback loop involving 5-lipoxygenase and fatty acid synthase. Neoplasia 2010; 12: 103–15.
14 Pearson G, Robinson F, Beers Gibson T, Xu BE, Karandikar M, Berman K, *et al.* Mitogen-activated protein (MAP) kinase pathways: regulation and physiological functions. Endocr Rev 2001; 22: 153–83.
15 Su B, Cheng J, Yang J, Guo Z. MEKK2 is required for T-cell receptor signals in JNK activation and interleukin-2 gene expression. J Biol Chem 2001; 276: 14784–90.
16 Chayama K, Papst PJ, Garrington TP, Pratt JC, Ishizuka T, Webb S, *et al.* Role of MEKK2-MEK5 in the regulation of TNF-alpha gene expression and MEKK2-MKK7 in the activation of c-Jun N-terminal kinase in mast cells. Proc Natl Acad Sci U S A 2001; 98: 4599–604.
17 Schaefer BC, Ware MF, Marrack P, Fanger GR, Kappler JW, Johnson GL, *et al.* Live cell fluorescence imaging of T cell MEKK2: redistribution and activation in response to antigen stimulation of the T cell receptor. Immunity 1999; 11: 411–21.
18 Sun W, Wei X, Kesavan K, Garrington TP, Fan R, Mei J, *et al.* MEK kinase 2 and the adaptor protein Lad regulate extracellular signal-regulated kinase 5 activation by epidermal growth factor via Src. Mol Cell Biol 2003; 23: 2298–308.
19 Yamashita M, Ying SX, Zhang GM, Li C, Cheng SY, Deng CX, *et al*. Ubiquitin ligase Smurf1 controls osteoblast activity and bone homeostasis by targeting MEKK2 for degradation. Cell 2005; 121: 101–13.
20 Hammaker DR, Boyle DL, Chabaud-Riou M, Firestein GS. Regulation of c-Jun N-terminal kinase by MEKK-2 and mitogen-activated protein kinase kinase kinases in rheumatoid arthritis. J Immunol 2004; 172: 1612–8.
21 Jacqueline B, Fei S, Margherita D, Robert JS. Hepatitis B virus HBx protein induces transcription factor AP-1 by activation of extracellular signal-regulated and c-Jun N-terminal mitogen-activated protein kinases. J Virol 1996; 70: 4978–85.
22 Witowsky J, Abell A, Johnson NL, Johnson GL, Cuevas BD. MEKK1 is required for inducible urokinase-type plasminogen activator expression. J Biol Chem 2003; 278: 5941–6.
23 Garrington TP, Ishizuka T, Papst PJ, Chayama K, Webb S, Yujiri T, *et al.* MEKK2 gene disruption causes loss of cytokine production in response to IgE and c-Kit ligand stimulation of ES cell-derived mast cells. EMBO J 2000; 19: 5387–95.
24 Cazares LH, Troyer D, Mendrinos S, Lance RA, Nyalwidhe JO, Beydoun HA, *et al*. Imaging mass spectrometry of a specific fragment of mitogen-activated protein kinase/extracellular signal-regulated kinase kinase kinase 2 discriminates cancer from uninvolved prostate tissue. Clin Cancer Res 2009; 15: 5541–51.
25 Salic A, Mitchison TJ. A chemical method for fast and sensitive detection of DNA synthesis *in vivo*. Proc Natl Acad Sci U S A 2008; 105: 2415–20.
26 Wang FZ, Sha L, Zhang WY, Wu LY, Qiao L, Li N, *et al.* Involvement of hepatitis B X-interacting protein (HBXIP) in proliferation regulation of cells. Acta Pharmacol Sin 2007; 28: 431–8.
27 Zhang X, Dong N, Yin L, Cai N, Ma H, You J, *et al.* Hepatitis B virus X protein upregulates survivin expression in hepatoma tissues. J Med Virol 2005; 77: 374–81.
28 Zhang H, Shan CL, Li N, Zhang X, Zhang XZ, Xu FQ, *et al.* Identification of a natural mutant of HBV X protein truncated 27 amino acids at the COOH terminal and its effect on liver cell proliferation. Acta Pharmacol Sin 2008; 29: 473–80.
29 Winsauer G, Resch U, Hofer-Warbinek R, Schichl YM, de Martin R. XIAP regulates bi-phasic NF-kappaB induction involving physical interaction and ubiquitination of MEKK2. Cell Signal 2008; 20: 2107–12.

30 Ye L, Dong N, Wang Q, Xu Z, Cai N, Wang H, *et al*. Progressive changes in hepatoma cells stably transfected with hepatitis B virus X gene. Intervirology 2008; 51: 50–8.
31 Shaulian E, Karin M. AP-1 as a regulator of cell life and death. Nat Cell Biol 2002; 4: E131–6.
32 Wang F, Zhou H, Xia X, Sun Q, Wang Y, Cheng B. Activated Notch signaling is required for hepatitis B virus X protein to promote proliferation and survival of human hepatic cells. Cancer Lett 2010; 298: 64–73.
33 Kim KH, Seong BL. Pro-apoptotic function of HBV X protein is mediated by interaction with c-FLIP and enhancement of death-inducing signal. EMBO J 2003; 22: 2104–16.
34 Shih WL, Kuo ML, Chuang SE, Cheng AL, Doong SL. Hepatitis B virus X protein inhibits transforming growth factor-beta-induced apoptosis through the activation of phosphatidylinositol 3-kinase pathway. J Biol Chem 2000; 275: 25858–64.
35 Nijhara R, Jana SS, Goswami SK, Rana A, Majumdar SS, Kumar V, *et al*. Sustained activation of mitogen-activated protein kinases and activator protein 1 by the hepatitis B virus X protein in mouse hepatocytes *in vivo*. J Virol 2001; 75: 10348–58.

Acta Pharmacologica Sinica (2011) 32: 1181–1190
 1671-4083/11 $32.00
www.nature.com/aps

Original Article

In vitro and *in vivo* percutaneous absorption of seleno-*L*-methionine, an antioxidant agent, and other selenium species

Chih-hung LIN[1], Chia-lang FANG[2], Saleh A AL-SUWAYEH[3], Shih-yun YANG[4], Jia-you FANG[3, 4, 5, *]

[1]Center for General Education, Chang Gung University of Science and Technology, Kweishan, Taoyuan, Taiwan, China; [2]Department of Pathology, College of Medicine, Taipei Medical University, Taipei, Taiwan, China; [3]Department of Pharmaceutics, College of Pharmacy, King Saud University, Riyadh, Saudi Arabia; [4]Pharmaceutics Laboratory, Graduate Institute of Natural Products, Chang Gung University, Kweishan, Taoyuan, Taiwan, China; [5]Department of Cosmetic Science, Chang Gung University of Science and Technology, Kweishan, Taoyuan, Taiwan, China

Aim: To investigate the *in vitro* and *in vivo* percutaneous absorption of seleno-*L*-methionine (Se-*L*-M), an ultraviolet (UV)-protecting agent, from aqueous solutions.
Methods: Aqueous solutions of Se-*L*-M were prepared in pH 4, 8, and 10.8 buffers. The pH 8 buffer contained 30% glycerol, propylene glycol (PG) and polyethylene glycol (PEG) 400. The *in vitro* skin permeation of Se-*L*-M via porcine skin and nude mouse skin was measured and compared using Franz diffusion cells. The *in vivo* skin tolerance study was performed, which examined transepidermal water loss (TEWL), skin pH and erythema.
Results: In the excised porcine skin, the flux was 0.1, 11.4 and 8.2 $\mu g \cdot cm^{-2} \cdot h^{-1}$ for the pH 4, 8, and 10.8 buffers, respectively. A linear correlation between the flux and skin deposition was determined. According to permeation across skin with different treatments (stripping, delipidation, and ethanol treatments), it was determined that the intracellular route comprised the predominant pathway for Se-*L*-M permeation from pH 8 buffer. Aqueous solutions of seleno-*DL*-methionine (Se-*DL*-M), selenium sulfide and selenium-containing quantum dot nanoparticles were also used as donor systems. The *DL* form showed a lower flux (7.0 *vs* 11.4 $\mu g \cdot cm^{-2} \cdot h^{-1}$) and skin uptake (23.4 *vs* 47.3 μg/g) as compared to the *L* form, indicating stereoselective permeation of this compound. There was no or only negligible permeation of selenium sulfide and quantum dots into and across the skin. With *in vivo* topical application for 4 and 8 h, the skin deposition of Se-*L*-M was about 7 μg/g, and values were comparable to each other. The topical application of Se-*L*-M for up to 5 d did not caused apparent skin irritation. However, slight inflammation of the dermis was noted according to the histopathological examination.
Conclusion: Se-*L*-M was readily absorbed by the skin in both the *in vitro* and *in vivo* experiments. The established profiles of Se-*L*-M skin absorption will be helpful in developing topical products of this compound.

Keywords: seleno-*L*-methionine; selenium; percutaneous absorption; topical delivery; skin

Acta Pharmacologica Sinica (2011) 32: 1181–1190; doi: 10.1038/aps.2011.89; published online 25 Jul 2011

Introduction

Skin is constantly exposed to prooxidant environmental stresses from an array of sources, such as air pollutants, solar ultraviolet (UV) light, chemical oxidants, microorganisms, and ozone[1]. Reactive oxygen species (ROS) were implicated in the etiology of several skin disorders including skin cancer and photoaging. Skin cancer constitutes about 30% of all newly diagnosed cancers in the world and solar UV radiation, particularly the UVB component, is an established cause of about 90% of skin cancers[2]. In recent years, particular antioxidants have gained considerable attention as means of neutralizing ROS. This group includes vitamins (C and E), phytochemicals (carotenoids and polyphenols), and minerals (zinc and selenium)[3]. There is much evidence to suggest that selenium has an important role in protecting skin from the harmful effects of UVB. Selenium, an essential trace element, is found in many foods, including meat, fish, eggs, dairy products, and grains[4]. The UVB protection afforded by selenium compounds is attributed to their ability to increase activities of glutathione peroxidase and thioredoxin reductase which are

* To whom correspondence should be addressed.
E-mail fajy@mail.cgu.edu.tw
Received 2011-03-09 Accepted 2011-05-30

antioxidant selenoenzymes[5]. In humans, a low selenium status is associated with up to a 4-fold increased risk of developing skin cancer[6]. Topical selenium compounds also increase the minimum dose of UV radiation required to cause skin reddening and protect against skin damage caused by UVB[7, 8]. Seleno-*L*-methionine (Se-*L*-M), the major component of dietary selenium, represents an organic form of selenium which may provide enhanced protection of the skin[9]. Se-*L*-M also decreases the oxidative stress of neurodegenerative diseases, rheumatoid arthritis, and HIV/AIDS[10, 11].

Most ingested selenium, whether in organic or inorganic form, is converted by liver metabolism[3]. In addition, selenium toxicity can produce gastrointestinal problems[12]. Delivery of pharmacologically active compounds via the skin is an attractive alternative to oral dosing for numerous reasons including stable plasma concentrations, bypass of first-pass effects, and reduction of some side effects[13, 14]. Topical delivery via the skin may provide direct selenium targeting to attain sufficient activity for skin prevention/therapy. Topical administration may also be a suitable route for selenium to achieve systemic bioavailability to maintain daily necessities and treat systemic disorders.

No evidence currently exists to support the notion that significant amounts of Se-*L*-M can be delivered into and across the skin. The number of specific metals that was investigated for skin permeation is also limited[15]. The aim of this work was to establish skin permeation profiles of Se-*L*-M from various vehicles. The permeation via the skin of other selenium species, such as seleno-*DL*-methionine (Se-*DL*-M), selenium sulfide (SeS_2), and cadmium selenium (CdSe) quantum dots was also evaluated. Both *in vitro* and *in vivo* skin absorption experiments were performed in this study. To study the *in vitro* potential of these compounds, a permeation study was performed with Franz diffusion cells using excised porcine and nude mouse skin. The optimal pH and type of vehicles for better absorption of Se-*L*-M were investigated. Possible pathways of this antioxidant via the skin were elucidated using porcine skin treated by stripping, delipidation, oleic acid, and α-terpineol to indicate the specific routes of skin absorption. Possible skin irritation of Se-*L*-M was studied by histopathology and *in vivo* bioengineering techniques using nude mice as the animal model.

Materials and methods

Materials

Se-*L*-M, Se-*DL*-M, selenium sulfide, Lumidot™ CdSe quantum dots, Lumidot™ CdSe/ZnS quantum dots, oleic acid, and α-terpineol were purchased from Sigma-Aldrich (St Louis, MO, USA). Cellulose membranes with a molecular weight (Mw) cutoff of 3500 (Spectra Por™ 3) were supplied by Spectrum Laboratories (Rancho Dominguez, CA, USA). All other chemicals and solvents were of analytical grade and were used as received.

Animals

Specific pathogen-free (SPF) pigs (1 week old) were supplied by the Animal Technology Institute Taiwan (Miaoli, Taiwan, China). Female nude mice (8 weeks old) were obtained from the National Laboratory Animal Center (Taipei, Taiwan, China). The animal experiment protocol was reviewed and approved by the Institutional Animal Care and Use Committee of Chang Gung University. Animals were housed and handled according to institutional guidelines.

Preparation of skin membranes

Full-thickness skin was excised from the dorsal region of pigs and mice. Subcutaneous fat, tissues, blood vessels, and epidermal hairs were carefully removed before use. The skin was stripped 20 times with adhesive tape in the study to obtain stratum corneum (SC)-stripped skin. To obtain delipidized skin, the SC side was pretreated with chloroform-methanol (2:1) for 2 h. Five percent oleic acid or α-terpineol in a 25% ethanol/water medium was used to pretreat the skin mounted on a Franz cell for 2 h before the *in vitro* skin permeation experiment.

In vitro skin permeation

Porcine or nude mouse skin with or without pretreatment was mounted on the receptor compartment of a Franz cell with the SC side facing upwards into the donor compartment. The receptor was filled with 5.5 mL of pH 7.4 citrate-phosphate buffer, and maintained at 37 °C under constant stirring. The donor compartment was occluded by parafilm and filled with 0.5 mL of vehicle containing Se-*L*-M or other selenium species at determined concentrations. The available diffusion area between the compartments was 0.79 cm^2. At appropriate intervals, 300-μL aliquots of the receptor medium were withdrawn and immediately replaced with an equal volume of fresh medium.

At the end of the *in vitro* experiment (24 h), the skin was removed from the cell and the skin surface was cleaned with a cotton wool swab immersed in water and methanol three times each for removing any contaminent. The skin was weighed, cut with scissors, positioned in a glass homogenizer containing 1 mL of 0.1 mol/L HCl, and homogenized for 10 min at 300 revolutions per minute. The resulting solution was centrifuged for 10 min at 10 000 revolutions per minute and then filtered through a polyvinylidene difluoride membrane with a pore size of 0.45 μm. All samples were analyzed by graphite furnace atomic absorption spectrophotometry (Z-5000, Hitachi, Tokyo, Japan). The wavelength set for selenium was 196 nm. At the range 0–40 μg/L, the concentration of selenium was linearly proportional to its absorbance. The limit of detection (LOD) of selenium was determined to be 3 μg/L. The intra- and inter-assay precision and accuracy values were evaluated at the concentration range 0–40 μg/L. The overall precision, defined by the relative standard deviation (RSD), ranged from 0.4% to 3.1% on average. Analytical accuracy, expressed as the percentage difference between the mean of measured value and the known concentration, varied from -3.3% to 2.1%.

In vivo skin permeation

Nude mice were used as the animal model in the *in vivo* experiment. All animals were starved overnight prior to the experiment. A glass cylinder with an available area of 0.79 cm^2 was placed on the dorsal skin with glue (Instant Super Glue™, Kokuyo, Tokyo, Japan). An aliquot of 0.2 mL of pH 8 citrate-phosphate buffer with Se-*L*-M at a concentration of 0.2% (*w/v*) was added to the cylinder. The application times of the vehicle were 4 and 8 h. The procedures for washing and extraction of the compound from the skin were the same as for the *in vitro* experiment.

In vivo skin tolerance test

A 0.6-mL aliquot of pH 8 buffer with 0.2% or 0.3% Se-*L*-M was uniformly spread over a sheet of non-woven polyethylene cloth (1.5 cm×1.5 cm), which was then applied to the back area of a nude mouse. The polyethylene cloth was fixed with Tegaderm™ adhesive dressing (3M, St Paul, MN, USA) and Fixomull™ stretch adhesive tape (Beiersdorf AG, Hamburg, Germany). After 24 h, the cloth was removed, and the treated skin area was swabbed clean with a cotton wool swab. The vehicle was applied daily for 5 d. After withdrawal of the vehicle, transepidermal water loss (TEWL), colorimetric parameters, and the pH of the applied skin were measured. These measurements were evaluated daily. TEWL was recorded using a Tewameter™ (TM300, Courage and Khazaka, Köln, Germany). Measurements taken at a stable level were performed 30 s after application of the TEWL probe to the skin. TEWL was automatically calculated and expressed in $g \cdot m^{-2} \cdot h^{-1}$. The skin-surface pH was determined by a Skin-pH-Meter™ PH905 (Courage and Khazaka). A spectrocolorimeter (CD100, Yokogawa Electrical, Tokyo, Japan) was used to measure the skin erythema (a*) according to recommendations of the Commission Internationale de l'Eclarirage (CIE). When recording color values, the measuring head was held perpendicular to the back skin. The reading was obtained within a few seconds on the display. The temperature and relative humidity in the laboratory were kept at 26 °C and 55%, respectively. The sample number for each experiment was six.

Histopathological examination

The dorsal skin of nude mouse was excised after topical administration of pH 8 buffer with 0.2% or 0.3% Se-*L*-M for 5 d. Each skin specimen was dehydrated using ethanol, embedded in paraffin wax, and stained with hematoxylin and eosin. For each skin sample, three different sites were examined and evaluated under light microscopy (Eclipse 4000, Nikon, Tokyo, Japan). Digital photomicrographs were then processed with Adobe PhotoDeluxe (Adobe Systems, San Jose, CA, USA).

Statistical analysis

Statistical analyses of differences between the various treatments were performed using an unpaired Student's *t*-test. A 0.05 level of probability ($P<0.05$) was taken as the level of significance. An analysis of variance (ANOVA) test was also used if necessary.

Results

Optimization of vehicles for *in vitro* skin permeation of Se-*L*-M

Optimization of topical drug bioavailability is an essential objective for the effective treatment of skin disorders. The pH and composition of vehicles, and the applied dose were shown to be major variables influencing the diffusivity of permeants. The effects of the pH 4–10.8 buffers on skin permeation of Se-*L*-M were examined. Se-*L*-M is an amino acid containing selenium. According to the dissociation constant (pK_a) values of Se-*L*-M (2.19 and 9.05)[16], this compound is mainly in cationic, zwitterionic, and anionic forms at pH 4, 8, and 10.8, respectively. The solubility of Se-*L*-M in water is up to 1000 mg/mL, which can be associated with a risk of local toxicity if applied topically. The finite dose technique was applied in this study, although the maximal thermodynamic activity could not be obtained. All donor samples for testing the pH effect were prepared by dispersing 0.2% Se-*L*-M in buffer. Figure 1 shows the permeation profiles of Se-*L*-M across porcine skin and nude mouse skin as the means and standard deviations plotted against time. The flux value ($\mu g \cdot cm^{-2} \cdot h^{-1}$) is equal to the slope of the linear permeation profile and was calculated from the experimental curves shown in Figure 1. Table 1 summarizes the Se-*L*-M flux from various buffer solutions. A zero-order equation was suitable for use with the curves of most

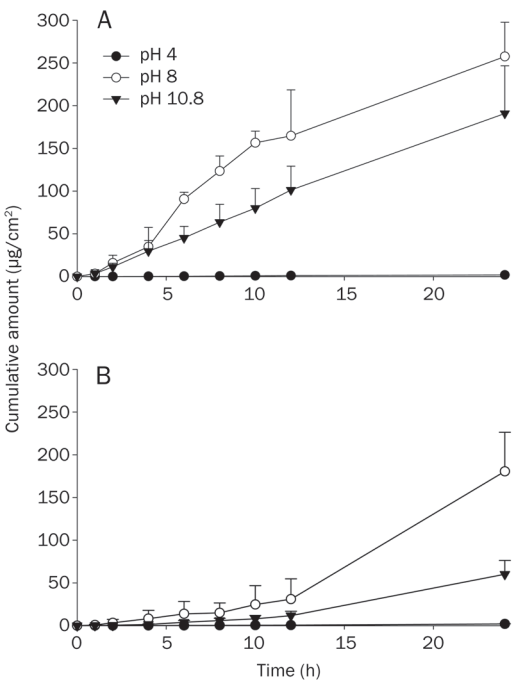

Figure 1. *In vitro* cumulative amount *versus* time profiles of the topical application of seleno-*L*-methionine permeating across porcine (A) and nude mouse skin (B) from pH 4, 8, and 10.8 buffers. All data are presented as mean±SD. $n=4$ experiments.

formulations, except the results of pH 8 buffer via nude mouse skin.

The pH of the vehicle had a significant effect on the transport of Se-*L*-M. As shown in Figure 1A, the permeability across porcine skin increased in the order of pH 8>pH 10.8>pH 4. The same trends were detected for both porcine and nude mouse skin (Figure 1A *vs* 1B). Based on the flux values shown in Table 1, the difference between pH 8 and 10.8 was not significant ($P>0.05$) according to a *t*-test in the case of porcine skin. For topical bioavailability purposes, the permeant retained in the strata of the skin should be included. Only considering the permeant flux reaching the receptor compartment may underestimate the true level of skin absorption. The skin deposition of Se-*L*-M by *in vitro* topical application is depicted in Table 1. The skin with no treatment (blank control) showed no selenium content above the detection limit of atomic absorption. A correlation was noted between porcine skin retention and the flux. A *t*-test revealed that there was no statistically significant difference ($P>0.05$) in the skin accumulation between pH 8 and 10.8 buffers in porcine skin. Se-*L*-M accumulation within nude mouse skin was greatest with the pH 8 buffer and least from the pH 4 buffer.

Table 1. *In vitro* flux and skin deposition of 0.2% seleno-*L*-methionine from buffers with various pH values via porcine skin and nude mouse skin. Each data represents the mean±SD. $n=4$.

Skin	pH	Flux ($\mu g \cdot cm^{-2} \cdot h^{-1}$)	Skin deposition ($\mu g/g$)
Porcine	4	0.09±0.07	5.29±1.54
	8	11.41±1.86	47.27±8.98
	10.8	8.22±2.39	47.31±5.47
Nude mouse	4	0.08±0.01	12.36±1.53
	8	7.56±1.90	123.87±35.75
	10.8	6.56±0.66	91.30±16.96

Table 2 summarizes the permeation data of Se-*L*-M from pH 8 buffer with 30% organic solvents of glycerol, PG, and PEG400. Porcine skin was used as the permeation barrier. The permeation of Se-*L*-M from the buffer containing the organic solvents was significantly lower ($P<0.05$) compared to the neat pH 8 buffer. The flux and skin reservoir of Se-*L*-M from pH 8 buffer were greater than those from the buffer with organic solvents by 2.5–5-fold. The general trend for the flux was PG>glycerol≥PEG400. There was no significant difference ($P>0.05$) among the skin deposition levels of the compound from the three vehicles.

Table 2. *In vitro* flux and skin deposition of 0.2% seleno-*L*-methionine from pH 8 buffers with various cosolvents via porcine skin. Each data represents the mean±SD. $n=4$.

Vehicle	Flux ($\mu g \cdot cm^{-2} \cdot h^{-1}$)	Skin deposition ($\mu g/g$)
30% Glycerol/pH 8 buffer	2.55±0.59	18.21±6.10
30% PG/pH 8 buffer[a]	4.45±1.04	12.26±2.36
30% PEG400/pH 8 buffer[b]	2.18±0.38	14.52±3.61

[a]PG, propylene glycol. [b]PEG400, polyethylene glycol 400.

The Se-*L*-M flux and skin deposition from pH 8 buffer with different doses of 0.05%–0.3% are respectively shown in Figure 2A and 2B. A linear correlation ($r=0.9748$) was apparent between the dose and flux across porcine skin. No significant difference ($P>0.05$) in the flux was observed between the doses of 0.2% and 0.3%. A linear relationship was not observed in nude mouse skin since a lower flux ($P<0.05$) was detected in the formulation with the 0.3% compound compared to that with 0.1% and 0.2%. As depicted in Figure 2B, the porcine skin reservoir generally increased with an increase in the Se-*L*-M dose except at 0.3%. A correlation of $r=0.7858$ was observed between the dose and porcine skin deposition. The same as the permeant flux via nude mouse skin, the skin deposition from the donor with 0.3% was relatively lower compared to that with 0.2% ($P<0.05$).

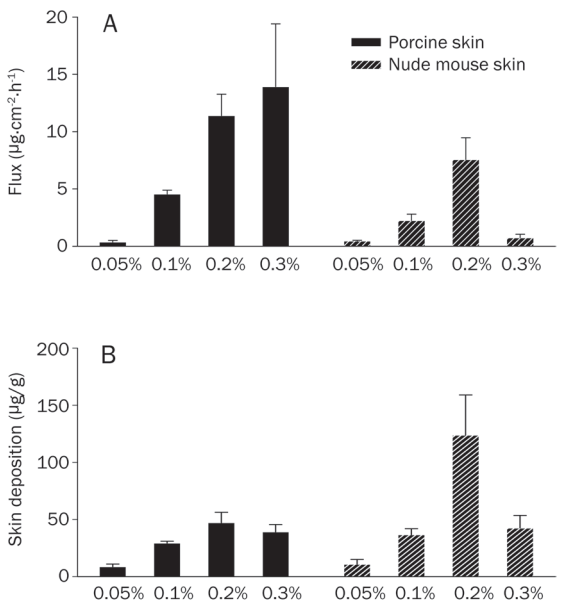

Figure 2. *In vitro* flux (A) and skin deposition (B) of seleno-*L*-methionine from pH 8 buffer with different doses of 0.05%–0.3% across porcine and nude mouse skin. All data are presented as mean±SD. $n=4$ experiments.

In vitro skin permeation of Se-*L*-M via various skin types

In order to elucidate the mechanisms involved in the skin permeation of Se-*L*-M, *in vitro* permeation experiments to examine the cumulative amount in the receptor were performed using various skin membranes. Although an examination of permeation across skin is less advantageous when targeting skin tissue, an understanding of the permeability is helpful in exploring the mechanisms or pathways of skin absorption. Figure 3 shows the cumulative amount–time profiles of Se-*L*-M from pH 4, 8, and 10.8 buffers via different skin types. Se-*L*-

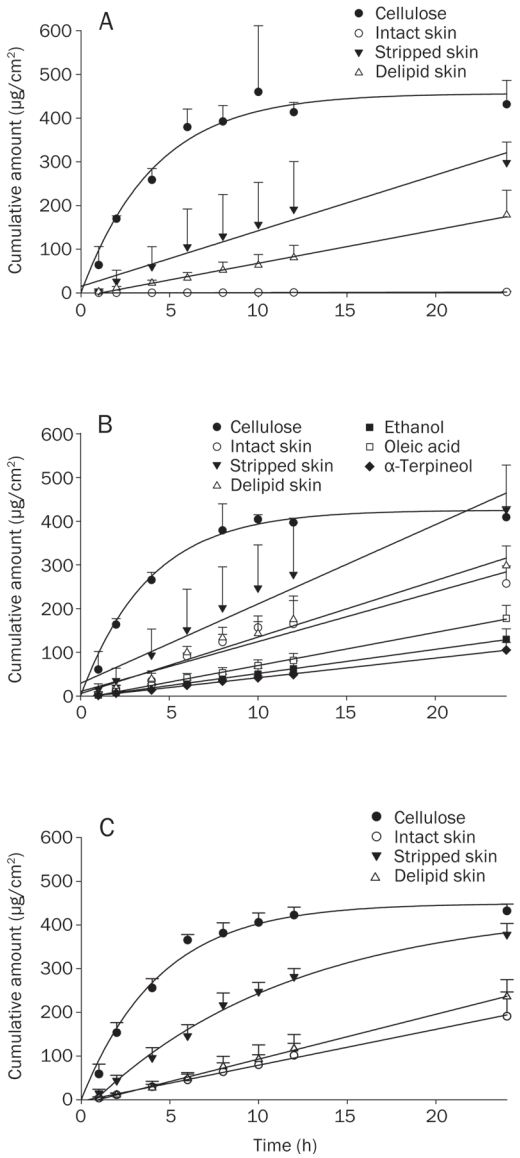

Figure 3. *In vitro* cumulative amount *versus* time profiles of the topical application of seleno-*L*-methionine permeating across various skin types from pH 4 (A), 8 (B), and 10.8 (C) buffers. All data are presented as mean±SD. *n*=4 experiments.

M diffusion across the cellulose membrane was determined to evaluate release rates from the buffers. The results indicated that the release of the permeant was faster than permeation across porcine skin. The release kinetics showed an initial burst (0–4 h), followed by a sustained burst (4–8 h), and a plateau (8–24 h). This trend and the level of release were similar for all buffers tested. Among the permeation curves, Se-*L*-M permeation across SC-stripped skin mostly approximated the data across the cellulose membrane, followed by delipidized skin and intact skin. According to the cumulative amount at 24 h (the end of the experiment), Se-*L*-M permeation across stripped skin was 158-, 1.7-, and 2.0-fold greater (P<0.05) than that across intact skin from pH 4, 8, and 10.8 buffers, respectively.

To further explore the permeation mechanisms, 3% oleic acid and α-terpineol in 25% ethanol/pH 7.4 buffer were used to pretreat porcine skin. Ethanol at 25% was used as the pretreatment medium for solubility considerations of oleic acid and α-terpineol. As shown in Figure 3B, pretreatment with 25% ethanol significantly reduced (P<0.05) Se-*L*-M permeation by 2-fold compared to intact skin. Treatment with oleic acid slightly but significantly increased (P<0.05) the cumulative amount over the 25% ethanol-treated group. On the other hand, pretreatment of the skin with α-terpineol did not further increase (P>0.05) permeation.

In vitro skin permeation of different selenium species

The skin delivery of other selenium species was also studied in the present work. These included Se-*DL*-M, selenium sulfide, and CdSe quantum dots. The flux and skin deposition of the selenium compounds are given in Table 3. The enantioselective transfer of selenomethionine via porcine skin was studied. Both the flux and skin deposition of Se-*L*-M increased more than those of Se-*DL*-M (P<0.05). From this, it is clear that the *L* form can pass more easily through the skin barrier than the *DL* form. This trend was especially significant with skin deposition since the *L* form showed 2-fold higher skin uptake than the *DL* form. Selenium sulfide could not pass across the skin into the receptor with a 24-h application. An *in vitro* uptake of 0.36 μg/g of selenium sulfide was found within the skin. The skin absorption of two types of quantum dots, CdSe and CdSe/ZnS, was tested. No selenium was detected in either the skin reservoir or receptor as shown in Table 3.

Table 3. *In vitro* flux and skin deposition of 0.2% different selenium species from pH 8 buffer via porcine skin. Each data represents the mean±SD. *n*=4.

Species	Flux ($\mu g \cdot cm^{-2} \cdot h^{-1}$)	Skin deposition (μg/g)
Seleno-*L*-methionine	11.41±1.86	47.27±8.98
Seleno-*DL*-methionine	7.04±1.85	23.42±8.90
Selenium sulfide	0	0.36±0.13
CdSe quantum dots	0	0
CdSe/ZnS quantum dots	0	0

In vivo skin permeation of Se-*L*-M

Levels of Se-*L*-M in the skin were determined following a single application of pH 8 buffer to the dorsal surface of nude mice. *In vivo* percutaneous absorption was evaluated using nude mice because they are easy to handle. Table 4 shows the *in vivo* skin deposition of Se-*L*-M after topical delivery for 4 and 8 h. Skin uptake of the compound exhibited values of 7.8 and 7.2 μg/g, respectively. There was no significant difference (P>0.05) between the intradermal concentrations of Se-*L*-M at 4 and 8 h.

Table 4. *In vivo* skin deposition (μg/g) of seleno-*L*-methionine from buffers with various pH values via nude mouse skin. Each data represents the mean±SD. *n*=6.

Time (h)	Skin deposition (μg/g)
4	7.82±0.36
8	7.24±0.18

Bioengineering methods such as TEWL, pH, and colorimetry were conducted *in vivo* to evaluate the preliminary safety of Se-*L*-M on skin. pH 8 buffer containing 0.2% and 0.3% Se-*L*-M was applied to the dorsal skin of nude mice for 24 h. The total duration of application was 5 d. Values of TEWL, pH, and erythema (a*) were determined every day as shown in Figure 4. Compared to the control group (pH 8 buffer without Se-*L*-M), no enhancement of TEWL and pH values was observed after application of Se-*L*-M for 5 d (Figure 4A, 4B). The same result was detected for skin erythema after topical Se-*L*-M delivery (Figure 4C). This suggests tolerable changes in the skin with topically applied Se-*L*-M. No visible disruption of the skin was observed at any point during this study of nude mice receiving Se-*L*-M.

Possible skin irritation by Se-*L*-M after 5 d of exposure was histologically investigated as shown in Figure 5. Light microscopy indicated no observable damage to intact skin in the untreated group (Figure 5A). Histopathologic analysis of skin samples isolated from the area treated with 0.2% Se-*L*-M revealed some chronic inflammatory cells such as macrophages and lymphocytes in the dermis (Figure 5B). A partial loss of the SC was exhibited with this dose. When the dose was increased from 0.2% to 0.3%, less significant inflammation was seen in the dermis and subcutis (Figure 5C). Some disarray and disarrangement of the SC were observed. Histological changes to the skin due to treatment with Se-*L*-M were generally mild.

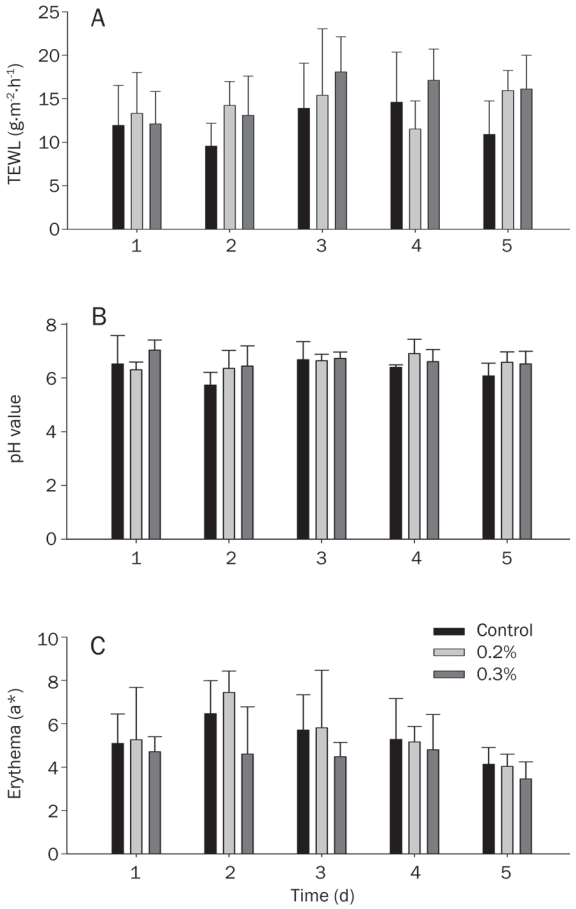

Figure 4. *In vivo* skin tolerance examination determined by transepidermal water loss (TEWL) (A), skin surface pH (B), and erythema (a*) (C) after an application of topically applied seleno-*L*-methionine from pH 8 buffer at a dose of 0.2% or 0.3% for 5 d. All data are presented as the mean±SD. *n*=6 experiments.

Discussion

Cumulative and prolonged exposure to UVB is now known to induce deleterious reactions in human skin, including cutaneous aging, immunosuppression, photo-carcinogenesis, and various inflammatory skin disorders[17]. Supplying topical exogenous antioxidants to the skin can prevent or minimize UVB-induced damage[18]. Despite various reports linking many of the beneficial properties of selenium to its use, no comprehensive study has been conducted to investigate the skin absorptive ability of related compounds. Moreover, penetration of the skin still needs to be separately determined for each metal species because of the large diversity permeation characteristics of various metal via the skin[15]. The present

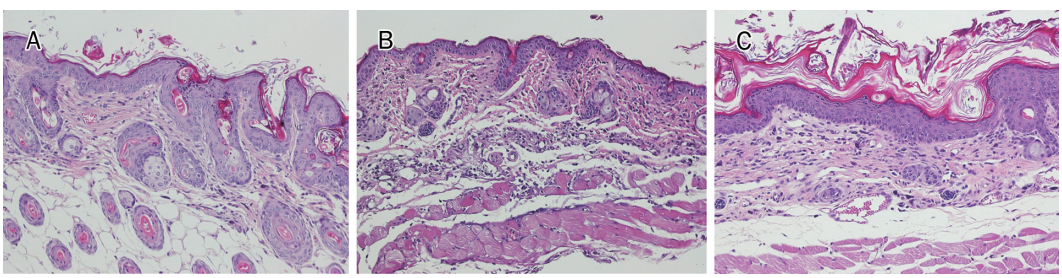

Figure 5. Histological examination of nude mouse skin stained with hematoxylin and eosin with no treatment (control group) (A), treatment with seleno-*L*-methionine from pH 8 buffer at a dose of 0.2% for 5 d (B), and treatment with seleno-*L*-methionine from pH 8 buffer at a dose of 0.3% for 5 d (C).

results showed that Se-*L*-M exhibited considerable absorption into the skin, especially with pH 8 buffer. The preliminary safety of Se-*L*-M to the skin was also evaluated. The results showed negligible irritation of the skin after *in vivo* topical administration, suggesting its feasibility for dermal use.

Porcine skin was initially used as the permeation barrier in this study because of its similarity to human skin. The skin of rodents is most commonly used for *in vitro* and *in vivo* skin permeation studies. There are a number of hairless species (*eg*, nude mice and hairless rats) in which the absence of a hairy coat mimics human skin better than hairy skin[19]. Hence nude mice were also utilized as an animal model in this study. The experimental results showed similar flux values between nude mouse skin and porcine skin in our case. This suggests that nude mice can be a successful model for evaluating the skin permeation of selenium compounds. Se-*L*-M in the buffers with higher pH values was found to penetrate more easily into and through the skin. The accumulation of a compound within the skin reflects the skin deposition after topical application. On the other hand, the concentration of a compound received in the Franz cell predicts the amount distributed to plasma or other organs in an *in vivo* status[20]. Both parameters were meaningful for Se-*L*-M. This selenium compound can prevent or treat UVB-related disorders in skin. The essential uptake for systemic levels of selenium in daily life was also achieved by a transdermal route.

Skin absorption of a permeant is determined by its physicochemical characteristics, in particular, its Mw and lipophilicity, which play major roles in the skin permeation process. Finnin and Morgan[21] indicated that molecules with a Mw of <500 Da can penetrate across the skin because of their small molecular volumes. Se-*L*-M fits this criterion (Mw 196.1 Da). Poor absorption is more likely when the octanol/water partition coefficient (logP) is >5 or <-1[17]. Se-*L*-M showed a logP of -3.01[22], which does not fulfill the criterion. This can explain the extremely low permeation of Se-*L*-M from pH 4 buffer. However, Se-*L*-M still demonstrated a considerable penetration in pH 8 and 10.8 buffers. Se-*L*-M is predominantly in a zwitterion form in pH 8 buffer, which is beneficial due to its lipophilicity. The neutral form of a compound always shows higher skin partitioning compared to the ionic form because of the lipophilic characteristics of the SC[23, 24]. The present findings suggest that the corresponding anions at pH 10.8 also showed high skin permeation. Increased pH can ionize a greater part of the intercellular fatty acids, changing the phase behavior and packing of the barrier lipid mixture[25]. The SC may be much more permeable to molecules in an alkaline vehicle[15]. This effect was not observed below pH 9 since the evidence indicates buffers at pH<9 did not compromise the barrier function[26].

A direct correlation between the skin deposition and flux was achieved for all Se-*L*-M formulations tested. The higher skin reservoir of the compound may result in high release into the receptor compartment because of the rapid diffusion due to the concentration gradient[24]. However, differences in skin deposition among formulations were smaller compared to those of flux values. For example, pH 8 buffer exhibited a 9-fold increase in skin deposition over pH 4 buffer, whereas a 127-fold increase was detected for the flux. The electrophilic nature of many metals determines their protein reactivity, which can result in depot formation in the SC[15, 27]. Se-*L*-M was found to replace methionine when incorporated into proteins[16], resulting in an abundance in the skin reservoir. A previous study[28] suggested that protection from UVB-radiation-induced human skin cell death can be obtained with concentrations of as low as 10 nmol/L with Se-*L*-M. This value can be calculated as 0.002 ng/g, a level that simulates skin deposition. Se-*L*-M showed skin deposition which was much greater than the minimum concentration for inducing protection efficiency.

The incorporation of an organic solvent such as glycerol, PG, or PEG400 in pH 8 buffer significantly reduced the permeation of Se-*L*-M. The addition of an organic solvent may have reduced the polarity of the aqueous vehicle as the solvent is relatively lipophilic. The decreased polarity with organic solvent incorporation in the vehicle hinders the partitioning of the permeant into the SC[29, 30]. Another explanation may be the higher viscosity of these solvents relative to the aqueous solution, making it difficult for the permeant to diffuse within the oil system. The data clearly showed an increased flux with PG compared to glycerol and PEG400. The permeation process is generally referred to as the drag-effect and may explain the effect of PG[31, 32]. Such data may indicate a polar route of delivery for Se-*L*-M.

It can be seen that the permeation of Se-*L*-M was not commensurate with the applied concentration. A 0.3% dose did not further increase the flux or skin deposition via porcine skin compared to a lower dose (0.2%). This can be interpreted as a saturation of the skin reservoir by the selenium compound. A dose of 0.3% Se-*L*-M even showed reduced permeation via nude mouse skin. This phenomenon is commonly observed with the skin delivery of metals. This is due to the buildup of a secondary diffusion barrier as a consequence of metals forming stable bonds with proteins of the skin[15]. In this way, a depot accumulates in the SC retarding further penetration in inverse proportion to the metal concentration. This effect may have been more pronounced for nude mouse skin than porcine skin.

With respect to drug permeation via the skin from the vehicle, a permeant should first diffuse out of the vehicle onto the skin surface. The release rate of Se-*L*-M across the cellulose membrane was significantly higher than that across porcine skin. This indicates that the skin exerted a significant barrier function against the transport of Se-*L*-M. The release profiles from various buffer systems approximated each other. Since a large discrepancy of skin penetration existed among the various buffers, the partitioning or permeation process via skin but not the release process was the rate-limiting step for Se-*L*-M. Tape stripping is a simple standard technique for evaluating the function of the SC in percutaneous absorption studies[33]. Se-*L*-M in pH 4 buffer showed the highest enhancement of skin permeation across SC-stripped skin compared

to the other buffer systems, suggesting that diffusion through the SC layer was important for permeation in a cationic form. Se-*L*-M permeation across stripped skin did not achieve the level of release across the cellulose membrane by the end of the experiment (24 h). This suggests that permeation was hindered by the SC, and the viable epidermis/dermis beneath the SC may have contributed to the aqueous resistance to its diffusion. The epidermal-dermal tight junction is an example of an important barrier for some materials[34]. This phenomenon was not observed for Se-*L*-M at pH 8 and 10.8 since the cumulative Se-*L*-M amount via stripped skin approximated the release amount at the end of the experiment.

Permeation through corneocytes (a transcellular pathway) and permeation through the lipid bilayers surrounding the corneocytes (an intercellular pathway) contribute to the routes of drug permeation across the SC. Delipidation greatly increased the skin permeation of Se-*L*-M at pH 4 compared to intact skin. This suggests that the intercellular lipid bilayers were the main barrier blocking the transit of Se-*L*-M in an acidic environment. The penetration rates of this compound via delipidized skin and intact skin were comparable in neutral and alkaline environments (pH 8 and 10.8). This indicates that the presence of lipid bilayers did not greatly influence the penetration of this selenium compound at these pH values. Intracellular or transappendageal routes may be pathways for Se-*L*-M delivery at pH 8 and 10.8. This result is in accordance with permeation from PG-containing vehicles. The penetration pathways of Se-*L*-M in pH 8 buffer were further investigated using ethanol, oleic acid, and α-terpineol as pretreatment media for the skin. Pretreatment with 25% ethanol resulted in a retardation of Se-*L*-M permeation. Changes in the skin's structure induced by ethanol reduced the delivery of some drugs[24, 35]. Protein denaturation in the SC may have been involved in this reduction. This result verified that the hydrophilic pathways through corneocytes can play an important role in the skin delivery of Se-*L*-M.

Oleic acid and α-terpineol were used as permeation enhancers for dermal/transdermal drug delivery. Oleic acid acts on the lipidic tail portion of intercellular lipid bilayers, while α-terpineol is known to act on the lipid polar heads of ceramides[36]. Oleic acid produced enhancement of the skin permeation of Se-*L*-M compared to the 25% ethanol-treated group. This suggests that the alkyl chain of the lipids could act as a barrier hindering permeation. It also confirms that the intracellular route may be essential for Se-*L*-M, since oleic acid can disrupt corneocytes[37]. Pretreatment with α-terpineol did not enhance the activity of Se-*L*-M permeation. This may indicate that hydrogen bonds between ceramides are not important for Se-*L*-M penetration across the SC.

Both inorganic and organic forms of selenium are commonly used for therapeutic and diagnostic purposes. The experimental results indicated that molecular stereochemical complexity can predominate the skin delivery of compounds. The *in vitro* skin permeation experiments demonstrated that the diffusion of the *L* and *DL* forms via porcine skin was stereoselective, with the *L* form showing higher permeation. This indicates that the SC contributed to the barrier function against percutaneous absorption of the *D* form. Since intracellular pathways were the predominant route for selenomethionine delivery, corneocytes may produce qualitative evidence of stereoselective interaction. This chiral interaction can cause differences in diffusion rates via the skin. Se-*L*-M may favor this interaction compared to the *D* form. According to previous studies involving the skin delivery of enantiomers[38-40], the *L* form (or *S* form) of ketorolac, ketoprofen, and selegiline also exhibited greater skin absorption than the *D* form (or *R* form).

Topical preparations containing selenium sulfide are frequently used to manage tinea versicolor, seborrheic dermatitis, and dandruff[41, 42]. It is commonly incorporated into shampoo for treating dandruff. Our results showed that the skin was virtually impermeable to selenium sulfide. Only a very low amount of selenium sulfide was retained in the skin reservoir. This is accordance with a previous study which found that selenium sulfide in shampoo is not absorbed by the skin[43].

Quantum dot nanoparticles have received attention due to their fluorescent characteristics and potential use in medical applications[34, 44]. Because the skin is the main target tissue for nanoparticle exposure, assessment of the skin penetration of quantum dots has attracted a great deal of attention. A recent development is utilization of selenium as a material for quantum dot preparations. The core of quantum dots consists of cadmium and selenium (CdSe), sometimes with a shell of ZnS to make them biologically compatible. Whether the quantum dots can permeate the skin is controversial. Recent investigations reported that skin penetration by quantum dots did not occur in intact mouse skin[45], was minimal in a murine model[46], and was detected in the lower SC layer of a human skin equivalent[47]. In our case, neither CdSe nor CdSe/ZnS quantum dots were absorbed by porcine skin. No or only negligible amounts in the receptor and skin reservoir were detected by analyzing selenium. This suggests that the shell of quantum dots was not damaged, and the CdSe core did not leach out. Penetration of quantum dots into the epidermal layers can result in a localized skin response, such as inflammation or cytotoxicity[26]. Cadmium and selenium are two components of the core that are known to be toxic to cells[34]. Our results indicated that quantum dots with a diameter of 6 nm may be safe for topical administration to skin tissue.

The electrophilic nature of many metals determines their protein interactions, which can result in depot formation in the skin. The *in vivo* skin uptake of Se-*L*-M was hence determined. The level of the *in vivo* skin reservoir was less than that in an *in vitro* condition. This was due to the significant diffusion and distribution of permeants from the skin to the systemic circulation or other tissues after *in vivo* topical administration, thus reducing the skin accumulation in an *in vivo* status. No significant difference in Se-*L*-M skin levels was observed between 4 and 8 h of administration. This can be explained by saturation of the skin reservoir. Another reason for the lower uptake of *in vivo* permeation was the shorter exposure time during the *in vivo* experiment compared to the *in vitro* experiment (24 h).

In addition to the efficiency of diffusion into the skin, the

skin tolerance is another concern for topical delivery systems. Selenium should be used with caution as a topically applied reagent since it may increase the risk of nonmelanoma skin cancer in excessive doses[48]. TEWL was utilized to assess the degree of SC disruption, and a good correlation between the chemical damage to the skin barrier and TEWL increment was demonstrated[49]. By evaluating established endpoints of skin irritation, the present work found that the topical application of Se-*L*-M for up to 5 d did not cause TEWL enhancement. Although Se-*L*-M caused some abrasion or disarray of the SC according to a histopathological examination, the barrier function of the SC did not fail. It was shown that the complete removal of lipids from the SC led to a 100-fold increase in water permeability[50]. Healthy skin has a slightly acidic pH, and the acidity of the skin maintains antimicrobial activity[18]. Disturbing this naturally acidic mantle may cause skin diseases. On the other hand, the a*-coordinate of colorimetry correlates well with inflammatory interactions of the skin, especially viable skin[24]. Se-*L*-M delivered by a topical route may be safe for both skin acidity and viable skin. Although inflammation occurred by monitoring skin slices, this irritation was not significant. An interesting result was that the inflammation induced by the 0.3% dose was less than that with 0.2%. This may have been due to a secondary barrier of the skin formed by the metals as cited above.

Conclusions

As demonstrated in this study, Se-*L*-M was readily absorbed by the skin in both the *in vitro* and *in vivo* experiments. Se-*L*-M in a zwitterion form revealed higher permeation compared to the other forms. A linear correlation was observed between the flux and skin deposition. The *DL* form of selenomethionine showed less skin absorption than did the *L* form, indicating a stereoselective character of this compound. Other selenium compounds including selenium sulfide and CdSe quantum dot nanoparticles exhibited no or only negligible skin delivery. Intracellular but not intercellular pathways were an important route for Se-*L*-M penetration via the SC. Summarizing the results of the present work, it was concluded that it may be suitable to develop dermal preparations of Se-*L*-M to protect against the harmful effects of UV. A preliminary safety examination of the skin indicated acceptable skin tolerance to Se-*L*-M. The established profiles of Se-*L*-M skin absorption will be helpful in developing topical products of this compound. More *in vivo* and clinical information on the efficacy and safety of the percutaneous absorption of Se-*L*-M is required to assess future practicability.

Acknowledgements

We thank the financial support from Chang Gung Memorial Hospital, Kweishan, Taoyuan, Taiwan, China (CMRPD170162).

Author contribution

Jia-you FANG and Saleh A AL-SUWAYEH designed research; Chih-hung LIN, Chia-lang FANG, and Shih-yun YANG performed research; Chih-hung LIN analyzed data; and Jia-you FANG and Saleh A AL-SUWAYEH wrote the paper.

References

1 Cross CE, van der Vliet A, Louie S, Thiele JJ, Halliwell B. Oxidative stress and antioxidants at biosurfaces: plants, skin, and respiratory tract surfaces. Environ Health Perspect 1998; 106: 1241–51.
2 Aziz MH, Reagan-Shaw S, Wu J, Longley BJ, Ahmad N. Chemoprevention of skin cancer by grape constituent resveratrol: relevance to human disease? FASEB J 2005; 19: 1193–5.
3 Richelle M, Sabatier M, Steiling H, Williamson G. Skin bioavailability of dietary vitamin E, carotenoids, polyphenols, vitamin C, zinc, and selenium. Br J Nutr 2006; 96: 227–38.
4 Nelson PS, Montgomery B. Unconventional therapy for prostate cancer: good, bad or questionable? Nat Rev Cancer 2003; 3: 845–58.
5 Wan XS, Ware JH, Zhou Z, Dohahue JJ, Guan J, Kennedy AR. Protection against radiation-induced oxidative stress in cultured human epithelial cells by treatment with antioxidant agents. Int J Radiat Oncol Biol Phys 2006; 64: 1475–81.
6 Clark LC, Graham GF, Crounse RG, Grimson R, Hulka B, Shy CM. Plasma selenium and skin neoplasms: a case control study. Nutr Cancer 1984; 6: 13–21.
7 Burke KE, Burford RG, Combs GF, French IW, Skeffington DR. The effect of topical *L*-selenomethionine on minimal erythema dose of ultraviolet irradiation in humans. Photodermatol Photoimmunol Photomed 1992; 9: 52–7.
8 McKenzie RC, Beckett GJ, McLean S, Arthur JR, Macve JC, Nicol F, *et al*. Differential effects of doses and forms of dietary selenium on immune cell numbers in the skin of ultraviolet-irradiated and unirradiated mice. Biol Trace Elem Res 2008; 125: 255–67.
9 Payette MJ, Whalen J, Grant-Kels JM. Nutrition and nonmelanoma skin cancers. Clin Dermatol 2010; 28: 650–62.
10 Ryan-Harshman M, Aldoori W. The relevance of selenium to immunity, cancer, and infectious/inflammatory diseases. Can J Diet Pract Res 2005; 66: 98–102.
11 Xiong S, Markesbery WR, Shao C, Lovell MA. Seleno-*L*-methionine protects against β-amyloid and iron/hydrogen peroxide-mediated neuron death. Antioxid Redox Signal 2007; 9: 457–67.
12 Vinceti M, Wei ET, Malagoli C, Bergomi M, Vivoli G. Adverse health effects of selenium in humans. Rev Environ Health 2001; 16: 233–51.
13 Heard CM, Johnson S, Moss G, Thomas CP. *In vitro* transdermal delivery of caffeine, theobromine, theophylline and catechin from extract of Guarana, *Paullinia Cupana*. Int J Pharm 2006; 317: 26–31.
14 Hung CF, Lin YK, Zhang LW, Chang CH, Fang JY. Topical delivery of silymarin constituents via the skin route. Acta Pharmacol Sin 2010; 31: 118–26.
15 Hostynek JJ. Factors determining percutaneous metal absorption. Food Chem Toxicol 2003; 41: 327–45.
16 Read JF, Wyand AEH. The kinetics and mechanism of the oxidation of seleno-*DL*-methionine by potassium ferrate. Transition Met Chem 1998; 23: 755–62.
17 Marti-Mestres G, Mestres JP, Bres J, Martin S, Ramos J, Vian L. The "*in vitro*" percutaneous penetration of three antioxidant compounds. Int J Pharm 2007; 331: 139–44.
18 Zhai H, Behnam S, Villarama CD, Arens-Corell M, Choi MJ, Maibach HI. Evaluation of the antioxidant capacity and preventive effects of a topical emulsion and its vehicle control on the skin response to UV exposure. Skin Pharmacol Physiol 2005; 18: 288–93.
19 Godin B, Touitou E. Transdermal skin delivery: predictions for humans from *in vivo*, *ex vivo* and animal models. Adv Drug Deliv Rev

2007; 59: 1152–61.
20 Pan TL, Wang PW, Al-Suwayeh SA, Chen CC, Fang JY. Skin toxicology of lead species evaluated by their permeability and proteomic profiles: a comparison of organic and inorganic lead. Toxicol Lett 2010; 197: 19–28.
21 Finnin BC, Morgan TM. Transdermal penetration enhancers: applications, limitations, and potential. J Pharm Sci 1999; 88: 955–8.
22 Meylan WM, Howard PH. Atom/fragment contribution method for estimating octanol-water partition coefficients. J Pharm Sci 1995; 84: 83–92.
23 Saija A, Tomaino A, Trombetta D, De Pasquale A, Uccella N, Barbuzzi T, *et al*. *In vitro* and *in vivo* evaluation of caffeic and ferulic acids as topical photoprotective agents. Int J Pharm 2000; 199: 39–47.
24 Zhang LW, Al-Suwayeh SA, Hsieh PW, Fang JY. A comparison of skin delivery of ferulic acid and its derivatives: evaluation of their efficacy and safety. Int J Pharm 2010; 399: 44–51.
25 Vávrová K, Lorencová K, Klimentová J, Novotný J, Holý A, Hrabálek A. Transdermal and dermal delivery of adefovir: effects of pH and permeation enhancers. Eur J Pharm Biopharm 2008; 69: 597–604.
26 Ryman-Rasmussen JP, Riviere JE, Monteiro-Riviere NA. Penetration of intact skin by quantum dots with diverse physicochemical properties. Toxicol Sci 2006; 91: 159–65.
27 Van Lierde V, Chéry CC, Roche N, Monstrey S, Moens L, Vanhaecke F. *In vitro* permeation of chromium species through porcine and human skin as determined by capillary electrophoresis-inductively coupled plasma-sector field mass spectrometry. Anal Bioanal Chem 2006; 384: 378–84.
28 Rafferty TS, McKenzie RC, Hunter JAA, Howie AF, Arthur JR, Nicol F, *et al*. Differential expression of selenoproteins by human skin cells and protection by selenium from UVB-radiation-induced cell death. Biochem J 1998; 332: 231–6.
29 Nicolazzo JA, Morgan TM, Reed BL, Finnin BC. Synergistic enhancement of testosterone transdermal delivery. J Control Release 2005; 103: 577–85.
30 Huang ZR, Hung CF, Lin YK, Fang JY. *In vitro* and *in vivo* evaluation of topical delivery and potential dermal use of soy isoflavones genistein and daidzein. Int J Pharm 2008; 364: 36–44.
31 Bowen JL, Heard CM. Film drying and complexation effects in the simultaneous skin permeation of ketoprofen and propylene glycol from simple gel formulations. Int J Pharm 2006; 307: 251–7.
32 Nicoli S, Bunge AL, Delgado-Charro MB, Guy RH. Dermatopharmacokinetics: factors influencing drug clearance from the stratum corneum. Pharm Res 2009; 26: 865–71.
33 Lademann J, Ilgevicius A, Zurbau O, Liess HD, Schanzer S, Weigmann HJ, *et al*. Penetration studies of topically applied substances: optical determination of the amount of stratum corneum removed by tape stripping. J Biomed Opt 2006; 11: 054026.
34 Zhang LW, Monteiro-Riviere NA. Assessment of quantum dot penetration into intact, tape-stripped, abraded and flexed rat skin. Skin Pharmacol Physiol 2008; 21: 166–80.
35 Wang JJ, Sung KC, Huang JF, Yeh CH, Fang JY. Ester prodrugs of morphine improve transdermal drug delivery: a mechanistic study. J Pharm Pharmacol 2007; 59: 917–25.
36 Panchagnula R, Desu H, Jain A, Khandavilli S. Effect of lipid bilayer alteration on transdermal delivery of a high-molecular-weight and lipophilic drug: studies with paclitaxel. J Pharm Sci 2004; 93: 2177–83.
37 Touitou E, Godin B, Karl Y, Bujanover S, Becker Y. Oleic acid, a skin penetration enhancer, affects Langerhans cells and corneocytes. J Control Release 2002; 80: 1–7.
38 Roy SD, Chatterjee DJ, Manoukian E, Divor A. Permeability of pure enantiomers of ketorolac through human cadaver skin. J Pharm Sci 1995; 84: 987–90.
39 Panus PC, Ferslew KE, Tober-Meyer B, Kao RL. Ketoprofen tissue permeation in swine following cathodic iontophoresis. Phys Ther 1999; 79: 40–9.
40 Fang JY, Hung CF, Chi CH, Chen CC. Transdermal permeation of selegiline from hydrogel-membrane drug delivery systems. Int J Pharm 2009; 380: 33–9.
41 Burke KE, Clive J, Combs GF, Nakamura RM. Effects of topical *L*-selenomethionine with topical and oral vitamin E on pigmentation and skin cancer induced by ultraviolet irradiation in Skh:2 hairless mice. J Am Acad Dermatol 2003; 49: 458–72.
42 Kakourou T, Uksal U. Guidelines for the management of tinea capitis in children. Pediatr Dermatol 2010; 27: 226–8.
43 Cummins LM, Kimuka ET. Safety evaluation of selenium sulfide shampoo in seborrheic dermatitis. Toxicol Appl Pharmacol 1971; 20: 89–96.
44 Frasco M, Chaniotakis N. Bioconjugated quantum dots as fluorescent probes for bioanalytical applications. Anal Bioanal Chem 2010; 396: 229–40.
45 Gopee NV, Roberts DW, Webb P, Cozart CR, Siitonen PH, Latendresse JR, *et al*. Quantitative determination of skin penetration of PEG-coated CdSe quantum dots in dermabraded but not intact SKH-1 hairless mouse skin. Toxicol Sci 2009; 111: 37–48.
46 Mortensen LJ, Oberdorster G, Pentland AP, Delouise LA. *In vivo* skin penetration of quantum dot nanoparticles in the murine model: the effect of UVR. Nano Lett 2008; 8: 2779–87.
47 Jeong SH, Kim JH, Yi SM, Lee JP, Kim JH, Sohn KH, *et al*. Assessment of penetration of quantum dots through *in vitro* and *in vivo* human skin using the human skin equivalent model and the tape stripping method. Biochem Biophys Res Commun 2010; 394: 612–5.
48 Duffield-Lillico AJ, Slate EH, Reid ME, Turnbull BW, Wilkins PA, Combs GF, *et al*. Selenium supplementation and secondary prevention of nonmelanoma skin cancer in a randomized trial. J Natl Cancer Inst 2003; 95: 1477–81.
49 Fang JY, Tsai TH, Lin YY, Wong WW, Wang MN, Huang JF. Transdermal delivery of tea catechins and theophylline enhanced by terpenes: a mechanistic study. Biol Pharm Bull 2007; 30: 343–9.
50 Serup J, Agner T. Colorimetric quantification of erythema — a comparison of two colorimeters (Lange Micro Color and Minolta Chroma Meter CR-200) with a clinical scoring scheme and laser-Doppler flowmetry. Clin Exp Dermatol 1990; 15: 267–72.